Title	The pyrolysis of 2-methylfuran: a quantum chemical, statistical rate theory and kinetic modelling study
Author(s)	Somers, Kieran P.; Simmie, John M.; Metcalfe, Wayne K.; Curran, Henry J.
Publication Date	2014-01-27
Publication Information	Somers, Kieran P., Simmie, John M., Metcalfe, Wayne K., & Curran, Henry J. (2014). The pyrolysis of 2-methylfuran: a quantum chemical, statistical rate theory and kinetic modelling study. Physical Chemistry Chemical Physics, 16(11), 5349-5367. doi: 10.1039/C3CP54915A
Publisher	Royal Society of Chemistry
Link to publisher's version	http://dx.doi.org/10.1039/C3CP54915A
Item record	http://hdl.handle.net/10379/6114
DOI	http://dx.doi.org/10.1039/c3cp54915a

PCCP

The Pyrolysis of 2-Methylfuran: A Quantum Chemical, Statistical Rate Theory and Kinetic Modelling Study

Journal:	*Physical Chemistry Chemical Physics*
Manuscript ID:	CP-ART-11-2013-054915.R1
Article Type:	Paper
Date Submitted by the Author:	n/a

Complete List of Authors:	Somers, Kieran; NUI Galway, School of Chemistry Simmie, John; NUI Galway, School of Chemistry Curran, Henry; NUI Galway, School of Chemistry; National University of Ireland, Chemistry Department Metcalfe, Wayne; National University of Ireland, Chemistry Department

Note: The following files were submitted by the author for peer review, but cannot be converted to PDF. You must view these files (e.g. movies) online.

2MF_Ab_initio.tex
All_Molecular_Data.dat
NUIG_ALKYLFURANS.MECH
NUIG_ALKYLFURANS.THERM
NUIG_ALKYLFURANS.TRAN
NUIG_ALKYLFURANS_FLAMES.MECH

Foreword

We are very grateful for the input of those who have taken the time to review our work; their comments should serve to improve the quality and presentation of the manuscript.

Referee 1 expressed the opinion that the quality of the work is high and that they were in favour of publication, after addressing minor queries. Reviewer 2 said the manuscript was well-written, comprehensive and had no revisions other than aesthetic ones. Referee 3 insisted the study was an original, stand-alone piece of work which should be accepted with revisions so minor that they did not need to re-review the work.

We feel we have addressed all comments both in the revised manuscript and in this document. Below, reviewers' comments are in black font and our response is in blue. Lines directly quoted from the updated manuscript are underlined and italicized for the editors/referees convenience.

Referee: 1

This paper presents a computational study of the pyrolysis of 2-Methylfuran. The approach adopted combines quantum chemistry calculations with master equation/RRKM simulations and some kinetic modeling. On the whole, it is my opinion that the quality of this work is high and I am therefore favorable to its publication. I think however that there are a few points that need to be fixed before recommending this work for publication. I list them below.

1)The paper is long. The authors know that and have already done a good job in moving a lot of material to SI. However I think that 24 pages are still too much. I suggest the authors to move some more material to the SI.

We have taken the referees advice and adopted effectively all of their requests. The new manuscript has been shortened by ~4 pages in length to 22 pages (some reviewers asked for extra detail in some cases so this added another ~2 pages). A recent similar study on the unimolecular decomposition of 2,5-dimethylfuran published in PCCP (Sirjean and Fournet, Phys. Chem.

Chem. Phys, 2013, 15, 596–611) was 16 pages in length. Bearing in mind that 2-MF has twice as many reaction pathways as 25DMF, and that we include a detailed kinetic modelling section to validate our calculations, 22 pages is not an unreasonable length for an encompassing discussion on the pyrolysis of 2-MF.

Though I leave to them the final choice of which materials to move, I suggest the following: part of the method section, for example the canonical TST equation and its description as well as the detailed description of the treatment of torsional motions;

We have removed the description of canonical TST from pages 5—6 of the original manuscript and as well as the treatment of torsional modes from page 6 of the original manuscript, as requested.

the PES of Figure 1 and its description (if I understood correctly, the reactivity on this PES is not relevant to the global reactivity of 2-Methylfuran);

We have taken the referees advice and moved this PES and its description to ESI and added the following paragraph to the start of this section to guide the reader (page 5, column 1):

"Potential energy surfaces for the formation and decomposition of β -carbenes are depicted in Figures 1 and 2 with corresponding rate constants (k_5–k_{13}) reported in Table 1. Unimolecular decomposition of 2MF through α-carbene intermediates was found to be uncompetitive with the β -carbene pathways due to due to the higher energy barriers encountered on their potential energy surfaces. A detailed discussion on these pathways can be found in ESI with the rate constants computed for these pathways (k_1–k_4) reported in Table 1."

the least important of the H-addition reactions of section 3.3. I also suggest to decrease the level of description of the PESs in the text, as the PES figures are almost self explanatory.

Again, we move these potential energy surfaces, discussions, and corresponding tables of rate constants, to supplementary material. We keep section 3.3 in the main text but refer the reader to ESI (page 14, column 2):

"Despite the rate constants for the initial hydrogen atom addition reactions at C-3 and C-4 being competitive with addition at C-2 and C-5, subsequent ring opening reactions are less facile, and these addition pathways are thus uncompetitive. For brevity in the main text, potential energy surfaces for hydrogen atom addition at C-3 and C-4 are shown and described in detail in ESI, along with relevant rate constants, k_{41}–k_{52} and k_{54}–k_{59}."

2)The author did not report how barrierless reactions were treated. Is it variational TST? Some comment is needed in the text (or in the SI).

Barrierless reactions were treated using an automatic feature of the ChemRate code where transition state properties are generated from the frequencies and rotational constants of the reactants and products. We did not use variational TST. The C-H fission reaction of 2MF was shown to be very minor based on our initial computations, and a full investigation of this reaction with high-level theory (Multi-reference quantum chemical calculations + variational TST) is probably not necessary as a result.

We include the following statement in the updated manuscript (page 8, column 1):

"Transition state properties (frequencies, rotational constants) for the C–H fission process have been generated automatically by the ChemRate code based on the properties of the reactants and products for the reaction and the microscopic rate constants, k(E), were then determined from the estimated transition state properties. k(E) were subsequently altered by an empirical fitting factor such that the high-pressure limiting rate constant described above was replicated at every temperature. The enthalpy of activation for the process was assumed equal to the the enthalpy of reaction at 0 K."

3)It is not clear why the authors have chosen a constant DEdown. There is now agreement that is should be temperature dependent. I think it would be useful if the authors could do some additional simulations on one of the most important PESs to check how this parameters affects the calculated rate constants.

$\langle \Delta E_d \rangle$ remains a rather empirical factor in RRKM models as energy transfer data is sparse in the literature and short of insightful kinetic experiments against which $\langle \Delta E_d \rangle$ can be optimised, empirical estimates are still rather frequent. We have based our constant $\langle \Delta E_d \rangle$ = 1000 cm^{-1} on similar studies in the recent literature for other aromatic compounds where constant $\langle \Delta E_d \rangle$ values have also been used ranging from 500—2000 cm^{-1} and have given a brief discussion in the text (page 4, column 2):

"For all simulations, the average energy transferred in a deactivating collision, $\langle \Delta E_d \rangle$, was assumed to have a temperature-independent value of 1000 cm^{-1}. Many recent literature studies have assumed constant $\langle \Delta E_d \rangle$ values for similar systems (large aromatic molecules). $\langle \Delta E_d \rangle$ estimates have ranged from 2000 cm^{-1} for the benzyl radical [50,51], 1000 cm^{-1} for a C7 heterocyclic ring [53], 718 cm^{-1} for a C10H10 biheterocycle [52], 500 cm^{-1} for pyrazole [54], fulveneallene [55] and benzyl hydroperoxide [56], and 260 cm^{-1} for 2,5-dimethylfuran [29–31] and furan [65]. Other recent studies have assumed temperature-dependent energy transfer parameters [57,58]. There is still remaining uncertainty in these energy transfer parameters but our empirical estimate of 1000 cm^{-1} lies well within the range of values adopted in recent literature studies. Some test calculations were carried out with $\langle \Delta E_d \rangle$ = 500 cm^{-1} and $\langle \Delta E_d \rangle$ = 2000 cm^{-1} to illustrate the variation in computed rate constants. The results are found in ESI and they show less than a factor of 2 variation in the computed rate constants for unimolecular decomposition pathways, and a factor of 2—3 variation in computed rate constants for major chemically activated pathways."

We have also included test calculations on the 2MF+H system and a unimolecular decomposition pathway of 2MF where $\langle \Delta E_d \rangle$ was varied ± a factor of two (500 and 2000 cm^{-1}) with results presented in ESI.

4)Reactions passing through TS3 and TS4 are of the Diels-Alder type. In this case a single reference method such CBS-QB3 or G3 is usually not a good choice to calculate barriers. This should be mentioned in the text. Reporting T1 diagnostic for TS3 and TS4 would also be useful. Luckily, if I got it right, these reactions are not competitive with the other channels for the system under study.

The reviewer is correct in that these pathways are insignificant. We have computed the T1 diagnostics for TS3 and TS4 and the resulting values are <0.02, thus indicating that multi-reference effects are negligible. We include the following statement in this section of the supplementary material:

"TS3 and TS4 correspond to those for Diels-Alder type reactions and multi-reference effects may be of importance. T1 diagnostics were therefore computed and found to be 0.019 for TS3 and 0.018 for TS4, thus indicating that the single-reference methods used suffice."

5)I see that the authors claim that they are able to compute phenomenological rate constants from a stochastic simulation. I am curious to know how they are able to distinguish between reaction channels starting from the same well that lead to stabilization of intermediate wells and reaction channels that pass through the well and proceed directly to form the products (in other terms, with reference to SI Table 1, how do they distinguish between M1 -> M9 and M1 -> P10 + P16 (BTW, I think there is a misspelling M10/P10 in the table) and why not, M1 -> P10+P15, M1 -> M8, M1 -> P3 +P4 (why are they not included?)).

The referee makes a good point. For the "chemically activated" reactions 2MF+H -> wells/bimolecular products, phenomenological rate constants can be determined from the concentration-time histories computed using the Multiwell code via the thermal decay method described by Pinches and da Silva. In this sense, the rate constants we report for 2MF+H -> stabilised wells/formally direct bimolecular products are "phenomenological"/"apparent" (which is what we state in the paper).

For multiple-well "thermally-activated" rate constants (the ones which the reviewer is specifically referring to above), the extraction of these apparent rate constants is much more difficult (to the extent that we cannot do it). We wrote to Prof. John Barker (the developer of the Multiwell code) at the outset of the project to get the best advice on how to achieve what the reviewer is asking, as we too were curious on how to do so. John told us:

"I don't know if it is possible to extract all of the possible rate constants from a complicated stochastic simulation, but it might be. I'd like to find out. It will

almost certainly require applying several different methods and carrying out multiple simulations under the same physical conditions of T,[M]."

He was clearly not quite sure on how and he is quite familiar with the state of the art in RRKM/ME methods. From what he told us, for a stochastic simulation of a multiple-well multiple-pathway thermally activated system, there is no ironclad description in the literature on how to extract phenomenological rate constants.

We fully understand why the reviewer is curious when we made this claim, but we did only make this claim for the reaction 2MF+H -> products, and not the reactions 2MF(+M)->intermediates(+M)->products(+M).

So, for the thermally activated systems we have investigated, we cannot seperate the reaction sequence M1->M9->P3+P4 into the two reactions (a) M1->M9, and (b) M1->P3+P4. We simply include pressure dependent rate constants from M1->M9 and in turn M9>M10 etc. based on calculations with the ChemRate code.

Ultimately our method for calculating the rate constants for 2MF+H->products are the same as a recent study by Sirjean and Fournet for 2,5-dimethylfuran+H (Proc. Combust. Inst., 2013, 34, 241–249.). Rate constants for our thermally activated systems use the same procedure as two recent works by Sirjean and Fournet on the thermal reactions of 2,5-dimethylfuran (Phys. Chem. Chem. Phys, 2013, 15, 596–611) and the 5-methyl-2-furanylmethyl radical (J. Phys. Chem. A, 2012, 116, 6675–6684.).

We hope that this clarifies the matter. With respect to other queries:

RE: The typo in the table in ESI (M10/P10), the reaction M1->M10+P17 is correct, it is the C-H fission process, so there is no typo.

RE: Why the reactions M1 -> P10 + P15 and M1 -> P10 + P16 do not have rate constants in the ESI? Even if we could extract these rate constants from our simulations (see previous discussion), they are not competitive with other product channels (P13+P14).

RE: The reaction M1->M8 (and the similar M1->M5), these are not included as we have simplified the potential energy surface for M1 decomposition as stated in the original manuscript (page 7, column 2)

"A number of simplifications are made to the potential energy surface for decomposition through β-carbenes. Both M4 and M7 are omitted from the RRKM/ME calculations as preliminary calculations showed that collisional stabilisation is inefficient for these species, owing to their shallow well depth. Only a single rotamer of 2,3-pentadiene-1-al (M6) and of 3,4-pentadiene-2-one (M9) is included in this analysis for simplicity."

6)I suggest to make the numbering of the reaction kx and that of the Tstates TSy coincide. It would help a lot the readability of the paper.

We have implemented the reviewers request and it certainly improves readability. We have added the following sentence at the start of the Results and Discussion section to guide the reader (page 5, column 1):

"In all subsequent sections, the subscript ($_x$) used to enumerate tabulated rate constants (k_x) corresponds with the number assigned to the transition state (TSx) for that reaction on a given potential energy surface. If a reaction does not have an accompanying potential energy surface (abstraction reactions or literature rate constants), other shorthand notations are used."

Referee: 2

Comments to the Author
This is a well written comprehenive manuscript. I suggest the 3D structures of the transition structures to be displayed either on the PES or in the SI.

We have included the geometries (Cartesian co-ordinates) of all stationary points in the ESI, which the reader can readily copy and paste into graphical visualisation software if they wish to analyse and manipulate these structures in 3-D. The ESI is already quite large (>100 pages), so it is probably best not to add another 50—100 pages with 2-D structures.

Referee: 3

Comments to the Author
Review of Somers et al on 2-methylfuran

This paper presents theoretical kinetic and kinetic modeling studies of 2-methylfuran, a potential biofuel. In the process of doing so the authors present a large number of results spanning mechanism, determination of rate constants and their pressure dependence, and Master Equation modeling, so it is certainly a stand-alone work. The work is very carefully done, original, and will be of interest to a number of investigators in physical chemistry. The paper is well written and provides detailed comparison with experiments. It conveys a number of insights about mechanism and the connection between kinetics and thermodynamics as applied to this system. This paper should be accepted with minor revision (no need to re-review).

I have some comments and corrections, which mostly range from minor to very minor. Page numbers start with the first page of the formatted manuscript.

Page 1, column 2, line 5: “re-think” seems colloquial

Changed to “re-consideration”

Page 2-3: The discussion of previous work provides more detail than necessary here. Much of the information presented is not directly referred to later on. This is especially true of the apparent 1st order rate constants for loss of 2MF. These might be interesting to compare in a graph later on (or in the ESI) but don’t work so well as text.

The reviewer is probably correct, and given that reviewer 1 also wanted the paper be shortened we have removed the detailed description of the work of Grela et al. and Bruinsma et al. and their pseudo-first order rate constants. Their experiments are not useful in our validation work as their experimental conditions are not well-defined.

Page 2, column 2, in discussing the work of Sendt “to energetic” should be “too endothermic”

Amended, page 2, column 1.

Page 3, column 1, in discussing the QRRK/MSC approach used in reference 32: It would be good to briefly comment on the differences in accuracy between the QRRK/MSC and RRKM/ME approaches.

We have added the following paragraphs (page 2, column 2—page 3, column 1) to highlight the two key differences between the QRRK/MSC and RRKM/ME approaches

“The QRRK/MSC approach varies from the RRKM/ME in two key respects. The first is that the former derives vibrational frequencies for reactants, and subsequent sums and densities of states, from a three-frequency fit to molecular heat capacities [34]. Microscopic rate constants, k(E), are in turn computed from the density of states of the reactant molecule together with an estimate of the high-pressure limiting rate constant for the reaction via the Inverse Laplace Transform (ILT) method. No knowledge of the transition state properties is required in this approach, although the high-pressure limiting rate constants can be computed from canonical transition state theory as was done in the work of Somers et al. [32] . The RRKM method derives sums and densities of states for reactants and transition states, and subsequently k(E), from more fundamental molecular ro-vibrational data typically obtained from quantum chemical calculations.

The second major difference lies in the approach to collisional energy transfer. Both the MSC and ME approaches assume that collisions occur based on the Lennard-Jones collision frequency. However, the MSC approximation assumes that every collision is completely activating or de-activating, and the Lennard-Jones collision frequency is simply altered by a weak-collision efficiency factor, B , which reduces the total rate of collisions in order to account for the fact that activation and de-activation require many collisions. The ME approach explicitly considers the transfer of energy between different energy levels and is thus a more physically realistic and accurate model for CET.”

Page 3 and elsewhere: “this work” is italicized for reasons that are unclear to me.

The emphasis indicates that this particular work is being referred to whereas “this work” can be referring to other studies; the English language is ambiguous in this regard and requires additional clarification by way of emphasis.

Page 3, Computational Methods: “6-31+G(d,P)” should be “6-31+G(d,p)”

Amended, page 3, column 2.

Page 4, column 1, the last full paragraph: the middle 50% of this paragraph seems to repeat itself a bit, and probably could be compressed somewhat without loss of clarity.

We have condensed this paragraph by using a scientific shorthand/symbology (page 4, column 1):

“Standard state enthalpies of formation ($\Delta_f H^{\ominus}$) of all C5H6O species are computed based on the $\Delta_f H^{\ominus}$ of 2-methylfuran[23], and $\Delta_R H^0$ (0 K) with subsequent extrapolation via enthalpy functions ($H_T - H_0$). $\Delta_f H^{\ominus}$ of ˙C5H7O radicals are derived from $\Delta_f H^0$ of 2MF and ˙H atom and $\Delta_R H^0$. For the 2-furanylmethyl radical, $\Delta_f H^0$ (78.07 kJ mol−1) is determined from $\Delta_R H^0$ (85.11 kJ mol−1) for the reaction 2MF -> ˙H + 2-furanylmethyl and the known $\Delta_f H^{\ominus}$ of 2MF and ˙H atom. $\Delta_f H^{\ominus}$ of all other ˙C5H5O radicals are computed relative to 2- furanylmethyl radical”

Page 4, column 2, 10 lines from the top: What was the test of numerical convergence?

A detailed description of the uncertainties associated with the stochastic method employed in the Barker Multiwell code is found in reference 47 of the manuscript and the manual of the Multiwell code, but to briefly demonstrate, below is a graph of two simulations for the reaction of 2MF+H (C2 addition) at 2.5 atm and 1250 K. The solid lines are simulations performed with 20,000,000 stochastic trials, the dashed lines were performed with 500,000 stochastic trials. With 20,000,000 trials the stochastic 'noise' is much reduced for minor reaction channels (M20 for instance)

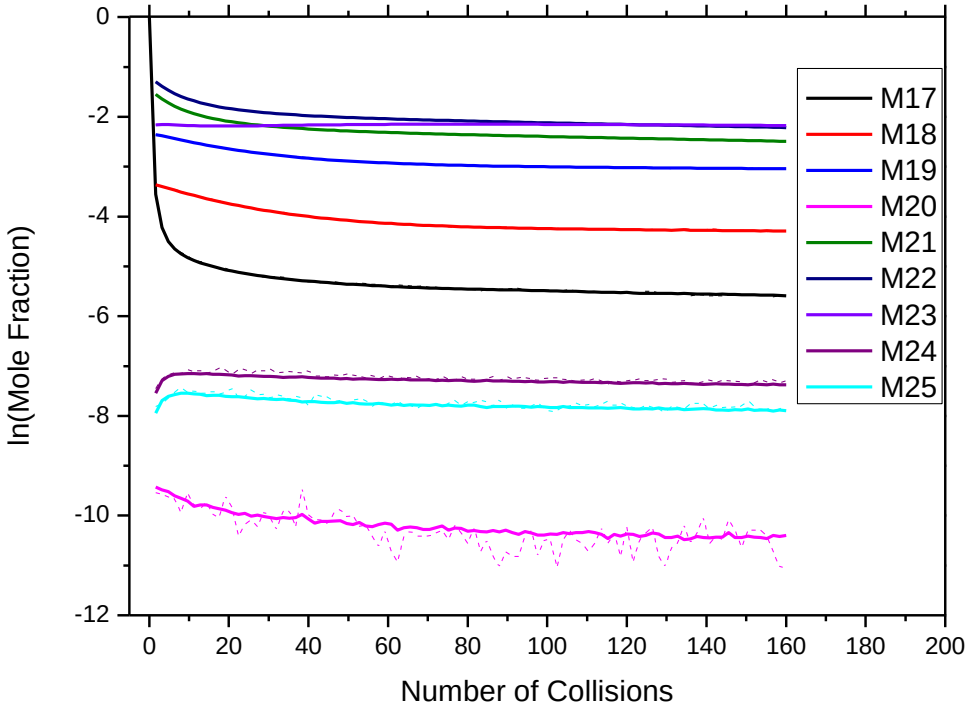

Rate constants can be extracted through linear fitting of the thermal decay region found in concentration-time profiles as in the graph overleaf (lower noise = more accurate linear fits). The method is described in further detail in the paper of Pinches and da Silva, Int. J. Chem. Kin, 2013, 45, 387–396.

20,000,000 stochastic trials gives good linearity in our fitted rate constants (it is also tending to an upper limit of what is computationally feasible.)

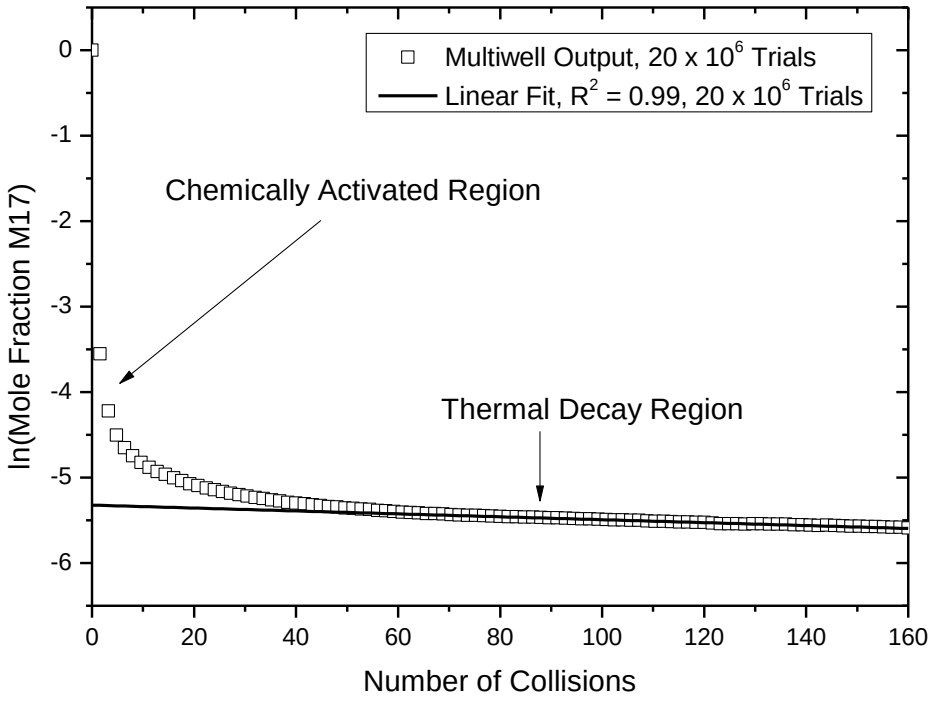

In summary, numerical convergence may have been the wrong term to use, we have changed the manuscript to highlight this by replacing "in order to achieve numerical convergence" with "*in order to minimise stochastic uncertainty for minor reaction pathways*" (page 4, column 1)

Page 4, column 2, 6 lines from the bottom: the value of ⟨_Ed⟩ is higher than what I recall seeing in other work. Some justification for this choice (at least a reference) would be good.

Referee number 1 had a similar query and references have been included as requested, please refer to Page 4, column 2, second paragraph of the manuscript.

Page 4, column 2, 4 lines from the bottom, describes how LJ parameters were determined for "2MF and its derivatives", and the reader is left to assume the same approach was used for fragments and the products of H-atom addition to 2MF.

Sentence added on page 4 column 2, second paragraph:

"All intermediates from 2MF decomposition, 2-furanylmethyl radical decomposition, and hydrogen atom addition pathways are assumed to have the same Lennard-Jones parameters."

A general comment: the three composite methods appear to agree very well with each other. This suggests an absence of multi-reference character/strong electron correlation, an issue which might be worth noting.

Line added on page 3 column 2:

"The three methods tend to give good agreement with each other, possibly indicating an absence of multi-reference character in the systems studied."

Page 5, the very last sentence before Section 3. I am not sure of the point of this sentence or the relevance of reference 53 here. Ref 53 does not mention the "Speed v0.72" code mentioned here.

The reviewer is correct, this is the recommended reference which ships with the code, but as they say, there is no reference to the code in the cited paper. We have removed this line and reference from the manuscript.

Page 5, Table 1 and the paragraph starting 3 lines below it: Specify that results are CBS-QB3

Amended, this section has been moved to ESI as requested by referee 1.

Page 5, column 2 gives an error bar for a reaction enthalpy. The authors should specify if this is 1 s.d. or 2.

Line added to computational methods section (page 3, column 2):

"Where uncertainties in quantum chemical calculations are reported in the text, it is to one standard deviation."

Page 5 column 2, in describing the failure of composite methods to find certain intermediates. It would be helpful to add the method used in the geometry optimizations at these points, since the failure is of a single method/basis set rather than of the composite method as a whole.

We have made a note of the model chemistry for the optimisation step in brackets at this point in the text (page 5, column 1).

Page 5 column 2, paragraph ending 11.6 •} 0.3 kJ/mol: It would be better to specify that this is _Hf

We assume the reviewer means $\Delta_r H$ (enthalpy of reaction), which is what we are reporting is equal to 11.6 +- 0.3 kJ/mol. We have re-computed our average and standard deviation (having found a minor error) and amended the text as follows (page 5, column 2)

"…with $\Delta_r H$ = 11.9 +- 0.7 kJ/mol."

Page 6, column 1, 6 lines from bottom: It would be good to specify _S# here, rather than at the end of the sentence.

Amended in manuscript (page 5, column 2).

Page 6, column 2, the paragraph that begins "Figure 4": It would be good to mention Tables 1 and 2 here.

Amended in manuscript (page 6, column 1)

Page 8, column 1, analogy with benzyl: I feel the authors should add (here rather than later) that they use Keq and the recombination rate constant to determine the addition rate constant.

Amended in manuscript, paragraph rearranged (page 7, column 2)

"From an estimated recombination rate constant of $9.25\times10^{13}\ T^{-0.01}\ exp(-96.9/T)\ cm^3\ mol^{-1}\ s^{-1}$ and the equilibrium constant for the reaction 2-furanylmethyl + $^{\cdot}$H atom <-> 2MF, a high-pressure limiting rate constant of $3.37\times10^{15}T^{-0.01}\ exp(-44026/T)\ s^{-1}$ for the dissociation reaction is computed through microscopic reversibility"

Page 8, column 1, last sentence of the paragraph referred to above: "The barrierless association" should be "The rate constant of the barrierless association"

Amended in manuscript (page 8, column 1).

Page 8, column 2, the one-sentence paragraph:

a) “Figure 6(a)” should be “As shown in Figure 6(a)”

Amended in manuscript (page 8, column 1)

b) It might help the reader to specify that M3 is the α-carbene.

Amended in manuscript (page 8, column 1)

c) It may be easier for the reader to interpret the word “and” if

“the formation of CH2CO and CHCCH through M3, and the simple fission of a C–H bond” is

changed to:

“the simple fission of a C–H bond and the formation of CH2CO and CHCCH through M3”

Amended in manuscript (page 8, column 1)

Page 9, Figure 6:

a) This is the Temperature dependence, not the pressure dependence.

Amended in manuscript (page 8, column 2)

b) It would help the reader, here and elsewhere, to specify the nature of the products rather than the number. Where this approach takes up too much space, it may still be possible to label pathways as, for example, α- versus β-carbene.

Extra detail has been added to the figure caption to clarify this matter (page 8, column 2).

Page 9, 2 lines below the caption to Figure 6: this is the temperature, not the pressure dependence.

Amended in manuscript (page 8, column 2).

Page 9, column 2, line 3: the CH≡CCH2• species is written as •CH=C=CH2 in Figure 3. It would be better to be consistent.

Amended in manuscript (page 8, column 2).

Page 9, column 2, start of Section 3.2: “Relevant computations” might be better as “Results of thermochemical and kinetic calculations” and “described” as “listed”

Amended in manuscript (page 9, column 1).

Page 9, column 2, 5th line of Section 3.2: There is an extra space before the period.

Amended in manuscript (page 9, column 1).

Page 9, column 2, 14th line of Section 3.2: “form” should be “from”

Amended in manuscript (page 9, column 1).

Page 10, column 2, last line: “implied from” should be “inferred from” or “implied by”

Amended in manuscript (page 9, column 2).

Page 11, column 1, 4 lines from the bottom: “resonant forms” is a potentially misleading description. Perhaps it would be better to write “resonance structures that lead to different configurational isomers” or some such.

Amended in manuscript (page 9, column 2).

Page 11, column 2, sentence starting on line 2: I suggest starting the sentence with “M15” and putting “M13” where “M15” is currently.

Amended in manuscript (page 11, column 1).

Page 13, column 2, middle: Figure 17 is listed prior to listing Figures 14-16.

Amended in manuscript, Figure 17 is now Figure 13 (page 15) and other Figures are re-numbered.

Page 13, column 2, 9 lines from bottom: “raidcal” should be “radical”

Amended in manuscript (page 14, column 2)

Page 13, column 2, last line: The issue of resonance stabilization was expressed previously, and does not need repeating (although it does not hurt).

We leave it as is, to jog the readers memory.

Page 14, Figure 12: Although not shown or discussed, M18 and M21 are conformers of each other, and M19 and M22 are conformers of each other. Their interconversion would have no effect on the kinetics, but it seems odd not to show the TS connecting each pair.

For isomerisation of M18<->M21 or M19<->M22, rotation about a double bond would have to occur. The double bond is highlighted as orange below (1—2) in a CBS-QB3 (B3LYP/CBSB7) optimisation of M21. The double bond character would make it very difficult for them to interconvert we believe. The influence of this on the kinetics as the reviewer says is probably quite minor also.

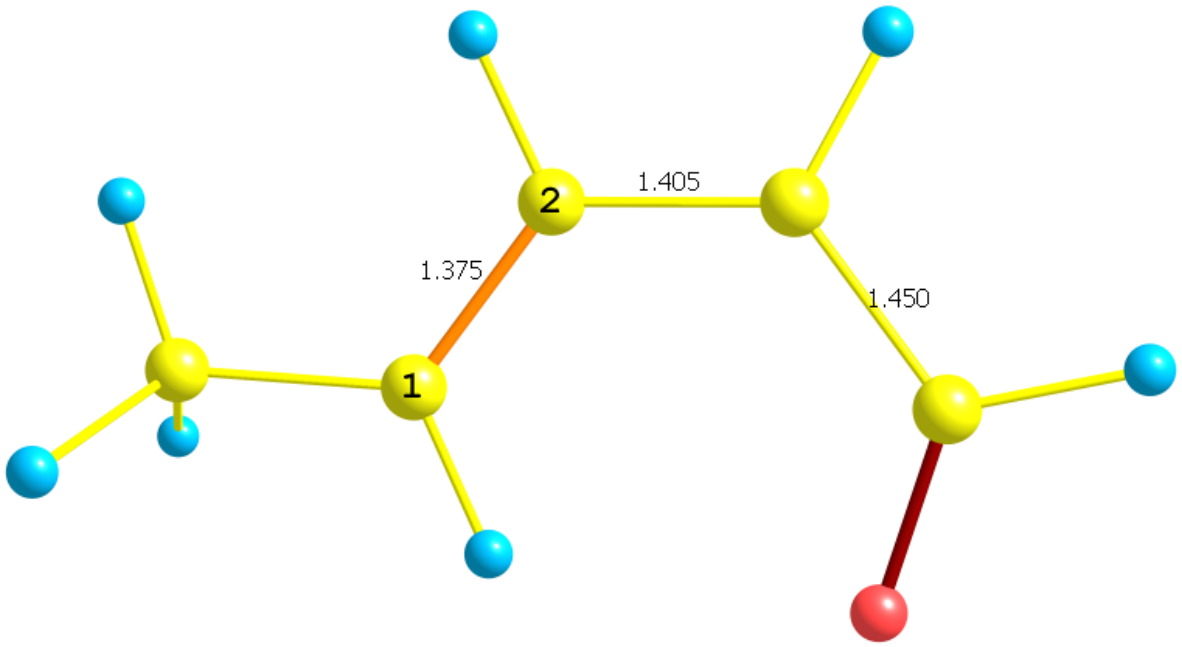

Page 14, Figure 12: M18, M19, M21, and M22 all have resonance structures with radical centers on the oxygen atom. Was there consideration of the possible reactions implied by that resonance structure? I do not see anything that looks likely to compete with the processes already described, but quantum chemistry sometimes challenges our intuition!

The reaction M18->M26 was considered as a possible reaction of the oxygen centered radical, but subsequent reactions of M26 were found to be uncompetitive.

Page 17, Start of Section 3.3.3: It would be good to point out similarities and contrasts to the reactions following H-addition to C-2. The pathways start out the same but then get very different, and while both produce CO, in one case the co-product is an allylic radical and in another case it is a vinylic radical.

We include a short paragraph at the end of Section 3.3.3 (page 16, column 1).

"In terms of the contrast between the addition of a hydrogen atom at the C-2 and C-5 positions of 2-methylfuran, both include a demethylation step with simultaneous formation of a C_4H_4O isomer. The relative stability of the furan ring is reflected in the fact that hydrogen atom addition forming a methyl radical and furan (C-2 addition), faces a much lower barrier than that forming a methyl radical and vinyl ketene (C-5 addition). Likewise, the elimination of CO is a common feature upon hydrogen atom addition at C-2/C-5. In both instances, the CO elimination process is quite rapid despite the differing nature of the co-products formed from these reactions (C-2 addition produces a vinylic radical, C-5 addition produces an allylic radical), and it is the hydrogen atom transfer reactions which precede the decarbonylation step, which will determine whether this process will ultimately occur."

Page 17, column 2, 3rd paragraph: The process M46 →M47 is not described.

Amended, (page 15, column 2).

"M46 can rearrange via β-scission (TS68) to form an aldehydic radical.."

Page 17, column 2, start of the 5th paragraph: "An analysis using RRKM/ME analysis theory" is redundant.

Amended in manuscript (page 16, column 1).

Page 20, Figure 19: the most noteworthy discrepancy between experiment and the present model is the time history of formaldehyde, but this is not commented on.

Formaldehyde (CH_2=O) was not detected in the study of Lifshitz et al., and we assume the reviewer is referring to ketene (CH_2=C=O, perhaps they misread the figure legend in Figure 16(d)?), for which we have given a detailed discussion of possible reasons for the discrepancy (Figure 17 and page 19 column 1 second paragraph).

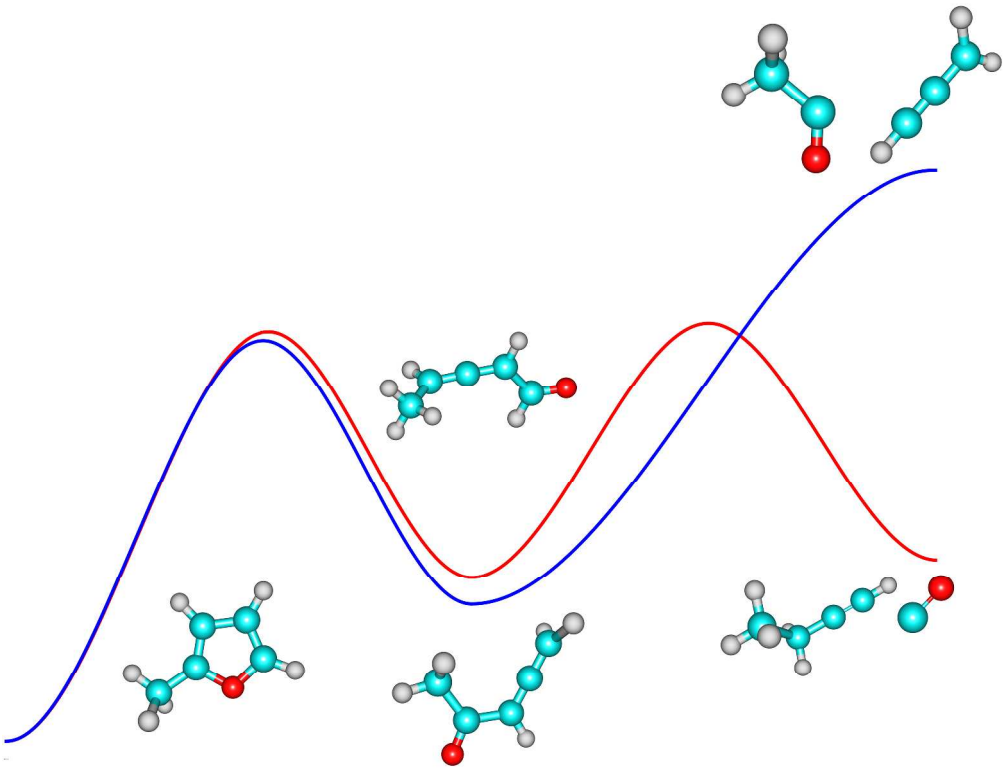

Pyrolysis of 2-methylfuran is initiated by hydrogen atom transfer reactions *via* β-carbene intermediates.
1357x1038mm (72 x 72 DPI)

ARTICLE TYPE
www.rsc.org/xxxxxx | XXXXXXXX

The Pyrolysis of 2-Methylfuran: A Quantum Chemical, Statistical Rate Theory and Kinetic Modelling Study†

Kieran P. Somers,*[a] John M. Simmie,[a] Wayne K. Metcalfe[a] and Henry J. Curran[a]

Received Xth XXXXXXXXXX 20XX, Accepted Xth XXXXXXXXX 20XX
First published on the web Xth XXXXXXXXXX 200X
DOI: 10.1039/b000000x

Due to the rapidly growing interest in the use of biomass derived furanic compounds as potential platform chemicals and fossil fuel replacements, there is a simultaneous need to understand the pyrolysis and combustion properties of such molecules. To this end, the potential energy surfaces for the pyrolysis relevant reactions of the biofuel candidate 2-methylfuran have been characterized using quantum chemical methods (CBS-QB3, CBS-APNO and G3). Canonical transition state theory is employed to determine the high-pressure limiting kinetics, $k(T)$, of elementary reactions. Rice-Ramsperger-Kassel-Marcus theory with an energy grained master equation is used to compute pressure dependent rate constants, $k(T, p)$, and product branching fractions for the multiple-well, multiple-channel reaction pathways which typify the pyrolysis reactions of the title species. The unimolecular decomposition of 2-methylfuran is shown to proceed *via* hydrogen atom transfer reactions through singlet carbene intermediates which readily undergo ring opening to form collisionally stabilised acyclic C_5H_6O isomers before further decomposition to C_1–C_4 species. Rate constants for abstraction by the hydrogen atom and methyl radical are reported with abstraction from the alkyl side chain calculated to dominate. The fate of the primary abstraction product, 2-furanylmethyl radical, is shown to be thermal decomposition to the *n*-butadienyl radical and carbon monoxide through a series of ring opening and hydrogen atom transfer reactions. The dominant bimolecular products of hydrogen atom addition reactions are found to be furan and methyl radical, 1-butene-1-yl radical and carbon monoxide and vinyl ketene and methyl radical. A kinetic mechanism is assembled with computer simulations in good agreement with shock tube speciation profiles taken from the literature. The kinetic mechanism developed herein can be used in future chemical kinetic modelling studies on the pyrolysis and oxidation of 2-methylfuran, or the larger molecular structures for which it is a known pyrolysis/combustion intermediate (e.g. cellulose, coals, 2,5-dimethylfuran).

1 Introduction

Dwindling energy reserves, increasing global energy demands and prices, and the threat of irreversible climate change have led to major research efforts focusing on the development of renewable energy sources, which can supplant fossil derived products and meet future demands in an economically, environmentally and socially sustainable manner.

Ethanol is currently the leading biofuel which offers an alternative to gasoline in the transportation sector, with 83.1 billion litres produced in 2012, primarily in Brazil and North America[1]. However, first-generation production methods which compete with food for feedstocks coupled with a low energy density, high vapor pressure, and complete miscibility with water have led to a re-consideration of its viability as a fossil fuel replacement[2].

Román-Leshkov and co-workers[3] reported a catalytic strategy for the conversion of fructose to 2,5-dimethylfuran (25DMF) *via* the platform chemical hydroxymethylfurfural (HMF) in 2007, with a host of research since following on processes for the conversion of waste biomass into HMF and in turn furanic based fuels[4–8].

25DMF has an energy density[3] of 31.5 MJ L^{-1} which is similar to a typical gasoline and a high boiling point, low water solubility, and the ability to use it in current internal combustion engines[9,10] makes it compatible with current infrastructure. These properties make 25DMF desirable when compared with ethanol, whose lower energy density, boiling point, and greater water solubility prove problematic, although engine tests[9,10] have shown that ethanol performs better than 25DMF in terms of knock resistance and hydrocarbon, nitrous oxide, carbon monoxide and particulate emissions.

[a] *Combustion Chemistry Centre, National University of Ireland, Galway, Galway, Republic of Ireland. E-mail: k.somers1@nuigalway.ie*

† Electronic Supplementary Information (ESI) available: [Tabulated pressure- and temperature-dependent rate constants derived from RRKM/ME computations; Potential energy surfaces for minor reaction pathways; Tabulated electronic energies (0 K and 298.15 K) and geometries for all stationary points; Frequencies, rotational constants and other information used in TST/RRKM computations are provided as input files compatible with the Thermo module of the Multiwell Program Suite; A comparison of high-pressure limiting rate constants reported in the work of Davis and Sarathy[35] with *this work*. The Chemkin-PRO format kinetics, thermochemistry and transport properties files used in the numerical modelling of all experiments; Results of computational modelling of literature burning velocities[32,64], ignition delay times[32,39] and flame speciation measurements[36]]. See DOI: 10.1039/b000000x/

Recently 2-methylfuran (2MF) has received similar attention to 25DMF as a possible alternative biofuel, with novel production methods under development[8]. Engine tests have ensued with Thewes et al.[11] and Wang et al.[12] studying the performance of 2MF in direct-injection spark-ignition engines. Thewes et al.[11] found that 2MF has excellent combustion stability, particularly in cold conditions, with hydrocarbon emission reductions of at least 61% compared to a conventional research octane number 95 fuel. Wang et al.[12] found that 2MF has a greater thermal efficiency than gasoline and 25DMF, that its overall regulated emissions are comparable with 25DMF, and that its aldehyde emissions are much lower than gasoline and ethanol.

Lifshitz and co-workers studied the decomposition of furan, 2MF and 25DMF[13–15] behind reflected shock waves at temperatures of 1050–1460 K, pressure of 1.5–3.0 atmospheres and residence times of 2 ms. Gas chromatography and mass spectrometry were used to quantify reactant and product species in the post-shock mixtures. A total of 17 products were quantified in their 2MF experiments[14] with CO found to be the major decomposition product. A range of C_1–C_4 species were also quantified with two oxygenated intermediates, ketene and furan. The order of reactivity of the series of furans was in line with previous studies (25DMF>2MF>furan)[16,17]. The experiments of Lifshitz *et al.*[14] will be discussed in detail in subsequent sections.

The theoretical work by Sendt[18] ultimately rationalised the decomposition pathways of furan, which were originally proposed as being routed through biradical intermediates[13,16,19]. The authors used CASSCF, CASPT2 and G2(MP2) computations to investigate the potential energy surfaces and kinetics of the thermal decomposition of furan. Hydrogen atom migrations on a singlet potential energy surface with the ultimate formation of CO and propyne, and C_2H_2 and ketene, were highlighted as the likely decomposition pathways and a chemical kinetic model constructed by the authors was capable of replicating experimental speciation profiles[19]. They concluded that ring scission of the C—O bond in furan, on either singlet or triplet potential energy surfaces, was simply too endothermic to contribute to the decomposition of the molecule, thus discounting the numerous postulates[13,16,19] of biradical initiated decomposition pathways for furan. Contemporaneously, Liu et al.[20,21] reached the same conclusion as Sendt *et al*.

Simmie and Curran[22] used quantum chemical calculations and isodesmic reactions to determine gas-phase formation enthalpies ($\Delta_f H^\ominus$) of a range of substituted furans and their radicals at 298.15 K, thus implying bond dissociation energies (BDEs). Their computed $\Delta_f H^\ominus$ of -80.8 ± 0.5 kJ mol^{-1} for 2MF is in good agreement with a calorimetric determination[24] of -76.4 ± 1.2 kJ mol^{-1} and subsequent very high-level theoretical determination by Feller and Simmie[23] of -80.3 ± 5 kJ mol^{-1}.

Simmie and Metcalfe[25] used electronic structure calculations to study the potential energy surfaces of a range of unimolecular decomposition, hydrogen atom addition and hydrogen atom abstraction reactions of 25DMF. Transition state theory was used to determine high-pressure limiting rate constants. Abstraction from the alkyl side chain of 25DMF to form the 5-methyl-2-furanylmethyl radical was highlighted as the preferred pathway for metathesis reactions. They also rationalised the formation of 2MF from 25DMF *via* a hydrogen-atom addition methyl-radical elimination sequence.

Quantum chemical calculations by Sirjean and Fournet[29–31] elaborated on the work of Simmie and Metcalfe[25] by further exploration of the potential energy surface for the decomposition reactions of 2,5-dimethylfuran, 5-methyl-2-furanylmethyl radical and the reactions of hydrogen atom with 25DMF. Rice-Ramsperger-Kassel-Marcus theory calculations with master equation analysis was used to determine pressure-dependent rate constants for each system. The decomposition of the 5-methyl-2-furanylmethyl radical was found to be result in the formation of cyclohexadienone isomers and a hydrogen atom. Hydrogen atom addition to 25DMF was found to primarily lead to the formation of 2MF and a methyl radical, and to a lesser extent, 1,3-butadiene and acetyl radical. Their computations on the total rate of hydrogen atom termination with 25DMF are in excellent agreement with the shock tube studies of Friese et al.[27,28].

Recently, Somers et al.[32] described experiments on the oxidation of 2MF, including measurements of ignition delay times and laminar burning velocities, with a chemical kinetic model developed which could adequately replicate these experiments. The model developed by Somers et al.[32] was based on preliminary *ab initio* calculations which were not described in detail at the time. The aim of *this work* is to describe those preliminary calculations in a more complete fashion. Quantum-Rice-Ramsperger-Kassel (QRRK) theory with a Modified Strong Collision (MSC) approach, as described by Chang *et al.*[33], was utilised in the previous work[32] to account for the influence of pressure on reaction rate constants. Here we utilize more rigorous Rice-Ramsperger-Kassel-Marcus (RRKM) theory calculations coupled with an energy grained master equation (ME) solution.

The QRRK/MSC approach varies from the RRKM/ME in two key respects. The first is that the former derives vibrational frequencies for reactants, and subsequent sums and densities of states, from a three-frequency fit to molecular heat capacities[34]. Microscopic rate constants, $k(E)$, are in turn computed from the density of states of the reactant molecule together with an estimate of the high-pressure limiting rate constant for the reaction *via* the Inverse Laplace Transform (ILT) method. No knowledge of the transition state properties is required in this approach, although the high-pressure limit-

ing rate constants can be computed from canonical transition state theory as performed in the work of Somers et al.[32]. The RRKM method derives sums and densities of states for reactants and transition states, and subsequently $k(E)$, from more molecular ro-vibrational data typically obtained from quantum chemical calculations.

The second major difference lies in the approach to collisional energy transfer (CET). Both the MSC and ME approaches assume that collisions occur based on the Lennard-Jones collision frequency. However, the MSC approximation assumes that every collision is completely activating or deactivating, and the Lennard-Jones collision frequency is simply altered by a weak-collision efficiency factor, β_c, which reduces the total rate of collisions in order to account for the fact that activation and de-activation require many collisions. The ME approach explicitly considers the transfer of energy between different energy levels and is thus a more physically realistic and accurate approximation for CET.

Since the development of the kinetic model by Somers *et al.*[32] a number of noteworthy studies on 2MF oxidation have been carried out contemporaneously with *this work*. Davis and Sarathy[35] reported reaction enthalpies, barrier heights and rate constants for several of the combustion and atmospheric reactions of 2-methylfuran based on quantum chemistry (CBS-QB3, G4) and canonical rate theory. Hydroxyl radical addition to the furan ring and subsequent O_2 addition reactions to the nascent adduct were investigated as possible reactions of significance under atmospheric and low-temperature combustion conditions. They also investigated unimolecular decomposition reactions of 2MF and abstraction reactions by hydrogen atom, although hydrogen atom addition reactions and the influence of pressure on the thermal decomposition pathways rate constants were not investigated. A small number of these high-temperature reactions are described in detail in *this work*, with the high-pressure limiting rate constants determined here in good agreement with the results of Davis and Sarathy[35]. A comparison of our results with Davis and Sarathy is presented in the ESI.

Tran and co-workers[36] recently studied the flame structure of two laminar premixed low-pressure (20 and 40 mbar) 2MF/O_2/Ar flames, with electron-ionization molecular beam mass spectrometry (EI-MBMS) and GC used to quantify reactant, intermediate and product concentrations as a function of distance from the burner. They provided a chemical mechanism for 2MF oxidation under these conditions, constructed largely by taking analogies to rate constants from 2,5-dimethylfuran[37] and furan[38] mechanisms available in the literature. Their mechanism was shown to satisfactorily reproduce their experimental results, as was the mechanism previously described by Somers et al.[32], although the former was not compared with the ignition delay time or laminar burning velocities against which the latter was also validated. The mechanism developed as part of *this work* is compared with these recently published measurements in the ESI, with good quantitative predictions of the major species reported experimentally.

Wei *et al.*[39] recently used a shock tube facility to determine ignition delay times of 2MF/O_2/Ar mixtures from equivalence ratios of 0.25–2.0, at temperatures of 1120–1700 K and at pressures of 1.25–10.65 bar. Their measurements are consistent with those of Somers *et al.*[32] at atmospheric pressure and provide valuable new data for kinetic modelling at elevated pressures. The kinetic model of Somers *et al.*[32] was used to numerically model the experimental results with reasonable agreement observed. The updated mechanism described herein is compared with these new ignition measurements in the ESI, with good reproduction of experimental measurements.

2 Computational Methods

Minima and transition states have been initially optimised using the B3LYP[40,41] functional coupled with the 6-31+G(d,p) basis set. Frequency analysis is employed to verify the nature of stationary points with the presence of a single imaginary frequency indicative of a transition structure, which is in turn connected to reactants and products *via* intrinsic reaction coordinate (IRC) calculations[42].

B3LYP optimised geometries are subject to further geometry optimisation, frequency analysis and single point energy calculations using the compound methods CBS-QB3[43], CBS-APNO[44] and G3[45] which have been used in numerous theoretical studies for the determination of thermochemistry and kinetics of furanic species of late[25,28–31,35,46]. The three methods tend to give good agreement with each other, possibly indicating an absence of multi-reference character in the systems studied. Calculations have been carried out using the Gaussian 03 and 09 applications[47]. Where uncertainties in quantum chemical calculations are reported in the text, it is to one standard deviation.

The Thermo application of the Multiwell program suite[48,49] has been used to determine thermochemical parameters (S, C_p and $H_T - H_0$, 298–2500 K) and high-pressure limiting rate constants, from canonical transition state theory. Internal rotations corresponding to low frequency torsional modes are analysed *via* relaxed potential energy surface scans, where geometries and energies are calculated as a function of dihedral angle in 10 degree increments. Potential energy and rotational constants (computed using the LAMM module of Multiwell) as a function of dihedral angle are fit to a series of truncated sine and cosine Fourier series and are used as input for a 1-D internal rotation approximation. For hydrogen atom transfer, abstraction, and addition reactions, the contribution of quantum mechanical tunneling has been accounted for *via*

the inclusion of asymmetric Eckart tunneling as implemented in Multiwell.

Standard state enthalpies of formation ($\Delta_f H^\ominus$) of all C_5H_6O species are computed based on the $\Delta_f H^\ominus$ of 2-methylfuran[23], and $\Delta_r H_0$ (0 K) with subsequent extrapolation *via* enthalpy functions ($H_T - H_0$). $\Delta_f H^\ominus$ of $\dot{C}_5H_7O$ radicals are derived from $\Delta_f H_0$ of 2MF and $\dot{H}$ atom and $\Delta_r H_0$. For the 2-furanylmethyl radical, $\Delta_f H_0$ (78.07 kJ mol^{-1}) is determined from $\Delta_r H_0$ (85.11 kJ mol^{-1}) for the reaction 2MF $\rightarrow \dot{H}$ + 2-furanylmethyl and the known $\Delta_f H^\ominus$ of 2MF and $\dot{H}$ atom. $\Delta_f H^\ominus$ of all other $\dot{C}_5H_5O$ radicals are computed relative to 2-furanylmethyl radical. Whilst isodesmic reactions could also be employed to determine the above parameters, the lack of well characterized companion species for error cancellation inhibits the development of suitable working reactions, particularly as the acyclic species which are formed upon opening of the 2MF ring are highly functionalised. The above method does ensure a consistent approach to thermochemical computations for inclusion in subsequent kinetic modelling work.

Many of the reactions investigated in *this work* correspond to those which are both temperature- and pressure-dependent. RRKM/ME calculations are used as a framework in order to evaluate the effect of the latter. RRKM/ME analyses of the chemically activated reactions of hydrogen atom with 2MF have been carried out using the stochastic method developed by Barker and co-workers implemented via the Multiwell program suite[48,49]. Sums and densities of states of reactants and transition states are evaluated using a direct count method with an energy grain size of 10 cm^{-1}, up to a maximum energy of 10^5 cm^{-1}. In order to minimise stochastic uncertainties for minor reaction pathways, 20×10^6 trials were carried out for 160 collisions at temperatures of 600–2000 K from 1–100 atm; for sub-atmospheric pressures, $1–2 \times 10^6$ trials were employed to minimise computational expense. Ro-vibrationally excited adducts were found to have undergone deactivation within the 160 simulated collisions under these conditions, before thermal unimolecular decay of the intermediate isomers subsequently occurred. Phenomological rate constants for the reaction 2MF + $\dot{H}$ $\rightarrow$ products were determined by monitoring concentration-time and vibrational energy-time profiles of the excited adducts using the Thermal Decay procedure recently described by Pinches and da Silva[50].

RRKM/ME analyses of the thermally activated unimolecular reactions of 2MF ~~was~~ carried out using the ChemRate code[51] as Multiwell is not optimally designed for the computation of slow steady state unimolecular reactions where the number of collisions being simulated is greater than a few thousand. In this case, the thermal unimolecular reaction of 2MF is slow below 1750 K and $>10^4$ collisions are required to achieve adequate consumption of the reactant for the extraction of rate constants from concentration-time profiles. For calculations using ChemRate, an energy grain size of 40–70 cm^{-1} was used up to a maximum of 10^5–1.5×10^5 cm^{-1} (depending on the specific temperature being studied). Convergence was monitored by ensuring that solutions to the Master Equation became time-independent with the "Divide and Conquer" method employed. The same method is used for computations on the thermal decomposition of the 2-furanylmethyl radical, although as chemical reaction for this species is much faster than for 2MF, a comparison of pressure-dependent rate constants derived from both Multiwell and ChemRate is presented. All RRKM/ME calculations are carried out based on ro-vibrational and energetic properties from CBS-QB3 calculations.

For all simulations, the average energy transferred in a deactivating collision, $\langle \Delta E_d \rangle$, was assumed to have a temperature-independent value of 1000 cm^{-1}. Many recent literature studies have assumed constant $\langle \Delta E_d \rangle$ values for similar systems (large aromatic molecules). $\langle \Delta E_d \rangle$ estimates have ranged from 2000 cm^{-1} for the benzyl radical[52,53], 1000 cm^{-1} for a C_7 heterocyclic ring[55], 718 cm^{-1} for a $C_{10}H_{10}$ biheterocycle[54], 500 cm^{-1} for pyrazole[56], fulveneallene[57] and benzyl hydroperoxide[58], and 260 cm^{-1} for 2,5-dimethylfuran[29–31] and furan[38]. Other recent studies have assumed temperature-dependent energy transfer parameters[59,60]. There is still remaining uncertainty in these energy transfer parameters but our empirical estimate of 1000 cm^{-1} lies well within the range of values adopted in recent literature studies. Some test calculations were carried out with $\langle \Delta E_d \rangle$ = 500 cm^{-1} and $\langle \Delta E_d \rangle$ = 2000 cm^{-1} to illustrate the variation in computed rate constants. The results are found in ESI and they show less than a factor of 2 variation in the computed rate constants for unimolecular decomposition pathways, and a factor of 23 variation in computed rate constants for major chemically activated pathways. All calculations are carried out in an argon bath gas with Lennard-Jones parameters for the third body taken as $\sigma = 3.47$ Å and $\varepsilon/k_B = 114$[61]. For 2MF and its derivatives Lennard-Jones parameters were determined empirically from the correlations provided by Kee and co-workers[62]. Together with recommended critical constants for 2MF[63], $\sigma = 5.36$ Å and $\varepsilon/k_B = 396$ are computed. All intermediates from 2MF decomposition, 2-furanylmethyl radical decomposition, and hydrogen atom addition pathways are assumed to have the same Lennard-Jones parameters.

Ultimately, the kinetics and thermochemistry produced as part of *this work* are used as input for a chemical kinetic model to describe the pyrolysis of 2MF, which is then compared with the shock tube data of Lifshitz et al.[14]. Shock tube simulations were carried out using the Aurora module (constant volume) of the Chemkin-Pro[65] software package with an average residence time of 2.05 ms and an average pressure of 2.5 atm.

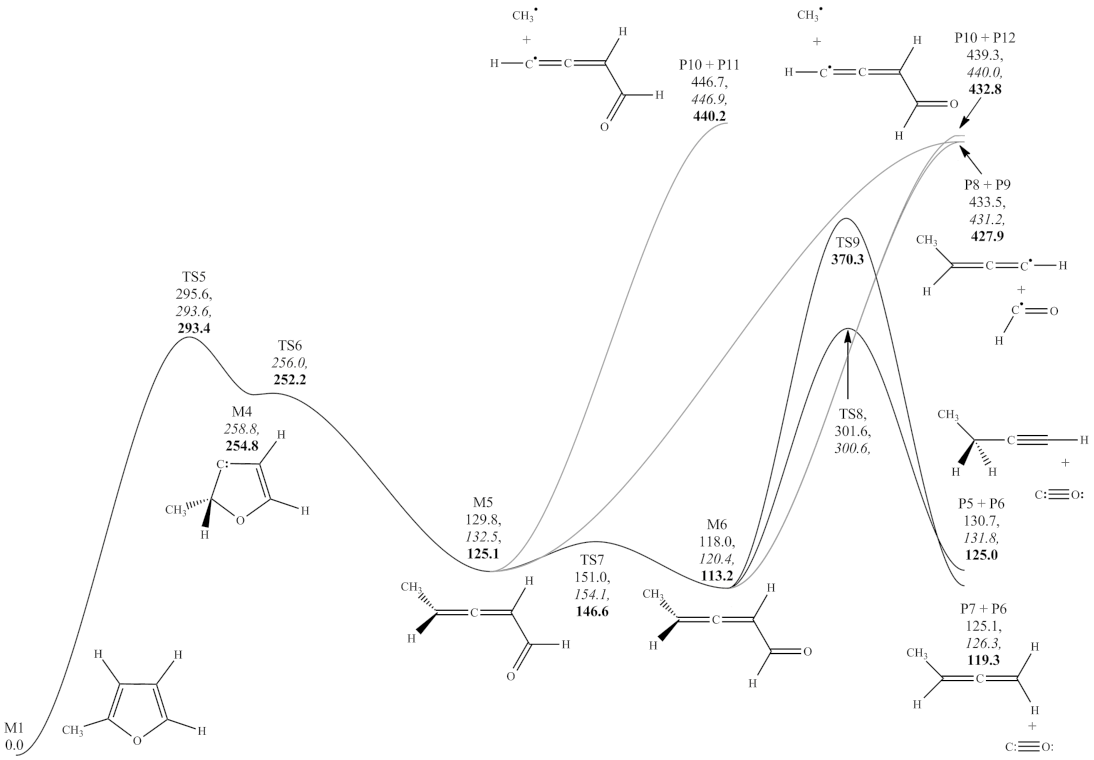

Fig. 1 Potential energy surface for the formation and decomposition of β-carbenes formed from 3→2 hydrogen shift. CBS-QB3, *CBS-APNO* and **G3** energies in kJ mol^{-1} at 0 K relative to 2-methylfuran.

3 Results and Discussion

In all subsequent sections, the subscript ($_x$) used to enumerate tabulated rate constants (k_x) corresponds with the number assigned to the transition state (**TSx**) for that reaction on a given potential energy surface. If a reaction does not have an accompanying potential energy surface (abstraction reactions or literature rate constants), other shorthand notations are used.

3.1 Carbene Mediated Unimolecular Decomposition

Potential energy surfaces for the formation and decomposition of β-carbenes are depicted in Figures 1 and 2 with corresponding rate constants (k_5–k_{13}) reported in Table 1. Unimolecular decomposition of 2MF through α-carbene intermediates was found to be uncompetitive with the β-carbene pathways due to due to the higher energy barriers encountered on their potential energy surfaces. A detailed discussion on these pathways can be found in ESI with the rate constants computed for these pathways (k_1–k_4) reported in Table 1.

A 3 → 2 hydrogen atom transfer, Figure 1, which forms a β-carbene intermediate (**M4**) has a computed barrier of 294.5 ± 1.6 kJ mol^{-1}. This intermediate could not be located using the CBS-QB3 method (B3LYP/CBSB7 optimisation step), which

Table 1 Arrhenius coefficients of high-pressure limiting rate constants for the decomposition of 2-methylfuran *via* carbene intermediates. $k(\mathrm{s}^{-1}) = AT^n \exp(-E_a/R)$, AT^n (s^{-1}), E_a/R (K).

No.	Reaction	A	n	E_a/R
k_1	M1 → M2	1.36×10^{11}	0.70	41593.
k_2	M1 → M3	2.26×10^{10}	0.99	32486.
k_3	M2 → P1 + P2	1.55×10^{12}	0.83	14343.
k_4	M3 → P3 + P4	8.54×10^{12}	0.68	15881.
k_5	M1 → M4	2.15×10^{10}	0.95	35145.
k_6	M4 → M5	2.80×10^{12}	0.30	−72.
k_7	M5 → M6	2.17×10^{13}	−0.24	2725.
k_8	M6 → P5 + P6	7.30×10^{10}	0.69	21872.
k_9	M6 → P6 + P7	3.40×10^{11}	1.00	30161.
k_{10}	M1 → M7	1.75×10^{10}	1.00	34174.
k_{11}	M7 → M8	6.11×10^{12}	0.09	552.
k_{12}	M8 → M9	1.26×10^{13}	−0.13	2146.
k_{13}	M9 → P3 + P4	3.91×10^{08}	1.48	33817.

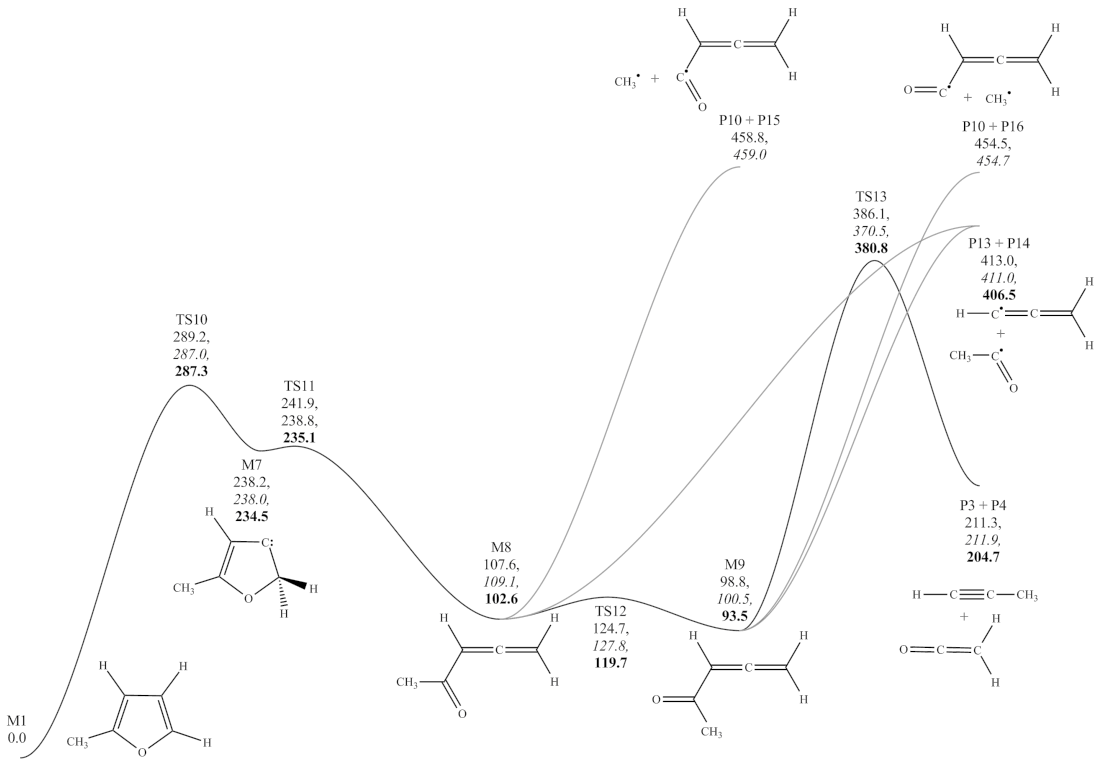

Fig. 2 Potential energy surface for the formation and decomposition of β-carbenes formed from 4→5 hydrogen shift. CBS-QB3, *CBS-APNO* and **G3** energies in kJ mol^{-1} at 0 K relative to 2-methylfuran. Variational processes in greyscale.

instead led to the cis conformer of 2,3-pentadiene-1-al upon optimisation. The same observation was noted in a computational study for the analogous process in 25DMF[25].

The CBS-APNO and G3 methods successfully locate this carbene intermediate existing at 256.8 ± 2.9 kJ mol^{-1} above 2MF. The subsequent ring opening reaction of the cyclic carbene is found to be extremely facile, with a transition state (**TS6**) being located 2.8 and 2.5 kJ mol^{-1} *below* the level of the reactants using the CBS-APNO and G3 methods respectively. The shallow nature of the β-carbene well likely contributes to the inability of the CBS-QB3 method to locate the reactant as a stationary point.

The product of ring opening exists in two rotameric forms (**M5** and **M6**) about the formyl group, which are connected by a rotational barrier of 21.4 ± 0.3 kJ mol^{-1}. The trans conformer (**M6**) can undergo CO elimination with a concomitant 1→4 hydrogen shift to form 1-butyne (k_8) in a near thermoneutral reaction with $\Delta_r H_0$ = 11.9 ± 0.7 kJ mol^{-1}.

The barrier for the process is computed as 183.6 kJ mol^{-1} based CBS-QB3 calculations, and 180.2 kJ mol^{-1} *via* the CBS-APNO method, in good agreement with G2(MP2) calculations[18] (175 kJ mol^{-1}) for the similar process in furan. A 1→2 hydrogen atom transfer to form 1,2-butadiene and CO is also possible, although the barrier is much greater at 252.2 kJ mol^{-1}.

Simple fission reactions are also possible for this acyclic species and BDEs of C—C bonds in the system have therefore been investigated, as they should coincide effectively with the barrier for these dissociation reactions. The formation of formyl radical (HĊO) and 1,2-butadiene-1-yl radical (ĊH=C=CH—CH$_3$) from the trans conformer is found to be endothermic by 321.7 kJ mol^{-1} based on standard state CBS-QB3 energetics, with fission to form a ĊH$_3$ radical and a formyl allene radical (ĊH=C=CH—CH=O) having a similar BDE of 327.9 kJ mol^{-1}. These homolytic processes face enthalpic barriers much greater than that computed for the lowest energy CO elimination process (circa 140 kJ mol^{-1}), and are therefore unlikely to contribute to the decomposition of the aldehyde.

β-carbene formation (**M7**) *via* a 4→5 hydrogen shift (Figure 2) proceeds through a barrier of 287.8 ± 1.2 kJ mol^{-1}, similar to that observed for the 2→3 hydrogen shift. The carbene can undergo ring opening through **TS11**, in an effectively barrierless process (1.69 ± 1.7 kJ mol^{-1}) to form 3,4-pentadiene-2-one.

Like the formyl butadiene product formed from a 3→2 hydrogen atom transfer, there exists cis and trans conformers of 3,4-pentadiene-2-one (**M8** and **M9**) with the trans conformer

(**M9**) capable of undergoing a 1→5 hydrogen shift in a concerted process to form ketene and propyne. A barrier of 287.3 kJ mol^{-1} is computed at the CBS-QB3 level of theory.

Given the tight nature of the transition state, we calculate a decrease in $\Delta^{\ddagger}S$ of −3.3 kJ mol^{-1} at standard temperature and only a slight increase in $\Delta^{\ddagger}S$ to 1.0 kJ mol^{-1} at 2000 K. C—C bond fission of the more stable trans conformer to acetyl radical (CH_3—$\dot{C}$=O) and the propargyl radical (CH≡C—$\dot{C}H_2$) is computed to be endothermic by 317.7 ± 1.8 kJ mol^{-1}, with the formation of a $\dot{C}H_3$ radical and a formyl allene radical (CH_2=C=CH—$\dot{C}$=O) found to be endothermic by 359.1 ± 4.5 kJ mol^{-1}.

The formation of CH_3—$\dot{C}$=O and CH≡C—$\dot{C}H_2$ radicals is energetically similar to the concerted elimination process and we therefore expect that simple fission is likely to be favoured over the elimination reaction at high temperatures, as the looser nature of the homolysis is likely to result in an increase in $\Delta^{\ddagger}S$ for the reaction.

Figure 3, and Tables 1 and 2, show calculated rate constants for the formation of carbenes in the homologous series furan, 2MF and 25DMF, with consistent rate constants emerging for the formation of α- and β-carbenes *via* hydrogen atom and methyl group shifts.

Table 2 Arrhenius coefficients of high-pressure limiting rate constants for –H and –CH_3 group shifts in 2,5-dimethylfuran and furan. $k(\mathrm{s}^{-1}) = AT^n \exp(-E_a/R)$, AT^n (s^{-1}), E_a/R (K).

No.	Reactant	Carbene, –R	A	n	E_a/R
$k_{Furan-\alpha}$	Furan[a]	α, –H	1.69×10^{12}	0.56	33782.
$k_{Furan-\beta}$	Furan[b]	β, –H	5.94×10^{13}	0.00	35372.
$k_{DMF-\alpha}$	25DMF[c]	α, –CH_3	7.77×10^{13}	0.00	41483.
$k_{DMF-\beta}$	25DMF[c]	β, –H	9.48×10^{13}	0.00	35230.

[a] *this work*, [b] Sendt *et al.*[18], [c] Simmie and Metcalfe[25]

Comparison is made with the computations of Simmie and Metcalfe[25] for the 25DMF system and Sendt *et al.*[18] who reported Arrhenius parameters for this process in furan. Rate constants for furan and 25DMF decomposition are reduced by a factor of two in Figure 3 for comparison with 2MF, given the loss of symmetry for the mono-alkylated furan, but those reported in Table 2 have not undergone this treatment. There is a close agreement within the computed rate constants amongst the homologous series, which may be of interest to kinetic modellers.

RRKM/ME analysis has been applied to determine pressure- and temperature-dependent rate constants for the multi-step collisionally activated decomposition pathways of 2MF. A number of simplifications are made to the potential energy surface for decomposition through β-carbenes. Both **M4** and **M7** are omitted from the RRKM/ME calculations as preliminary calculations showed that collisional stabilisation

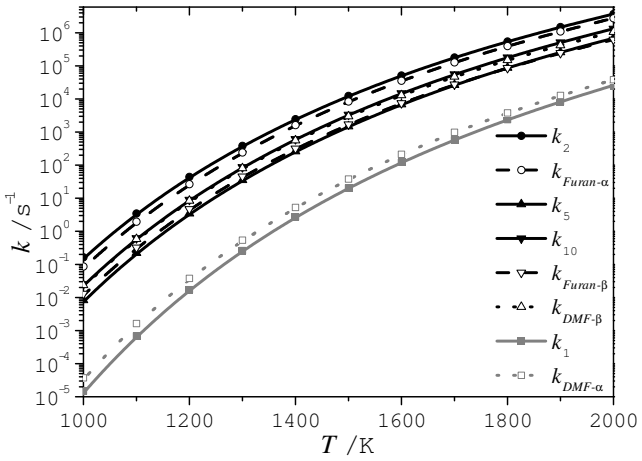

Fig. 3 A comparison of the high-pressure limiting rate constants for –H (black) and –CH_3 (grey) group transfer reactions in the homologous series furan (– –), 2-methylfuran (—) and 2,5-dimethylfuran (⋯). Furan and 2,5-dimethylfuran rate constants are reduced by a factor of two to account for the external symmetry number of 1 for 2-methylfuran.

is inefficient for these species, owing to their shallow well-depth. Only a single rotamer of 2,3-pentadiene-1-al (**M6**) and of 3,4-pentadiene-2-one (**M9**) is included in this analysis for simplicity.

Pressure-dependent rate constants for the β-carbene mediated decomposition of 2-methylfuran are shown in Figure 4. Under the experimental conditions of Lifshitz *et al.* (1150–1500 K, 2.5 atm), both reaction pathways are approximately at the high-pressure limit, with only ≈ 20% reduction in the computed high-pressure limiting rate constants at 1500 K and 2.5 atm. With increasing temperature and decreasing pressure however, the deviation of the rate constants from the high-pressure limiting case becomes more pronounced and there may be a need to account for fall-off effects under these conditions.

As part of our RRKM/ME calculations, we also consider the simple fission of 2MF into 2-furanylmethyl radical and $\dot{H}$ atom. The high-pressure limiting rate constant for this barrierless process is estimated based on an analogy with a literature[66] rate constant for the recombination of a $\dot{H}$ atom with the resonantly stabilised benzyl radical. From an estimated recombination rate constant of $9.25\times10^{13}T^{-0.01}\exp(-96.9/T)$ cm^3 mol^{-1} s^{-1} and the equilibrium constant for the reaction 2-furanylmethyl + $\dot{H}$ atom ⇌ 2MF, a high-pressure limiting rate constant of $3.37\times10^{15}T^{-0.01}\exp(-44026/T)$ s^{-1} for the dissociation reaction is computed through microscopic reversibility.

For the alkyl side chains of 2MF[22] and toluene[67] similar BDEs have previously been reported, 360.9 ± 5.2 and 375 ±

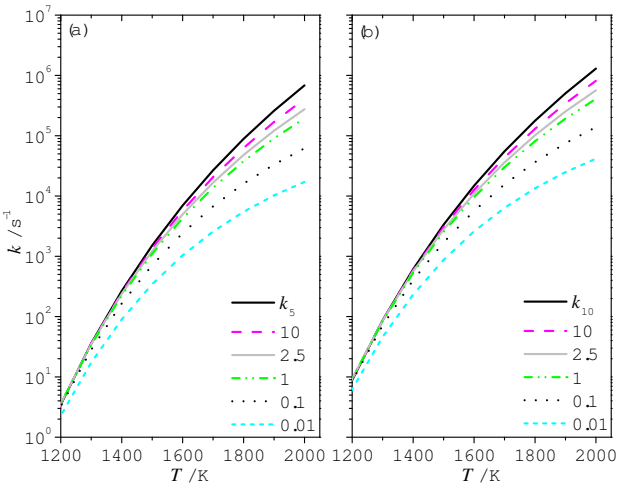

Fig. 4 Computed pressure-dependent rate constants (atm) for the decomposition of 2-methylfuran to (a) 2,3-pentadiene-1-al (**M6**) and (b) 3,4-pentadiene-2-one (**M9**).

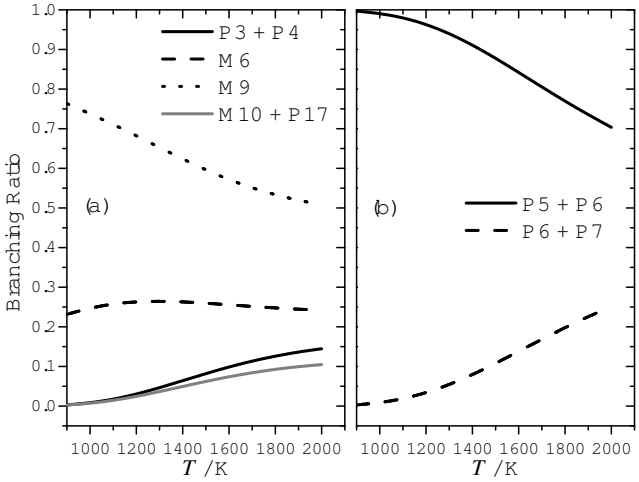

Fig. 5 Temperature-dependent branching ratios for the thermal decomposition of 2-methylfuran under the conditions of the Lifshitz *et al.*[14] study (2.5 atm). (a) 2-methylfuran → products; **P3 + P4** (ketene + propyne *via* α-carbene), **M6** (2,3-pentadiene-1-al *via* β-carbene), **M9** (3,4-pentadiene-2-one *via* β-carbene), **M10 + P17** (C–H fission) (b) **M6** → products; **P5 + P6** (1-butyne + CO), **P6 + P7** (1,2-butadiene + CO).

5.0 kJ mol^{-1} respectively. A BDE of 361.2 kJ mol^{-1} for 2MF is determined in *this work*. The high-pressure limiting rate constant of the barrierless association of a Ḣ atom with the 2-furanylmethyl radical may be expected to be of a similar order as that for the recombination of Ḣ atom with benzyl radical, and the high-pressure limiting rate constant described above should therefore be of a reasonable order.

Transition state properties (frequencies, rotational constants) for the C–H fission process have been generated automatically by the ChemRate code based on the properties of the reactants and products for the reaction and the microscopic rate constants, $k(E)$, were then determined from the estimated transition state properties. $k(E)$ were subsequently altered by an empirical fitting factor such that the high-pressure limiting rate constant described above was replicated at every temperature. The enthalpy of activation for the process was assumed equal to the the enthalpy of reaction at 0 K.

Based on temperature- and pressure-dependent RRKM/ME calculations under the conditions of Lifshitz *et al.* study[14], as shown in Figure 5 (a), decomposition *via* β-carbene intermediates is found to be dominant over the temperature range 1000–2000 K. 3→2 and 4→5 hydrogen atom shift reactions forming **M6** and **M9** are preferred to the simple fission of a C–H bond, and the formation of $CH_2{=}C{=}O$ and $CH{\equiv}C{-}CH$ through an α-carbene (**M3**).

Whilst a hydrogen atom transfer reaction to form an α-carbene (**M3**) is initially competitive with β-carbene formation (Figure 3), unlike the β-carbenes which can readily undergo ring opening, the α-carbene faces subsequent and much more substantial barriers in order to decompose to bimolecular products. A steady state analysis is employed at each pressure to compute the fraction of 2MF which will form $CH_2{=}C{=}O$ and $CH{\equiv}C{-}CH$ *via* **M3** and the results show that only above 1500 K and pressures of 1 atm will this pathway become competitive. C–H fission is found to be the least important unimolecular decomposition pathway of 2MF based on the present analysis.

The temperature-dependent branching ratios for the decomposition of **M6** are shown in Figure 5 (b). **M6** can decompose to form 1-butyne and CO or 1,2-butadiene and CO, with the former being favoured over the entire temperature and pressure range of Lifshitz *et al.* study[14]. The latter becomes competitive only at higher temperatures. **M9** is found to decompose exclusively to $CH_3{-}\dot{C}{=}O$ and $CH{\equiv}C{-}\dot{C}H_2$ radicals under all conditions of temperature and pressure. The high-pressure limiting rate constant for this reaction has been estimated in a similar fashion to the C–H fission reaction of 2MF, with an assumed rate constant for the recombination of $CH_3{-}\dot{C}{=}O$ and $\dot{C}H_2{-}C{\equiv}CH$ radicals of $5.2 \times 10^{12} T^{0.01} \exp(-114/T)$ cm^3 mol^{-1} s^{-1}. This implies a forward decomposition rate constant of $1.52 \times 10^{25} T^{-2.48} \exp(-39621/T)$ s^{-1}, which is ≈ 200 times faster than the tighter process (k_{13}) forming ketene and propyne.

In conclusion, the unimolecular decomposition of 2-methylfuran is shown to be initiated by 3→2 and 4→5 hydrogen atom shift reactions which are quite close to their high-pressure limits under the experimental conditions of Lifshitz *et al.*[14]. Once sufficient free radical species are formed from

the initial decomposition processes, abstraction of a hydrogen atom from the alkyl side chain should assume importance in the pyrolysis of this species. The unimolecular decomposition of 1-butyne and acetyl radical, which are formed as fragmentation products of 2MF, should result in the formation of methyl radicals, with the formation of hydrogen atoms from simple fission also possible but of lesser importance initially. Rate constants for abstraction processes by these radicals are therefore of interest, as is the fate of the primary fuel radical.

3.2 Abstraction Reactions and Thermal Decomposition of 2-Furanylmethyl Radical

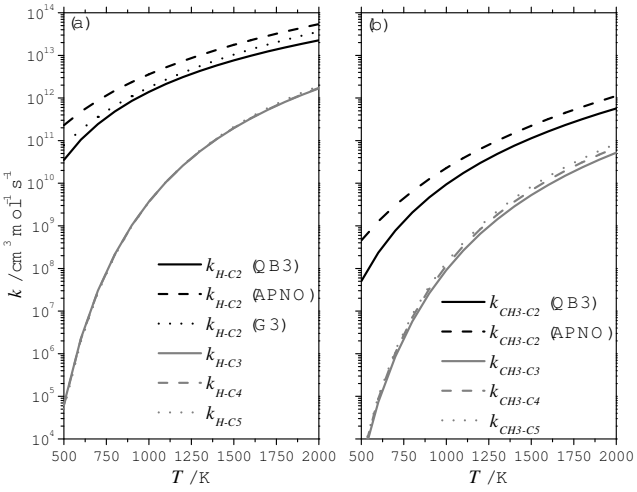

Fig. 6 Rate constants for hydrogen atom abstraction from 2-methylfuran by (a) hydrogen atom and (b) methyl radical. k_{H-C3}, k_{H-C4} and k_{H-C5} are effectively superimposed.

Results of thermochemical and kinetic computations on hydrogen atom abstraction reactions by $\dot{H}$ atom and $\dot{C}H_3$ radical are listed in Table 3.

Abstraction of a hydrogen atom from the methyl group of 2MF by a $\dot{C}H_3$ radical is calculated to be exothermic by -74.9 ± 4.0 kJ mol^{-1}, with a barrier of 39.3 ± 4.0 kJ mol^{-1}. Abstraction from the same site by a $\dot{H}$ atom faces lower barriers (27.9 ± 2.8 kJ mol^{-1}) but the exothermicity (-77.7 ± 2.8 kJ mol^{-1}) is of a similar order to that for abstraction by a $\dot{C}H_3$ radical.

Abstraction of any of the hydrogen atoms directly bonded to the furan ring is thought to be unlikely given their highly vinylic nature, with BDEs circa 505 kJ mol^{-1} reported previously[22]. Consistent rate constants for hydrogen atom abstraction by a $\dot{C}H_3$ radical and a $\dot{H}$ atom are reported for abstraction from these sites but it is evident that these processes are of little importance, Figure 6. As a result, the consumption reactions of the furyl radicals formed from these abstraction processes are not considered here.

Rate constants for abstraction from the alkyl group by a $\dot{H}$ atom, k_{H-C2}, are reported in Table 3 at three levels of theory, thus allowing for an assessment of the uncertainty in the computed rate constants. A factor of 2.5 variation is computed at temperatures of 1000–2000 K. In the same range of T, abstraction by methyl radical (k_{CH3-C2}) varies by a similar order.

The fate of the primary radical (**M10**) formed from abstraction from the alkyl side chain is depicted in Figure 7 with corresponding rate constant computations given in Table 4. Lifshitz included decomposition reactions for this radical in their proposed kinetic scheme with the formation of CO and the internal butadienyl radical ($CH_2{=}\dot{C}{-}CH{=}CH_2$) proposed as the major decomposition product. Decomposition to $H\dot{C}O$ radical and vinylacetylene ($HC{\equiv}C{-}CH{=}CH_2$), ketene and propyne, or $CH{\equiv}CH$, $\dot{C}_2H_3$ radical and CO was also included in their scheme, although no mechanistic proposals were made. In the temperature range 1100–1600 K, a total decomposition rate constant of $3.81 \times 10^{15} T^{0.11} \exp(-32149/T)$ s^{-1} is inferred from their work.

Ring opening of **M10** proceeds *via* cleavage of the C—O bond through a barrier of 167.9 kJ mol^{-1} from CBS-QB3 calculations with both CBS-APNO and G3 failing to locate the transition structure **TS14**. A high-pressure limiting rate constant of $1.38 \times 10^{13} T^{0.3} \exp(-20480/T)$ s^{-1} is calculated for the ring opening process from CBS-QB3 calculations.

The ring opening product, 3,4-pentadiene-1-one-2-yl radical, has multiple conformers but only two are of interest mechanistically, **M11** and **M12**. The latter conformer can undergo a 1→4 intramolecular hydrogen abstraction reaction through a five membered ring transition state (**TS17**), in a relatively low barrier (99.5 ± 3.1 kJ mol^{-1}) exothermic (-58.7 ± 2.3 kJ mol^{-1}) process. This reaction faces the highest barrier on the $\dot{C}_5H_5O$ potential energy surface, and reformation of **M12** from **M13** is unlikely due to the exothermicity of the reaction, and subsequent low energy exit channels which exist for the consumption of **M13**.

The β-scission of a C—H bond in **M11** to form 1,3,4-pentatriene-1-one (**P18**) was investigated as this species was detected experimentally in the flames of 25DMF[26] and 2MF[69]. With an endothermicity of 202.2 ± 3.9 kJ mol^{-1} and critical energy of 218.4 ± 1.5 kJ mol^{-1}, its formation is not competitive with the 1→4 intramolecular hydrogen abstraction reaction.

The product of the 1→4 hydrogen atom transfer reaction has two resonance structures that lead to different configurational isomers, **M13** and **M14**, connected by a transition state which lies 33.1 kJ mol^{-1} above **M13** and 3.4 kJ mol^{-1} above **M14**. IRC analysis (B3LYP/CBSB7) verifies the latter isomer undergoes decarbonylation (**TS19**) to form *n*-butadienyl radical ($\dot{C}H{=}CH{-}CH{=}CH_2$) and CO through a barrier of 99.4 kJ mol^{-1}. **M15**, a second conformer of **M13**, can undergo ring

Table 3 Computed barrier heights and enthalpies of reaction (kJ mol^{-1}, 0 K) and Arrhenius coefficients of high-pressure limiting rate constants for the reaction 2-methylfuran + $\dot{X} \rightarrow \dot{R}$ + XH. $k(\mathrm{cm^3mol^{-1}s^{-1}}) = AT^n \exp(-E_a/R)$, AT^n ($\mathrm{cm^3mol^{-1}s^{-1}}$), E_a/R (K).

No.	$\dot{X}$	Site	$\Delta^{\ddagger}H^0$	$\Delta_r H^0$	A	n	E_a/R
k_{H-C2} (QB3)	$\dot{H}$		26.6	−80.9	5.36×10^{4}	2.73	1785.
k_{H-C2} (APNO)	$\dot{H}$	C-2	25.9	−76.4	8.71×10^{0}	3.88	57.
k_{H-C2} (G3)	$\dot{H}$		31.1	−75.7	5.51×10^{-1}	4.20	216.
			± 2.8	± 2.8			
k_{H-C3}	$\dot{H}$	C-3	85.1 ± 3.4	64.1 ± 3.3	1.53×10^{8}	1.86	9666.
k_{H-C4}	$\dot{H}$	C-4	84.2 ± 3.3	63.4 ± 3.1	1.37×10^{8}	1.88	9700.
k_{H-C5}	$\dot{H}$	C-5	87.3 ± 3.7	63.4 ± 3.8	1.03×10^{8}	1.94	9838.
k_{CH3-C2} (QB3)	$\dot{C}H_3$	C-2	40.0	−78.1	1.21×10^{-2}	4.29	2254.
k_{CH3-C2} (APNO)	$\dot{C}H_3$		38.6	−76.2	4.36×10^{-7}	5.58	50.
			± 1.0	± 4.0			
k_{CH3-C3}	$\dot{C}H_3$	C-3	82.0 ± 0.3	66.9 ± 4.5	1.04×10^{2}	3.18	8274.
k_{CH3-C4}	$\dot{C}H_3$	C-4	82.5 ± 0.4	66.2 ± 4.3	1.31×10^{2}	3.19	8336.
k_{CH3-C5}	$\dot{C}H_3$	C-5	82.9 ± 0.8	66.2 ± 5.1	1.54×10^{2}	3.20	8397.

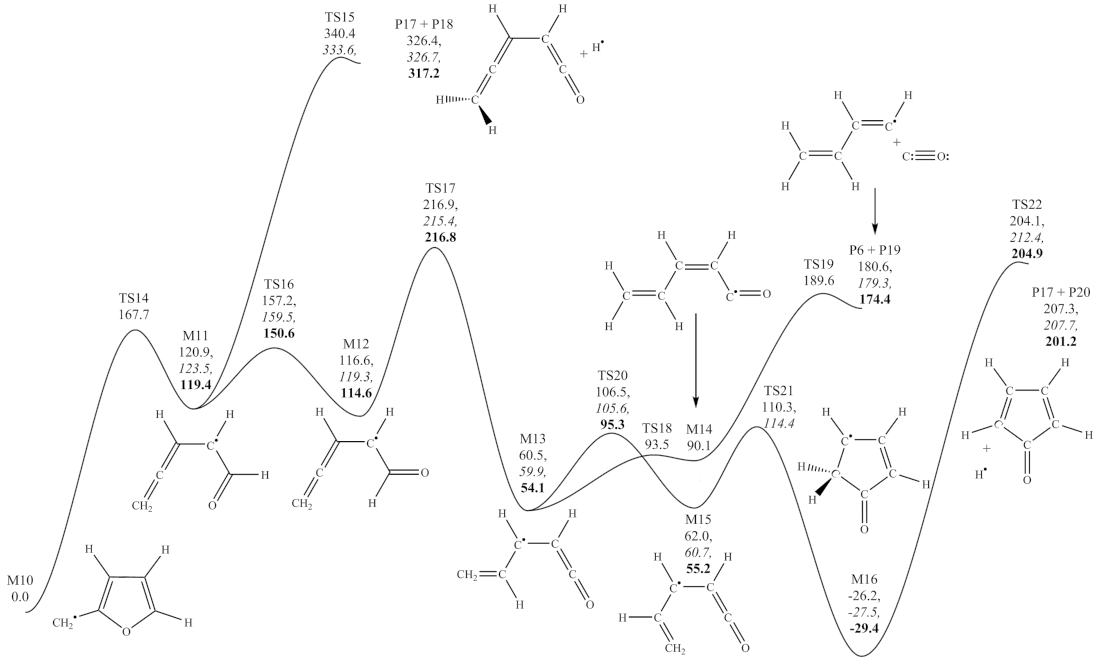

Fig. 7 Potential energy surface for the decomposition of the 2-furanylmethyl radical. CBS-QB3, *CBS-APNO* and **G3** energies in kJ mol^{-1} at 0 K relative to 2-furanylmethyl.

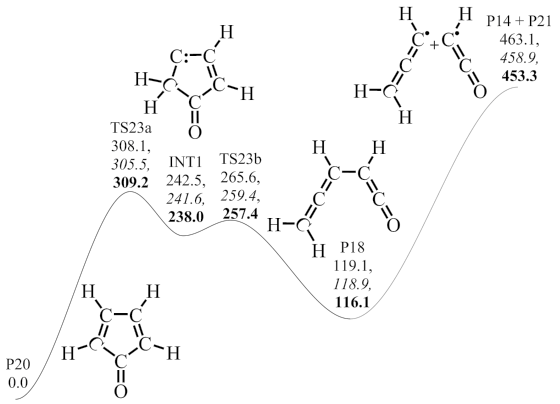

Fig. 8 Carbene intermediate in the isomerisation of 2,4-cyclopendadienone and 1,3,4-pentatrieneone. CBS-QB3, *CBS-APNO* and **G3** energies in kJ mol^{-1} at 0 K relative to reactant.

closure *via* a barrier of 51.0 ± 3.9 kJ mol^{-1} (**TS21**) to form a resonantly stabilised cyclopentenone radical (**M16**) which is is computed to be 27.7 ± 1.6 kJ mol^{-1} more stable than the 2-furanylmethyl radical.

The β-scission of a C—H bond is the only plausible consumption channel envisaged for (**M16**), forming cyclopentadienone (**P20**) and a hydrogen atom. The barrier for the endothermic process (233.1 ± 4.8 kJ mol^{-1}) is calculated to be 234.8 ± 4.8 kJ mol^{-1}, although the CBS-QB3 method predicts a negative critical energy (−3.19 kJ mol^{-1}) if viewed from the perspective of hydrogen atom addition across the double bond of cyclopentadienone.

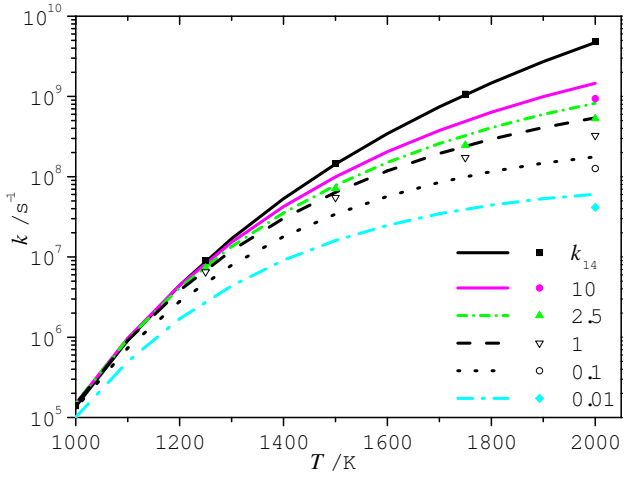

Fig. 9 Pressure- (atm) and temperature-dependent rate constants for the thermal decomposition of 2-furanylmethyl (**M10**) based on RRKM/ME calculations. ChemRate (—) , Multiwell (symbols).

Cyclopentadienone is a known intermediate in the combustion of cyclopentadiene and it is interesting to see a common feature between this five-membered ring and 2MF, namely, the formation and consumption of β-carbenes through a 1→ 2 hydrogen shift reaction on a singlet potential energy surface, Figure 8. The energetics and kinetics of the process were not considered in a previous analysis of cyclopentadienone decomposition[68]. Here we find they are of a similar order to those found in the decomposition of 2MF, with the computed rate constant for the hydrogen transfer reaction (k_{23a}) within a factor of two of those calculated for 2MF (k_5 and k_{10}) in the high-temperature regime. The carbene intermediate (**INT1**) can undergo ring-opening to form 1,3,4-pentatriene-1-one, which was detected in low-pressure flames of 25DMF[26] and 2MF[69].

Table 4 Arrhenius coefficients of high-pressure limiting rate constants for the decomposition of 2-furanylmethyl radical (**M10**) and related intermediates. $k(\mathrm{s}^{-1}) = AT^n \exp(-E_a/R)$, AT^n (s^{-1}), E_a/R (K).

No.	Reaction	A	n	E_a/R
k_{14}	M10 → M11	1.38×10^{13}	0.30	20480.
k_{15}	M11 → P17 + P18	9.12×10^{10}	1.15	26634.
k_{16}	M11 → M12	4.01×10^{13}	−0.08	4541.
k_{17}	M12 → M13	9.54×10^{06}	1.62	10071.
k_{18}	M13 → M14	1.50×10^{13}	−0.19	4046.
k_{19}	M14 → P6 + P19	8.61×10^{14}	0.19	12822.
k_{20}	M13 → M15	2.31×10^{13}	−0.13	5663.
k_{21}	M15 → M16	4.06×10^{12}	−0.15	5622.
k_{22}	M16 → P17 + P20	2.99×10^{11}	1.14	28149.
k_{23a}	P20 → INT1	1.03×10^{10}	1.21	36232.
k_{23b}	INT1 → P18	8.72×10^{12}	0.21	2987.

The formation of CO and *n*-butadienyl radical appears dominant in our scheme, once **M13** is formed the rate limiting steps for the formation of products are given by k_{19} and k_{22}, with k_{19} dominant in the temperature ranges we have studied.

Multiple-well, multiple-channel RRKM/ME calculations have been carried out to study the influence of pressure on the consumption of all $\dot{C}_5H_5O$ isomers. As a test of the uncertainty in the computed rate constants, both the Multiwell and ChemRate codes were employed in this analysis, with 10^6 trials used in the former. The computed rate constants for the thermal decomposition of **M10** (Figure 9) are within 30% of each other under all conditions studied. For all other intermediates, a factor of two difference was observed in the worst case scenario for the reaction **M15** → **M16** at 0.01 atm and 2000 K. The computed rate constants from the two codes are therefore in excellent agreement and a comparison of computed rate constants is presented in the ESI. The fall-off in the rate constant k_{14} appears to be non-negligible under high-temperature, low-pressure conditions and this fall-off effect must be considered in kinetic modelling studies, for example

the low-pressure flames of Tran and co-workers[36] and Wei *et al.*[69]. Rate constants computed using the ChemRate code from 0.01–100 atm and 800–2000 K are provided in the ESI for all reactions on the $\dot{C}_5H_5O$ potential energy surface, and are incorporated into our kinetic model as pressure-dependent reactions (Chemkin-Pro PLOG format).

3.3 Hydrogen Atom Addition Reactions

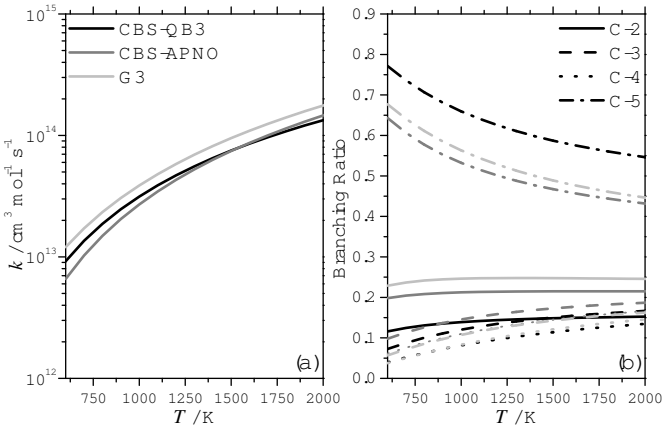

Fig. 10 (a) Total high-pressure limiting rate constant for hydrogen atom addition to 2-methylfuran and (b) site-specific branching ratios at various levels of theory. Colour scheme for theoretical methods in (a) also applies to (b).

Computed barrier heights, enthalpies of reaction and rate constants for $\dot{H}$ atom addition to 2MF are presented in Table 5 and Figure 10. Consistent reaction barriers and enthalpies of reaction are calculated for these processes. $\dot{H}$ atom addition to carbons adjacent to the oxygen atom of the furan ring are much more exothermic ($\approx$ 45 kJ mol^{-1}) than addition to C-3/C-4, and are thus favoured in terms of computed barriers heights. The difference in the computed $\Delta_r H_0$ upon addition at C-2 and C-5 versus C-3 or C-4 stems from the ability of the radicals to delocalise their unpaired electrons within the furan ring, with addition at sites removed from the oxygen atom resulting in radicals incapable of doing so. Rate constants are presented at three levels of theory for an assessment of their uncertainty. The total rate constant for hydrogen atom addition to 2MF varies by less than a factor of two across the three levels of theory applied, with site-specific branching ratios also predicting the following trend quite consistently amongst the methods: C-5 > C-2 > C-3 = C-4. This trend is in line with the reaction exothermicity upon addition at each site.

3.3.1 Addition at C-2. The potential energy surface for hydrogen atom addition to C-2 of 2MF is illustrated in Figures 11 and 12 with the corresponding rate constants provided in Table 6. The fate of the adduct formed from hydrogen atom addition at C-2 (**M17**) was previously investigated by Simmie and Metcalfe[25]. The authors calculated a rate constant of $2.232 \times 10^{14} \exp(-16292/T)$ for the demethylation process forming furan and a $\dot{C}H_3$ radical *via* **TS24**.

However, the authors did not investigate the result of cleavage of the C—O bond which could open the furan ring. Two chiral transition states were identified for this process (**TS26** and **TS30**) which are verified by IRC analysis to form Z- and E- conformers (**M18** and **M21**) of 3-pentene-1-one-2-yl radical. A total rate constant for ring opening can be determined from the summation of k_{26} and k_{30}. A rate constant of $8.69 \times 10^{12} T^{0.16} \exp(-11042/T)$ s^{-1} is thus computed, indicating that ring opening should be competitive with demethylation throughout the temperature range 1,000–2,000 K.

Both **M19** and **M22** can undergo a 1→4 hydrogen atom shift reaction to form an aldehydic radical (**M20**) which can decarbonylate through **TS29** in a reasonably low barrier process (101.9 kJ mol^{-1}) forming 1-butene-1-yl radical and CO. Mechanistically, this process is similar to that observed in the decomposition of the 2-furanylmethyl radical, where an aldehydic-type radical is formed before subsequent α-scission to form CO and *n*-butadienyl radical.

Further reactions of **M18** which could lead to the formation of either 1,3-butadiene and $H\dot{C}O$ radical or cyclopentadiene and $\dot{O}H$ radical were also investigated, Figure 12. The formation of 1,3-butadiene and $H\dot{C}O$ radical is inhibited firstly by a 1→4 hydrogen atom transfer from **M23** to form **M24** *via* **TS34**, for which a barrier of 171.0 ± 0.6 kJ mol^{-1} is calculated. On simple thermodynamic grounds the formation of these products was not envisaged to be competitive as the products are computed to lie 25.9 ± 3.7 kJ mol^{-1} above 2MF and hydrogen at 298.15 K, which is likely too endothermic ~~too~~ compete with the exothermic formation of furan and a $\dot{C}H_3$ radical or the 1-butene-1-yl radical and CO.

A 1→6 hydrogen atom transfer from the methyl group of **M18** to its oxygen atom to form an alcohol (**M26**), was found to face a very low initial barrier (**TS36**) of 85.0 kJ mol^{-1}. However, the subsequent ring closing reaction *via* **TS38** is too energetic (155.6 ± 0.9 kJ mol^{-1} relative to **M26**) for this reaction channel to be important. The products were computed to lie 36.9 ± 3.7 kJ mol^{-1} above the reactants, and pre- and post- reaction complexes are probably found in the process, but these are not investigated.

RRKM/ME derived product branching ratios from the chemically activated recombination of hydrogen atom with 2MF at C-2 are presented in Figure 13. Branching ratios for the formation of $\dot{C}_5H_7O$ isomers of the nascent adduct are lumped for clarity in Figure 13, but product specific rate constants are reported in the ESI. At high pressures (100 atm) the initially activated well (**M17**) is stabilised up to $\approx$ 1200 K, above this temperature the formation and stabilization of linear $\dot{C}_5H_7O$ radicals becomes dominant, thus indicating that

Table 5 Computed barrier heights and enthalpies of reaction (kJ mol^{-1}, 0 K), and Arrhenius coefficients of high-pressure limiting rate constants for hydrogen atom addition reactions to 2-methylfuran. $k(\mathrm{cm^3mol^{-1}s^{-1}}) = AT^n \exp(-E_a/R)$, AT^n ($\mathrm{cm^3mol^{-1}s^{-1}}$), E_a/R (K).

No.	Site	$\Delta^{\ddagger}H^0$	$\Delta^R H^0$	A	n	E_a/R
k_{24} (QB3)		12.2	−126.5	2.10×10^8	1.57	904.
k_{24} (APNO)	C-2	12.9	−128.0	2.67×10^7	1.89	776.
k_{24} (G3)		9.5	−127.3	3.33×10^7	1.88	421.
		11.54 ± 1.8	-127.3 ± 0.7			
k_{40} (QB3)		17.5	−80.9	3.72×10^8	1.54	1414.
k_{40} (APNO)	C-3	18.9	−82.4	3.48×10^7	1.87	1282.
k_{40} (G3)		18.7	−80.7	3.94×10^7	1.86	1281.
		18.4 ± 0.8	-81.3 ± 0.9			
k_{53} (QB3)		19.9	−84.6	2.01×10^8	1.61	1672.
k_{53} (APNO)	C-4	20.7	−85.9	1.88×10^7	1.95	1500.
k_{53} (G3)		20.1	−85.3	2.10×10^7	1.94	1460.
		20.2 ± 0.4	-85.3 ± 0.7			
k_{60} (QB3)		7.0	−133.2	1.20×10^9	1.48	468.
k_{60} (APNO)	C-5	9.6	−133.9	9.06×10^7	1.80	457.
k_{60} (G3)		6.2	−132.3	1.30×10^8	1.76	127.
		7.59 ± 1.8	-133.1 ± 0.8			

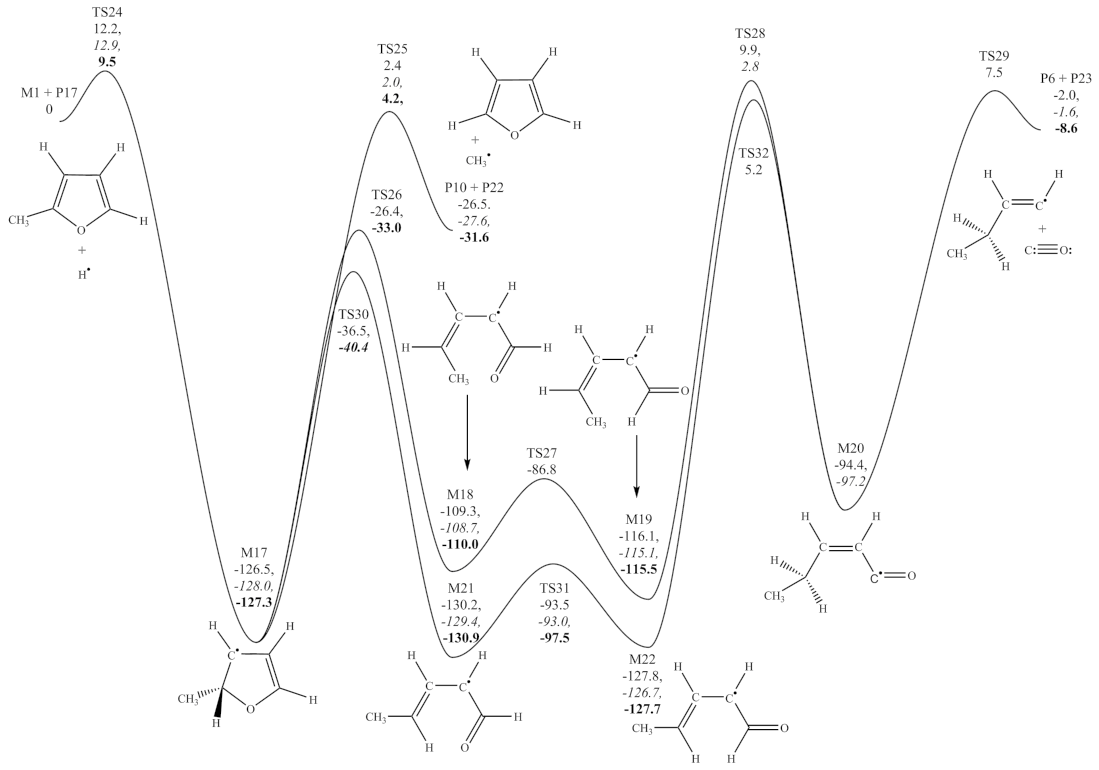

Fig. 11 Potential energy surface for hydrogen atom addition at carbon 2 of 2-methylfuran. CBS-QB3, *CBS-APNO* and **G3** energies in kJ mol^{-1} at 0 K relative to reactants.

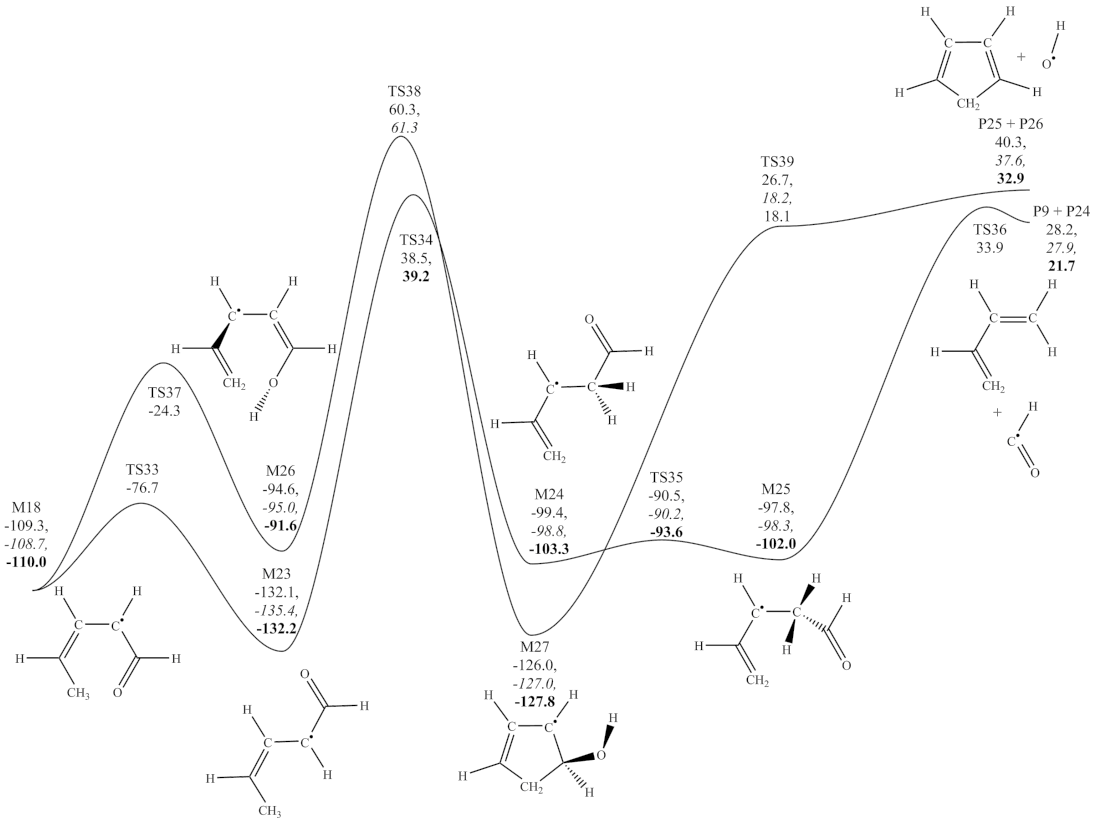

Fig. 12 Potential energy surface for hydrogen atom transfer reactions of 3-pentene-1-al-3-yl radical. CBS-QB3, *CBS-APNO* and **G3** energies in kJ mol^{-1} at 0 K relative to 2-methylfuran and hydrogen.

ring opening has become competitive with quenching of **M17**. Above 1600 K, furan and a methyl radical and 1-butene-1-yl radical and CO become major products, accounting for 40+% of the chemically activated yield.

These formally direct pathways become increasingly significant with decreasing pressure and in particular the formation of 1-butene-1-yl radical and CO, which must occur through multiple well-skipping reactions, starts to become the dominant bimolecular products of the reaction. The increasing branching ratio for 1-butene-1-yl radical and CO formation corresponds with the lack of quenching of linear $\dot{C}_5H_7O$ radicals with decreasing pressure. On the other hand, the branching ratio for formation of furan and n[illegible]l radical shows a lesser dependency on pressure ~~on the other hand~~, owing to the fact it is formed directly from the the initial chemically activated species (**M17**).

3.3.2 Addition at C-3 and C-4. Despite the rate constants for the initial hydrogen atom addition reactions at C-3 and C-4 being competitive with addition at C-2 and C-5, subsequent ring opening reactions are less facile, and these pathways are thus uncompetitive with addition at C-2 and C-5. For

Table 6 Arrhenius coefficients of high-pressure limiting rate constants for for reactions relevant to hydrogen atom addition at C-2 of 2-methylfuran. $k(s^{-1}) = AT^n \exp(-E_a/R)$, AT^n (s^{-1}), E_a/R (K).

No.	Reaction	A (s^{-1})	n	E_a/R
k_{25}	M17 → P10 + P22	9.23×10^{12}	0.38	15837.
k_{26}	M17 → M18	3.85×10^{13}	−0.09	12216.
k_{27}	M18 → M19	2.61×10^{11}	0.58	2710.
k_{28}	M19 → M20	2.49×10^{03}	2.59	12236.
k_{29}	M20 → P6 + P23	1.19×10^{15}	0.26	13053.
k_{30}	M17 → M21	3.85×10^{13}	−0.09	11003.
k_{31}	M21 → M22	2.33×10^{12}	0.26	4422.
k_{32}	M22 → M20	3.77×10^{05}	2.03	13440.
k_{33}	M18 → M23	9.21×10^{10}	0.53	3834.
k_{34}	M23 → M24	1.83×10^{08}	1.41	19235.
k_{35}	M24 → M25	2.18×10^{10}	0.50	746.
k_{36}	M25 → P9 + P24	2.67×10^{10}	1.20	15994.
k_{37}	M18 → M26	7.50×10^{00}	3.10	6584.
k_{38}	M26 → M27	1.45×10^{11}	0.42	18323.

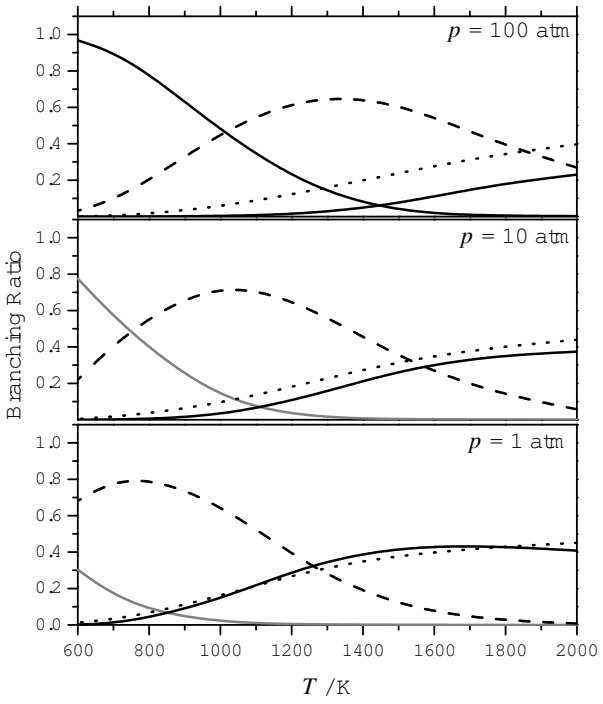

Fig. 13 Major product branching ratios as a function of temperature and pressure from RRKM/ME calculations on the chemically activated recombination of hydrogen atom with 2-methylfuran at C-2. — M17, – – ∑ other $\dot{C}_5H_7O$, ⋯ P10 + P22, – · – P6 + P23.

brevity in the main text, potential energy surfaces for hydrogen atom addition at C-3 and C-4 are described in detail in ESI, with relevant rate constants also reported therein, k_{41}–k_{52}, and k_{54}–k_{59}.

3.3.3 Addition at C-5. Figure 14 displays the potential energy surface investigated upon hydrogen atom addition at C-5. Ring opening of the adduct occurs through **TS61** with a ring-opening rate constant of a similar order to that computed upon hydrogen atom addition at C-2 (k_{26} and k_{30}). Demethylation of the ring opening product occurs through **TS62** to form vinyl ketene and a methyl radical, in a reaction computed to be endothermic by 176.4 ± 4.7 kJ mol^{-1}. A barrier of 202.0 ± 5.3 kJ mol^{-1} is computed for the process relative to the reactant and 61.7 ± 4.9 kJ mol^{-1} relative to 2MF and a hydrogen atom.

A secondary conformer of the ring opening product (**M43**) can undergo a hydrogen atom transfer reaction with a barrier of 124.6 kJ mol^{-1} (**TS64**) to form an acetonyl-like radical (**M44**), which can undergo β-scission to form ketene and a vinyl propene radical (k_{66}).

Ring closure of **M45** to form a cyclopropanone radical derivative (**M46**) is energetically more favourable than the formation of ketene and a vinyl propene radical, with the transition state for the process (**TS67**) computed to lie only 19.3 ± 3.1 kJ mol^{-1} above 2MF and hydrogen atom. **M46** can rearrange *via* β-scission (**TS68**) to form an aldehydic radical which is capable of eliminating CO through **TS70** to produce the resonantly stabilised butenyl radical (**P36**).

The potential energy surface investigated indicates that hydrogen atom addition at C-5 will proceed with competition between back dissociation to form 2MF and a hydrogen atom, the endothermic formation of vinyl ketene and a methyl radical in a relatively straightforward 3-step process, and exothermic formation of CO and $CH_2{=}CH{-}\dot{C}H{-}CH_3$ which faces many possible bottlenecks before formation. In terms of the contrast between the addition of a hydrogen atom at the C-2 and C-5 positions of 2-methylfuran, both include a demethylation step with simultaneous formation of a C_4H_4O isomer. The relative stability of the furan ring is reflected in the fact that hydrogen atom addition forming a methyl radical and furan (C-2 addition), faces a much lower barrier than that forming a methyl radical and vinyl ketene (C-5 addition). Likewise, the elimination of CO is a common feature upon hydrogen atom addition at C-2/C-5. In both instances, the CO elimination process is quite rapid despite the differing nature of the co-products formed from these reactions (C-2 addition produces a vinylic radical, C-5 addition produces an allylic radical), and it is the hydrogen atom transfer reactions which precede the decarbonylation step, which will determine whether this process will ultimately occur.

An RRKM/ME analysis, Figure 15, shows similar trends to those observed for hydrogen atom addition at the C-2 position. At 100 atm collisional deactivation of chemically activated **M41** dominates the product branching fractions up to 1000 K, at which point linear $\dot{C}_5H_7O$ radicals start to form and subsequently stabilize. As a result, the formation of bimolecular products is insignificant at temperatures up to ≈ 1700 K. At 1 atm the furanyl radical does not persist above 1000 K and above 1300 K, the formation of bimolecular products (vinyl ketene and a methyl radical, 2MF and a hydrogen atom) are dominant.

The formation of vinyl ketene and a methyl radical shows a stronger pressure dependency than the formation of 2MF and a hydrogen atom. Again, this is the result of multiple well skipping reactions occurring at lower pressures to produce the latter. Negligible quantities of CO and $CH_2{=}CH{-}\dot{C}H{-}CH_3$ radical are produced as formally direct products of hydrogen atom addition to 2MF.

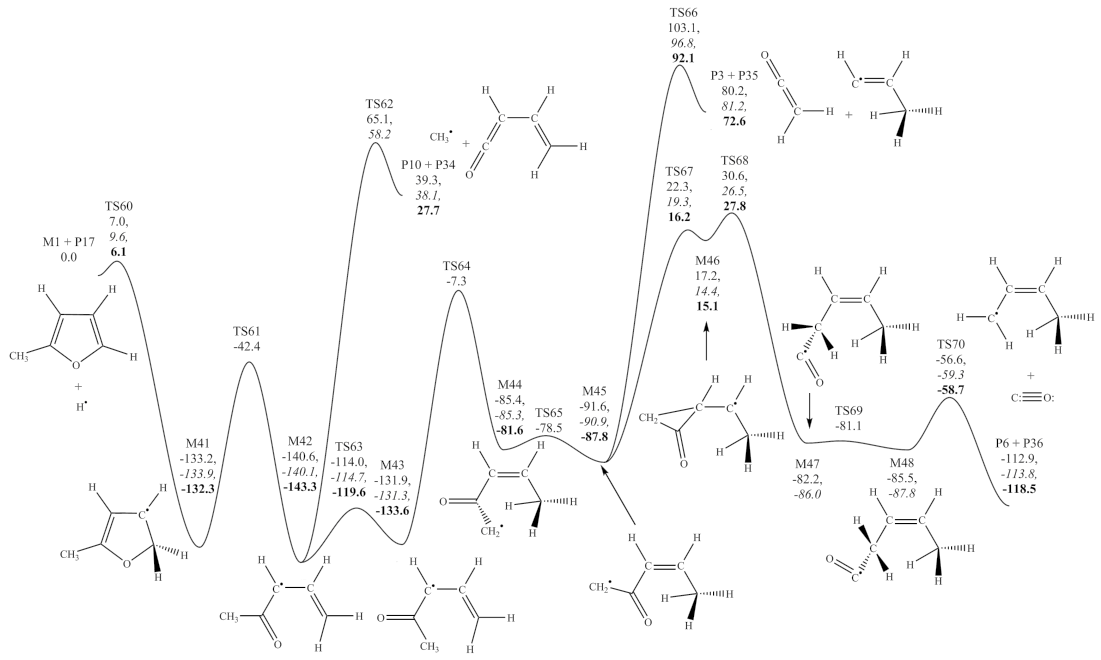

Fig. 14 Potential energy surface for hydrogen atom addition at carbon 5 of 2-methylfuran. CBS-QB3, *CBS-APNO* and **G3** energies in kJ mol^{-1} at 0 K relative to reactants.

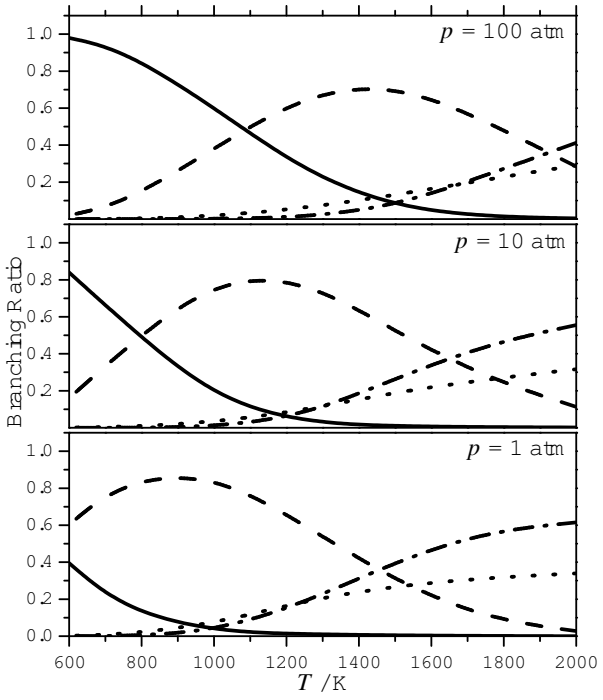

Fig. 15 Major product branching ratios as a function of temperature and pressure from RRKM/ME calculations on the chemically activated recombination of hydrogen atom with 2-methylfuran at C-5. — M41, – – $\sum$ other $\dot{C}_5H_7O$, ⋯ M1 + P17, – · – P10 + P34.

Table 7 Arrhenius coefficients of high-pressure limiting rate constants for for reactions relevant to hydrogen atom addition at C-5 of 2-methylfuran. $k(\mathrm{s}^{-1}) = AT^n \exp(-E_a/R)$, AT^n (s^{-1}), E_a/R (K).

No.	Reaction	A	n	E_a/R (K)
k_{61}	M41 → M42	1.52×10^{12}	0.31	10931.
k_{62}	M42 → P10 + P34	6.01×10^{14}	0.16	25568.
k_{63}	M42 → M43	3.24×10^{13}	−0.28	3301.
k_{64}	M43 → M44	3.64×10^{04}	2.25	11977.
k_{65}	M44 → M45	7.18×10^{12}	−0.16	900.
k_{66}	M45 → P3 + P35	4.29×10^{12}	0.56	23690.
k_{67}	M45 → M46	1.74×10^{13}	−0.42	13859.
k_{68}	M46 → M47	8.27×10^{07}	1.28	940.
k_{69}	M47 → M48	5.08×10^{07}	1.25	−313.
k_{70}	M48 → P6 + P36	5.84×10^{10}	0.74	3377.

4 Kinetic Modelling

The preceding calculations have been assimilated into a previously published kinetic scheme for 2-methylfuran and 2,5-dimethylfuran combustion by Somers and co-workers[32,70] wherein details of the oxidative reactions are found. Where rate constants are determined at several levels of theory, we utilise the CBS-QB3 calculations in the current work. Furan[18,38] and aromatic[71] mechanisms are also incorporated. The C_0–C_4 sub-mechanism is based on the mechanism de-

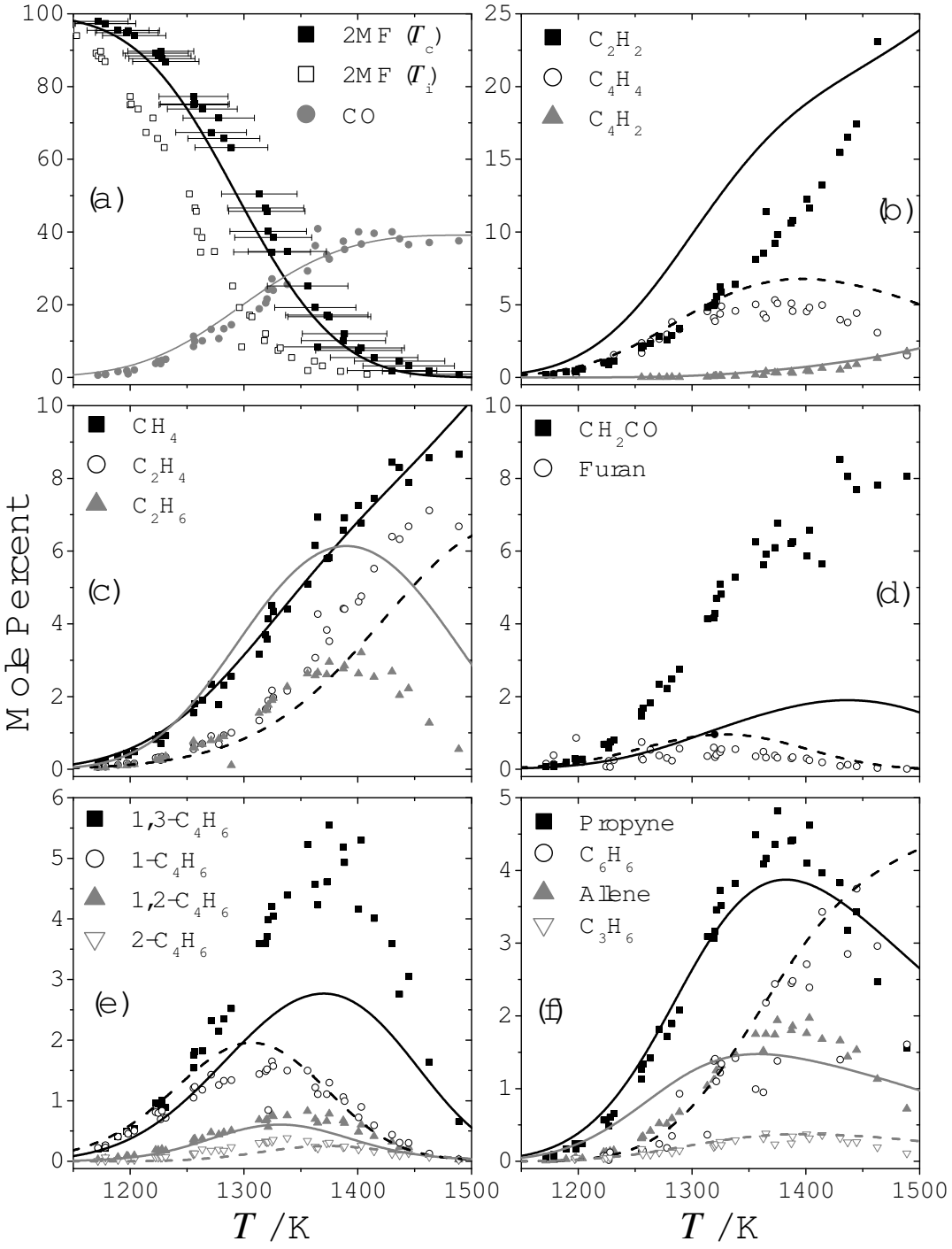

Fig. 16 Experimental speciation profiles for the pyrolysis of 0.5% 2-methylfuran at 2.5 atm and ≈ 2 ms residence time with modelling predictions (lines). Solid lines correspond with closed symbols and dashed lines with open symbols. T_c = corrected reflected shock temperatures, T_i = original reflected shock temperatures.

scribed by Healy and co-workers[72–76]. Further validation of this chemistry set is described in the work of Kochar and co-workers[77] and in a recent study of C_1–C_2 hydrocarbon and oxygenated fuels from Metcalfe *et al.*[78]. The H_2/O_2 sub-mechanism is adopted from the work of Kéromnès *et al.*[79].

Experimental profiles from Lifshitz *et al.*[14] are presented in Figure 16 along with numerical modelling results based on the current kinetic mechanism. Some comments on the experimental results are now appropriate before a comparison of modelling predictions with experiment is presented in detail. Mole percents are calculated *via* equation 1 in accord with the experimental definition[80], where x_i is the computed mole fraction of a species.

$$\text{Mole}\,\% = x_i / \sum_i x_i \qquad (1)$$

Only species which were quantified and included in this mole % calculation experimentally, are included in the corresponding computational results depicted in Figure 16.

The experimentalists used the chemical thermometer (1,1,1-trifluoroethane) method to determine the temperatures behind the reflected shock wave according to equations 2 and 3:

$$T = -(E/R) / \left[\ln \left\{ -\frac{\ln(1-\chi)}{A\,t} \right\} \right] \qquad (2)$$

where E and A are the activation energy and pre-exponential factor assumed for the molecular elimination reaction (CH_3—CF_3 → CH_2=CF_2 + H—F) of the chemical thermometer, t is the reaction dwell time and χ is given by:

$$\chi = [CH_2{=}CF_2]_t / ([CH_2{=}CF_2]_t + [CH_3{-}CF_3]_t) \qquad (3)$$

This makes the determination of the temperature sensitive to both the rate constant used for the decomposition and the determination of the concentrations of the reactant and product of the chemical thermometer. The temperature behind the reflected shock wave was calculated by Lifshitz *et al.* based on a literature assignment of the rate constant[81] for the decomposition of CH_3—CF_3 of $k = 10^{14.51}\exp(-36533/T)$ s^{-1}.

The same chemical thermometer method was employed in the Lifshitz *et al.*[15] study on the thermal decomposition of 2,5-dimethylfuran, although a slightly different rate constant (within 10–20%) was estimated for the thermometer decomposition. Recent experimental and kinetic modelling studies[37,70] have shown that the rate constant assumed by Lifshitz *et al.* in their 2,5-dimethylfuran work was likely in error. Somers *et al.*[70] carried out single pulse shock tube experiments under similar conditions to those of Lifshitz *et al.*[15] where temperatures were determined independent of a chemical thermometer. The results showed that 25DMF underwent decomposition at temperatures up to ≈ 90 K greater than those determined by Lifshitz *et al.*[15].

Sirjean *et al.*[37] carried out quantum chemical (CBS-QB3) and RRKM/ME calculations to determine the rate constant for the molecular elimination reaction, recommending a rate constant at 2.5 bar of $k = 6.17 \times 10^{13}\exp(-36060/T)$ s^{-1}. At 1200 K, their computed value is up to 3.8 times lower than that assumed by Lifshitz *et al.* in their 2,5-dimethylfuran work[15], and 3.5 times lower than that assumed in the experiments we are aiming to model here. Sirjean *et al.*[37] corrected the temperature measurements of Lifshitz *et al.* accordingly, with the resultant measurements from Somers *et al.*[70] and the corrected ones of Sirjean *et al.*[37] being within 25 K of each other and in good agreement with kinetic modelling calculations.

We therefore correct the temperature reported by Lifshitz *et al.*[14] for their 2-methylfuran experiments based on the rate constant recommended by Sirjean *et al.*[37] and equations 2 and 3. The result is a ≈ 50 K *increase* in the experimental temperature at the lowest conversions of 2-methylfuran, and up to 80 K at the highest temperatures studied. The corrected temperature can be described adequately by $T_c(\text{K}) = 1.12 \times T_i - 82.54$.

The experimental yields (Figure 16) of 2MF are presented with temperature uncertainty bars which assume a residual factor of two uncertainty in the recommended rate constant for the thermal decomposition of 1,1,1-TFE, which is reasonable based on the theoretical methods employed therein[37]. Figure 16 (a) also shows the temperature uncorrected yields of 2MF, which clearly lie outside the uncertainty in this updated temperature profile.

In order to obtain better agreement with the corrected 2MF and methane profiles, we have reduced the rate constant for hydrogen atom abstraction by methyl radical from the alkyl side chain of 2MF, k_{CH3-C2}(QB3), by a factor of two, which is within the theoretical uncertainty. The rate constant for hydrogen atom abstraction by hydrogen atom, k_{H-C2}(QB3), has been increased by a factor of two in order to retain agreement with laminar burning velocity measurements[32], as was carried out in the previous kinetic modelling study of Somers *et al.*[32]. The rate constant for this reaction shows little sensitivity to the pyrolysis results described here and our predictions of the fuel conversion in Figure 16 (a) are well within the experimental uncertainty.

Lifshitz *et al.*[14] originally recommended a pseudo-first order rate constant of $9.71 \times 10^{13}\exp(-34,400/T)$ s^{-1} for the thermal decomposition of 2MF in this temperature and pressure regime. After correction of their data, we arrive at $8.41 \times 10^{13}\exp(-34,450/T)$ s^{-1} with our kinetic model predicting a rate constant of $1.97 \times 10^{14}\exp(-35,071/T)$ s^{-1}. For all three derived rate constants, the activation energies are of the order of ≈ 286–291 kJ mol^{-1}, which corresponds closely with the barrier heights calculated for the 3 → 2 and 4 → 5 hydrogen atom shift reactions shown to be the dominant unimolecular decomposition pathways for 2MF in previous sections. This is an interesting result, as free radical

reactions are found to be important in the consumption of the reactant species. One might expect the activation energy to be smaller than the activation energies for the primary unimolecular initiation pathways but the thermal decomposition of 2MF seems to obey first order kinetics quite well in this temperature range.

The fate of the oxygen containing fragments of the fuel are of obvious interest and other than 2MF, only three species containing were experimentally measured which contained an oxygen atom; CO, ketene and furan. CO, which was found to be the primary decomposition product, was detected in yields of up to 40%, and is well-predicted by our kinetic model. Its formation is well rationalised within our quantum chemical calculations through multiple channels. Opening of the furan ring, followed by a hydrogen transfer reaction and CO elimination is common to the unimolecular decomposition reactions of the fuel and the primary fuel radical, and is also seen after hydrogen atom addition reactions. The reaction $CH_3{-}\dot{C}{=}O \rightarrow CO + \dot{C}H_3$ is also an important source of CO, with the majority of the $CH_3{-}\dot{C}{=}O$ radical formed in a 1:1 ratio with $CH_2{=}C{=}\dot{C}H$ radical from the decomposition of **M9**.

Ketene yields of up to 8% were implied from experiment but the determination of its concentrations proved difficult due to analytical issues. A series of isolated experiments were performed by Lifshitz *et al.* [14] where small quantities of methanol were added to the post-shock mixture in order convert ketene to the more readily quantifiable methyl acetate. Methyl acetate was subsequently identified although its concentrations could not be quantitatively determined. It was therefore assumed that if ketene was formed in the same unimolecular process as propyne and allene, its concentrations should equal the sum of the C_3H_4 isomers. Despite multiple pathways (Figures 2 and 14, and Figures 1 and 2 of ESI) leading to the production of ketene within our assembled reaction scheme, its formation is consistently found to be non-competitive with alternate pathways.

We find vinyl ketene, which went experimentally undetected by Lifshitz [14] but which was identified in 2MF flames [69], to be a major product upon hydrogen atom addition at C-5 of the furan ring. Computed vinyl ketene yields are in good agreement with the experimentally estimated ketene concentrations if this undetected species is incorporated into our mole % calculation, Figure 17. Vinyl ketene may therefore account for the missing carbon and oxygen which the experimentalists assumed would be found in ketene.

Furan yields are well-predicted and its formation pathway was clearly rationalised in a previous work by Simmie and Metcalfe [25]. However, the ring opening step presented in Figure 11 is central to the accurate prediction of its yields shown in Figure 16 (d), with the exclusion of this process resulting in over-prediction of the experimental yield.

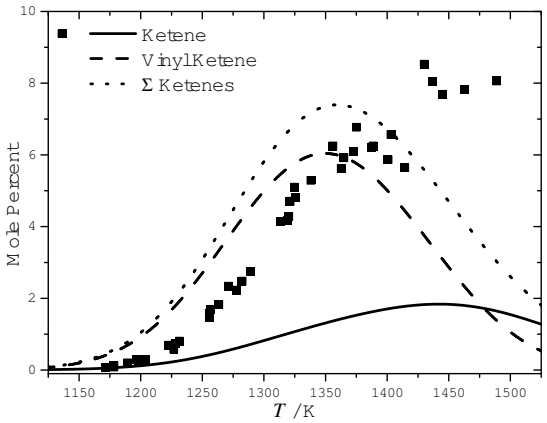

Fig. 17 Experimentally estimated yields [14] (see text) of ketene (symbols) with computational yields of ketene and vinyl ketene.

The yield of methane, which is primarily formed by hydrogen atom abstraction from the alkyl side chain by methyl radical, is also well-predicted although yields of ethane, which is formed from methyl radical self-recombination, is over-predicted by the mechanism. Ethylene is formed from the decomposition of ethyl radical which is in turn formed from the decomposition of **P23** and from the reaction $C_2H_6 + \dot{C}H_3 = \dot{C}_2H_5 + CH_4$. Yields of the C_4H_6 isomers 1-butyne, 2-butyne, 1,2-butadiene and 1,3-butadiene are all reasonably-well estimated by our kinetic mechanism.

Like ketene, many pathways leading to the formation of propyne were identified in our quantum calculations (k_4, k_{13}, k_{47}, k_{66}) but none were found to be competitive. Nonetheless, propyne, allene, and benzene yields are all accounted for. The former are produced *via* abstraction by propargyl radical from the alkyl side chain of 2MF, and the latter *via* the recombination of propargyl radicals. It is worth noting that propargyl radical was identified by Grela *et al.* [16] in the thermal decomposition of 2MF, based on the presence of its ion at m/z 39 in their MS analysis. Our work proposes two clear channels to its formation from 2MF *via* the reactions sequences (a) 2MF $\rightarrow$ **M6** $\rightarrow CO + CH{\equiv}C{-}CH_2{-}CH_3 \rightarrow \dot{C}H_3 + CH_2{=}C{=}\dot{C}H$ and (b) 2MF $\rightarrow$ **M9** $\rightarrow CH_3{-}\dot{C}{=}O + CH_2{=}C{=}\dot{C}H$.

The decomposition of *n*-butadienyl radical, which is the primary product of the decomposition of the 2-furanylmethyl radical, Figure 7, accounts for the acetylene and vinylacetylene concentrations detected experimentally. Vinylacetylene predictions are in excellent agreement with experiment, although acetylene yields are consistently over-estimated, possibly indicating refinements to the kinetics of *n*-butadienyl radical decomposition are necessary.

5 Conclusions

This work presents a comprehensive investigation of the potential energy surfaces for the pyrolysis reactions of the biofuel candidate 2-methylfuran. Kinetics for the thermal unimolecular reactions of 2-methylfuran and the 2-furanylmethyl radical, the chemically activated recombination of hydrogen atoms with 2-methylfuran and several hydrogen atom abstraction processes have been investigated. Canonical and microcanonical rate theories have been employed to determine rate constants as a function of temperature and pressure (if applicable) for each reaction pathway.

Unimolecular decomposition is initiated primarily by hydrogen shift reactions routed through β-carbene intermediates to form stable acyclic intermediates which further decompose to either 1-butyne and CO, or acetyl and propargyl radicals. As temperatures approach 2000 K, the formation of 1,2-butadiene and CO, ketene and propyne, and 2-furanylmethyl radical and a hydrogen atom become competitive. The decomposition of the 2-furanylmethyl radical is shown to proceed through C–O bond cleavage which opens the furan ring. Subsequent hydrogen atom transfer and α-scission leads to the formation of the dominant products, CO and the *n*-butadienyl radical. Hydrogen atom addition to carbon atoms adjacent to the oxygen of the furan ring are kinetically favoured over addition to atoms remote from the oxygen moiety. In terms of bimolecular products, hydrogen atom addition results predominantly in the formation of furan and a methyl radical, 1-butene-1-yl radical and CO, and vinyl ketene and a methyl radical.

The calculated rate constants are incorporated into a previously published oxidative mechanism for 2-methylfuran[32] and 2,5-dimethylfuran[70] which is then compared with experimental speciation profiles[14] recorded for the pyrolysis of 2-methylfuran. Once the experimental measurements are corrected for an erroneous temperature determination the agreement between theory and experimental is overall quite good, thus giving some credibility to the proposed pyrolysis mechanism and kinetics. The mechanism is also compared to literature oxidation experiments of 2MF in the ESI, with good performance observed against all experimental targets.

The fundamental molecular data provided in this study should be of interest to those who wish to carry out RRKM/ME calculations on 2-methylfuran in the future with the chemical mechanism being of utility to those modelling the combustion behavior of 2-methylfuran under pyrolysis and oxidative conditions. Furan, 2-methylfuran and 2,5-dimethylfuran are also know intermediates and model compounds considered in the pyrolysis of biomass[82,83] and coals[17], and the kinetic scheme developed herein is likely to be useful in kinetic modelling work in these areas.

6 Acknowledgments

We would like to acknowledge the support of Science Foundation Ireland under grant number [08/IN1./I2055] as part of their Principal Investigator Awards. We acknowledge the provision of computational resources from the e-Irish National Infrastructure programme, e-INIS, and the Irish Centre for High-End Computing, ICHEC. We thank Prof. John Barker and Dr. Gabriel da Silva for useful discussions on the Multiwell code and the latter again for sharing with us the Speed v0.72 code for automatic generation of potential energy surfaces.

References

1 Renewable Energy Policy Network for the 21st Centry. Renewables 2013 Global Status Report. http://www.ren21.net/REN21Activities/GlobalStatusReport.aspx (accessed October 21, 2013).
2 J.R. Regalbuto, Science, 2009, 325, 822–824.
3 Y. Román-Leshkov, C.J. Barrett, Z.Y. Liu, J.A. Dumesic, Nature, 2007, 447, 982–985.
4 H. Zhao, J.E. Holladay, H. Brown, Z.C. Zhang, Science 2007, 316, 1597–1599.
5 J.B. Binder, R.T. Raines, J. Am. Chem. Soc., 2009, 131, 1979–1985
6 Y. Su, H.M. Brown, X. Huang, X. Zhou, J.E. Amonette, Z.C. Zhang, Applied Catalysis A: General 2009, 361, 117–122.
7 A.A. Rosatella, S.P. Simeonov, R.F.M. Frade, C.M. Afonso, Green Chemistry, 2011, 13, 754–793.
8 F. Geilen, T. vom Stein, B. Engendahl, S. Winterle, M. Liauw, J. Klankermayer, W. Leitner, Angew. Chem. Int. Ed. 2011, 50, 6831–6834.
9 S. Zhong, R. Daniel, H. Xu, J. Zhang, D. Turner, M.L. Wyszynski, P. Richards, Energy Fuels, 2010, 24, 2891–2899.
10 R. Daniel, G. Tian, H. Xu, M.L. Wyszynski, X. Wu, Z. Huang, Fuel, 2011, 90, 449–458.
11 M. Thewes, M.Muether, S. Pischinger, M. Budde, A. Sehr, P. Adomeit, J. Klankermayer, Energy Fuels, 2011, 25, 5549–5561.
12 C. Wang, H. Xu, R. Daniel, A. Ghafourian, J.M. Herreros, S. Shuai, X. Ma, Fuel, 2013, 103, 200–211.
13 A. Lifshitz, M. Bidani, S. Bidani, J. Phys. Chem., 1986, 90, 5373–5377.
14 A. Lifshitz, C. Tamburu, R. Shashua, J. Phys. Chem. A, 1997, 101, 1018–1029.
15 A. Lifshitz, C. Tamburu, R. Shashua, J. Phys. Chem. A, 1998, 102, 10655–10670.

16 M.A. Grela, V.T. Amorebieta, A.J. Colussi, J. Phys. Chem., 1985, 89, 38–41.
17 O.S.L. Bruinsma, P.J.J. Tromp, H.J.J. de Sauvage Nolting, J.A. Moulijn, Fuel, 1988, 67, 334–340.
18 K. Sendt, G.B. Backsay, J.C. Mackie, J. Phys. Chem. A, 2000, 104, 1861–1875.
19 P.P. Organ, J.C. Mackie, J. Chem. Soc. Faraday Trans., 1991, 87, 815–823.
20 R. Liu, X. Zhou, L. Zhai, J. Comput. Chem., 1998, 19, 240–249.
21 R. Liu, X. Zhou, T. Zuo, Chem. Phys. Lett., 2000, 325, 457–464.
22 J.M. Simmie, H.J. Curran, J. Phys. Chem. A, 2009, 113, 5128–5137.
23 D. Feller, J.M. Simmie, J. Phys. Chem. A., 2013, 116, 11768–11775.
24 Ribeiro da Silva, M.A.V, Amaral, L.M.P.F., J. Therm. Anal. Calorim, 2010, 100, 375–380.
25 J.M. Simmie, W.K. Metcalfe, J. Phys. Chem. A, 2011, 115, 8877–8888.
26 X. Wu, Z. Huang, T. Yuan, K. Zhang, L. Wei, Combust. Flame., 2009, 156, 365–376.
27 P. Friese, T. Bentz, M. Olzmann, J. Simmie, Proceedings of the European Combustion Meeting, 2011.
28 P. Friese, J.M. Simmie, M. Olzmann, Proc. Combust. Inst., 2013, 34, 233–239.
29 B. Sirjean, R. Fournet, Phys. Chem. Chem. Phys, 2013, 15, 596–611.
30 B. Sirjean, R. Fournet, Proc. Combust. Inst., 2013, 34, 241–249.
31 B. Sirjean, R. Fournet, J. Phys. Chem. A, 2012, 116, 6675–6684.
32 K.P. Somers, J.M. Simmie, F. Gillespie, U. Burke, J. Connolly,W.K. Metcalfe, F. Battin-Leclerc, P. Dirrenberger, O. Herbinet, P.-A. Glaude, H.J. Curran, Proc. Combust. Inst., 2013, 34, 225–232.
33 A.Y. Chang, J.W. Bozzelli, A.M. Dean, Zeitschrift fur Physikalische Chemie, 2000, 214, 1533–1568.
34 J.W. Bozzelli, A.M Chang, A.M. Dean, Int. J. Chem. Kin., 1997, 29, 161–170.
35 A.C. Davis, S. M. Sarathy, J. Phys. Chem. A, 2013, 117, 7670–7685.
36 L.-S. Tran, C. Togbé, D. Liu, D. Felsmann, P. Oßwald, P.-A. Glaude, R. Fournet, B. Sirjean, F. Battin-Leclerc, K. Kohse-Höinghaus, Combust. Flame, 2013, http://dx.doi.org/10.1016/j.combustflame.2013.05.027
37 B. Sirjean, R. Fournet, P.-A Glaude, F. Battin-Leclerc, W. Wang, M.A. Oehlschlaeger, J. Phys. Chem. A, 2013, 117, 1371–1392.
38 Z. Tian, T. Yuan, R. Fournet, P.-A. Glaude, B. Sirjean, R. Battin-Leclerc, K. Zhang, F. Qi, Combust. Flame, 2011 , 158, 756–773.
39 L. Wei, C. Tang, X. Man, Z. Huang, Energy Fuels, 2013, Just Accepted Manuscript. DOI: 10.1021/ef401809y
40 A.D. Becke, J. Chem. Phys., 1993, 98, 5648–5652.
41 C. Lee, W. Yang, R.G. Parr, Phys. Rev. B, 1988, 37, 785–789.
42 H.P. Hratchian, H.B. Schlegel, J. Chem. Theory Comput., 2005, 1, 61-69.
43 J.A. Montgomery, M.J. Frisch, J.W. Ochterski, G.A. Petersson, J. Chem. Phys., 2000, 112, 6532–6542.
44 J.W. Ochterski, G.A. Petersson, J.A. Montgomery, J. Chem. Phys., 1996, 104, 2598–2619.
45 L.A. Curtiss, K. Raghavachari, P.C. Redfern, V. Rassolov, J.A. Pople, J. Chem. Phys., 1998, 109, 7764–7776.
46 J.M. Simmie, K.P. Somers, W.K. Metcalfe, H.J. Curran, J. Chem. Thermo., 2013, 58, 117–128.
47 Gaussian 03, Revision E.01 and Gaussian 09, Revision C.01, M. J. Frisch, G. W. Trucks, H. B. Schlegel, G. E. Scuseria, M. A. Robb, J. R. Cheeseman, J. A. Montgomery, Jr., T. Vreven, K. N. Kudin, J. C. Burant, J. M. Millam, S. S. Iyengar, J. Tomasi, V. Barone, B. Mennucci, M. Cossi, G. Scalmani, N. Rega, G. A. Petersson, H. Nakatsuji, M. Hada, M. Ehara, K. Toyota, R. Fukuda, J. Hasegawa, M. Ishida, T. Nakajima, Y. Honda, O. Kitao, H. Nakai, M. Klene, X. Li, J. E. Knox, H. P. Hratchian, J. B. Cross, V. Bakken, C. Adamo, J. Jaramillo, R. Gomperts, R. E. Stratmann, O. Yazyev, A. J. Austin, R. Cammi, C. Pomelli, J. W. Ochterski, P. Y. Ayala, K. Morokuma, G. A. Voth, P. Salvador, J. J. Dannenberg, V. G. Zakrzewski, S. Dapprich, A. D. Daniels, M. C. Strain, O. Farkas, D. K. Malick, A. D. Rabuck, K. Raghavachari, J. B. Foresman, J. V. Ortiz, Q. Cui, A. G. Baboul, S. Clifford, J. Cioslowski, B. B. Stefanov, G. Liu, A. Liashenko, P. Piskorz, I. Komaromi, R. L. Martin, D. J. Fox, T. Keith, M. A. Al-Laham, C. Y. Peng, A. Nanayakkara, M. Challacombe, P. M. W. Gill, B. Johnson, W. Chen, M. W. Wong, C. Gonzalez, and J. A. Pople, Gaussian, Inc., Wallingford CT, 2004.
48 MultiWell-2013 Software, Jan 2013, designed and maintained by J.R. Barker with contributors N.F. Ortiz, J.M. Preses, L.L. Lohr, A. Maranzana, P.J. Stimac, T. L. Nguyen, and T. J. Dhilip Kumar, University of Michigan, Ann Arbor, MI; http://aoss.engin.umich.edu/multiwell/
49 J.R Barker, (a) Int. J. Chem. Kinetics 2001, 33, 232–245; (b) Int. J. Chem. Kinetics 2001, 33, 246–261; (c) Int. J. Chem. Kinetics 2009, 41, 748–763.
50 S.J. Pinches, G. da Silva, Int. J. Chem. Kin, 2013, 45, 387–396.
51 Mokrushin, V.; Tsang, W. ChemRate version 1.5.8, NIST, Gaithersburg, MD 20899, http://mokrushin.com/ChemRate/chemrate.html (ac-

cessed June 21 2013).
52 D. Polino, C. Cavalotti, J. Phys. Chem. A, 2011, 115, 10281–10289.
53 G. da Silva, J.A. Cole, J.W. Bozzelli, J. Phys. Chem. A, 2009, 113, 6111–6120.
54 C. Cavallotti, D. Polino, Proc. Combust. Inst., 2013, 34, 557–564.
55 G. da Silva, A.J. Trevitt, Phys. Chem. Chem. Phys., 2011, 13, 8940-8952.
56 G. da Silva, Chem. Phys. Lett., 2009, 474, 13–17.
57 G. da Silva, J.A. Cole, J.W. Bozzelli, J. Phys. Chem. A, 2010, 114, 2275-2283.
58 G. da Silva, M. Rafiq Hamdan, J.W. Bozzelli, J. Chem. Theory Comput., 2009, 5, 3185-3194.
59 J.A. Miller, S.J. Klippenstein, J. Phys. Chem. A, 2013, 117, 2718–2727.
60 A.W. Jasper, J.A. Miller, S.J. Klippenstein, J. Phys. Chem. A, 2013, 117, 12243–12255.
61 H. Hippler, J. Troe, and H. J. Wendelken, J. Chem. Phys., 1983, 78, 6709–6717.
62 R.J. Kee, M.E. Coltrin, P. Glarborg, Chemically Reacting Flow Theory and Practice, 1st ed.; John Wiley & Son, Inc.; New Jersey, 2003; pp 496–499.
63 W.M Haynes, Critical Constants of Organic Compounds. In CRC Handbook of Chemistry and Physics, 91st ed; CRC Press; Boca Raton, Florida; p 67.
64 X. Ma, C. Jian, H. Xu, H. Ding, S. Shuai, H. Ding, Energy Fuels, 2013, 27, 6212–6221.
65 Chemkin-Pro, Reaction Design Inc., San Diego, Calif. 2010.
66 L.B. Harding, S.J. Klippenstein, J. Phys. Chem. A, 2007, 111, 3789–3801.
67 Y.-R. Luo. Comprehensive Handbook of Chemical Bond Energies, CRC Press, Boca Raton, FL, 2007, p. 41.
68 H. Wang, K. Brenzinsky, J. Phys. Chem. A, 1998, 102, 1530-1541.
69 L. Wei, Z. Li, L. Tong, Z. Wang, H. Jin, M. Yao, Z. Zheng, C. Wang, H. Xu, Energy Fuels, 2012, 26, 6651–6660.
70 K.P. Somers, J.M. Simmie, F. Gillespie, C. Conroy, G. Black, W.K. Metcalfe, F. Bttin-Leclerc, P. Dirrenberger, O. Herbinet, P.-A Glaude, P. Dagaut, C. Togbé, K. Yasunaga, R.X. Fernandes, C. Lee, R. Tripathi, H.J. Curran, Combust. Flame, 2013, 160, 2291–2318.
71 W.K. Metcalfe, S. Dooley, F.L. Dryer, J. Phys. Chem. A., 2011, 25, 4915–4936.
72 D. Healy, N.S. Donato, C.J. Aul, E.L. Petersen, C.M. Zinner, G. Bourque, H.J. Curran, Combust. Flame, 2010, 157, 1526–1539.
73 N. Donato, C. Aul, E. Petersen, C. Zinner, H. Curran, G. Bourque, J. Eng. Gas Turb. Power, 2010, 132, 051502.
74 D. Healy, N.S. Donato, C.J. Aul, E.L. Petersen, C.M. Zinner, G. Bourque, H.J. Curran, Combust. Flame, 2010, 157, 1540–1551.
75 D. Healy, D.M. Kalitan, C.J. Aul, E.L. Petersen, G. Bourque, H.J. Curran, Energy Fuels, 2010, 24, 1521–1528.
76 D. Healy, M.M. Kopp, N.L. Polley, E.L. Petersen, G. Bourque, H.J. Curran, Energy Fuels, 2010, 24, 1617–1627.
77 Y. Kochar, J. Seitzman, T. Lieuwen, W.K. Metcalfe, S.M. Burke, H.J. Curran, M. Krejci, W. Lowry, E. Petersen, G. Bourque, 2011, ASME Paper GT2011-45122, 56th ASME Turbo Expo.
78 W.K. Metcalfe, S.M. Burke, S.S. Ahmed, H.J. Curran, Int. J. Chem. Kin, 2013, 45, 638–675.
79 A. Kéromnès, W.K. Metcalfe, K.A. Heufer, N. Donohoe, A.K. Das, C.J. Sung, J. Herzler, C. Naumann, P. Griebel, O. Mathieu, M.C. Krejci, E.L. Petersen, W.J. Pitz, H.J. Curran, Combust. Flame, 2013, 160, 995–1011.
80 A. Lifshitz, M. Bidani, S. Bidani, J. Phys. Chem., 1986, 90, 3422-3429.
81 A.S. Rodgers, W.G.F. Ford, Int. J. Chem. Kin., 1973, 5, 965–975.
82 E. Ranzi, A. Cuoci, T. Faravelli, A. Frassoldati, G. Migliavacca, S. Pierucci, S. Sommariva, Energy Fuels, 2008, 22, 4292–4300.
83 K. Norinaga, T. Shoji, S. Kudo, J. Hayashia, Fuel, 2013, 103, 141–150.

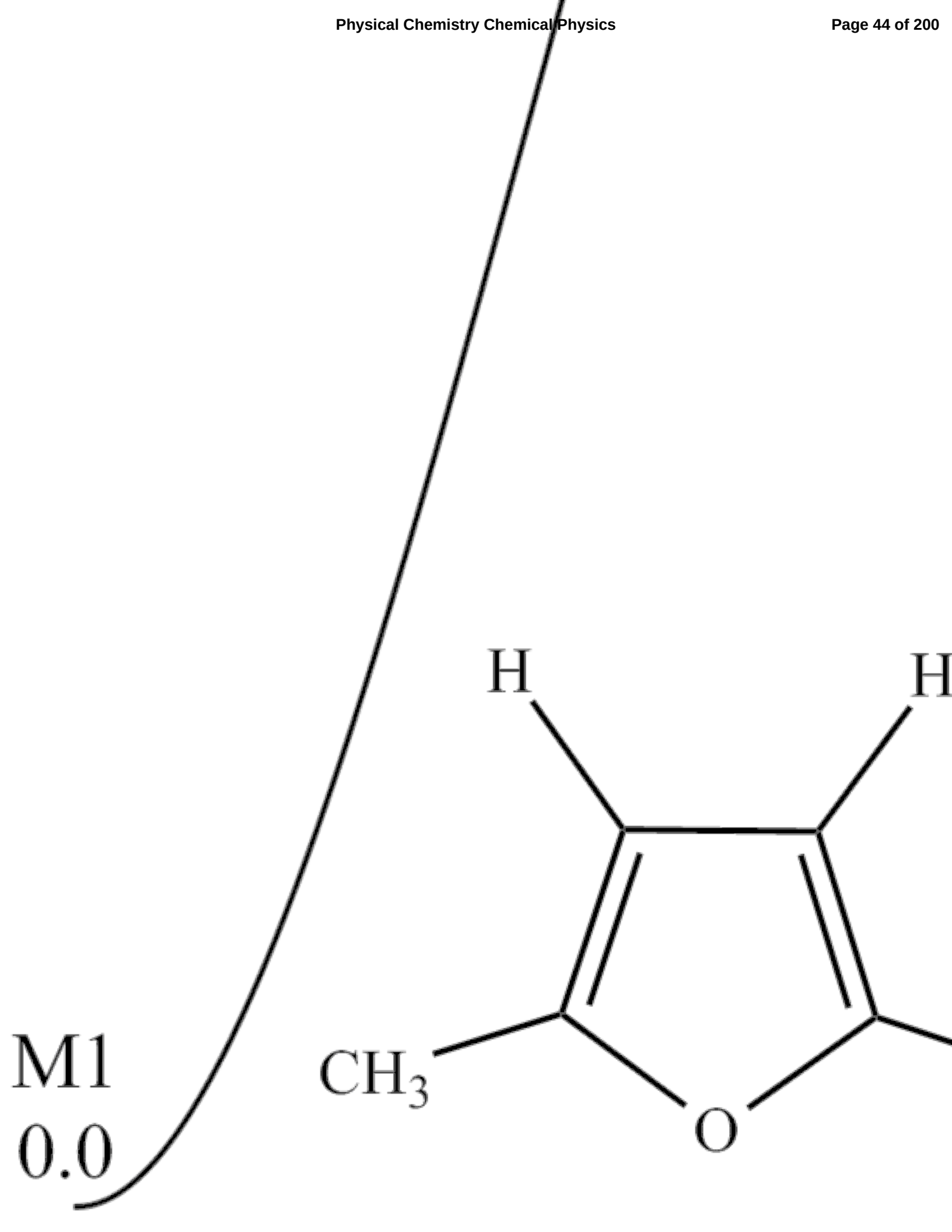
M1
0.0
H
H
CH3
O

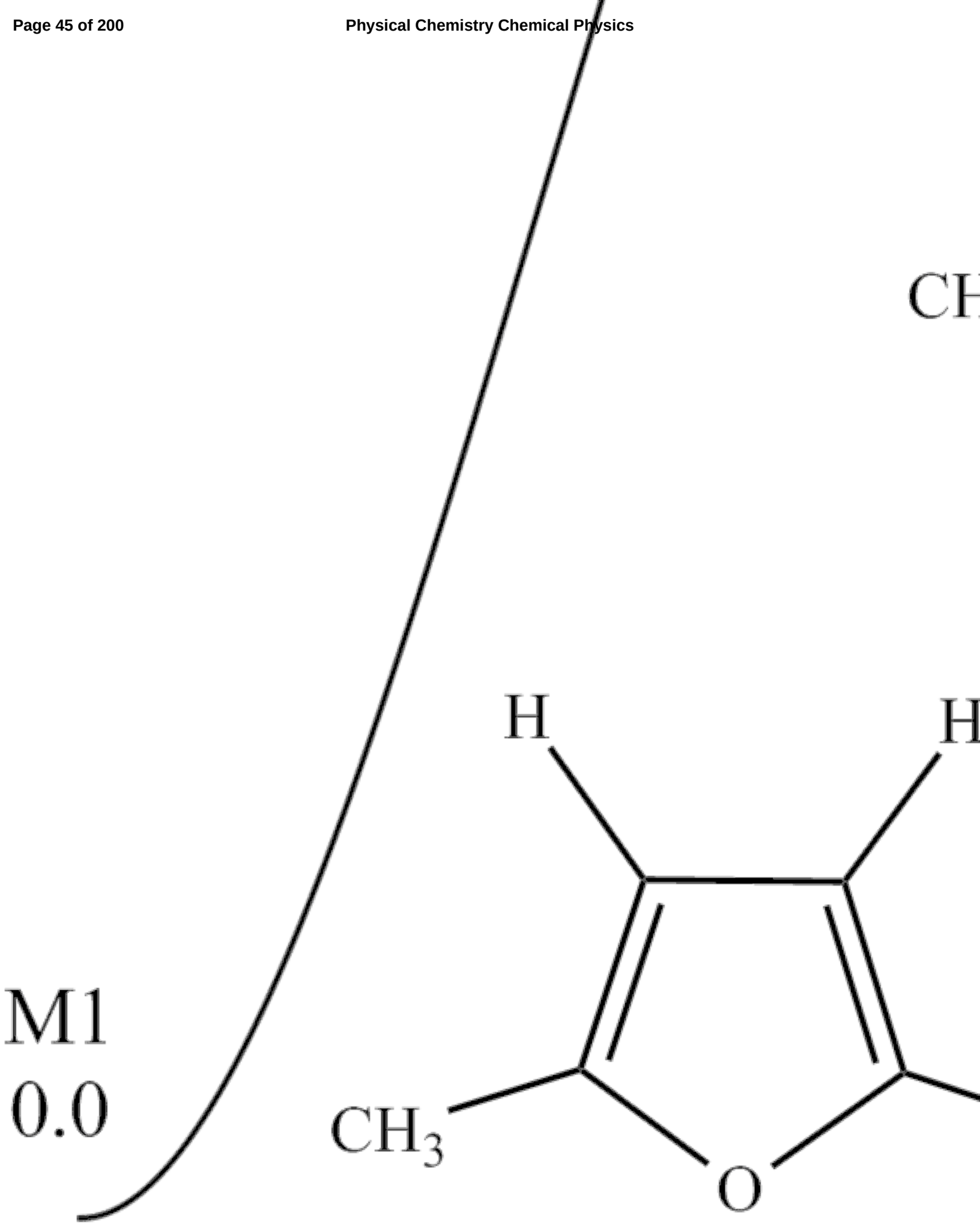
CH
H
H
M1
0.0
CH3
O

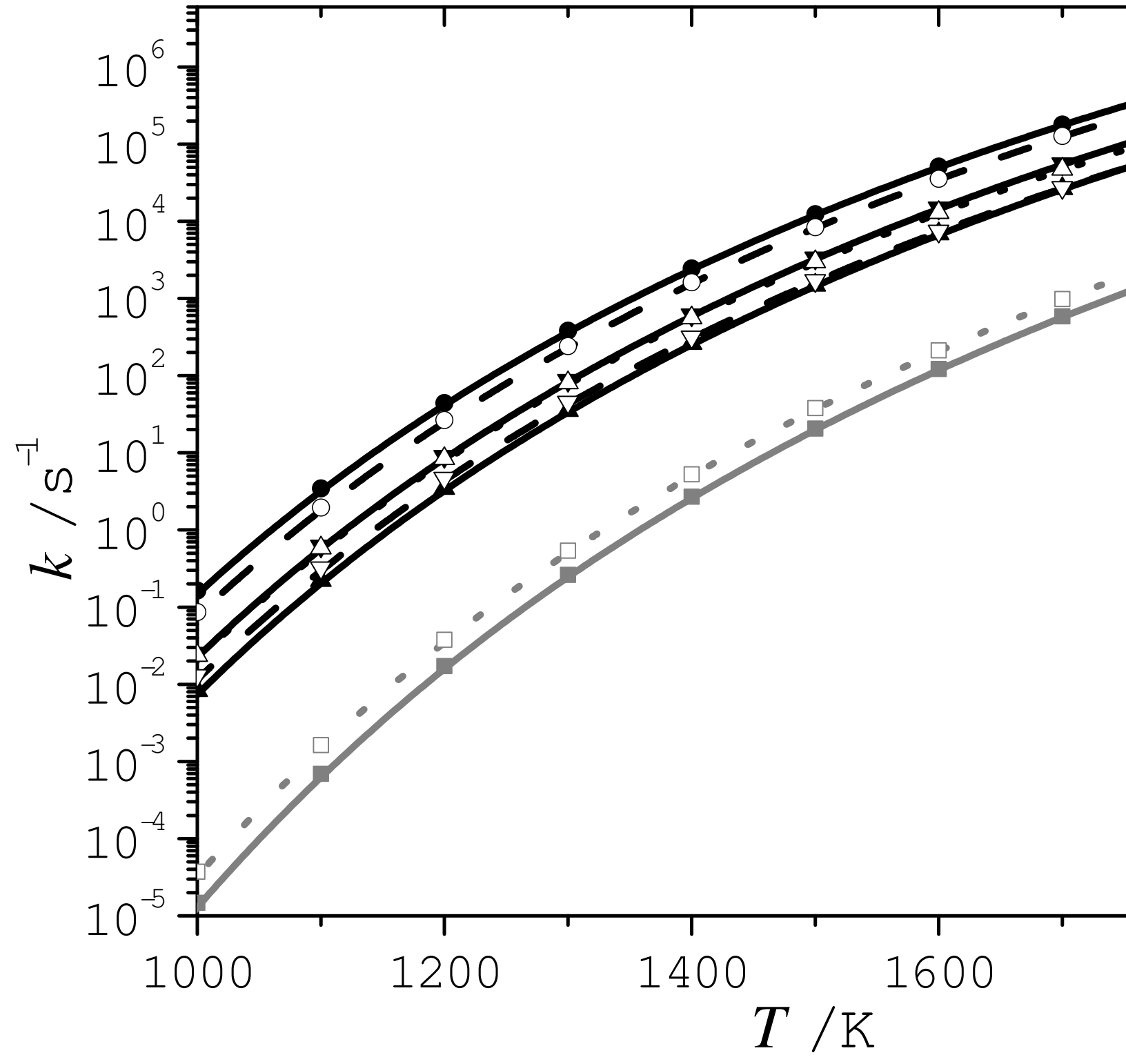
10^{6}
10^{5}
10^{4}
10^{3}
10^{2}
10^{1}
10^{0}
10^{-1}
10^{-2}
10^{-3}
10^{-4}
10^{-5}
k / s^{-1}
1000
1200
1400
1600
T /K

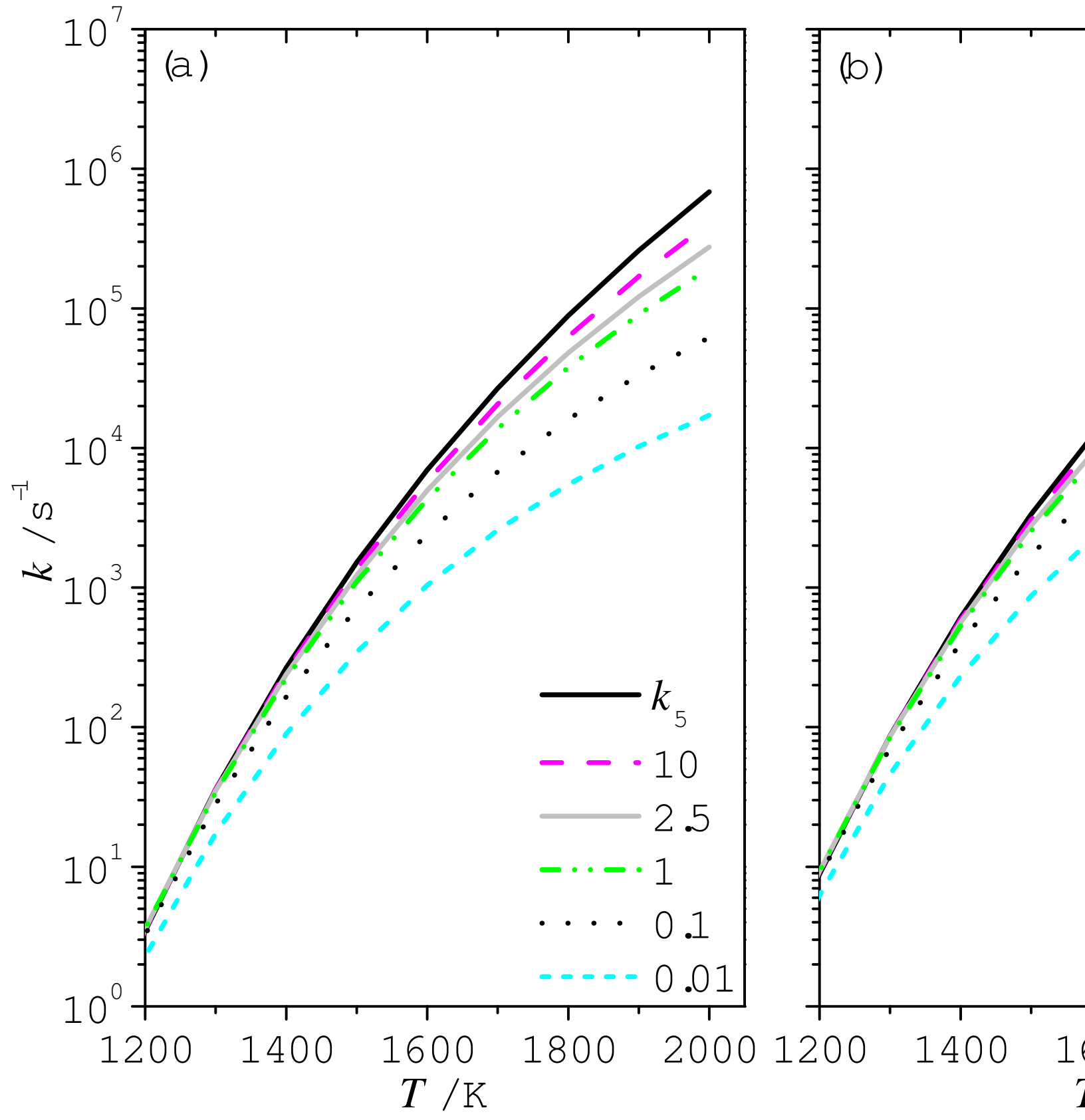
(a)
(b)
10^7
10^6
10^5
10^4
10^3
10^2
10^1
10^0
k / s^{-1}
1200
1400
1600
1800
2000
T /K
k_5
10
2.5
1
0.1
0.01

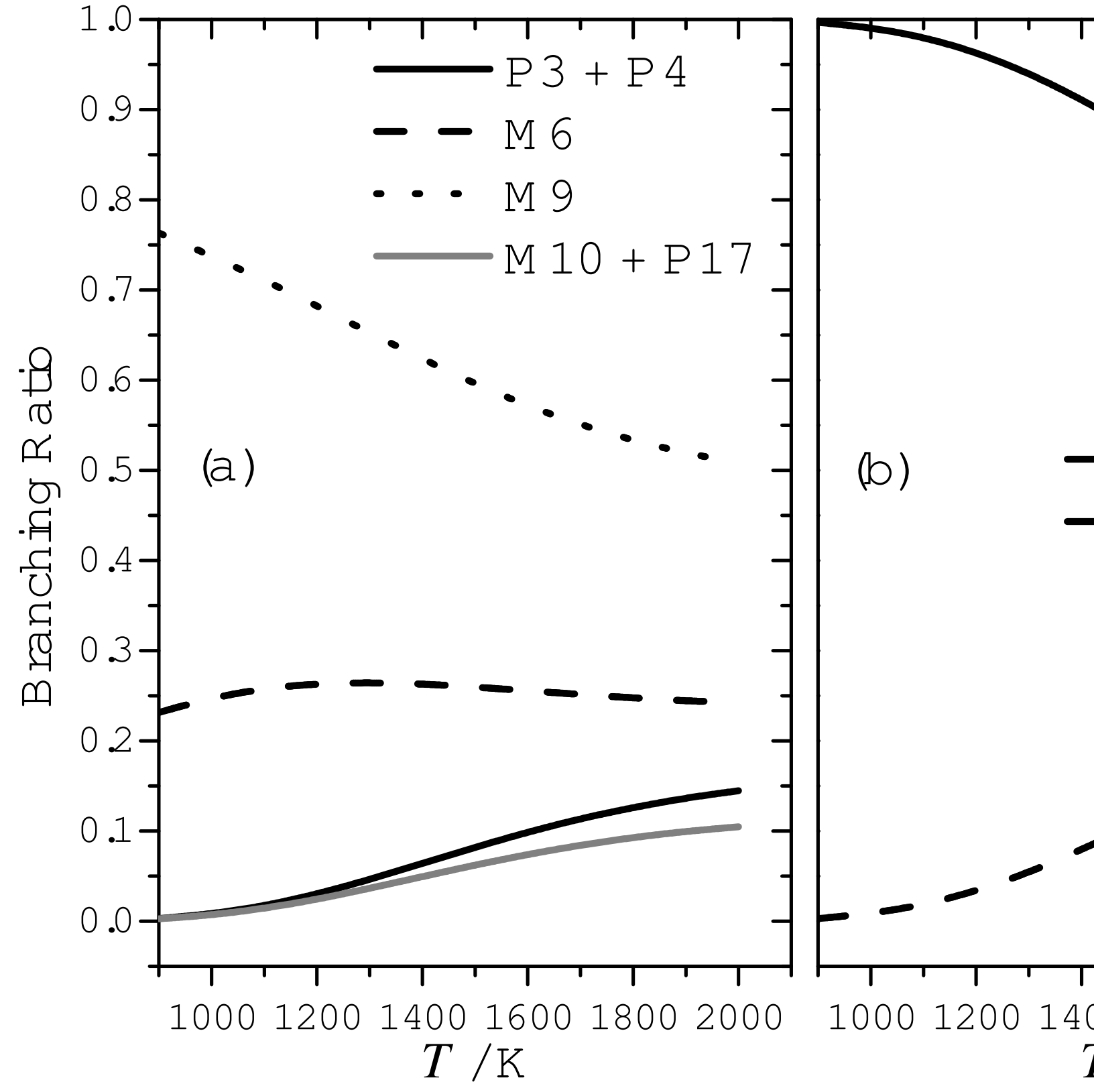
P3 + P4
M6
M9
M10 + P17
(a)
(b)
Branching Ratio
1.0
0.9
0.8
0.7
0.6
0.5
0.4
0.3
0.2
0.1
0.0
1000 1200 1400 1600 1800 2000
1000 1200 140
T /K

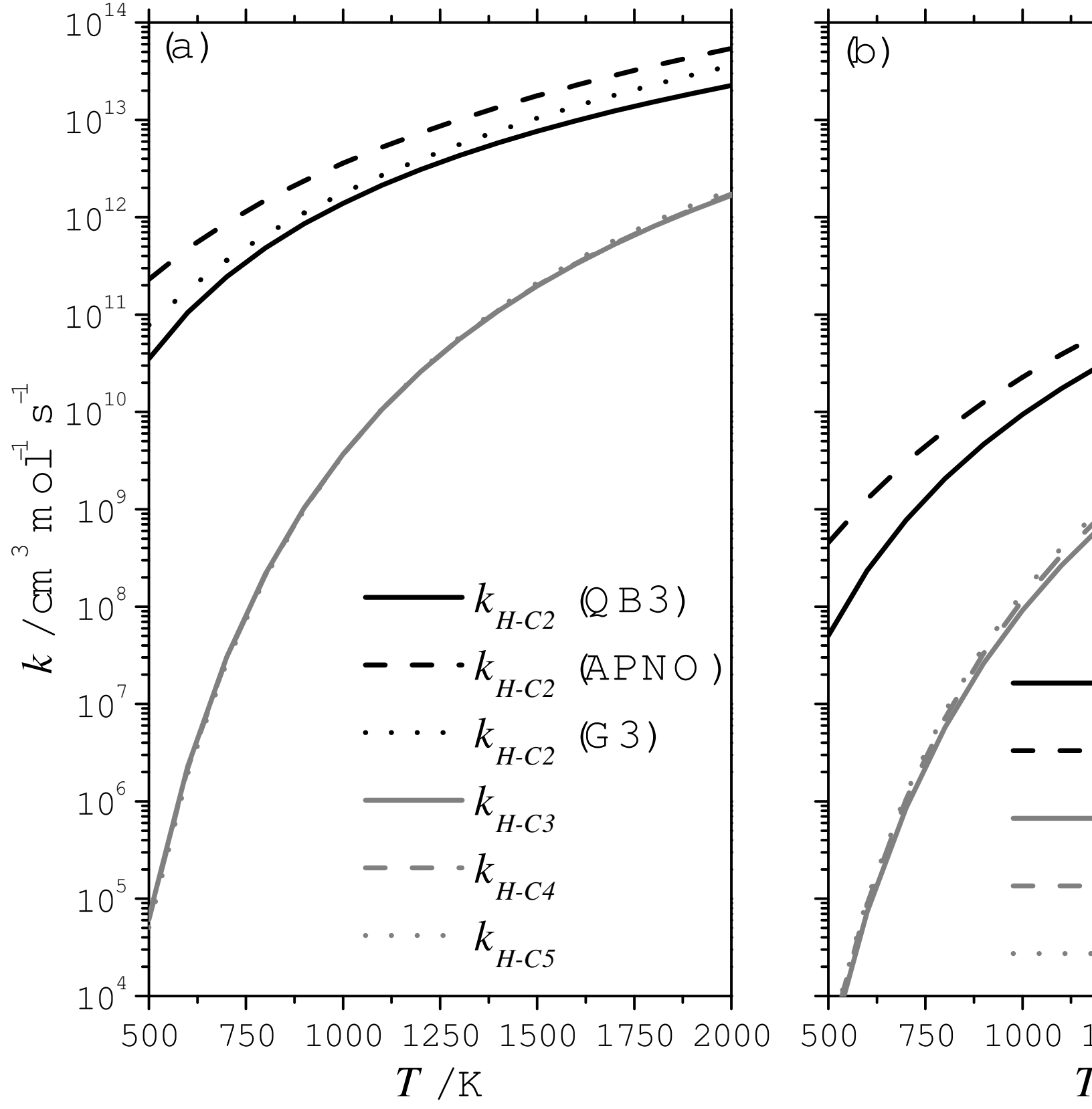
(a)
(b)
10^{14}
10^{13}
10^{12}
10^{11}
10^{10}
10^{9}
10^{8}
10^{7}
10^{6}
10^{5}
10^{4}
k /cm^3 mol^{-1} s^{-1}
500 750 1000 1250 1500 1750 2000
T /K
$k_{H\text{-}C2}$ (QB3)
$k_{H\text{-}C2}$ (APNO)
$k_{H\text{-}C2}$ (G3)
$k_{H\text{-}C3}$
$k_{H\text{-}C4}$
$k_{H\text{-}C5}$

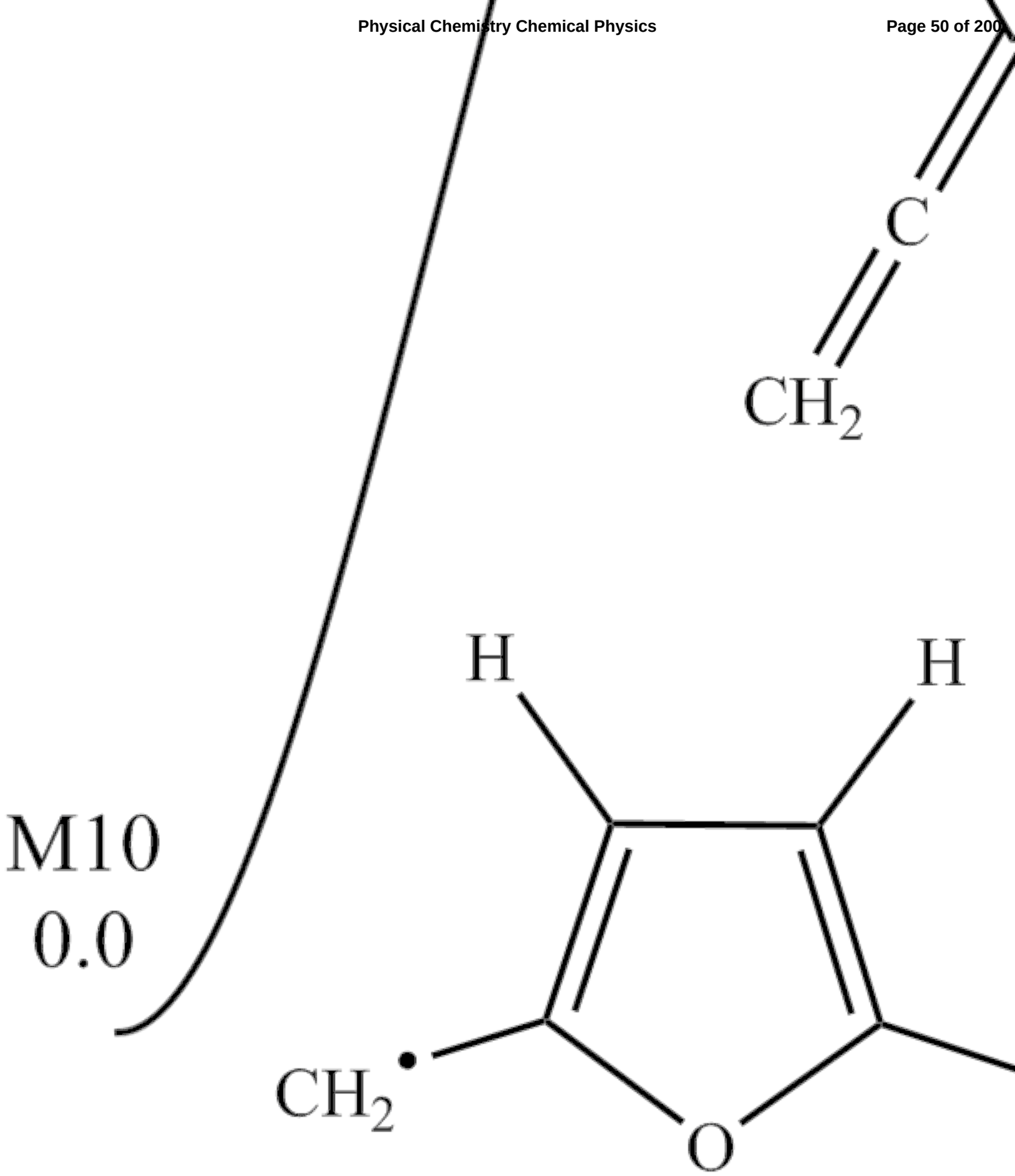
C
CH2
H
H
M10
0.0
CH2
O

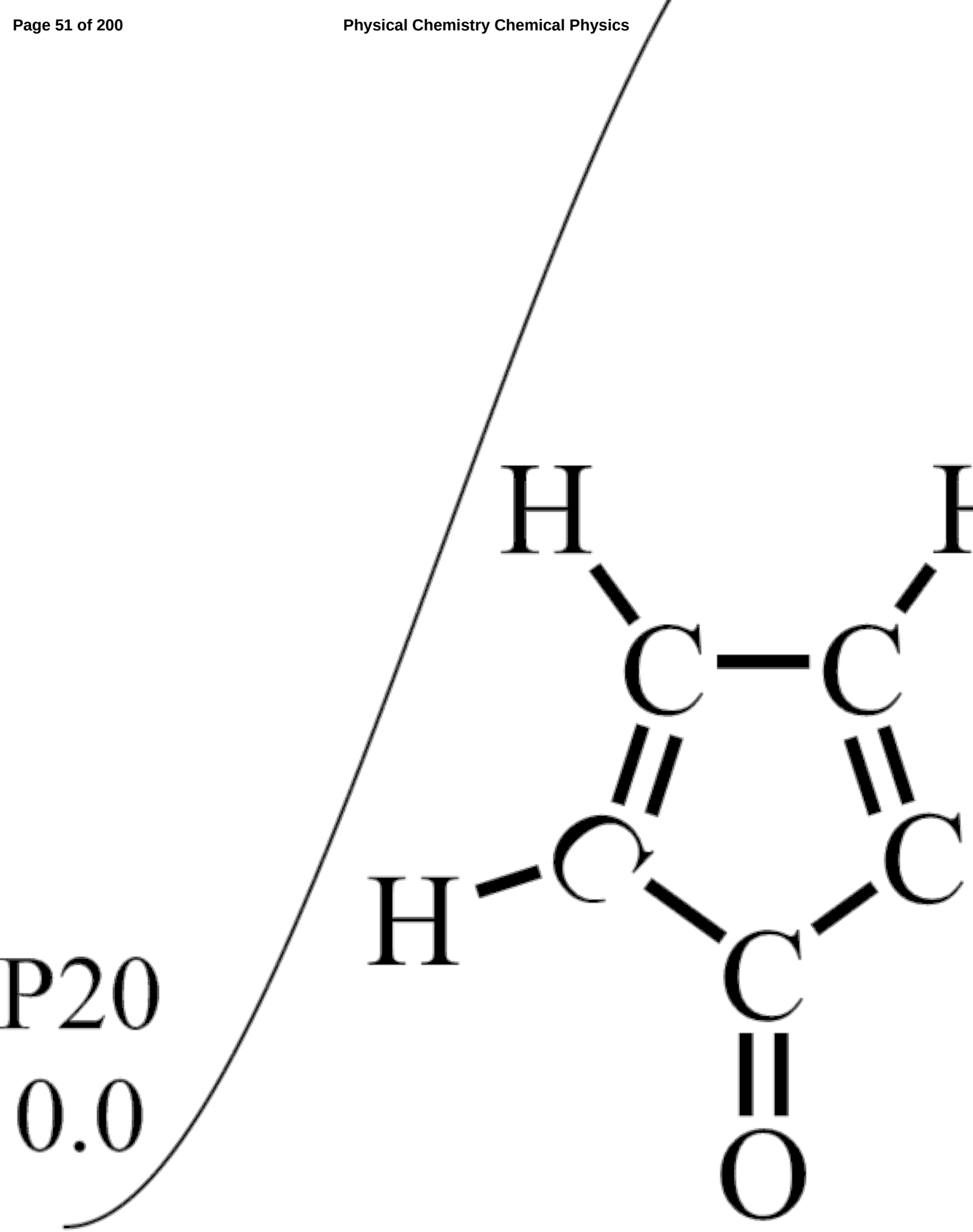
H
H
C
C
C
C
H
C
O
P20
0.0

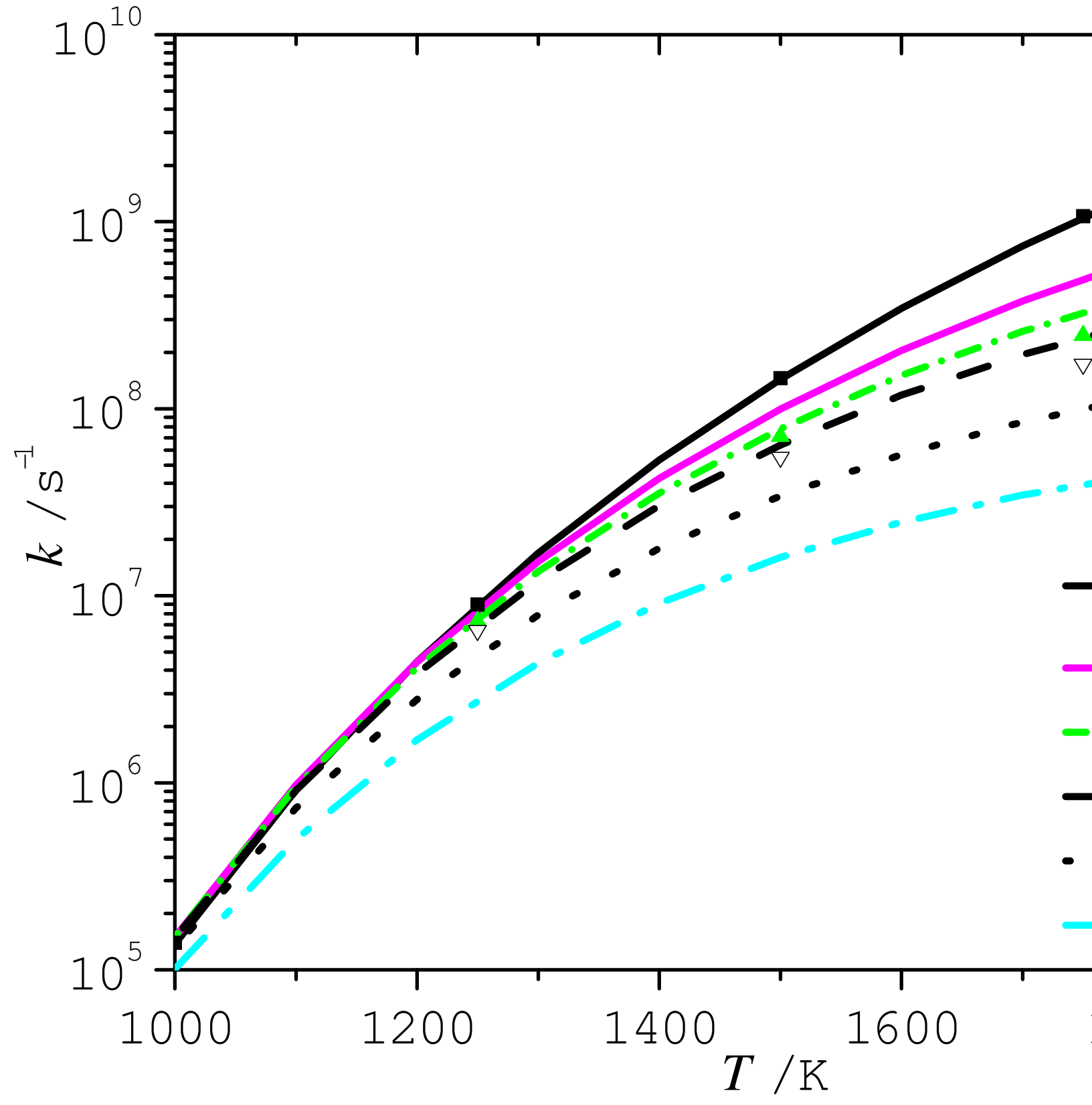
10^10
10^9
10^8
10^7
10^6
10^5
k /s^-1
1000
1200
1400
1600
T /K

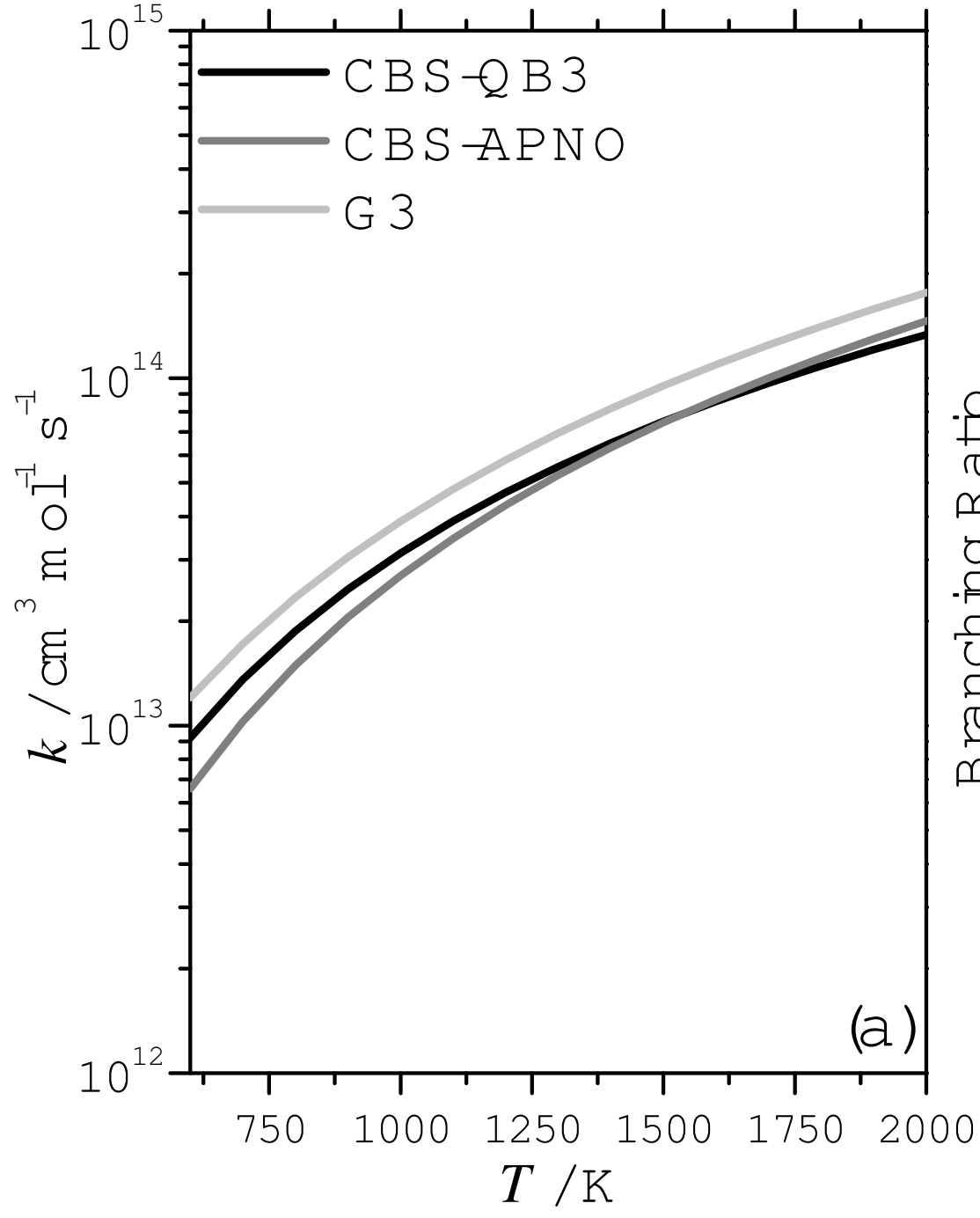
CBS-QB3
CBS-APNO
G3
(a)
10^{15}
10^{14}
10^{13}
10^{12}
k /cm^3 mol^{-1} s^{-1}
750
1000
1250
1500
1750
2000
T /K

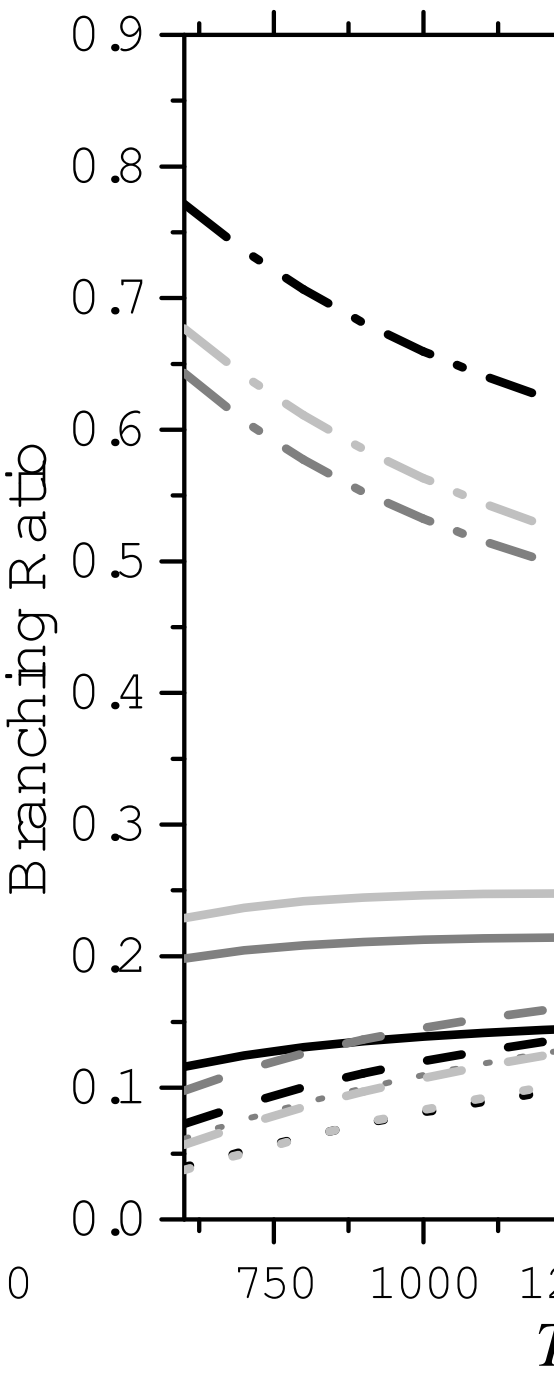
Branching Ratio
0.0
0.1
0.2
0.3
0.4
0.5
0.6
0.7
0.8
0.9
750
1000

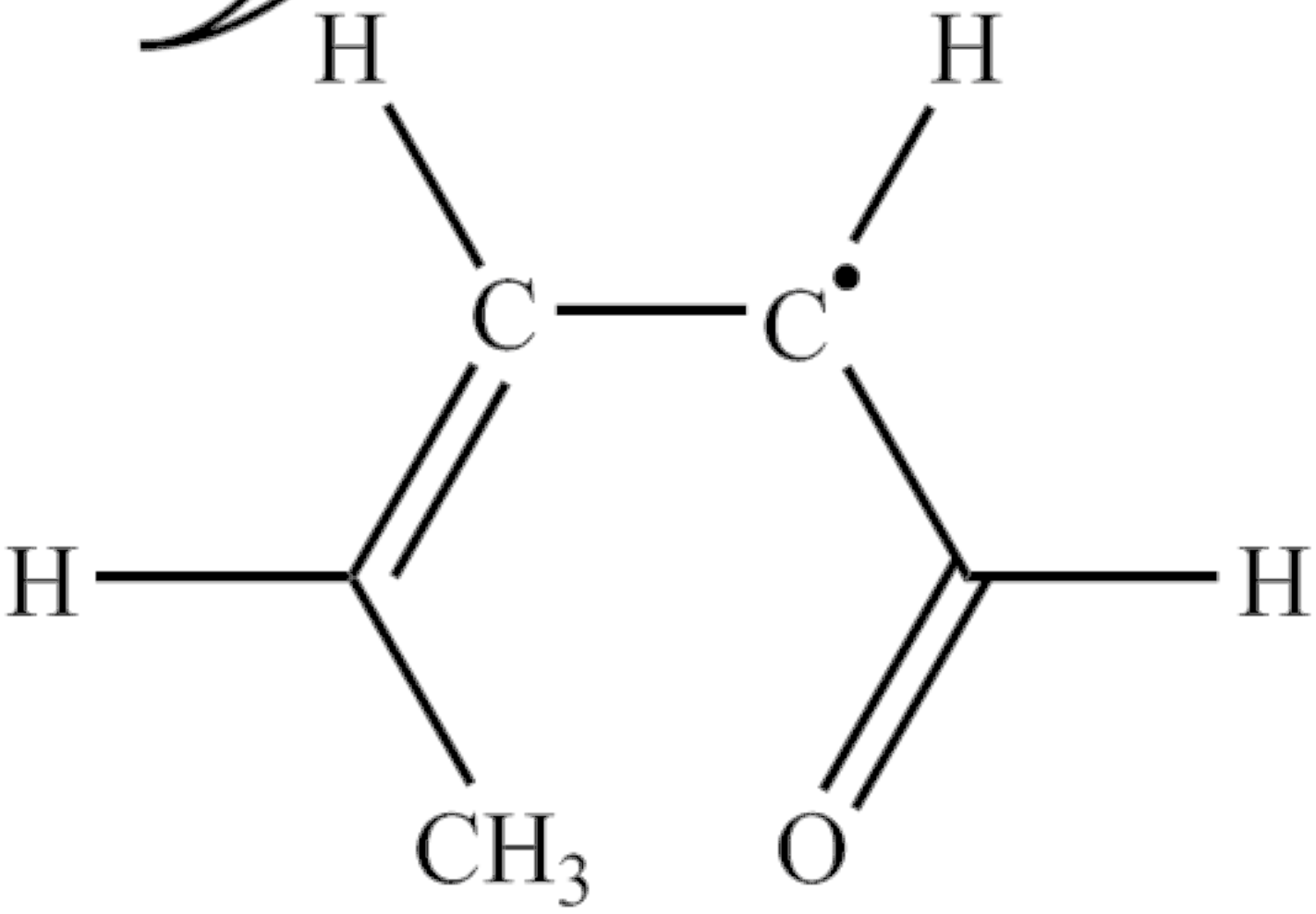
H
H
C
C
H
H
CH3
O

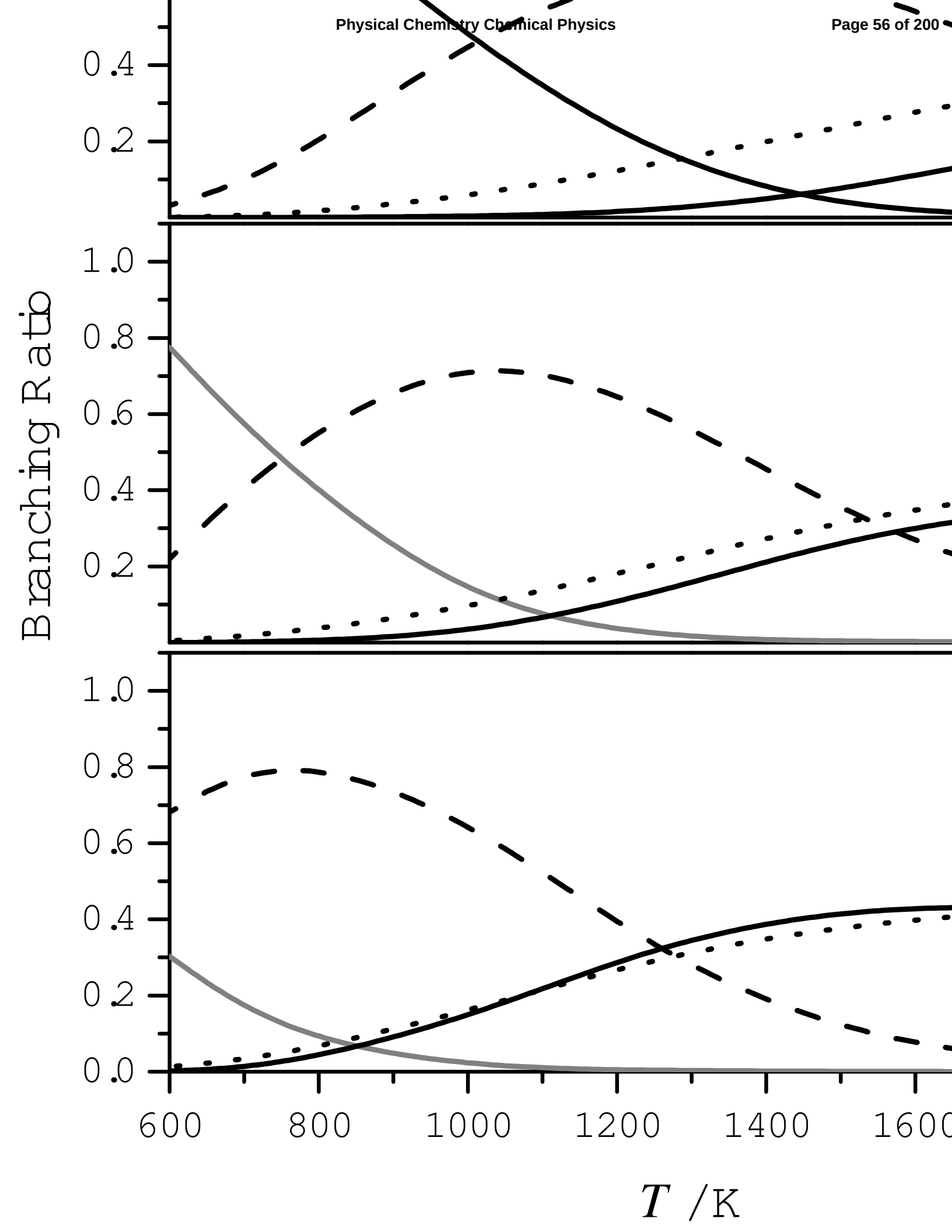
Branching Ratio
0.0
0.2
0.4
0.6
0.8
1.0
600
800
1000
1200
1400
1600
T /K

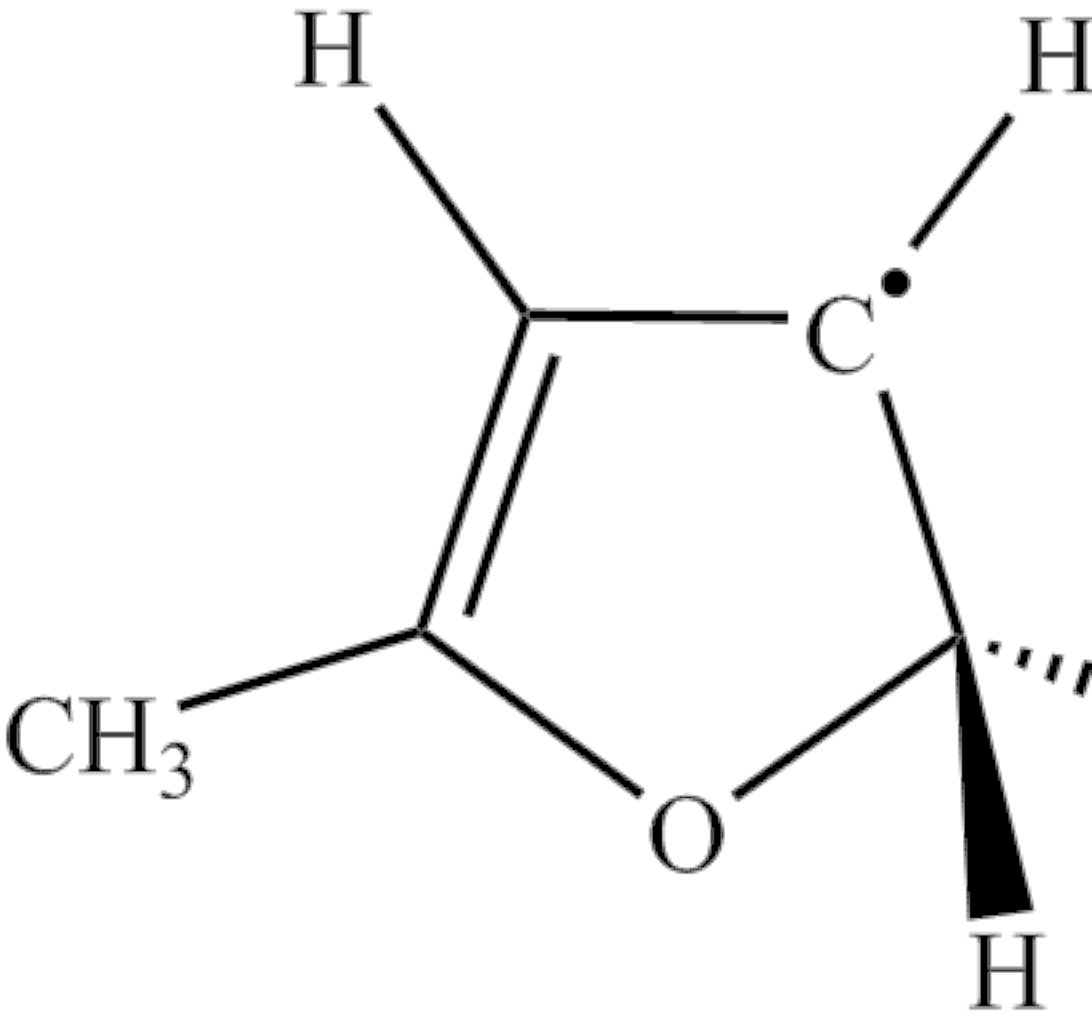
H
H
C
CH3
O
H

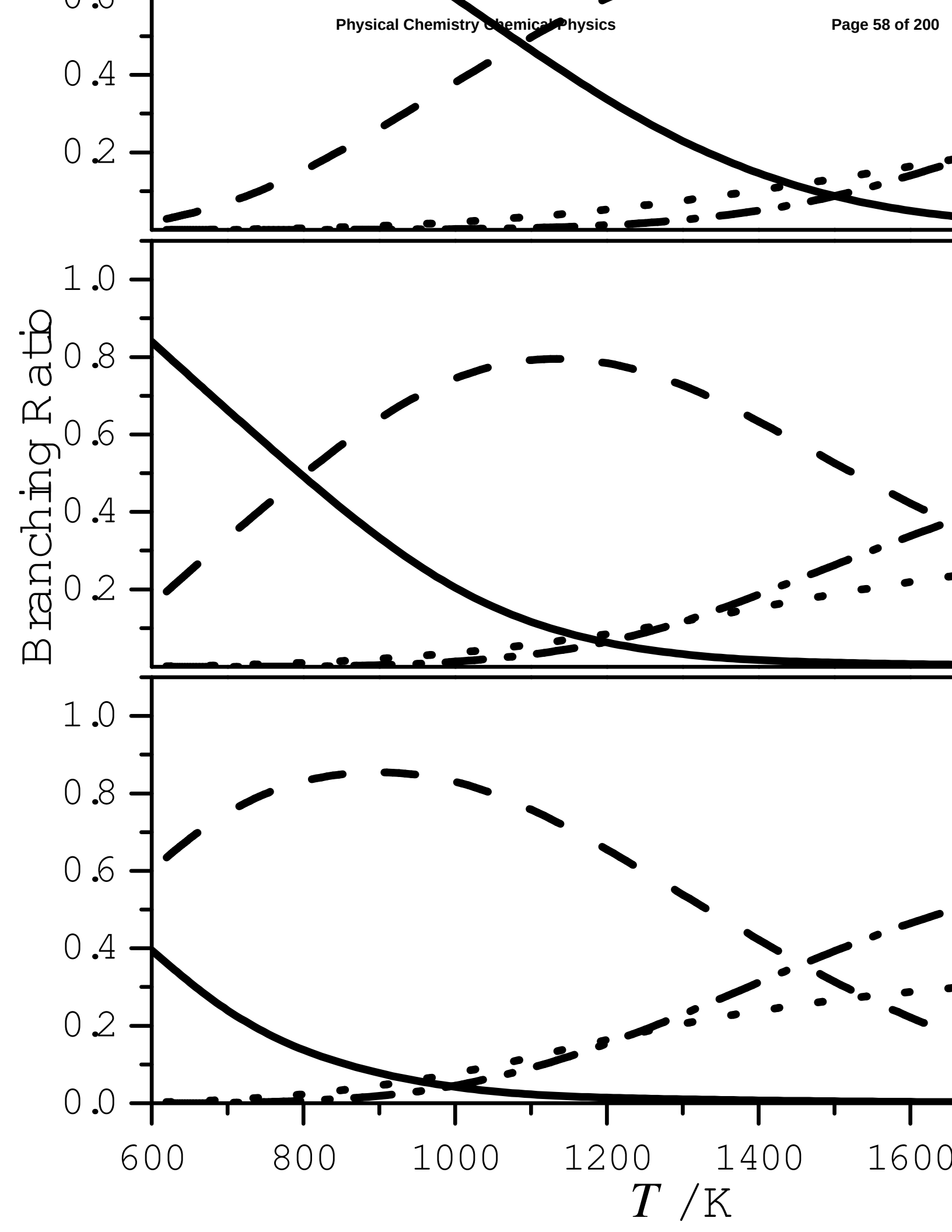
0.4
0.2
1.0
0.8
0.6
0.4
0.2
Branching Ratio
1.0
0.8
0.6
0.4
0.2
0.0
600
800
1000
1200
1400
1600
T /K

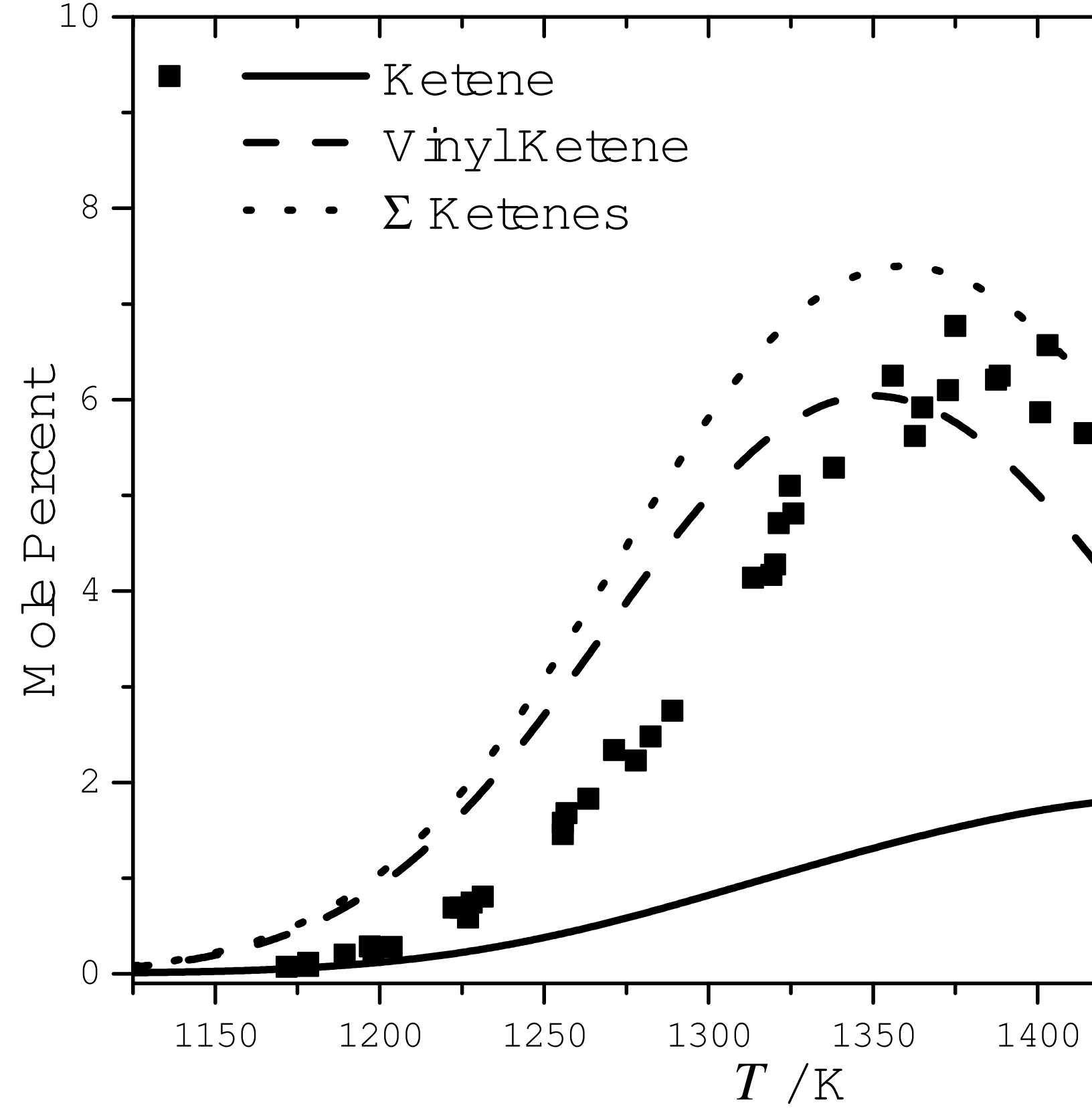
Ketene
Vinylketene
Σ Ketenes
Mole Percent
T /K
0
2
4
6
8
10
1150
1200
1250
1300
1350
1400

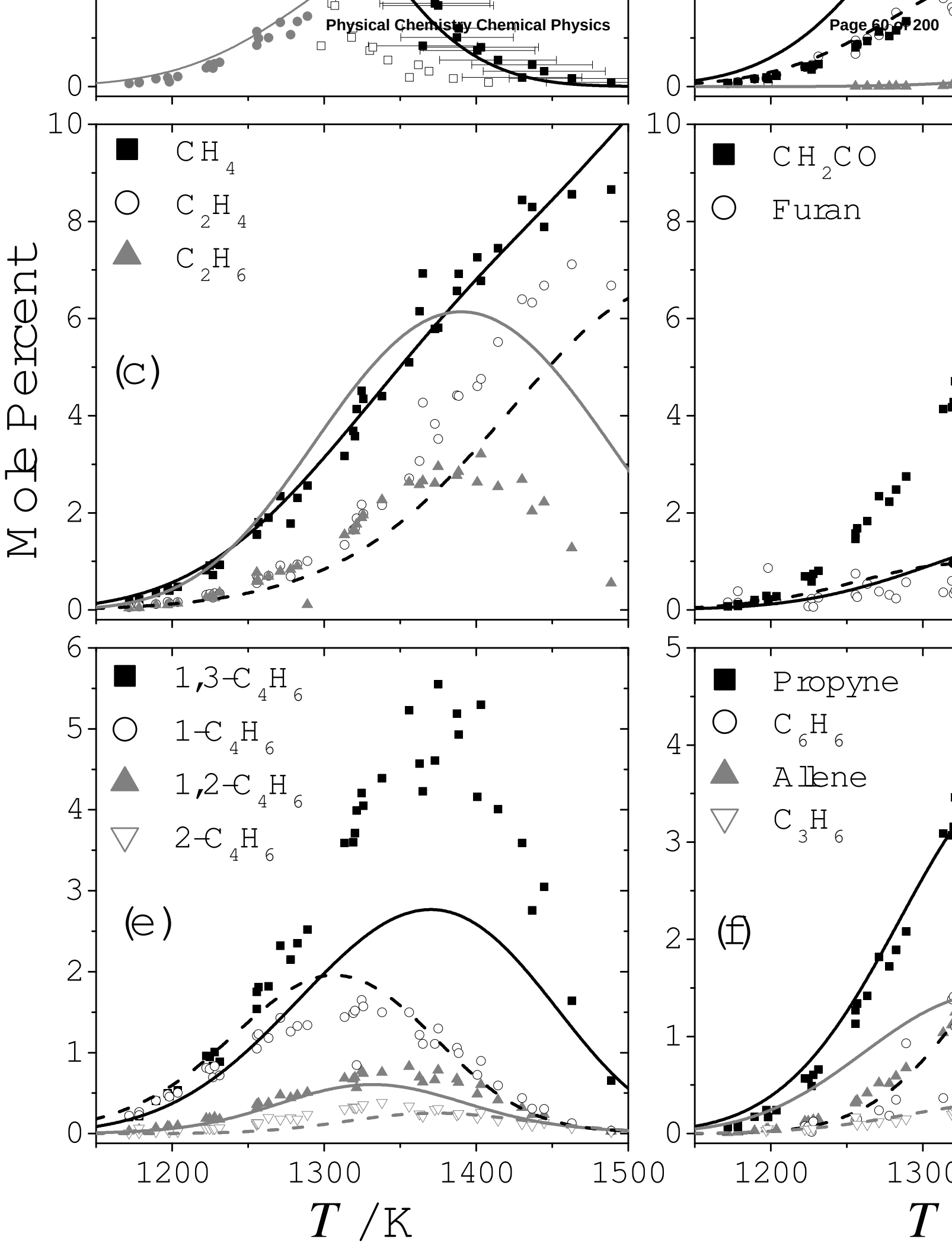
Mole Percent
T /K
CH4
C2H4
C2H6
(c)
CH2CO
Furan
1,3-C4H6
1-C4H6
1,2-C4H6
2-C4H6
(e)
Propyne
C6H6
Allene
C3H6
(f)
1200
1300
1400
1500

ARTICLE TYPE www. rsc.org/xxxxxx | XXXXXXXX

The Pyrolysis of 2-Methylfuran: A Quantum Chemical, Statistical Rate Theory and Kinetic Modelling Study†

Kieran P. Somers,*[a] John M. Simmie,[a] Wayne K. Metcalfe[a] and Henry J. Curran[a]

Received Xth XXXXXXXXXX 20XX, Accepted Xth XXXXXXXXX 20XX
First published on the web Xth XXXXXXXXXX 200X
DOI: 10.1039/b000000x

Due to the rapidly growing interest in the use of biomass derived furanic compounds as potential platform chemicals and fossil fuel replacements, there is a simultaneous need to understand the pyrolysis and combustion properties of such molecules. To this end, the potential energy surfaces for the pyrolysis relevant reactions of the biofuel candidate 2-methylfuran have been characterized using quantum chemical methods (CBS-QB3, CBS-APNO and G3). Canonical transition state theory is employed to determine the high-pressure limiting kinetics, $k(T)$, of elementary reactions. Rice-Ramsperger-Kassel-Marcus theory with an energy grained master equation is used to compute pressure dependent rate constants, $k(T, p)$, and product branching fractions for the multiple-well, multiple-channel reaction pathways which typify the pyrolysis reactions of the title species. The unimolecular decomposition of 2-methylfuran is shown to proceed *via* hydrogen atom transfer reactions through singlet carbene intermediates which readily undergo ring opening to form collisionally stabilised acyclic C_5H_6O isomers before further decomposition to C_1–C_4 species. Rate constants for abstraction by the hydrogen atom and methyl radical are reported with abstraction from the alkyl side chain calculated to dominate. The fate of the primary abstraction product, 2-furanylmethyl radical, is shown to be thermal decomposition to the *n*-butadienyl radical and carbon monoxide through a series of ring opening and hydrogen atom transfer reactions. The dominant bimolecular products of hydrogen atom addition reactions are found to be furan and methyl radical, 1-butene-1-yl radical and carbon monoxide and vinyl ketene and methyl radical. A kinetic mechanism is assembled with computer simulations in good agreement with shock tube speciation profiles taken from the literature. The kinetic mechanism developed herein can be used in future chemical kinetic modelling studies on the pyrolysis and oxidation of 2-methylfuran, or the larger molecular structures for which it is a known pyrolysis/combustion intermediate (e.g. cellulose, coals, 2,5-dimethylfuran).

1 Introduction

Dwindling energy reserves, increasing global energy demands and prices, and the threat of irreversible climate change have led to major research efforts focusing on the development of renewable energy sources, which can supplant fossil derived products and meet future demands in an economically, environmentally and socially sustainable manner.

Ethanol is currently the leading biofuel which offers an alternative to gasoline in the transportation sector, with 83.1 billion litres produced in 2012, primarily in Brazil and North America[1]. However, first-generation production methods which compete with food for feedstocks coupled with a low energy density, high vapor pressure, and complete miscibility with water have led to a re-consideration of its viability as a fossil fuel replacement[2].

Román-Leshkov and co-workers[3] reported a catalytic strategy for the conversion of fructose to 2,5-dimethylfuran (25DMF) *via* the platform chemical hydroxymethylfurfural (HMF) in 2007, with a host of research since following on processes for the conversion of waste biomass into HMF and in turn furanic based fuels[4–8].

25DMF has an energy density[3] of 31.5 MJ L^{-1} which is similar to a typical gasoline and a high boiling point, low water solubility, and the ability to use it in current internal combustion engines[9,10] makes it compatible with current infrastructure. These properties make 25DMF desirable when compared with ethanol, whose lower energy density, boiling point, and greater water solubility prove problematic, although engine tests[9,10] have shown that ethanol performs better than 25DMF in terms of knock resistance and hydrocarbon, nitrous oxide, carbon monoxide and particulate emissions.

[a] *Combustion Chemistry Centre, National University of Ireland, Galway, Galway, Republic of Ireland. E-mail: k.somers1@nuigalway.ie*

† Electronic Supplementary Information (ESI) available: [Tabulated pressure- and temperature-dependent rate constants derived from RRKM/ME computations; Potential energy surfaces for minor reaction pathways; Tabulated electronic energies (0 K and 298.15 K) and geometries for all stationary points; Frequencies, rotational constants and other information used in TST/RRKM computations are provided as input files compatible with the Thermo module of the Multiwell Program Suite; A comparison of high-pressure limiting rate constants reported in the work of Davis and Sarathy[35] with *this work*. The Chemkin-PRO format kinetics, thermochemistry and transport properties files used in the numerical modelling of all experiments; Results of computational modelling of literature burning velocities[32,64], ignition delay times[32,39] and flame speciation measurements[36]]. See DOI: 10.1039/b000000x/

Recently 2-methylfuran (2MF) has received similar attention to 25DMF as a possible alternative biofuel, with novel production methods under development[8]. Engine tests have ensued with Thewes et al.[11] and Wang et al.[12] studying the performance of 2MF in direct-injection spark-ignition engines. Thewes et al.[11] found that 2MF has excellent combustion stability, particularly in cold conditions, with hydrocarbon emission reductions of at least 61% compared to a conventional research octane number 95 fuel. Wang et al.[12] found that 2MF has a greater thermal efficiency than gasoline and 25DMF, that its overall regulated emissions are comparable with 25DMF, and that its aldehyde emissions are much lower than gasoline and ethanol.

Lifshitz and co-workers studied the decomposition of furan, 2MF and 25DMF[13–15] behind reflected shock waves at temperatures of 1050–1460 K, pressure of 1.5–3.0 atmospheres and residence times of 2 ms. Gas chromatography and mass spectrometry were used to quantify reactant and product species in the post-shock mixtures. A total of 17 products were quantified in their 2MF experiments[14] with CO found to be the major decomposition product. A range of C_1–C_4 species were also quantified with two oxygenated intermediates, ketene and furan. The order of reactivity of the series of furans was in line with previous studies (25DMF>2MF>furan)[16,17]. The experiments of Lifshitz *et al.*[14] will be discussed in detail in subsequent sections.

The theoretical work by Sendt[18] ultimately rationalised the decomposition pathways of furan, which were originally proposed as being routed through biradical intermediates[13,16,19]. The authors used CASSCF, CASPT2 and G2(MP2) computations to investigate the potential energy surfaces and kinetics of the thermal decomposition of furan. Hydrogen atom migrations on a singlet potential energy surface with the ultimate formation of CO and propyne, and C_2H_2 and ketene, were highlighted as the likely decomposition pathways and a chemical kinetic model constructed by the authors was capable of replicating experimental speciation profiles[19]. They concluded that ring scission of the C—O bond in furan, on either singlet or triplet potential energy surfaces, was simply too endothermic to contribute to the decomposition of the molecule, thus discounting the numerous postulates[13,16,19] of biradical initiated decomposition pathways for furan. Contemporaneously, Liu et al.[20,21] reached the same conclusion as Sendt *et al*.

Simmie and Curran[22] used quantum chemical calculations and isodesmic reactions to determine gas-phase formation enthalpies ($\Delta_f H^\ominus$) of a range of substituted furans and their radicals at 298.15 K, thus implying bond dissociation energies (BDEs). Their computed $\Delta_f H^\ominus$ of -80.8 ± 0.5 kJ mol^{-1} for 2MF is in good agreement with a calorimetric determination[24] of -76.4 ± 1.2 kJ mol^{-1} and subsequent very high-level theoretical determination by Feller and Simmie[23] of -80.3 ± 5 kJ mol^{-1}.

Simmie and Metcalfe[25] used electronic structure calculations to study the potential energy surfaces of a range of unimolecular decomposition, hydrogen atom addition and hydrogen atom abstraction reactions of 25DMF. Transition state theory was used to determine high-pressure limiting rate constants. Abstraction from the alkyl side chain of 25DMF to form the 5-methyl-2-furanylmethyl radical was highlighted as the preferred pathway for metathesis reactions. They also rationalised the formation of 2MF from 25DMF *via* a hydrogen-atom addition methyl-radical elimination sequence.

Quantum chemical calculations by Sirjean and Fournet[29–31] elaborated on the work of Simmie and Metcalfe[25] by further exploration of the potential energy surface for the decomposition reactions of 2,5-dimethylfuran, 5-methyl-2-furanylmethyl radical and the reactions of hydrogen atom with 25DMF. Rice-Ramsperger-Kassel-Marcus theory calculations with master equation analysis was used to determine pressure-dependent rate constants for each system. The decomposition of the 5-methyl-2-furanylmethyl radical was found to be result in the formation of cyclohexadienone isomers and a hydrogen atom. Hydrogen atom addition to 25DMF was found to primarily lead to the formation of 2MF and a methyl radical, and to a lesser extent, 1,3-butadiene and acetyl radical. Their computations on the total rate of hydrogen atom termination with 25DMF are in excellent agreement with the shock tube studies of Friese et al.[27,28].

Recently, Somers et al.[32] described experiments on the oxidation of 2MF, including measurements of ignition delay times and laminar burning velocities, with a chemical kinetic model developed which could adequately replicate these experiments. The model developed by Somers et al.[32] was based on preliminary *ab initio* calculations which were not described in detail at the time. The aim of *this work* is to describe those preliminary calculations in a more complete fashion. Quantum-Rice-Ramsperger-Kassel (QRRK) theory with a Modified Strong Collision (MSC) approach, as described by Chang *et al.*[33], was utilised in the previous work[32] to account for the influence of pressure on reaction rate constants. Here we utilize more rigorous Rice-Ramsperger-Kassel-Marcus (RRKM) theory calculations coupled with an energy grained master equation (ME) solution.

The QRRK/MSC approach varies from the RRKM/ME in two key respects. The first is that the former derives vibrational frequencies for reactants, and subsequent sums and densities of states, from a three-frequency fit to molecular heat capacities[34]. Microscopic rate constants, $k(E)$, are in turn computed from the density of states of the reactant molecule together with an estimate of the high-pressure limiting rate constant for the reaction *via* the Inverse Laplace Transform (ILT) method. No knowledge of the transition state properties is required in

this approach, although the high-pressure limiting rate constants can be computed from canonical transition state theory as performed in the work of Somers et al.[32] . The RRKM method derives sums and densities of states for reactants and transition states, and subsequently $k(E)$, from more molecular ro-vibrational data typically obtained from quantum chemical calculations.

-The second major difference lies in the approach to collisional energy transfer (CET). Both the MSC and ME approaches assume that collisions occur based on the Lennard-Jones collision frequency. However, the MSC approximation assumes that every collision is completely activating or de-activating, and the Lennard-Jones collision frequency is simply altered by a weak-collision efficiency factor, β_c, which reduces the total rate of collisions in order to account for the fact that activation and de-activation require many collisions. The ME approach explicitly considers the transfer of energy between different energy levels and is thus a more physically realistic and accurate approximation for CET.

Since the development of the kinetic model by Somers *et al.*[32] a number of noteworthy studies on 2MF oxidation have been carried out contemporaneously with *this work*. Davis and Sarathy[35] reported reaction enthalpies, barrier heights and rate constants for several of the combustion and atmospheric reactions of 2-methylfuran based on quantum chemistry (CBS-QB3, G4) and canonical rate theory. Hydroxyl radical addition to the furan ring and subsequent O_2 addition reactions to the nascent adduct were investigated as possible reactions of significance under atmospheric and low-temperature combustion conditions. They also investigated unimolecular decomposition reactions of 2MF and abstraction reactions by hydrogen atom, although hydrogen atom addition reactions and the influence of pressure on the thermal decomposition pathways rate constants were not investigated. A small number of these high-temperature reactions are described in detail in *this work*, with the high-pressure limiting rate constants determined here in good agreement with the results of Davis and Sarathy[35]. A comparison of our results with Davis and Sarathy is presented in the ESI.

Tran and co-workers[36] recently studied the flame structure of two laminar premixed low-pressure (20 and 40 mbar) 2MF/O_2/Ar flames, with electron-ionization molecular beam mass spectrometry (EI-MBMS) and GC used to quantify reactant, intermediate and product concentrations as a function of distance from the burner. They provided a chemical mechanism for 2MF oxidation under these conditions, constructed largely by taking analogies to rate constants from 2,5-dimethylfuran[37] and furan[38] mechanisms available in the literature. Their mechanism was shown to satisfactorily reproduce their experimental results, as was the mechanism previously described by Somers et al.[32], although the former was not compared with the ignition delay time or laminar burning velocities against which the latter was also validated. The mechanism developed as part of *this work* is compared with these recently published measurements in the ESI, with good quantitative predictions of the major species reported experimentally.

Wei *et al.*[39] recently used a shock tube facility to determine ignition delay times of 2MF/O_2/Ar mixtures from equivalence ratios of 0.25–2.0, at temperatures of 1120–1700 K and at pressures of 1.25–10.65 bar. Their measurements are consistent with those of Somers *et al.*[32] at atmospheric pressure and provide valuable new data for kinetic modelling at elevated pressures. The kinetic model of Somers *et al.*[32] was used to numerically model the experimental results with reasonable agreement observed. The updated mechanism described herein is compared with these new ignition measurements in the ESI, with good reproduction of experimental measurements.

2 Computational Methods

Minima and transition states have been initially optimised using the B3LYP[40,41] functional coupled with the 6-31+G(d,p) basis set. Frequency analysis is employed to verify the nature of stationary points with the presence of a single imaginary frequency indicative of a transition structure, which is in turn connected to reactants and products *via* intrinsic reaction coordinate (IRC) calculations[42].

B3LYP optimised geometries are subject to further geometry optimisation, frequency analysis and single point energy calculations using the compound methods CBS-QB3[43], CBS-APNO[44] and G3[45] which have been used in numerous theoretical studies for the determination of thermochemistry and kinetics of furanic species of late[25,28–31,35,46]. The three methods tend to give good agreement with each other, possibly indicating an absence of multi-reference character in the systems studied. Calculations have been carried out using the Gaussian 03 and 09 applications[47]. Where uncertainties in quantum chemical calculations are reported in the text, it is to one standard deviation.

The Thermo application of the Multiwell program suite[48,49] has been used to determine thermochemical parameters (S, C_p and $H_T - H_0$, 298–2500 K) and high-pressure limiting rate constants, from canonical transition state theory. Internal rotations corresponding to low frequency torsional modes are analysed *via* relaxed potential energy surface scans, where geometries and energies are calculated as a function of dihedral angle in 10 degree increments. Potential energy and rotational constants (computed using the LAMM module of Multiwell) as a function of dihedral angle are fit to a series of truncated sine and cosine Fourier series and are used as input for a 1-D internal rotation approximation. For hydrogen atom

transfer, abstraction, and addition reactions, the contribution of quantum mechanical tunneling has been accounted for *via* the inclusion of asymmetric Eckart tunneling as implemented in Multiwell.

Standard state enthalpies of formation ($\Delta_f H^\ominus$) of all C_5H_6O species are computed based on the $\Delta_f H^\ominus$ of 2-methylfuran[23], and $\Delta_r H_0$ (0 K) with subsequent extrapolation *via* enthalpy functions ($H_T - H_0$). $\Delta_f H^\ominus$ of $\dot{C}_5H_7O$ radicals are derived from $\Delta_f H_0$ of 2MF and $\dot{H}$ atom and $\Delta_r H_0$. For the 2-furanylmethyl radical, $\Delta_f H_0$ (78.07 kJ mol^{-1}) is determined from $\Delta_r H_0$ (85.11 kJ mol^{-1}) for the reaction 2MF $\rightarrow \dot{H}$ + 2-furanylmethyl and the known $\Delta_f H^\ominus$ of 2MF and $\dot{H}$ atom. $\Delta_f H^\ominus$ of all other $\dot{C}_5H_5O$ radicals are computed relative to 2-furanylmethyl radical. Whilst isodesmic reactions could also be employed to determine the above parameters, the lack of well characterized companion species for error cancellation inhibits the development of suitable working reactions, particularly as the acyclic species which are formed upon opening of the 2MF ring are highly functionalised. The above method does ensure a consistent approach to thermochemical computations for inclusion in subsequent kinetic modelling work.

Many of the reactions investigated in *this work* correspond to those which are both temperature- and pressure-dependent. RRKM/ME calculations are used as a framework in order to evaluate the effect of the latter. RRKM/ME analyses of the chemically activated reactions of hydrogen atom with 2MF have been carried out using the stochastic method developed by Barker and co-workers implemented via the Multiwell program suite[48,49]. Sums and densities of states of reactants and transition states are evaluated using a direct count method with an energy grain size of 10 cm^{-1}, up to a maximum energy of 10^5 cm^{-1}. In order to minimise stochastic uncertainties for minor reaction pathways, 20 $\times 10^6$ trials were carried out for 160 collisions at temperatures of 600–2000 K from 1–100 atm; for sub-atmospheric pressures, 1–2 $\times 10^6$ trials were employed to minimise computational expense. Ro-vibrationally excited adducts were found to have undergone deactivation within the 160 simulated collisions under these conditions, before thermal unimolecular decay of the intermediate isomers subsequently occurred. Phenomological rate constants for the reaction 2MF + $\dot{H} \rightarrow$ products were determined by monitoring concentration-time and vibrational energy-time profiles of the excited adducts using the Thermal Decay procedure recently described by Pinches and da Silva[50].

RRKM/ME analyses of the thermally activated unimolecular reactions of 2MF was carried out using the ChemRate code[51] as Multiwell is not optimally designed for the computation of slow steady state unimolecular reactions where the number of collisions being simulated is greater than a few thousand. In this case, the thermal unimolecular reaction of 2MF is slow below 1750 K and $>10^4$ collisions are required to achieve adequate consumption of the reactant for the extraction of rate constants from concentration-time profiles. For calculations using ChemRate, an energy grain size of 40–70 cm^{-1} was used up to a maximum of 10^5–1.5 $\times 10^5$ cm^{-1} (depending on the specific temperature being studied). Convergence was monitored by ensuring that solutions to the Master Equation became time-independent with the "Divide and Conquer" method employed. The same method is used for computations on the thermal decomposition of the 2-furanylmethyl radical, although as chemical reaction for this species is much faster than for 2MF, a comparison of pressure-dependent rate constants derived from both Multiwell and ChemRate is presented. All RRKM/ME calculations are carried out based on ro-vibrational and energetic properties from CBS-QB3 calculations.

For all simulations, the average energy transferred in a deactivating collision, $\langle \Delta E_d \rangle$, was assumed to have a temperature-independent value of 1000 cm^{-1}. Many recent literature studies have assumed constant $\langle \Delta E_d \rangle$ values for similar systems (large aromatic molecules). $\langle \Delta E_d \rangle$ estimates have ranged from 2000 cm^{-1} for the benzyl radical[52,53], 1000 cm^{-1} for a C_7 heterocyclic ring[55], 718 cm^{-1} for a $C_{10}H_{10}$ biheterocycle[54], 500 cm^{-1} for pyrazole[56], fulveneallene[57] and benzyl hydroperoxide[58], and 260 cm^{-1} for 2,5-dimethylfuran[29–31] and furan[38]. Other recent studies have assumed temperature-dependent energy transfer parameters[59,60]. There is still remaining uncertainty in these energy transfer parameters but our empirical estimate of 1000 cm^{-1} lies well within the range of values adopted in recent literature studies. Some test calculations were carried out with $\langle \Delta E_d \rangle$ = 500 cm^{-1} and $\langle \Delta E_d \rangle$ = 2000 cm^{-1} to illustrate the variation in computed rate constants. The results are found in ESI and they show less than a factor of 2 variation in the computed rate constants for unimolecular decomposition pathways, and a factor of 23 variation in computed rate constants for major chemically activated pathways. All calculations are carried out in an argon bath gas with Lennard-Jones parameters for the third body taken as $\sigma = 3.47$ Å and $\varepsilon/k_B = 114$[61]. For 2MF and its derivatives Lennard-Jones parameters were determined empirically from the correlations provided by Kee and co-workers[62]. Together with recommended critical constants for 2MF[63], $\sigma = 5.36$ Å and $\varepsilon/k_B = 396$ are computed. All intermediates from 2MF decomposition, 2-furanylmethyl radical decomposition, and hydrogen atom addition pathways are assumed to have the same Lennard-Jones parameters.

Ultimately, the kinetics and thermochemistry produced as part of *this work* are used as input for a chemical kinetic model to describe the pyrolysis of 2MF, which is then compared with the shock tube data of Lifshitz et al.[14]. Shock tube simulations were carried out using the Aurora module (constant volume) of the Chemkin-Pro[65] software package with an average resi-

dence time of 2.05 ms and an average pressure of 2.5 atm.

3 Results and Discussion

In all subsequent sections, the subscript ($_x$) used to enumerate tabulated rate constants (k_x) corresponds with the number assigned to the transition state (**TSx**) for that reaction on a given potential energy surface. If a reaction does not have an accompanying potential energy surface (abstraction reactions or literature rate constants), other shorthand notations are used.

3.1 Carbene Mediated Unimolecular Decomposition

Table 1 Arrhenius coefficients of high-pressure limiting rate constants for the decomposition of 2-methylfuran *via* carbene intermediates. $k(\mathrm{s}^{-1}) = AT^n \exp(-E_a/R)$, AT^n (s^{-1}), E_a/R (K).

No.	Reaction	A	n	E_a/R
k_1	M1 → M2	1.36×10^{11}	0.70	41593.
k_2	M1 → M3	2.26×10^{10}	0.99	32486.
k_3	M2 → P1 + P2	1.55×10^{12}	0.83	14343.
k_4	M3 → P3 + P4	8.54×10^{12}	0.68	15881.
k_5	M1 → M4	2.15×10^{10}	0.95	35145.
k_6	M4 → M5	2.80×10^{12}	0.30	−72.
k_7	M5 → M6	2.17×10^{13}	−0.24	2725.
k_8	M6 → P5 + P6	7.30×10^{10}	0.69	21872.
k_9	M6 → P6 + P7	3.40×10^{11}	1.00	30161.
k_{10}	M1 → M7	1.75×10^{10}	1.00	34174.
k_{11}	M7 → M8	6.11×10^{12}	0.09	552.
k_{12}	M8 → M9	1.26×10^{13}	−0.13	2146.
k_{13}	M9 → P3 + P4	3.91×10^{08}	1.48	33817.

Potential energy surfaces for the formation and decomposition of β-carbenes are depicted in Figures 1 and 2 with corresponding rate constants (k_5–k_{13}) reported in Table 1. Unimolecular decomposition of 2MF through α-carbene intermediates was found to be uncompetitive with the β-carbene pathways due to due to the higher energy barriers encountered on their potential energy surfaces. A detailed discussion on these pathways can be found in ESI with the rate constants computed for these pathways (k_1–k_4) reported in Table 1.

A 3 → 2 hydrogen atom transfer, Figure 1, which forms a β-carbene intermediate (**M4**) has a computed barrier of 294.5 ± 1.6 kJ mol^{-1}. This intermediate could not be located using the CBS-QB3 method (B3LYP/CBSB7 optimisation step), which instead led to the cis conformer of 2,3-pentadiene-1-al upon optimisation. The same observation was noted in a computational study for the analogous process in 25DMF[25].

The CBS-APNO and G3 methods successfully locate this carbene intermediate existing at 256.8 ± 2.9 kJ mol^{-1} above 2MF. The subsequent ring opening reaction of the cyclic carbene is found to be extremely facile, with a transition state (**TS6**) being located 2.8 and 2.5 kJ mol^{-1} *below* the level of the reactants using the CBS-APNO and G3 methods respectively. The shallow nature of the β-carbene well likely contributes to the inability of the CBS-QB3 method to locate the reactant as a stationary point.

The product of ring opening exists in two rotameric forms (**M5** and **M6**) about the formyl group, which are connected by a rotational barrier of 21.4 ± 0.3 kJ mol^{-1}. The trans conformer (**M6**) can undergo CO elimination with a concomitant 1→4 hydrogen shift to form 1-butyne (k_8) in a near thermoneutral reaction with $\Delta_r H_0$ = 11.9 ± 0.7 kJ mol^{-1}.

The barrier for the process is computed as 183.6 kJ mol^{-1} based CBS-QB3 calculations, and 180.2 kJ mol^{-1} *via* the CBS-APNO method, in good agreement with G2(MP2) calculations[18] (175 kJ mol^{-1}) for the similar process in furan. A 1→2 hydrogen atom transfer to form 1,2-butadiene and CO is also possible, although the barrier is much greater at 252.2 kJ mol^{-1}.

Simple fission reactions are also possible for this acyclic species and BDEs of C—C bonds in the system have therefore been investigated, as they should coincide effectively with the barrier for these dissociation reactions. The formation of formyl radical (HĊO) and 1,2-butadiene-1-yl radical (ĊH=C=CH—CH$_3$) from the trans conformer is found to be endothermic by 321.7 kJ mol^{-1} based on standard state CBS-QB3 energetics, with fission to form a ĊH$_3$ radical and a formyl allene radical (ĊH=C=CH—CH=O) having a similar BDE of 327.9 kJ mol^{-1}. These homolytic processes face enthalpic barriers much greater than that computed for the lowest energy CO elimination process (circa 140 kJ mol^{-1}), and are therefore unlikely to contribute to the decomposition of the aldehyde.

β-carbene formation (**M7**) *via* a 4→5 hydrogen shift (Figure 2) proceeds through a barrier of 287.8 ± 1.2 kJ mol^{-1}, similar to that observed for the 2→3 hydrogen shift. The carbene can undergo ring opening through **TS11**, in an effectively barrierless process (1.69 ± 1.7 kJ mol^{-1}) to form 3,4-pentadiene-2-one.

Like the formyl butadiene product formed from a 3→2 hydrogen atom transfer, there exists cis and trans conformers of 3,4-pentadiene-2-one (**M8** and **M9**) with the trans conformer (**M9**) capable of undergoing a 1→5 hydrogen shift in a concerted process to form ketene and propyne. A barrier of 287.3 kJ mol^{-1} is computed at the CBS-QB3 level of theory.

Given the tight nature of the transition state, we calculate a decrease in $\Delta^{\ddagger}S$ of −3.3 kJ mol^{-1} at standard temperature and only a slight increase in $\Delta^{\ddagger}S$ to 1.0 kJ mol^{-1} at 2000 K. C—C bond fission of the more stable trans conformer to acetyl radical (CH$_3$—Ċ=O) and the propargyl radical (CH≡C—ĊH$_2$) is computed to be endothermic by 317.7 ± 1.8 kJ mol^{-1}, with

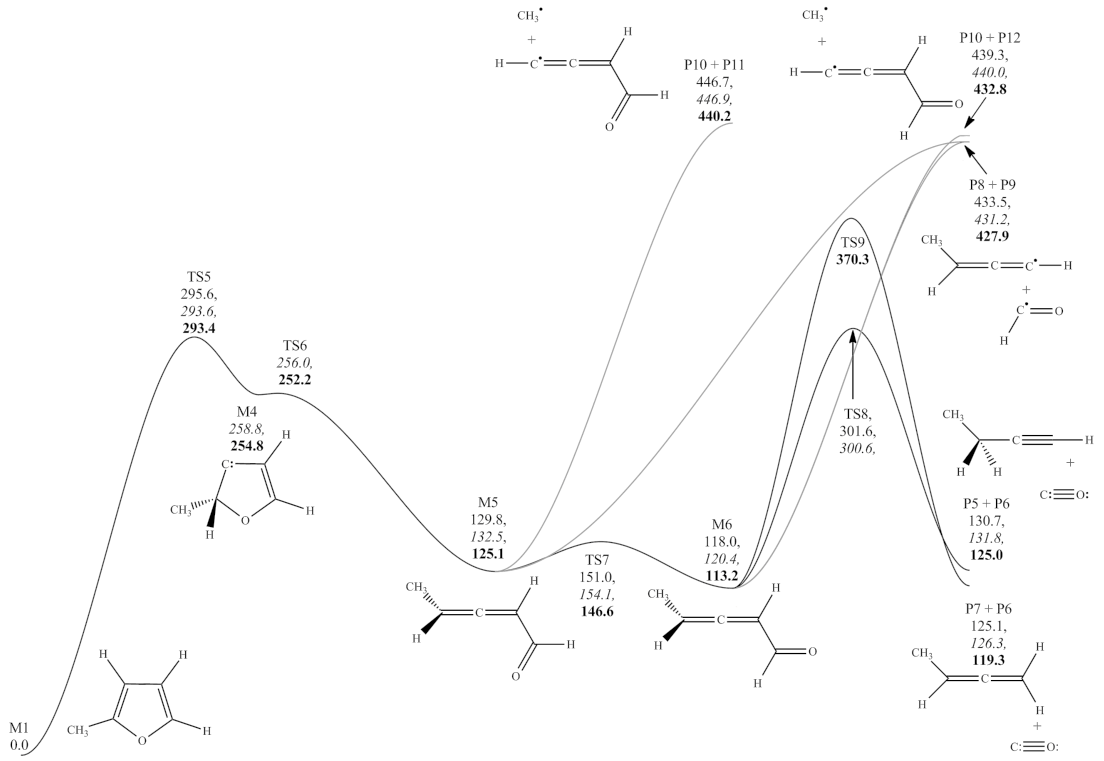

Fig. 1 Potential energy surface for the formation and decomposition of β-carbenes formed from 3→2 hydrogen shift. CBS-QB3, *CBS-APNO* and **G3** energies in kJ mol^{-1} at 0 K relative to 2-methylfuran.

the formation of a $\dot{C}H_3$ radical and a formyl allene radical ($CH_2{=}C{=}CH{-}\dot{C}{=}O$) found to be endothermic by 359.1 ± 4.5 kJ mol^{-1}.

The formation of $CH_3{-}\dot{C}{=}O$ and $CH{\equiv}C{-}\dot{C}H_2$ radicals is energetically similar to the concerted elimination process and we therefore expect that simple fission is likely to be favoured over the elimination reaction at high temperatures, as the looser nature of the homolysis is likely to result in an increase in $\Delta^{\ddagger}S$ for the reaction.

Figure 3, and Tables 1 and 2, show calculated rate constants for the formation of carbenes in the homologous series furan, 2MF and 25DMF, with consistent rate constants emerging for the formation of α- and β-carbenes *via* hydrogen atom and methyl group shifts.

Comparison is made with the computations of Simmie and Metcalfe[25] for the 25DMF system and Sendt *et al.*[18] who reported Arrhenius parameters for this process in furan. Rate constants for furan and 25DMF decomposition are reduced by a factor of two in Figure 3 for comparison with 2MF, given the loss of symmetry for the mono-alkylated furan, but those reported in Table 2 have not undergone this treatment. There is a close agreement within the computed rate constants amongst the homologous series, which may be of interest to kinetic modellers.

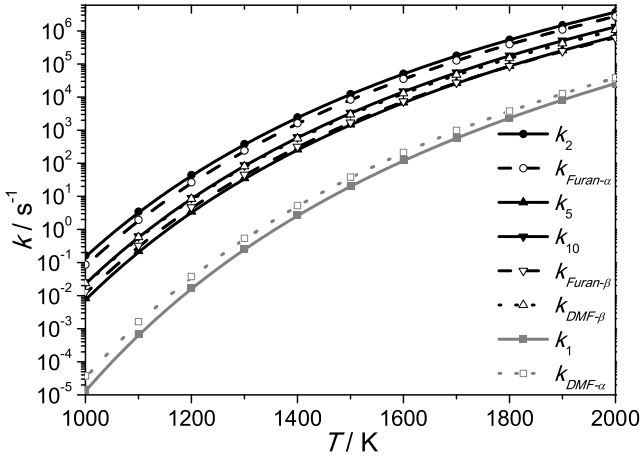

Fig. 3 A comparison of the high-pressure limiting rate constants for –H (black) and –CH_3 (grey) group transfer reactions in the homologous series furan (– –), 2-methylfuran (—) and 2,5-dimethylfuran (···). Furan and 2,5-dimethylfuran rate constants are reduced by a factor of two to account for the external symmetry number of 1 for 2-methylfuran.

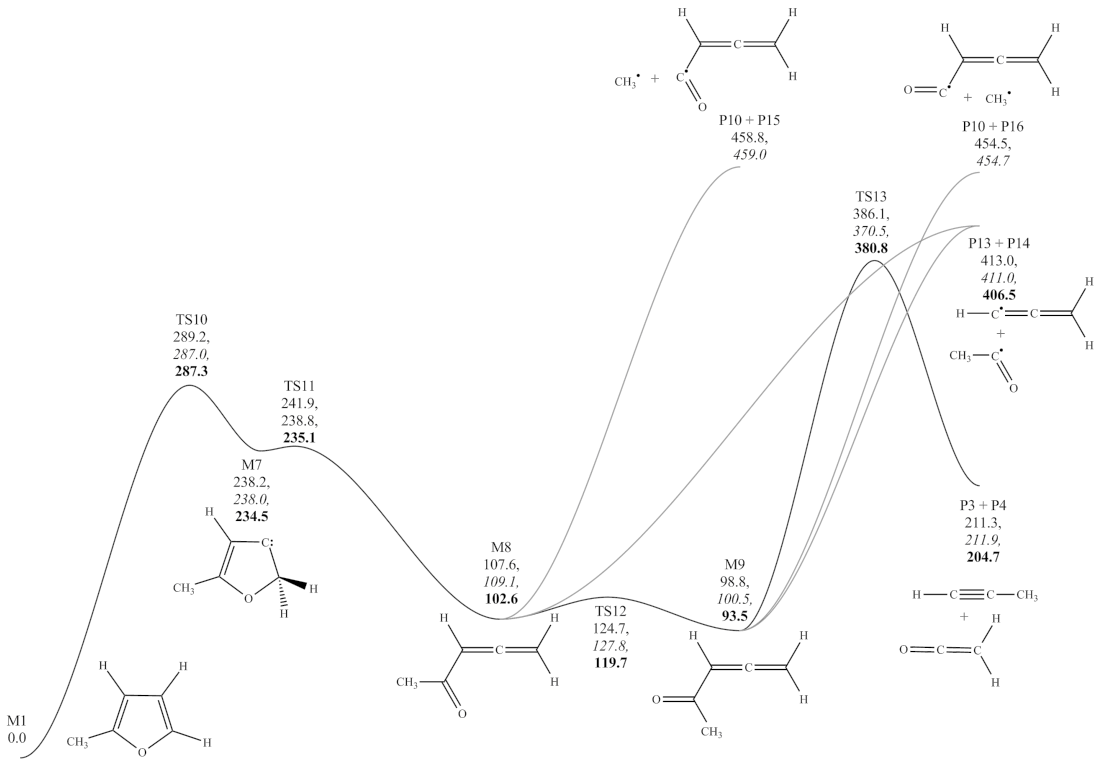

Fig. 2 Potential energy surface for the formation and decomposition of β-carbenes formed from 4→5 hydrogen shift. CBS-QB3, *CBS-APNO* and **G3** energies in kJ mol^{-1} at 0 K relative to 2-methylfuran. Variational processes in greyscale.

Table 2 Arrhenius coefficients of high-pressure limiting rate constants for –H and –CH_3 group shifts in 2,5-dimethylfuran and furan. $k(s^{-1}) = AT^n \exp(-E_a/R)$, AT^n (s^{-1}), E_a/R (K).

No.	Reactant	Carbene, –R	A	n	E_a/R
$k_{Furan-\alpha}$	Furan[a]	α, –H	1.69×10^{12}	0.56	33782.
$k_{Furan-\beta}$	Furan[b]	β, –H	5.94×10^{13}	0.00	35372.
$k_{DMF-\alpha}$	25DMF[c]	α, –CH_3	7.77×10^{13}	0.00	41483.
$k_{DMF-\beta}$	25DMF[c]	β, –H	9.48×10^{13}	0.00	35230.

[a] *this work*, [b] Sendt *et al.*[18], [c] Simmie and Metcalfe[25]

RRKM/ME analysis has been applied to determine pressure- and temperature-dependent rate constants for the multi-step collisionally activated decomposition pathways of 2MF. A number of simplifications are made to the potential energy surface for decomposition through β-carbenes. Both **M4** and **M7** are omitted from the RRKM/ME calculations as preliminary calculations showed that collisional stabilisation is inefficient for these species, owing to their shallow well-depth. Only a single rotamer of 2,3-pentadiene-1-al (**M6**) and of 3,4-pentadiene-2-one (**M9**) is included in this analysis for simplicity.

Pressure-dependent rate constants for the β-carbene mediated decomposition of 2-methylfuran are shown in Figure 4. Under the experimental conditions of Lifshitz *et al.* (1150–1500 K, 2.5 atm), both reaction pathways are approximately at the high-pressure limit, with only $\approx$ 20% reduction in the computed high-pressure limiting rate constants at 1500 K and 2.5 atm. With increasing temperature and decreasing pressure however, the deviation of the rate constants from the high-pressure limiting case becomes more pronounced and there may be a need to account for fall-off effects under these conditions.

As part of our RRKM/ME calculations, we also consider the simple fission of 2MF into 2-furanylmethyl radical and Ḣ atom. The high-pressure limiting rate constant for this barrierless process is estimated based on an analogy with a literature[66] rate constant for the recombination of a Ḣ atom with the resonantly stabilised benzyl radical. From an estimated recombination rate constant of $9.25\times10^{13}T^{-0.01}\exp(-96.9/T)$ cm^3 mol^{-1} s^{-1} and the equilibrium constant for the reaction 2-furanylmethyl + Ḣ atom $\rightleftharpoons$ 2MF, a high-pressure limiting rate constant of $3.37\times10^{15}T^{-0.01}\exp(-44026/T)$ s^{-1} for the dissociation reaction is computed through microscopic reversibility.

For the alkyl side chains of 2MF[22] and toluene[67] similar

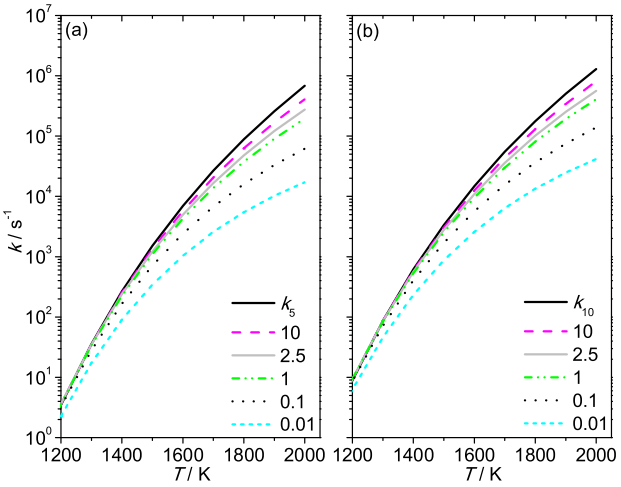

Fig. 4 Computed pressure-dependent rate constants (atm) for the decomposition of 2-methylfuran to (a) 2,3-pentadiene-1-al (**M6**) and (b) 3,4-pentadiene-2-one (**M9**).

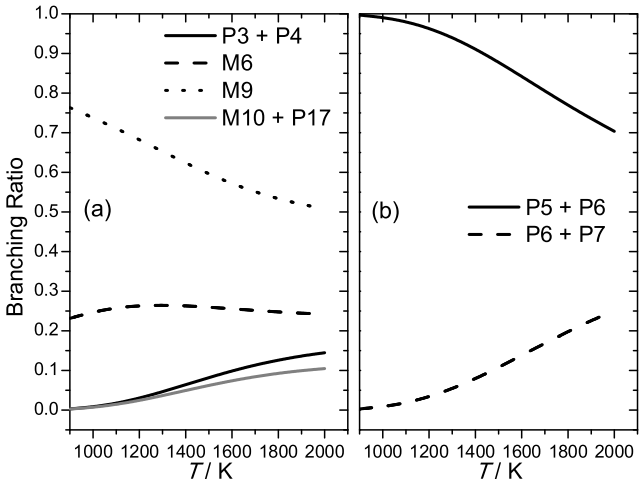

Fig. 5 Temperature-dependent branching ratios for the thermal decomposition of 2-methylfuran under the conditions of the Lifshitz *et al.*[14] study (2.5 atm). (a) 2-methylfuran → products; **P3** + **P4** (ketene + propyne *via* α-carbene), **M6** (2,3-pentadiene-1-al *via* β-carbene), **M9** (3,4-pentadiene-2-one *via* β-carbene), **M10** + **P17** (C–H fission) (b) **M6** → products; **P5** + **P6** (1-butyne + CO), **P6** + **P7** (1,2-butadiene + CO).

BDEs have previously been reported, 360.9 ± 5.2 and 375 ± 5.0 kJ mol^{-1} respectively. A BDE of 361.2 kJ mol^{-1} for 2MF is determined in *this work*. The high-pressure limiting rate constant of the barrierless association of a Ḣ atom with the 2-furanylmethyl radical may be expected to be of a similar order as that for the recombination of Ḣ atom with benzyl radical, and the high-pressure limiting rate constant described above should therefore be of a reasonable order.

Transition state properties (frequencies, rotational constants) for the C–H fission process have been generated automatically by the ChemRate code based on the properties of the reactants and products for the reaction and the microscopic rate constants, $k(E)$, were then determined from the estimated transition state properties. $k(E)$ were subsequently altered by an empirical fitting factor such that the high-pressure limiting rate constant described above was replicated at every temperature. The enthalpy of activation for the process was assumed equal to the the enthalpy of reaction at 0 K.

Based on temperature- and pressure-dependent RRKM/ME calculations under the conditions of Lifshitz *et al.* study[14], as shown in Figure 5 (a), decomposition *via* β-carbene intermediates is found to be dominant over the temperature range 1000–2000 K. 3→2 and 4→5 hydrogen atom shift reactions forming **M6** and **M9** are preferred to the simple fission of a C–H bond, and the formation of $CH_2{=}C{=}O$ and $CH{\equiv}C{-}CH$ through an α-carbene (**M3**).

Whilst a hydrogen atom transfer reaction to form an α-carbene (**M3**) is initially competitive with β-carbene formation (Figure 3), unlike the β-carbenes which can readily undergo ring opening, the α-carbene faces subsequent and much more substantial barriers in order to decompose to bimolecular products. A steady state analysis is employed at each pressure to compute the fraction of 2MF which will form $CH_2{=}C{=}O$ and $CH{\equiv}C{-}CH$ *via* **M3** and the results show that only above 1500 K and pressures of 1 atm will this pathway become competitive. C–H fission is found to be the least important unimolecular decomposition pathway of 2MF based on the present analysis.

The temperature-dependent branching ratios for the decomposition of **M6** are shown in Figure 5 (b). **M6** can decompose to form 1-butyne and CO or 1,2-butadiene and CO, with the former being favoured over the entire temperature and pressure range of Lifshitz *et al.* study[14]. The latter becomes competitive only at higher temperatures. **M9** is found to decompose exclusively to $CH_3{-}\dot{C}{=}O$ and $CH{\equiv}C{-}\dot{C}H_2$ radicals under all conditions of temperature and pressure. The high-pressure limiting rate constant for this reaction has been estimated in a similar fashion to the C–H fission reaction of 2MF, with an assumed rate constant for the recombination of $CH_3{-}\dot{C}{=}O$ and $\dot{C}H_2{-}C{\equiv}CH$ radicals of $5.2 \times 10^{12} T^{0.01} \exp(-114/T)$ cm^3 mol^{-1} s^{-1}. This implies a forward decomposition rate constant of $1.52 \times 10^{25} T^{-2.48} \exp(-39621/T)$ s^{-1}, which is ≈ 200 times faster than the tighter process (k_{13}) forming ketene and propyne.

In conclusion, the unimolecular decomposition of 2-methylfuran is shown to be initiated by 3→2 and 4→5 hydrogen atom shift reactions which are quite close to their high-pressure limits under the experimental conditions of Lifshitz

et al.[14]. Once sufficient free radical species are formed from the initial decomposition processes, abstraction of a hydrogen atom from the alkyl side chain should assume importance in the pyrolysis of this species. The unimolecular decomposition of 1-butyne and acetyl radical, which are formed as fragmentation products of 2MF, should result in the formation of methyl radicals, with the formation of hydrogen atoms from simple fission also possible but of lesser importance initially. Rate constants for abstraction processes by these radicals are therefore of interest, as is the fate of the primary fuel radical.

3.2 Abstraction Reactions and Thermal Decomposition of 2-Furanylmethyl Radical

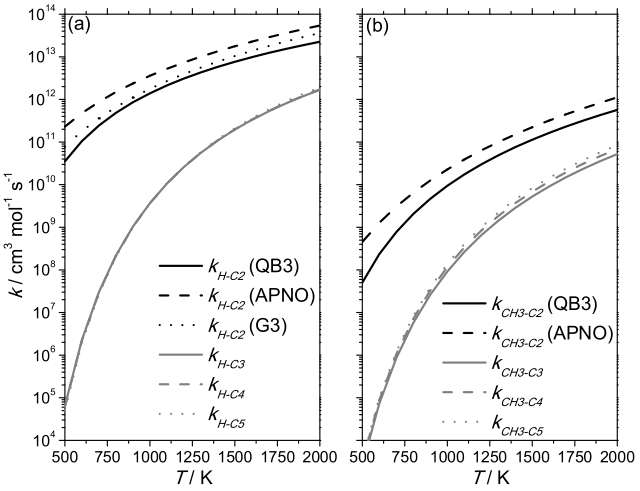

Fig. 6 Rate constants for hydrogen atom abstraction from 2-methylfuran by (a) hydrogen atom and (b) methyl radical. k_{H-C3}, k_{H-C4} and k_{H-C5} are effectively superimposed.

Results of thermochemical and kinetic computations on hydrogen atom abstraction reactions by $\dot{H}$ atom and $\dot{C}H_3$ radical are listed in Table 3.

Abstraction of a hydrogen atom from the methyl group of 2MF by a $\dot{C}H_3$ radical is calculated to be exothermic by -74.9 ± 4.0 kJ mol^{-1}, with a barrier of 39.3 ± 4.0 kJ mol^{-1}. Abstraction from the same site by a $\dot{H}$ atom faces lower barriers (27.9 ± 2.8 kJ mol^{-1}) but the exothermicity (-77.7 ± 2.8 kJ mol^{-1}) is of a similar order to that for abstraction by a $\dot{C}H_3$ radical.

Abstraction of any of the hydrogen atoms directly bonded to the furan ring is thought to be unlikely given their highly vinylic nature, with BDEs circa 505 kJ mol^{-1} reported previously[22]. Consistent rate constants for hydrogen atom abstraction by a $\dot{C}H_3$ radical and a $\dot{H}$ atom are reported for abstraction from these sites but it is evident that these processes are of little importance, Figure 6. As a result, the consumption reactions of the furyl radicals formed from these abstraction processes are not considered here.

Rate constants for abstraction from the alkyl group by a $\dot{H}$ atom, k_{H-C2}, are reported in Table 3 at three levels of theory, thus allowing for an assessment of the uncertainty in the computed rate constants. A factor of 2.5 variation is computed at temperatures of 1000–2000 K. In the same range of T, abstraction by methyl radical (k_{CH3-C2}) varies by a similar order.

The fate of the primary radical (**M10**) formed from abstraction from the alkyl side chain is depicted in Figure 7 with corresponding rate constant computations given in Table 4. Lifshitz included decomposition reactions for this radical in their proposed kinetic scheme with the formation of CO and the internal butadienyl radical ($CH_2{=}\dot{C}{-}CH{=}CH_2$) proposed as the major decomposition product. Decomposition to $H\dot{C}O$ radical and vinylacetylene ($HC{\equiv}C{-}CH{=}CH_2$), ketene and propyne, or $CH{\equiv}CH$, $\dot{C}_2H_3$ radical and CO was also included in their scheme, although no mechanistic proposals were made. In the temperature range 1100–1600 K, a total decomposition rate constant of $3.81 \times 10^{15} T^{0.11} \exp(-32149/T)$ s^{-1} is inferred from their work.

Ring opening of **M10** proceeds *via* cleavage of the C—O bond through a barrier of 167.9 kJ mol^{-1} from CBS-QB3 calculations with both CBS-APNO and G3 failing to locate the transition structure **TS14**. A high-pressure limiting rate constant of $1.38 \times 10^{13} T^{0.3} \exp(-20480/T)$ s^{-1} is calculated for the ring opening process from CBS-QB3 calculations.

The ring opening product, 3,4-pentadiene-1-one-2-yl radical, has multiple conformers but only two are of interest mechanistically, **M11** and **M12**. The latter conformer can undergo a 1→4 intramolecular hydrogen abstraction reaction through a five membered ring transition state (**TS17**), in a relatively low barrier (99.5 ± 3.1 kJ mol^{-1}) exothermic (-58.7 ± 2.3 kJ mol^{-1}) process. This reaction faces the highest barrier on the $\dot{C}_5H_5O$ potential energy surface, and reformation of **M12** from **M13** is unlikely due to the exothermicity of the reaction, and subsequent low energy exit channels which exist for the consumption of **M13**.

The β-scission of a C—H bond in **M11** to form 1,3,4-pentatriene-1-one (**P18**) was investigated as this species was detected experimentally in the flames of 25DMF[26] and 2MF[69]. With an endothermicity of 202.2 ± 3.9 kJ mol^{-1} and critical energy of 218.4 ± 1.5 kJ mol^{-1}, its formation is not competitive with the 1→4 intramolecular hydrogen abstraction reaction.

The product of the 1→4 hydrogen atom transfer reaction has two resonance structures that lead to different configurational isomers, **M13** and **M14**, connected by a transition state which lies 33.1 kJ mol^{-1} above **M13** and 3.4 kJ mol^{-1} above **M14**. IRC analysis (B3LYP/CBSB7) verifies the latter isomer undergoes decarbonylation (**TS19**) to form *n*-butadienyl radical ($\dot{C}H{=}CH{-}CH{=}CH_2$) and CO through a barrier of 99.4

Table 3 Computed barrier heights and enthalpies of reaction (kJ mol^{-1}, 0 K) and Arrhenius coefficients of high-pressure limiting rate constants for the reaction 2-methylfuran + $\dot{X} \rightarrow \dot{R}$ + XH. $k(\mathrm{cm^3mol^{-1}s^{-1}}) = AT^n \exp(-E_a/R)$, AT^n ($\mathrm{cm^3mol^{-1}s^{-1}}$), E_a/R (K).

No.	$\dot{X}$	Site	$\Delta^{\ddagger}H^0$	$\Delta_r H^0$	A	n	E_a/R
k_{H-C2} (QB3)	$\dot{H}$		26.6	−80.9	5.36×10^{4}	2.73	1785.
k_{H-C2} (APNO)	$\dot{H}$	C-2	25.9	−76.4	8.71×10^{0}	3.88	57.
k_{H-C2} (G3)	$\dot{H}$		31.1	−75.7	5.51×10^{-1}	4.20	216.
			± 2.8	± 2.8			
k_{H-C3}	$\dot{H}$	C-3	85.1 ± 3.4	64.1 ± 3.3	1.53×10^{8}	1.86	9666.
k_{H-C4}	$\dot{H}$	C-4	84.2 ± 3.3	63.4 ± 3.1	1.37×10^{8}	1.88	9700.
k_{H-C5}	$\dot{H}$	C-5	87.3 ± 3.7	63.4 ± 3.8	1.03×10^{8}	1.94	9838.
k_{CH3-C2} (QB3)	$\dot{C}H_3$	C-2	40.0	−78.1	1.21×10^{-2}	4.29	2254.
k_{CH3-C2} (APNO)	$\dot{C}H_3$		38.6	−76.2	4.36×10^{-7}	5.58	50.
			± 1.0	± 4.0			
k_{CH3-C3}	$\dot{C}H_3$	C-3	82.0 ± 0.3	66.9 ± 4.5	1.04×10^{2}	3.18	8274.
k_{CH3-C4}	$\dot{C}H_3$	C-4	82.5 ± 0.4	66.2 ± 4.3	1.31×10^{2}	3.19	8336.
k_{CH3-C5}	$\dot{C}H_3$	C-5	82.9 ± 0.8	66.2 ± 5.1	1.54×10^{2}	3.20	8397.

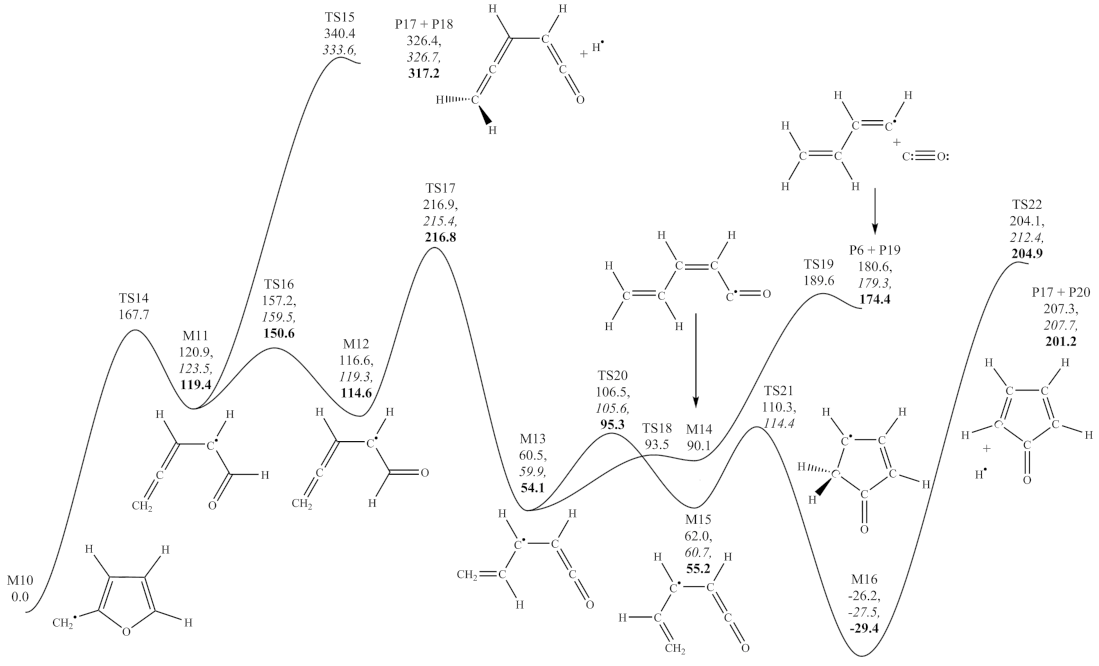

Fig. 7 Potential energy surface for the decomposition of the 2-furanylmethyl radical. CBS-QB3, *CBS-APNO* and **G3** energies in kJ mol^{-1} at 0 K relative to 2-furanylmethyl.

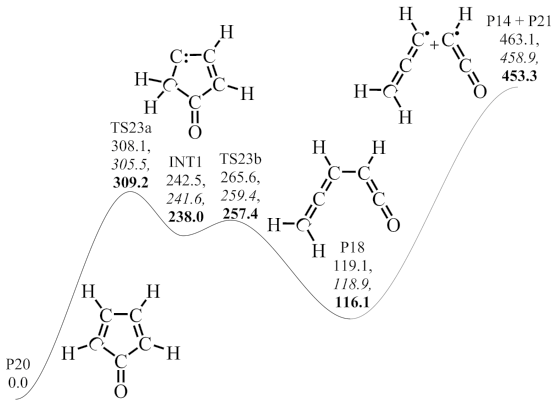

Fig. 8 Carbene intermediate in the isomerisation of 2,4-cyclopendadienone and 1,3,4-pentatrieneone. CBS-QB3, *CBS-APNO* and **G3** energies in kJ mol^{-1} at 0 K relative to reactant.

kJ mol^{-1}. **M15**, a second conformer of **M13**, can undergo ring closure *via* a barrier of 51.0 ± 3.9 kJ mol^{-1} (**TS21**) to form a resonantly stabilised cyclopentenone radical (**M16**) which is is computed to be 27.7 ± 1.6 kJ mol^{-1} more stable than the 2-furanylmethyl radical.

The β-scission of a C—H bond is the only plausible consumption channel envisaged for (**M16**), forming cyclopentadienone (**P20**) and a hydrogen atom. The barrier for the endothermic process (233.1 ± 4.8 kJ mol^{-1}) is calculated to be 234.8 ± 4.8 kJ mol^{-1}, although the CBS-QB3 method predicts a negative critical energy (−3.19 kJ mol^{-1}) if viewed from the perspective of hydrogen atom addition across the double bond of cyclopentadienone.

Cyclopentadienone is a known intermediate in the combustion of cyclopentadiene and it is interesting to see a common feature between this five-membered ring and 2MF, namely, the formation and consumption of β-carbenes through a 1→ 2 hydrogen shift reaction on a singlet potential energy surface, Figure 8. The energetics and kinetics of the process were not considered in a previous analysis of cyclopentadienone decomposition[68]. Here we find they are of a similar order to those found in the decomposition of 2MF, with the computed rate constant for the hydrogen transfer reaction (k_{23a}) within a factor of two of those calculated for 2MF (k_5 and k_{10}) in the high-temperature regime. The carbene intermediate (**INT1**) can undergo ring-opening to form 1,3,4-pentatriene-1-one, which was detected in low-pressure flames of 25DMF[26] and 2MF[69].

The formation of CO and *n*-butadienyl radical appears dominant in our scheme, once **M13** is formed the rate limiting steps for the formation of products are given by k_{19} and k_{22}, with k_{19} dominant in the temperature ranges we have studied.

Multiple-well, multiple-channel RRKM/ME calculations have been carried out to study the influence of pressure on the consumption of all $\dot{C}_5H_5O$ isomers. As a test of the uncertainty in the computed rate constants, both the Multiwell and ChemRate codes were employed in this analysis, with 10^6 trials used in the former. The computed rate constants for the thermal decomposition of **M10** (Figure 9) are within 30% of each other under all conditions studied. For all other intermediates, a factor of two difference was observed in the worst case scenario for the reaction **M15** → **M16** at 0.01 atm and 2000 K. The computed rate constants from the two codes are therefore in excellent agreement and a comparison of computed rate constants is presented in the ESI. The fall-off in the rate constant k_{14} appears to be non-negligible under high-temperature, low-pressure conditions and this fall-off effect must be considered in kinetic modelling studies, for example the low-pressure flames of Tran and co-workers[36] and Wei *et al.*[69]. Rate constants computed using the ChemRate code from 0.01–100 atm and 800–2000 K are provided in the ESI for all reactions on the $\dot{C}_5H_5O$ potential energy surface, and are incorporated into our kinetic model as pressure-dependent reactions (Chemkin-Pro PLOG format).

Table 4 Arrhenius coefficients of high-pressure limiting rate constants for the decomposition of 2-furanylmethyl radical (**M10**) and related intermediates. $k(s^{-1}) = AT^n \exp(-E_a/R)$, AT^n (s^{-1}), E_a/R (K).

No.	Reaction	A	n	E_a/R
k_{14}	M10 → M11	1.38×10^{13}	0.30	20480.
k_{15}	M11 → P17 + P18	9.12×10^{10}	1.15	26634.
k_{16}	M11 → M12	4.01×10^{13}	−0.08	4541.
k_{17}	M12 → M13	9.54×10^{06}	1.62	10071.
k_{18}	M13 → M14	1.50×10^{13}	−0.19	4046.
k_{19}	M14 → P6 + P19	8.61×10^{14}	0.19	12822.
k_{20}	M13 → M15	2.31×10^{13}	−0.13	5663.
k_{21}	M15 → M16	4.06×10^{12}	−0.15	5622.
k_{22}	M16 → P17 + P20	2.99×10^{11}	1.14	28149.
k_{23a}	P20 → INT1	1.03×10^{10}	1.21	36232.
k_{23b}	INT1 → P18	8.72×10^{12}	0.21	2987.

3.3 Hydrogen Atom Addition Reactions

Computed barrier heights, enthalpies of reaction and rate constants for $\dot{H}$ atom addition to 2MF are presented in Table 5 and Figure 10. Consistent reaction barriers and enthalpies of reaction are calculated for these processes. $\dot{H}$ atom addition to carbons adjacent to the oxygen atom of the furan ring are much more exothermic (≈ 45 kJ mol^{-1}) than addition to C-3/C-4, and are thus favoured in terms of computed barriers heights. The difference in the computed $\Delta_r H_0$ upon addition at C-2 and C-5 versus C-3 or C-4 stems from the ability of the radicals to delocalise their unpaired electrons within the furan ring, with

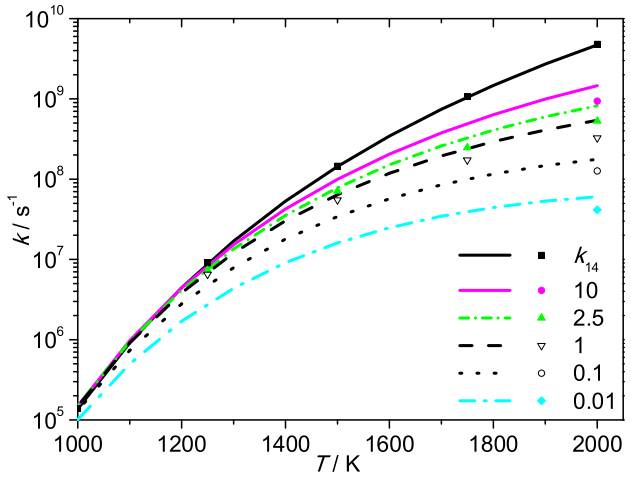

Fig. 9 Pressure- (atm) and temperature-dependent rate constants for the thermal decomposition of 2-furanylmethyl (**M10**) based on RRKM/ME calculations. ChemRate (—) , Multiwell (symbols).

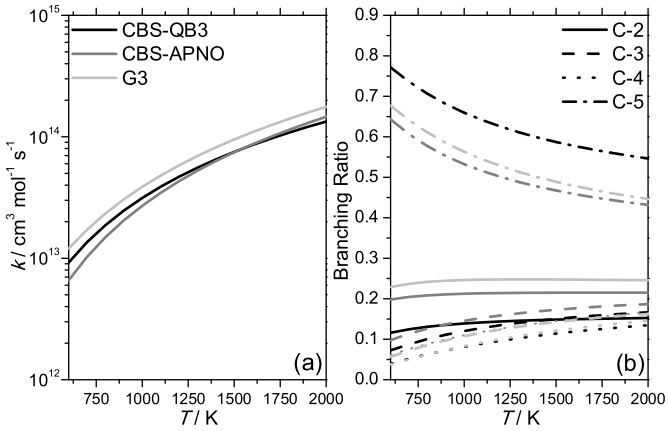

Fig. 10 (a) Total high-pressure limiting rate constant for hydrogen atom addition to 2-methylfuran and (b) site-specific branching ratios at various levels of theory. Colour scheme for theoretical methods in (a) also applies to (b).

addition at sites removed from the oxygen atom resulting in radicals incapable of doing so. Rate constants are presented at three levels of theory for an assessment of their uncertainty. The total rate constant for hydrogen atom addition to 2MF varies by less than a factor of two across the three levels of theory applied, with site-specific branching ratios also predicting the following trend quite consistently amongst the methods: C-5 > C-2 > C-3 = C-4. This trend is in line with the reaction exothermicity upon addition at each site.

3.3.1 Addition at C-2. The potential energy surface for hydrogen atom addition to C-2 of 2MF is illustrated in Figures 11 and 12 with the corresponding rate constants provided in Table 6. The fate of the adduct formed from hydrogen atom addition at C-2 (**M17**) was previously investigated by Simmie and Metcalfe[25]. The authors calculated a rate constant of $2.232 \times 10^{14} \exp(-16292/T)$ for the demethylation process forming furan and a $\dot{C}H_3$ radical *via* **TS24**.

Table 6 Arrhenius coefficients of high-pressure limiting rate constants for for reactions relevant to hydrogen atom addition at C-2 of 2-methylfuran. $k(\mathrm{s}^{-1}) = AT^n \exp(-E_a/R)$, AT^n (s^{-1}), E_a/R (K).

No.	Reaction	A (s^{-1})	n	E_a/R
k_{25}	M17 → P10 + P22	9.23×10^{12}	0.38	15837.
k_{26}	M17 → M18	3.85×10^{13}	−0.09	12216.
k_{27}	M18 → M19	2.61×10^{11}	0.58	2710.
k_{28}	M19 → M20	2.49×10^{03}	2.59	12236.
k_{29}	M20 → P6 + P23	1.19×10^{15}	0.26	13053.
k_{30}	M17 → M21	3.85×10^{13}	−0.09	11003.
k_{31}	M21 → M22	2.33×10^{12}	0.26	4422.
k_{32}	M22 → M20	3.77×10^{05}	2.03	13440.
k_{33}	M18 → M23	9.21×10^{10}	0.53	3834.
k_{34}	M23 → M24	1.83×10^{08}	1.41	19235.
k_{35}	M24 → M25	2.18×10^{10}	0.50	746.
k_{36}	M25 → P9 + P24	2.67×10^{10}	1.20	15994.
k_{37}	M18 → M26	7.50×10^{00}	3.10	6584.
k_{38}	M26 → M27	1.45×10^{11}	0.42	18323.

However, the authors did not investigate the result of cleavage of the C—O bond which could open the furan ring. Two chiral transition states were identified for this process (**TS26** and **TS30**) which are verified by IRC analysis to form Z- and E- conformers (**M18** and **M21**) of 3-pentene-1-one-2-yl radical. A total rate constant for ring opening can be determined from the summation of k_{26} and k_{30}. A rate constant of $8.69 \times 10^{12} T^{0.16} \exp(-11042/T)$ s^{-1} is thus computed, indicating that ring opening should be competitive with demethylation throughout the temperature range 1,000–2,000 K.

Both **M19** and **M22** can undergo a 1→4 hydrogen atom shift reaction to form an aldehydic radical (**M20**) which can decarbonylate through **TS29** in a reasonably low barrier process (101.9 kJ mol^{-1}) forming 1-butene-1-yl radical and CO. Mechanistically, this process is similar to that observed in the decomposition of the 2-furanylmethyl radical, where an aldehydic-type radical is formed before subsequent α-scission to form CO and *n*-butadienyl radical.

Further reactions of **M18** which could lead to the formation of either 1,3-butadiene and HĊO radical or cyclopentadiene and ȮH radical were also investigated, Figure 12. The formation of 1,3-butadiene and HĊO radical is inhibited firstly by a 1→4 hydrogen atom transfer from **M23** to form **M24** *via* **TS34**, for which a barrier of 171.0 ± 0.6 kJ mol^{-1} is calculated. On simple thermodynamic grounds the formation

Table 5 Computed barrier heights and enthalpies of reaction (kJ mol^{-1}, 0 K), and Arrhenius coefficients of high-pressure limiting rate constants for hydrogen atom addition reactions to 2-methylfuran. $k(\mathrm{cm^3mol^{-1}s^{-1}}) = AT^n \exp(-E_a/R)$, AT^n (cm^{3}mol^{-1}s^{-1}), E_a/R (K).

No.	Site	$\Delta^{\ddagger}H^0$	$\Delta^R H^0$	A	n	E_a/R
k_{24} (QB3)		12.2	−126.5	2.10×10^8	1.57	904.
k_{24} (APNO)	C-2	12.9	−128.0	2.67×10^7	1.89	776.
k_{24} (G3)		9.5	−127.3	3.33×10^7	1.88	421.
		11.54 ± 1.8	-127.3 ± 0.7			
k_{40} (QB3)		17.5	−80.9	3.72×10^8	1.54	1414.
k_{40} (APNO)	C-3	18.9	−82.4	3.48×10^7	1.87	1282.
k_{40} (G3)		18.7	−80.7	3.94×10^7	1.86	1281.
		18.4 ± 0.8	-81.3 ± 0.9			
k_{53} (QB3)		19.9	−84.6	2.01×10^8	1.61	1672.
k_{53} (APNO)	C-4	20.7	−85.9	1.88×10^7	1.95	1500.
k_{53} (G3)		20.1	−85.3	2.10×10^7	1.94	1460.
		20.2 ± 0.4	-85.3 ± 0.7			
k_{60} (QB3)		7.0	−133.2	1.20×10^9	1.48	468.
k_{60} (APNO)	C-5	9.6	−133.9	9.06×10^7	1.80	457.
k_{60} (G3)		6.2	−132.3	1.30×10^8	1.76	127.
		7.59 ± 1.8	-133.1 ± 0.8			

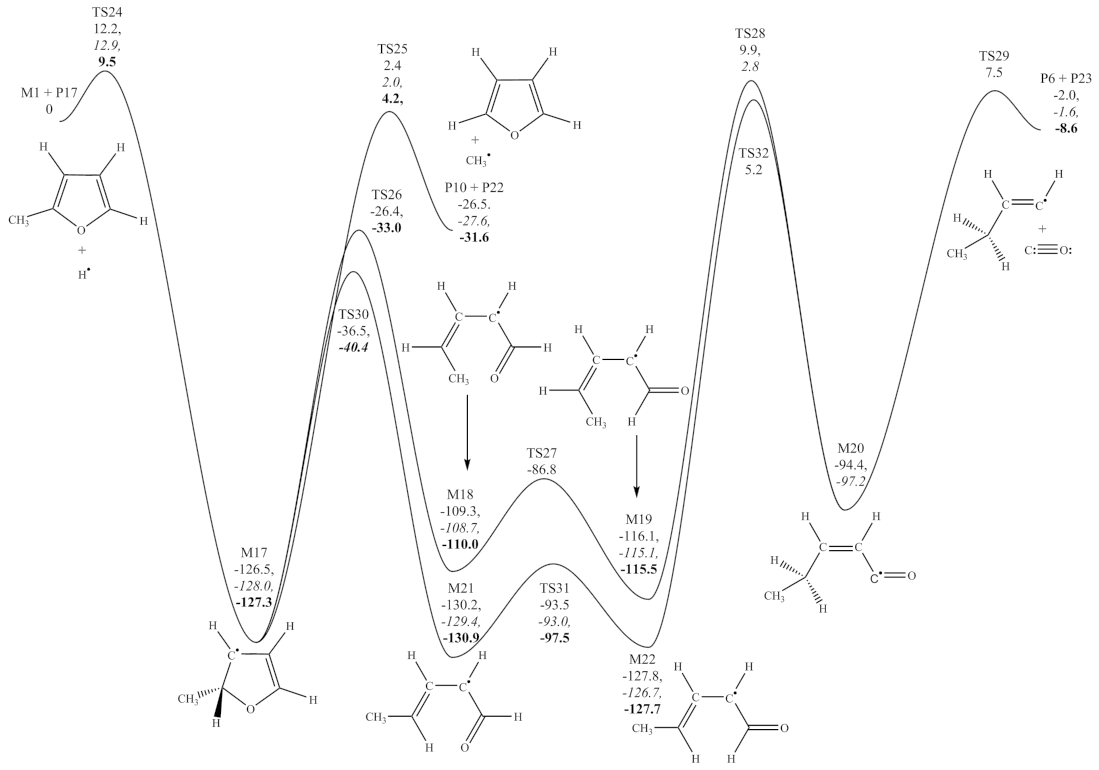

Fig. 11 Potential energy surface for hydrogen atom addition at carbon 2 of 2-methylfuran. CBS-QB3, *CBS-APNO* and **G3** energies in kJ mol^{-1} at 0 K relative to reactants.

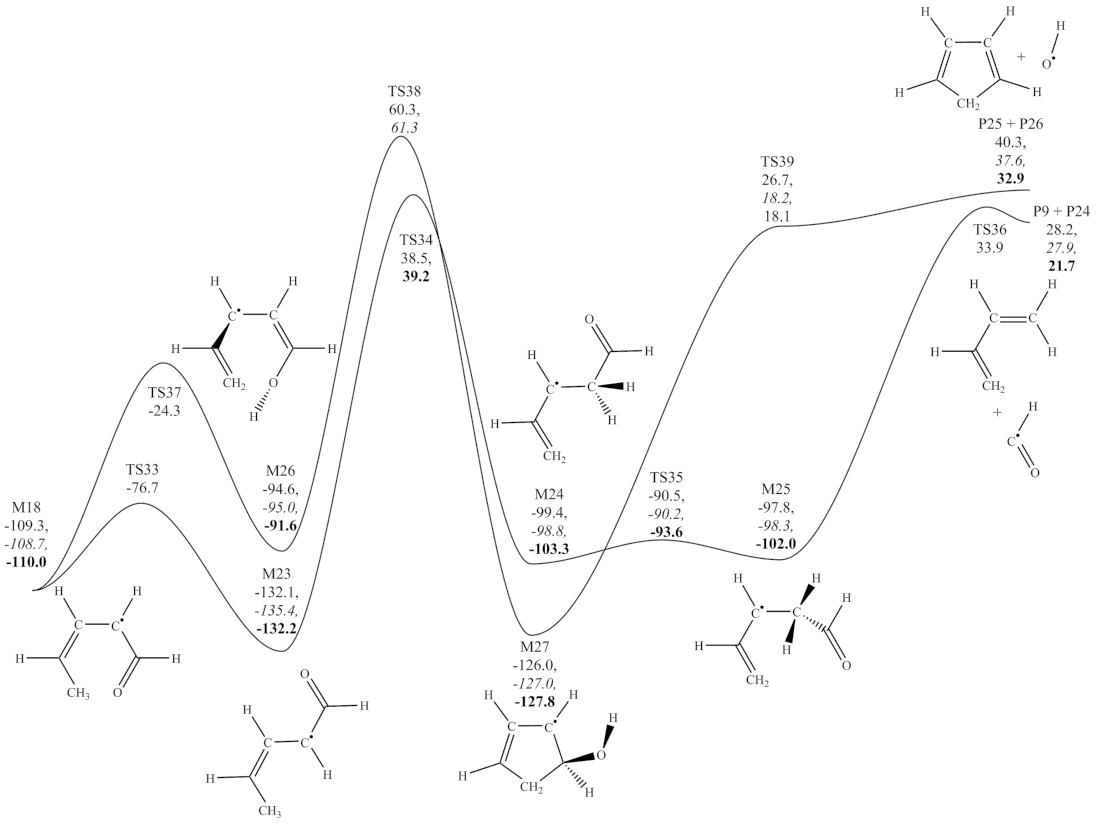

Fig. 12 Potential energy surface for hydrogen atom transfer reactions of 3-pentene-1-al-3-yl radical. CBS-QB3, *CBS-APNO* and **G3** energies in kJ mol^{-1} at 0 K relative to 2-methylfuran and hydrogen.

of these products was not envisaged to be competitive as the products are computed to lie 25.9 $\pm$ 3.7 kJ mol^{-1} above 2MF and hydrogen at 298.15 K, which is likely too endothermic too compete with the exothermic formation of furan and a $\dot{C}H_3$ radical or the 1-butene-1-yl radical and CO.

A 1→6 hydrogen atom transfer from the methyl group of **M18** to its oxygen atom to form an alcohol (**M26**), was found to face a very low initial barrier (**TS36**) of 85.0 kJ mol^{-1}. However, the subsequent ring closing reaction *via* **TS38** is too energetic (155.6 $\pm$ 0.9 kJ mol^{-1} relative to **M26**) for this reaction channel to be important. The products were computed to lie 36.9 $\pm$ 3.7 kJ mol^{-1} above the reactants, and pre- and post- reaction complexes are probably found in the process, but these are not investigated.

RRKM/ME derived product branching ratios from the chemically activated recombination of hydrogen atom with 2MF at C-2 are presented in Figure 13. Branching ratios for the formation of $\dot{C}_5H_7O$ isomers of the nascent adduct are lumped for clarity in Figure 13, but product specific rate constants are reported in the ESI. At high pressures (100 atm) the initially activated well (**M17**) is stabilised up to $\approx$ 1200 K, above this temperature the formation and stabilization of linear $\dot{C}_5H_7O$ radicals becomes dominant, thus indicating that ring opening has become competitive with quenching of **M17**. Above 1600 K, furan and a methyl radical and 1-butene-1-yl radical and CO become major products, accounting for 40+% of the chemically activated yield.

These formally direct pathways become increasingly significant with decreasing pressure and in particular the formation of 1-butene-1-yl radical and CO, which must occur through multiple well-skipping reactions, starts to become the dominant bimolecular products of the reaction. The increasing branching ratio for 1-butene-1-yl radical and CO formation corresponds with the lack of quenching of linear $\dot{C}_5H_7O$ radicals with decreasing pressure. On the other hand, the branching ratio for formation of furan and methyl radical shows a lesser dependency on pressure on the other hand, owing to the fact it is formed directly from the the initial chemically activated species (**M17**).

3.3.2 Addition at C-3 and C-4. Despite the rate constants for the initial hydrogen atom addition reactions at C-3 and C-4 being competitive with addition at C-2 and C-5, subsequent ring opening reactions are less facile, and these path-

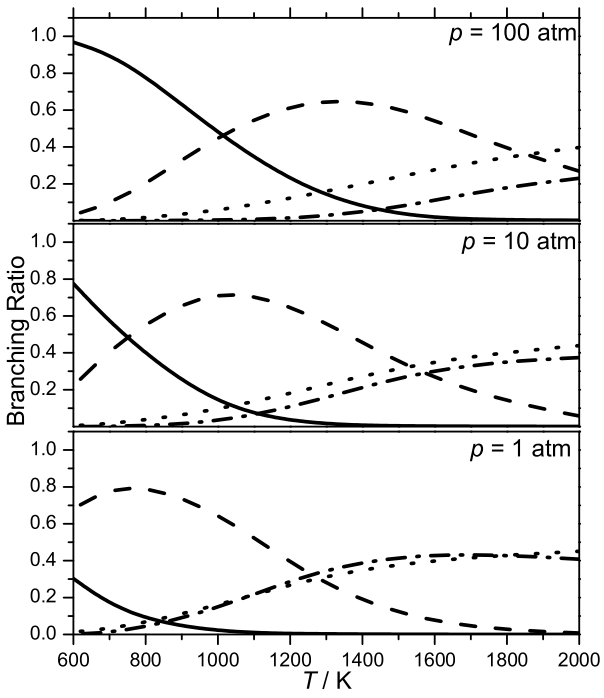

Fig. 13 Major product branching ratios as a function of temperature and pressure from RRKM/ME calculations on the chemically activated recombination of hydrogen atom with 2-methylfuran at C-2. — M17, – – ∑ other $\dot{C}_5H_7O$, ⋯ P10 + P22, – · – P6 + P23.

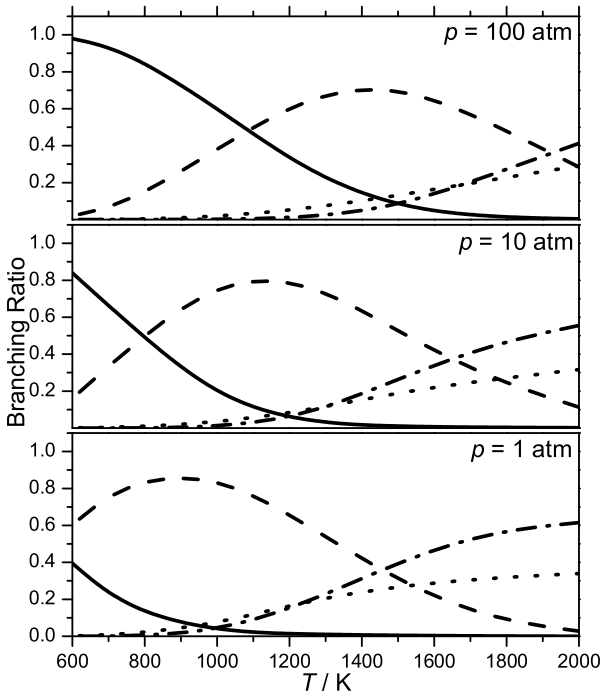

Fig. 15 Major product branching ratios as a function of temperature and pressure from RRKM/ME calculations on the chemically activated recombination of hydrogen atom with 2-methylfuran at C-5. — M41, – – ∑ other $\dot{C}_5H_7O$, ⋯ M1 + P17, – · – P10 + P34.

ways are thus uncompetitive with addition at C-2 and C-5. For brevity in the main text, potential energy surfaces for hydrogen atom addition at C-3 and C-4 are described in detail in ESI, with relevant rate constants also reported therein, k_{41}–k_{52}, and k_{54}–k_{59}.

Table 7 Arrhenius coefficients of high-pressure limiting rate constants for for reactions relevant to hydrogen atom addition at C-5 of 2-methylfuran. $k(s^{-1}) = AT^n \exp(-E_a/R)$, AT^n (s^{-1}), E_a/R (K).

No.	Reaction	A	n	E_a/R (K)
k_{61}	M41 → M42	1.52×10^{12}	0.31	10931.
k_{62}	M42 → P10 + P34	6.01×10^{14}	0.16	25568.
k_{63}	M42 → M43	3.24×10^{13}	−0.28	3301.
k_{64}	M43 → M44	3.64×10^{04}	2.25	11977.
k_{65}	M44 → M45	7.18×10^{12}	−0.16	900.
k_{66}	M45 → P3 + P35	4.29×10^{12}	0.56	23690.
k_{67}	M45 → M46	1.74×10^{13}	−0.42	13859.
k_{68}	M46 → M47	8.27×10^{07}	1.28	940.
k_{69}	M47 → M48	5.08×10^{07}	1.25	−313.
k_{70}	M48 → P6 + P36	5.84×10^{10}	0.74	3377.

3.3.3 Addition at C-5. Figure 14 displays the potential energy surface investigated upon hydrogen atom addition at C-5. Ring opening of the adduct occurs through **TS61** with a ring-opening rate constant of a similar order to that computed upon hydrogen atom addition at C-2 (k_{26} and k_{30}). Demethylation of the ring opening product occurs through **TS62** to form vinyl ketene and a methyl radical, in a reaction computed to be endothermic by 176.4 ± 4.7 kJ mol^{-1}. A barrier of 202.0 ± 5.3 kJ mol^{-1} is computed for the process relative to the reactant and 61.7 ± 4.9 kJ mol^{-1} relative to 2MF and a hydrogen atom.

A secondary conformer of the ring opening product (**M43**) can undergo a hydrogen atom transfer reaction with a barrier of 124.6 kJ mol^{-1} (**TS64**) to form an acetonyl-like radical (**M44**), which can undergo β-scission to form ketene and a vinyl propene radical (k_{66}).

Ring closure of **M45** to form a cyclopropanone radical derivative (**M46**) is energetically more favourable than the formation of ketene and a vinyl propene radical, with the transition state for the process (**TS67**) computed to lie only 19.3 ± 3.1 kJ mol^{-1} above 2MF and hydrogen atom. **M46** can rearrange *via* β-scission (**TS68**) to form an aldehydic radical which is now capable of eliminating CO through **TS70** to produce the resonantly stabilised butenyl radical (**P36**).

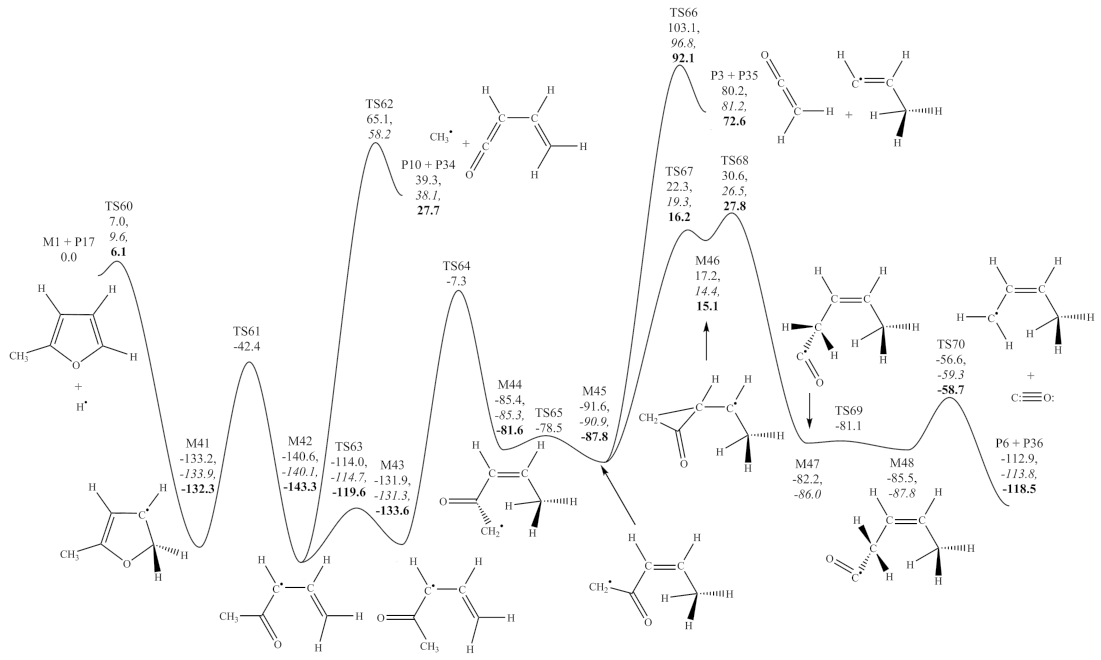

Fig. 14 Potential energy surface for hydrogen atom addition at carbon 5 of 2-methylfuran. CBS-QB3, *CBS-APNO* and **G3** energies in kJ mol^{-1} at 0 K relative to reactants.

The potential energy surface investigated indicates that hydrogen atom addition at C-5 will proceed with competition between back dissociation to form 2MF and a hydrogen atom, the endothermic formation of vinyl ketene and a methyl radical in a relatively straightforward 3-step process, and the exothermic formation of CO and $CH_2{=}CH{-}\dot{C}H{-}CH_3$ which faces many possible bottlenecks before formation. In terms of the contrast between the addition of a hydrogen atom at the C-2 and C-5 positions of 2-methylfuran, both include a demethylation step with simultaneous formation of a C_4H_4O isomer. The relative stability of the furan ring is reflected in the fact that hydrogen atom addition forming a methyl radical and furan (C-2 addition), faces a much lower barrier than that forming a methyl radical and vinyl ketene (C-5 addition). Likewise, the elimination of CO is a common feature upon hydrogen atom addition at C-2/C-5. In both instances, the CO elimination process is quite rapid despite the differing nature of the co-products formed from these reactions (C-2 addition produces a vinylic radical, C-5 addition produces an allylic radical), and it is the hydrogen atom transfer reactions which precede the decarbonylation step, which will determine whether this process will ultimately occur.

An RRKM/ME analysis, Figure 15, shows similar trends to those observed for hydrogen atom addition at the C-2 position. At 100 atm collisional deactivation of chemically activated **M41** dominates the product branching fractions up to 1000 K, at which point linear $\dot{C}_5H_7O$ radicals start to form and subsequently stabilize. As a result, the formation of bimolecular products is insignificant at temperatures up to $\approx$ 1700 K. At 1 atm the furanyl radical does not persist above 1000 K and above 1300 K, the formation of bimolecular products (vinyl ketene and a methyl radical, 2MF and a hydrogen atom) are dominant.

The formation of vinyl ketene and a methyl radical shows a stronger pressure dependency than the formation of 2MF and a hydrogen atom. Again, this is the result of multiple well skipping reactions occurring at lower pressures to produce the latter. Negligible quantities of CO and $CH_2{=}CH{-}\dot{C}H{-}CH_3$ radical are produced as formally direct products of hydrogen atom addition to 2MF.

4 Kinetic Modelling

The preceding calculations have been assimilated into a previously published kinetic scheme for 2-methylfuran and 2,5-dimethylfuran combustion by Somers and co-workers[32,70] wherein details of the oxidative reactions are found. Where rate constants are determined at several levels of theory, we utilise the CBS-QB3 calculations in the current work. Furan[18,38] and aromatic[71] mechanisms are also incorporated. The C_0–C_4 sub-mechanism is based on the mechanism described by Healy and co-workers[72–76]. Further validation of this chemistry set is described in the work of Kochar and co-workers[77] and in a recent study of C_1–C_2 hydrocarbon and

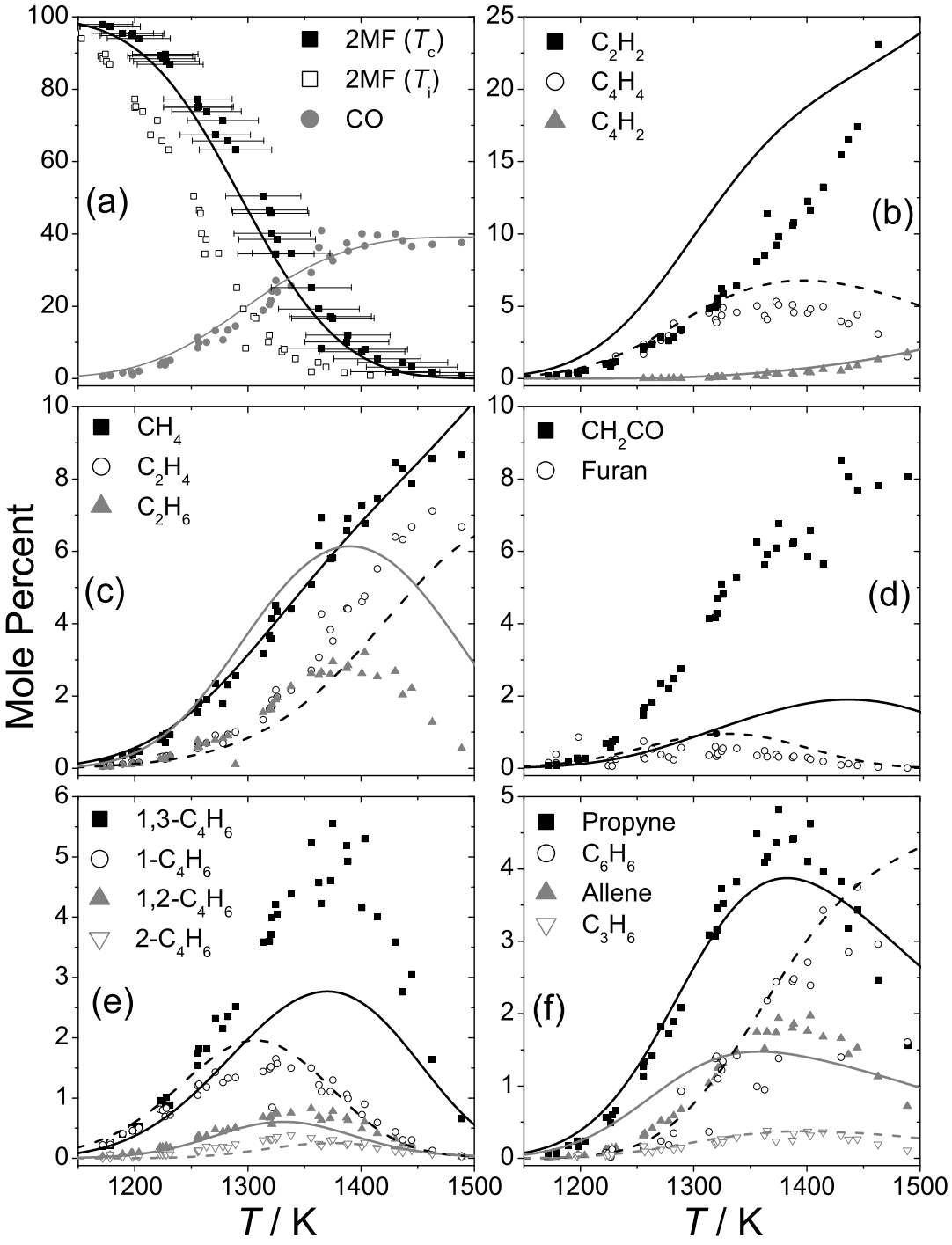

Fig. 16 Experimental speciation profiles for the pyrolysis of 0.5% 2-methylfuran at 2.5 atm and ≈ 2 ms residence time with modelling predictions (lines). Solid lines correspond with closed symbols and dashed lines with open symbols. T_c = corrected reflected shock temperatures, T_i = original reflected shock temperatures.

oxygenated fuels from Metcalfe *et al.*[78]. The H_2/O_2 submechanism is adopted from the work of Kéromnès *et al.*[79].

Experimental profiles from Lifshitz *et al.*[14] are presented in Figure 16 along with numerical modelling results based on the current kinetic mechanism. Some comments on the experimental results are now appropriate before a comparison of modelling predictions with experiment is presented in detail. Mole percents are calculated *via* equation 1 in accord with the experimental definition[80], where x_i is the computed mole fraction of a species.

$$\text{Mole}\,\% = x_i / \sum_i x_i \qquad (1)$$

Only species which were quantified and included in this mole % calculation experimentally, are included in the corresponding computational results depicted in Figure 16.

The experimentalists used the chemical thermometer (1,1,1-trifluoroethane) method to determine the temperatures behind the reflected shock wave according to equations 2 and 3:

$$T = -(E/R) / \left[\ln \left\{ -\frac{\ln(1-\chi)}{A\,t} \right\} \right] \qquad (2)$$

where E and A are the activation energy and pre-exponential factor assumed for the molecular elimination reaction ($CH_3{-}CF_3 \rightarrow CH_2{=}CF_2$ + H−F) of the chemical thermometer, t is the reaction dwell time and χ is given by:

$$\chi = [CH_2{=}CF_2]_t / ([CH_2{=}CF_2]_t + [CH_3{-}CF_3]_t) \qquad (3)$$

This makes the determination of the temperature sensitive to both the rate constant used for the decomposition and the determination of the concentrations of the reactant and product of the chemical thermometer. The temperature behind the reflected shock wave was calculated by Lifshitz *et al.* based on a literature assignment of the rate constant[81] for the decomposition of $CH_3{-}CF_3$ of $k = 10^{14.51} \exp(-36533/T)\ \text{s}^{-1}$.

The same chemical thermometer method was employed in the Lifshitz *et al.*[15] study on the thermal decomposition of 2,5-dimethylfuran, although a slightly different rate constant (within 10–20%) was estimated for the thermometer decomposition. Recent experimental and kinetic modelling studies[37,70] have shown that the rate constant assumed by Lifshitz *et al.* in their 2,5-dimethylfuran work was likely in error. Somers *et al.*[70] carried out single pulse shock tube experiments under similar conditions to those of Lifshitz *et al.*[15] where temperatures were determined independent of a chemical thermometer. The results showed that 25DMF underwent decomposition at temperatures up to ≈ 90 K greater than those determined by Lifshitz *et al.*[15].

Sirjean *et al.*[37] carried out quantum chemical (CBS-QB3) and RRKM/ME calculations to determine the rate constant for the molecular elimination reaction, recommending a rate constant at 2.5 bar of $k = 6.17 \times 10^{13} \exp(-36060/T)\ \text{s}^{-1}$. At 1200 K, their computed value is up to 3.8 times lower than that assumed by Lifshitz *et al.* in their 2,5-dimethylfuran work[15], and 3.5 times lower than that assumed in the experiments we are aiming to model here. Sirjean *et al.*[37] corrected the temperature measurements of Lifshitz *et al.* accordingly, with the resultant measurements from Somers *et al.*[70] and the corrected ones of Sirjean *et al.*[37] being within 25 K of each other and in good agreement with kinetic modelling calculations.

We therefore correct the temperature reported by Lifshitz *et al.*[14] for their 2-methylfuran experiments based on the rate constant recommended by Sirjean *et al.*[37] and equations 2 and 3. The result is a ≈ 50 K *increase* in the experimental temperature at the lowest conversions of 2-methylfuran, and up to 80 K at the highest temperatures studied. The corrected temperature can be described adequately by $T_c(\text{K}) = 1.12 \times T_i - 82.54$.

The experimental yields (Figure 16) of 2MF are presented with temperature uncertainty bars which assume a residual factor of two uncertainty in the recommended rate constant for the thermal decomposition of 1,1,1-TFE, which is reasonable based on the theoretical methods employed therein[37]. Figure 16 (a) also shows the temperature uncorrected yields of 2MF, which clearly lie outside the uncertainty in this updated temperature profile.

In order to obtain better agreement with the corrected 2MF and methane profiles, we have reduced the rate constant for hydrogen atom abstraction by methyl radical from the alkyl side chain of 2MF, k_{CH3-C2}(QB3), by a factor of two, which is within the theoretical uncertainty. The rate constant for hydrogen atom abstraction by hydrogen atom, k_{H-C2}(QB3), has been increased by a factor of two in order to retain agreement with laminar burning velocity measurements[32], as was carried out in the previous kinetic modelling study of Somers *et al.*[32]. The rate constant for this reaction shows little sensitivity to the pyrolysis results described here and our predictions of the fuel conversion in Figure 16 (a) are well within the experimental uncertainty.

Lifshitz *et al.*[14] originally recommended a pseudo-first order rate constant of $9.71 \times 10^{13} \exp(-34,400/T)\ \text{s}^{-1}$ for the thermal decomposition of 2MF in this temperature and pressure regime. After correction of their data, we arrive at $8.41 \times 10^{13} \exp(-34,450/T)\ \text{s}^{-1}$ with our kinetic model predicting a rate constant of $1.97 \times 10^{14} \exp(-35,071/T)\ \text{s}^{-1}$. For all three derived rate constants, the activation energies are of the order of ≈ 286–291 kJ mol^{-1}, which corresponds closely with the barrier heights calculated for the 3 → 2 and 4 → 5 hydrogen atom shift reactions shown to be the dominant unimolecular decomposition pathways for 2MF in previous sections. This is an interesting result, as free radical reactions are found to be important in the consumption of the reactant species. One might expect the activation energy to be

smaller than the activation energies for the primary unimolecular initiation pathways but the thermal decomposition of 2MF seems to obey first order kinetics quite well in this temperature range.

The fate of the oxygen containing fragments of the fuel are of obvious interest and other than 2MF, only three species containing were experimentally measured which contained an oxygen atom; CO, ketene and furan. CO, which was found to be the primary decomposition product, was detected in yields of up to 40%, and is well-predicted by our kinetic model. Its formation is well rationalised within our quantum chemical calculations through multiple channels. Opening of the furan ring, followed by a hydrogen transfer reaction and CO elimination is common to the unimolecular decomposition reactions of the fuel and the primary fuel radical, and is also seen after hydrogen atom addition reactions. The reaction $CH_3—\dot{C}=O \rightarrow CO + \dot{C}H_3$ is also an important source of CO, with the majority of the $CH_3—\dot{C}=O$ radical formed in a 1:1 ratio with $CH_2=C=\dot{C}H$ radical from the decomposition of **M9**.

Ketene yields of up to 8% were implied from experiment but the determination of its concentrations proved difficult due to analytical issues. A series of isolated experiments were performed by Lifshitz *et al.*[14] where small quantities of methanol were added to the post-shock mixture in order convert ketene to the more readily quantifiable methyl acetate. Methyl acetate was subsequently identified although its concentrations could not be quantitatively determined. It was therefore assumed that if ketene was formed in the same unimolecular process as propyne and allene, its concentrations should equal the sum of the C_3H_4 isomers. Despite multiple pathways (Figures 2 and 14, and Figures 1 and 2 of ESI) leading to the production of ketene within our assembled reaction scheme, its formation is consistently found to be non-competitive with alternate pathways.

We find vinyl ketene, which went experimentally undetected by Lifshitz[14] but which was identified in 2MF flames[69], to be a major product upon hydrogen atom addition at C-5 of the furan ring. Computed vinyl ketene yields are in good agreement with the experimentally estimated ketene concentrations if this undetected species is incorporated into our mole % calculation, Figure 17. Vinyl ketene may therefore account for the missing carbon and oxygen which the experimentalists assumed would be found in ketene.

Furan yields are well-predicted and its formation pathway was clearly rationalised in a previous work by Simmie and Metcalfe[25]. However, the ring opening step presented in Figure 11 is central to the accurate prediction of its yields shown in Figure 16 (d), with the exclusion of this process resulting in over-prediction of the experimental yield.

The yield of methane, which is primarily formed by hydrogen atom abstraction from the alkyl side chain by methyl radical, is also well-predicted although yields of ethane, which is formed from methyl radical self-recombination, is over-predicted by the mechanism. Ethylene is formed from the decomposition of ethyl radical which is in turn formed from the decomposition of **P23** and from the reaction $C_2H_6 + \dot{C}H_3 = \dot{C}_2H_5 + CH_4$. Yields of the C_4H_6 isomers 1-butyne, 2-butyne, 1,2-butadiene and 1,3-butadiene are all reasonably-well estimated by our kinetic mechanism.

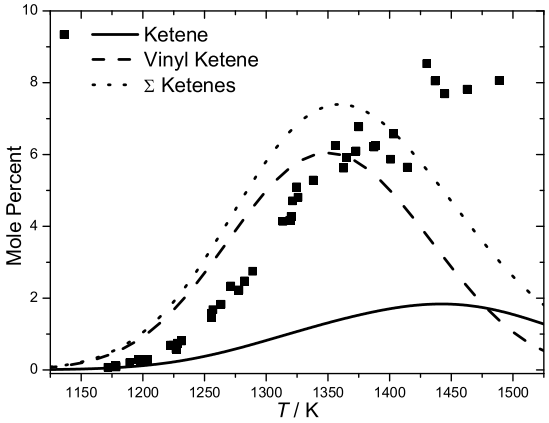

Fig. 17 Experimentally estimated yields[14] (see text) of ketene (symbols) with computational yields of ketene and vinyl ketene.

Like ketene, many pathways leading to the formation of propyne were identified in our quantum calculations (k_4, k_{13}, k_{47}, k_{66}) but none were found to be competitive. Nonetheless, propyne, allene, and benzene yields are all accounted for. The former are produced *via* abstraction by propargyl radical from the alkyl side chain of 2MF, and the latter *via* the recombination of propargyl radicals. It is worth noting that propargyl radical was identified by Grela *et al.*[16] in the thermal decomposition of 2MF, based on the presence of its ion at m/z 39 in their MS analysis. Our work proposes two clear channels to its formation from 2MF *via* the reactions sequences (a) 2MF → **M6** → $CO + CH\equiv C—CH_2—CH_3 \rightarrow \dot{C}H_3 + CH_2=C=\dot{C}H$ and (b) 2MF → **M9** → $CH_3—\dot{C}=O + CH_2=C=\dot{C}H$.

The decomposition of *n*-butadienyl radical, which is the primary product of the decomposition of the 2-furanylmethyl radical, Figure 7, accounts for the acetylene and vinylacetylene concentrations detected experimentally. Vinylacetylene predictions are in excellent agreement with experiment, although acetylene yields are consistently over-estimated, possibly indicating refinements to the kinetics of *n*-butadienyl radical decomposition are necessary.

5 Conclusions

This work presents a comprehensive investigation of the potential energy surfaces for the pyrolysis reactions of the bio-

fuel candidate 2-methylfuran. Kinetics for the thermal unimolecular reactions of 2-methylfuran and the 2-furanylmethyl radical, the chemically activated recombination of hydrogen atoms with 2-methylfuran and several hydrogen atom abstraction processes have been investigated. Canonical and microcanonical rate theories have been employed to determine rate constants as a function of temperature and pressure (if applicable) for each reaction pathway.

Unimolecular decomposition is initiated primarily by hydrogen shift reactions routed through β-carbene intermediates to form stable acyclic intermediates which further decompose to either 1-butyne and CO, or acetyl and propargyl radicals. As temperatures approach 2000 K, the formation of 1,2-butadiene and CO, ketene and propyne, and 2-furanylmethyl radical and a hydrogen atom become competitive. The decomposition of the 2-furanylmethyl radical is shown to proceed through C–O bond cleavage which opens the furan ring. Subsequent hydrogen atom transfer and α-scission leads to the formation of the dominant products, CO and the *n*-butadienyl radical. Hydrogen atom addition to carbon atoms adjacent to the oxygen of the furan ring are kinetically favoured over addition to atoms remote from the oxygen moiety. In terms of bimolecular products, hydrogen atom addition results predominantly in the formation of furan and a methyl radical, 1-butene-1-yl radical and CO, and vinyl ketene and a methyl radical.

The calculated rate constants are incorporated into a previously published oxidative mechanism for 2-methylfuran [32] and 2,5-dimethylfuran [70] which is then compared with experimental speciation profiles [14] recorded for the pyrolysis of 2-methylfuran. Once the experimental measurements are corrected for an erroneous temperature determination the agreement between theory and experimental is overall quite good, thus giving some credibility to the proposed pyrolysis mechanism and kinetics. The mechanism is also compared to literature oxidation experiments of 2MF in the ESI, with good performance observed against all experimental targets.

The fundamental molecular data provided in this study should be of interest to those who wish to carry out RRKM/ME calculations on 2-methylfuran in the future with the chemical mechanism being of utility to those modelling the combustion behavior of 2-methylfuran under pyrolysis and oxidative conditions. Furan, 2-methylfuran and 2,5-dimethylfuran are also know intermediates and model compounds considered in the pyrolysis of biomass [82,83] and coals [17], and the kinetic scheme developed herein is likely to be useful in kinetic modelling work in these areas.

6 Acknowledgments

We would like to acknowledge the support of Science Foundation Ireland under grant number [08/IN1./I2055] as part of their Principal Investigator Awards. We acknowledge the provision of computational resources from the e-Irish National Infrastructure programme, e-INIS, and the Irish Centre for High-End Computing, ICHEC. We thank Prof. John Barker and Dr. Gabriel da Silva for useful discussions on the Multiwell code and the latter again for sharing with us the Speed v0.72 code for automatic generation of potential energy surfaces.

References

1 Renewable Energy Policy Network for the 21st Centry. Renewables 2013 Global Status Report. http://www.ren21.net/REN21Activities/GlobalStatusReport.aspx (accessed October 21, 2013).
2 J.R. Regalbuto, Science, 2009, 325, 822–824.
3 Y. Román-Leshkov, C.J. Barrett, Z.Y. Liu, J.A. Dumesic, Nature, 2007, 447, 982–985.
4 H. Zhao, J.E. Holladay, H. Brown, Z.C. Zhang, Science 2007, 316, 1597–1599.
5 J.B. Binder, R.T. Raines, J. Am. Chem. Soc., 2009, 131, 1979–1985
6 Y. Su, H.M. Brown, X. Huang, X. Zhou, J.E. Amonette, Z.C. Zhang, Applied Catalysis A: General 2009, 361, 117–122.
7 A.A. Rosatella, S.P. Simeonov, R.F.M. Frade, C.M. Afonso, Green Chemistry, 2011, 13, 754–793.
8 F. Geilen, T. vom Stein, B. Engendahl, S. Winterle, M. Liauw, J. Klankermayer, W. Leitner, Angew. Chem. Int. Ed. 2011, 50, 6831–6834.
9 S. Zhong, R. Daniel, H. Xu, J. Zhang, D. Turner, M.L. Wyszynski, P. Richards, Energy Fuels, 2010, 24, 2891–2899.
10 R. Daniel, G. Tian, H. Xu, M.L. Wyszynski, X. Wu, Z. Huang, Fuel, 2011, 90, 449–458.
11 M. Thewes, M.Muether, S. Pischinger, M. Budde, A. Sehr, P. Adomeit, J. Klankermayer, Energy Fuels, 2011, 25, 5549–5561.
12 C. Wang, H. Xu, R. Daniel, A. Ghafourian, J.M. Herreros, S. Shuai, X. Ma, Fuel, 2013, 103, 200–211.
13 A. Lifshitz, M. Bidani, S. Bidani, J. Phys. Chem., 1986, 90, 5373–5377.
14 A. Lifshitz, C. Tamburu, R. Shashua, J. Phys. Chem. A, 1997, 101, 1018–1029.
15 A. Lifshitz, C. Tamburu, R. Shashua, J. Phys. Chem. A, 1998, 102, 10655–10670.
16 M.A. Grela, V.T. Amorebieta, A.J. Colussi, J. Phys. Chem., 1985, 89, 38–41.
17 O.S.L. Bruinsma, P.J.J. Tromp, H.J.J. de Sauvage Nolting, J.A. Moulijn, Fuel, 1988, 67, 334–340.
18 K. Sendt, G.B. Backsay, J.C. Mackie, J. Phys. Chem. A, 2000, 104, 1861–1875.

19 P.P. Organ, J.C. Mackie, J. Chem. Soc. Faraday Trans., 1991, 87, 815–823.

20 R. Liu, X. Zhou, L. Zhai, J. Comput. Chem., 1998, 19, 240–249.

21 R. Liu, X. Zhou, T. Zuo, Chem. Phys. Lett., 2000, 325, 457–464.

22 J.M. Simmie, H.J. Curran, J. Phys. Chem. A, 2009, 113, 5128–5137.

23 D. Feller, J.M. Simmie, J. Phys. Chem. A., 2013, 116, 11768–11775.

24 Ribeiro da Silva, M.A.V, Amaral, L.M.P.F., J. Therm. Anal. Calorim, 2010, 100, 375–380.

25 J.M. Simmie, W.K. Metcalfe, J. Phys. Chem. A, 2011, 115, 8877–8888.

26 X. Wu, Z. Huang, T. Yuan, K. Zhang, L. Wei, Combust. Flame., 2009, 156, 365–376.

27 P. Friese, T. Bentz, M. Olzmann, J. Simmie, Proceedings of the European Combustion Meeting, 2011.

28 P. Friese, J.M. Simmie, M. Olzmann, Proc. Combust. Inst., 2013, 34, 233–239.

29 B. Sirjean, R. Fournet, Phys. Chem. Chem. Phys, 2013, 15, 596–611.

30 B. Sirjean, R. Fournet, Proc. Combust. Inst., 2013, 34, 241–249.

31 B. Sirjean, R. Fournet, J. Phys. Chem. A, 2012, 116, 6675–6684.

32 K.P. Somers, J.M. Simmie, F. Gillespie, U. Burke, J. Connolly,W.K. Metcalfe, F. Battin-Leclerc, P. Dirrenberger, O. Herbinet, P.-A. Glaude, H.J. Curran, Proc. Combust. Inst., 2013, 34, 225–232.

33 A.Y. Chang, J.W. Bozzelli, A.M. Dean, Zeitschrift fur Physikalische Chemie, 2000, 214, 1533–1568.

34 J.W. Bozzelli, A.M Chang, A.M. Dean, Int. J. Chem. Kin., 1997, 29, 161–170.

35 A.C. Davis, S. M. Sarathy, J. Phys. Chem. A, 2013, 117, 7670–7685.

36 L.-S. Tran, C. Togbé, D. Liu, D. Felsmann, P. Oßwald, P.-A. Glaude, R. Fournet, B. Sirjean, F. Battin-Leclerc, K. Kohse-Höinghaus, Combust. Flame, 2013, http://dx.doi.org/10.1016/j.combustflame.2013.05.027

37 B. Sirjean, R. Fournet, P.-A Glaude, F. Battin-Leclerc, W. Wang, M.A. Oehlschlaeger, J. Phys. Chem. A, 2013, 117, 1371–1392.

38 Z. Tian, T. Yuan, R. Fournet, P.-A. Glaude, B. Sirjean, R. Battin-Leclerc, K. Zhang, F. Qi, Combust. Flame, 2011 , 158, 756–773.

39 L. Wei, C. Tang, X. Man, Z. Huang, Energy Fuels, 2013, Just Accepted Manuscript. DOI: 10.1021/ef401809y

40 A.D. Becke, J. Chem. Phys., 1993, 98, 5648–5652.

41 C. Lee, W. Yang, R.G. Parr, Phys. Rev. B, 1988, 37, 785–789.

42 H.P. Hratchian, H.B. Schlegel, J. Chem. Theory Comput., 2005, 1, 61-69.

43 J.A. Montgomery, M.J. Frisch, J.W. Ochterski, G.A. Petersson, J. Chem. Phys., 2000, 112, 6532–6542.

44 J.W. Ochterski, G.A. Petersson, J.A. Montgomery, J. Chem. Phys., 1996, 104, 2598–2619.

45 L.A. Curtiss, K. Raghavachari, P.C. Redfern, V. Rassolov, J.A. Pople, J. Chem. Phys., 1998, 109, 7764–7776.

46 J.M. Simmie, K.P. Somers, W.K. Metcalfe, H.J. Curran, J. Chem. Thermo., 2013, 58, 117–128.

47 Gaussian 03, Revision E.01 and Gaussian 09, Revision C.01, M. J. Frisch, G. W. Trucks, H. B. Schlegel, G. E. Scuseria, M. A. Robb, J. R. Cheeseman, J. A. Montgomery, Jr., T. Vreven, K. N. Kudin, J. C. Burant, J. M. Millam, S. S. Iyengar, J. Tomasi, V. Barone, B. Mennucci, M. Cossi, G. Scalmani, N. Rega, G. A. Petersson, H. Nakatsuji, M. Hada, M. Ehara, K. Toyota, R. Fukuda, J. Hasegawa, M. Ishida, T. Nakajima, Y. Honda, O. Kitao, H. Nakai, M. Klene, X. Li, J. E. Knox, H. P. Hratchian, J. B. Cross, V. Bakken, C. Adamo, J. Jaramillo, R. Gomperts, R. E. Stratmann, O. Yazyev, A. J. Austin, R. Cammi, C. Pomelli, J. W. Ochterski, P. Y. Ayala, K. Morokuma, G. A. Voth, P. Salvador, J. J. Dannenberg, V. G. Zakrzewski, S. Dapprich, A. D. Daniels, M. C. Strain, O. Farkas, D. K. Malick, A. D. Rabuck, K. Raghavachari, J. B. Foresman, J. V. Ortiz, Q. Cui, A. G. Baboul, S. Clifford, J. Cioslowski, B. B. Stefanov, G. Liu, A. Liashenko, P. Piskorz, I. Komaromi, R. L. Martin, D. J. Fox, T. Keith, M. A. Al-Laham, C. Y. Peng, A. Nanayakkara, M. Challacombe, P. M. W. Gill, B. Johnson, W. Chen, M. W. Wong, C. Gonzalez, and J. A. Pople, Gaussian, Inc., Wallingford CT, 2004.

48 MultiWell-2013 Software, Jan 2013, designed and maintained by J.R. Barker with contributors N.F. Ortiz, J.M. Preses, L.L. Lohr, A. Maranzana, P.J. Stimac, T. L. Nguyen, and T. J. Dhilip Kumar, University of Michigan, Ann Arbor, MI; http://aoss.engin.umich.edu/multiwell/

49 J.R Barker, (a) Int. J. Chem. Kinetics 2001, 33, 232–245; (b) Int. J. Chem. Kinetics 2001, 33, 246–261; (c) Int. J. Chem. Kinetics 2009, 41, 748–763.

50 S.J. Pinches, G. da Silva, Int. J. Chem. Kin, 2013, 45, 387–396.

51 Mokrushin, V.; Tsang, W. ChemRate version 1.5.8, NIST, Gaithersburg, MD 20899, http://mokrushin.com/ChemRate/chemrate.html (accessed June 21 2013).

52 D. Polino, C. Cavalotti, J. Phys. Chem. A, 2011, 115, 10281–10289.

53 G. da Silva, J.A. Cole, J.W. Bozzelli, J. Phys. Chem. A, 2009, 113, 6111–6120.

54 C. Cavallotti, D. Polino, Proc. Combust. Inst., 2013, 34,

557–564.
55 G. da Silva, A.J. Trevitt, Phys. Chem. Chem. Phys., 2011, 13, 8940-8952.
56 G. da Silva, Chem. Phys. Lett., 2009, 474, 13–17.
57 G. da Silva, J.A. Cole, J.W. Bozzelli, J. Phys. Chem. A, 2010, 114, 2275-2283.
58 G. da Silva, M. Rafiq Hamdan, J.W. Bozzelli, J. Chem. Theory Comput., 2009, 5, 3185-3194.
59 J.A. Miller, S.J. Klippenstein, J. Phys. Chem. A, 2013, 117, 2718–2727.
60 A.W. Jasper, J.A. Miller, S.J. Klippenstein, J. Phys. Chem. A, 2013, 117, 12243–12255.
61 H. Hippler, J. Troe, and H. J. Wendelken, J. Chem. Phys., 1983, 78, 6709–6717.
62 R.J. Kee, M.E. Coltrin, P. Glarborg, Chemically Reacting Flow Theory and Practice, 1st ed.; John Wiley & Son, Inc.; New Jersey, 2003; pp 496–499.
63 W.M Haynes, Critical Constants of Organic Compounds. In CRC Handbook of Chemistry and Physics, 91st ed; CRC Press; Boca Raton, Florida; p 67.
64 X. Ma, C. Jian, H. Xu, H. Ding, S. Shuai, H. Ding, Energy Fuels, 2013, 27, 6212–6221.
65 Chemkin-Pro, Reaction Design Inc., San Diego, Calif. 2010.
66 L.B. Harding, S.J. Klippenstein, J. Phys. Chem. A, 2007, 111, 3789–3801.
67 Y.-R. Luo. Comprehensive Handbook of Chemical Bond Energies, CRC Press, Boca Raton, FL, 2007, p. 41.
68 H. Wang, K. Brenzinsky, J. Phys. Chem. A, 1998, 102, 1530-1541.
69 L. Wei, Z. Li, L. Tong, Z. Wang, H. Jin, M. Yao, Z. Zheng, C. Wang, H. Xu, Energy Fuels, 2012, 26, 6651–6660.
70 K.P. Somers, J.M. Simmie, F. Gillespie, C. Conroy, G. Black, W.K. Metcalfe, F. Bttin-Leclerc, P. Dirrenberger, O. Herbinet, P.-A Glaude, P. Dagaut, C. Togbé, K. Yasunaga, R.X. Fernandes, C. Lee, R. Tripathi, H.J. Curran, Combust. Flame, 2013, 160, 2291–2318.
71 W.K. Metcalfe, S. Dooley, F.L. Dryer, J. Phys. Chem. A., 2011, 25, 4915–4936.
72 D. Healy, N.S. Donato, C.J. Aul, E.L. Petersen, C.M. Zinner, G. Bourque, H.J. Curran, Combust. Flame, 2010, 157, 1526–1539.
73 N. Donato, C. Aul, E. Petersen, C. Zinner, H. Curran, G. Bourque, J. Eng. Gas Turb. Power, 2010, 132, 051502.
74 D. Healy, N.S. Donato, C.J. Aul, E.L. Petersen, C.M. Zinner, G. Bourque, H.J. Curran, Combust. Flame, 2010, 157, 1540–1551.
75 D. Healy, D.M. Kalitan, C.J. Aul, E.L. Petersen, G. Bourque, H.J. Curran, Energy Fuels, 2010, 24, 1521–1528.
76 D. Healy, M.M. Kopp, N.L. Polley, E.L. Petersen, G. Bourque, H.J. Curran, Energy Fuels, 2010, 24, 1617–1627.
77 Y. Kochar, J. Seitzman, T. Lieuwen, W.K. Metcalfe, S.M. Burke, H.J. Curran, M. Krejci, W. Lowry, E. Petersen, G. Bourque, 2011, ASME Paper GT2011-45122, 56th ASME Turbo Expo.
78 W.K. Metcalfe, S.M. Burke, S.S. Ahmed, H.J. Curran, Int. J. Chem. Kin, 2013, 45, 638–675.
79 A. Kéromnès, W.K. Metcalfe, K.A. Heufer, N. Donohoe, A.K. Das, C.J. Sung, J. Herzler, C. Naumann, P. Griebel, O. Mathieu, M.C. Krejci, E.L. Petersen, W.J. Pitz, H.J. Curran, Combust. Flame, 2013, 160, 995–1011.
80 A. Lifshitz, M. Bidani, S. Bidani, J. Phys. Chem., 1986, 90, 3422-3429.
81 A.S. Rodgers, W.G.F. Ford, Int. J. Chem. Kin., 1973, 5, 965–975.
82 E. Ranzi, A. Cuoci, T. Faravelli, A. Frassoldati, G. Migliavacca, S. Pierucci, S. Sommariva, Energy Fuels, 2008, 22, 4292–4300.
83 K. Norinaga, T. Shoji, S. Kudo, J. Hayashia, Fuel, 2013, 103, 141–150.

Supplementary Material for "The Pyrolysis of 2-Methylfuran: A Quantum Chemical, Statistical Rate Theory and Kinetic Modelling Study"

Kieran P. Somers[1], John M. Simmie[1], Wayne K. Metcalfe[1], and Henry J. Curran[1]

[1]Combustion Chemistry Centre, National University of Ireland, University Road, Galway, Ireland

December 31, 2013

Contents

1 Potential Energy Surfaces for α-Carbene mediated Unimolecular Decomposition **3**

2 Potential Energy Surfaces for Hydrogen Atom Addition at C-3 and C-4. **3**

3 Influence of $\langle \Delta E_d \rangle$ on RRKM/ME Derived $k(T, p)$ **6**
3.1 Unimolecular Decomposition of 2-Methlyfuran 6
3.2 Hydrogen Atom Addition at Carbon 2 of 2-Methylfuran 9

4 Pressure Dependent Rate Constants from RRKM/ME Calculations **12**
4.1 Chemkin-PRO Compatible PLOG Rate Constants 12
4.2 Comparison of RRKM/ME Results from the ChemRate and Multiwell Codes for the Thermal Decomposition of 2-furanylmethyl and related intermediates 19

5 Comparison of High Pressure Limiting Rate Constants with Literature **27**

6 Comparison of Mechanism with Literature Oxidation Experiments **29**
6.1 Atmospheric Pressure Ignition Delay Times of 1% 2-Methylfuran/Argon Mixtures 29
6.2 Ignition Delay Times of 2-Methylfuran/O_2/Argon Mixtures at Elevated Pressures 30
6.3 Atmospheric Pressure Laminar Burning Velocities of 2-Methylfuran-Synthetic Air Mixtures . . . 34
6.4 Speciation in Low-Pressure 2-Methylfuran/O_2/Ar Flames 35
6.4.1 $\phi = 1.0$ 35
6.4.2 $\phi = 1.7$ 45

7 Electronic Energies of Stationary Points **55**

8 Geometries of Stationary Points **59**

1 Potential Energy Surfaces for α-Carbene mediated Unimolecular Decomposition

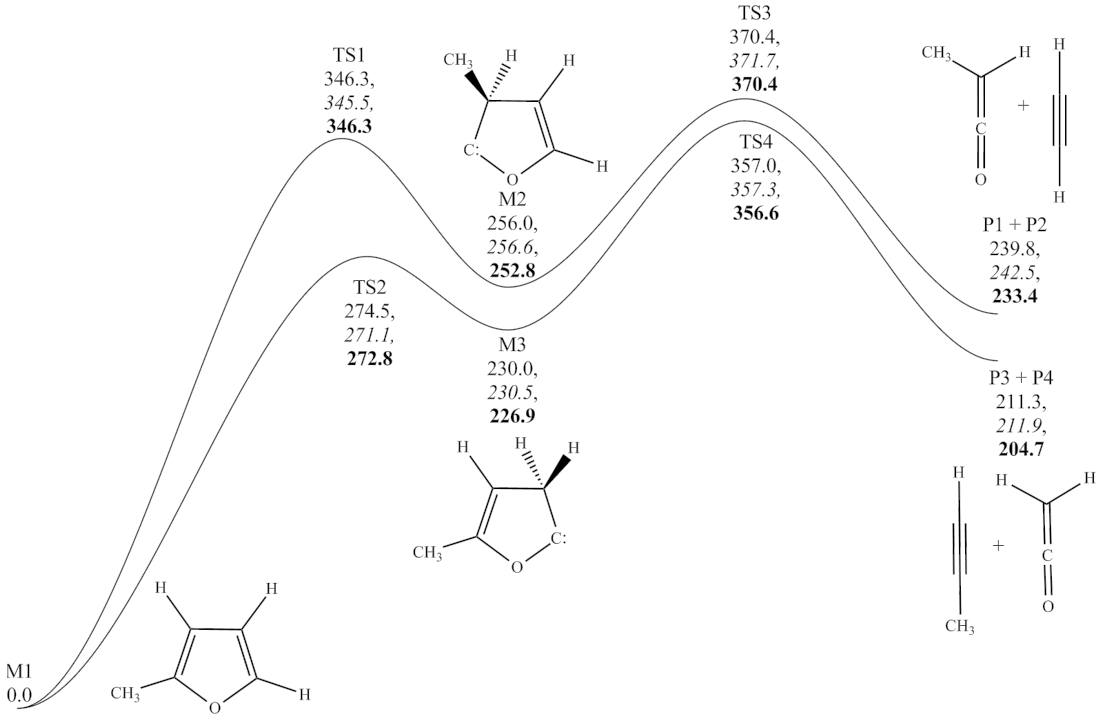

Figure 1: Potential energy surface for the formation and decomposition of α-carbenes. CBS-QB3, *CBS-APNO* and **G3** Energies in kJ mol^{-1} at 0 K relative to 2-methylfuran.

Figure 1 delineates the potential energy surfaces for the decomposition of 2-methylfuran through α-carbene intermediates. Based on CBS-QB3 calculations, a 2 $\rightarrow$ 3 methyl shift to form a singlet α-carbene (**M2**) occurs with a transition state lying 346.3 kJ mol^{-1} above the reactant in a reaction which is endothermic by 256.0 kJ mol^{-1}, in good agreement with values computed for the analagous 25DMF [1] and those of Davis for 2MF [2]. The carbene subsequently decomposes in a mildly exothermic ($-$16.2 kJ mol^{-1}) reaction forming methyl ketene ($CH_3-CH{=}C{=}O$) and acetylene ($HC{\equiv}CH$) with the transition structure lying 114.5 kJ mol^{-1} above the carbene intermediate and 370.4 kJ mol^{-1} above 2MF.

The formation of an α-carbene (**M3**) from a 5 $\rightarrow$ 4 hydrogen transfer proceeds through a barrier of only 274.5 kJ mol^{-1} based on a CBS-QB3 computation with a reaction enthalpy of 230 kJ mol^{-1}. Decomposition to $CH_2{=}C{=}O$ and $HC{\equiv}C-CH$ follows through a barrier 127.0 kJ mol^{-1} above the carbene and 357.0 kJ mol^{-1} above 2MF. The energetics of this multistep process are in excellent agreement with G3(MP2), CASPT2 and CBS-QB3 calculations carried out for the similar process in furan [3,4].**TS3** and **TS4** correspond to those for Diels-Alder type reactions and multi-reference effects may be of importance. T1 diagnostics were therefore computed and found to be 0.019 for **TS3** and 0.018 for **TS4**, thus indicating that single-reference methods used suffice. The computed decomposition rate constants for the α-carbenes (k_3 and k_4) are in excellent agreement as one might expect, given their similar decomposition mechanism and products.

Methyl ketene was identified in the low pressure flames of 25DMF, which is formed along with $HC{\equiv}C-CH$, in an effectively identical process to the above [1]. Based on the computed energetics and kinetics of this process however, its production from 2MF and 25DMF is insignificant.

2 Potential Energy Surfaces for Hydrogen Atom Addition at C-3 and C-4.

Figure 2 describes the potential energy surface for hydrogen atom addition at C-3 of 2MF. Despite the rate constant for addition at C-3 being competitive with addition at C-2, the addition forming **M28** is much less exothermic than that forming **M17** *via* $\dot{H}$ atom addition at C-2, with the latter capable of undergoing resonance stabilisation to delocalise the radical formed.

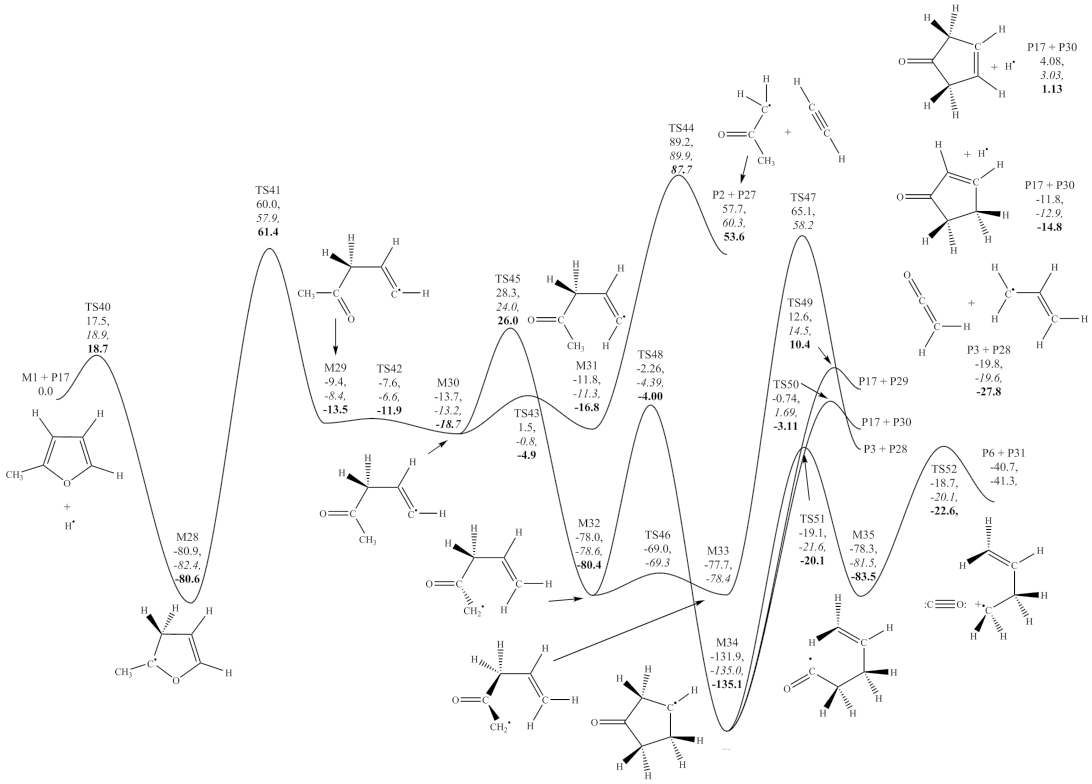

Figure 2: Potential energy surface for hydrogen atom addition at carbon 3 of 2-methylfuran. CBS-QB3, *CBS-APNO* and **G3** energies in kJ mol^{-1} at 0 K relative to reactants.

In turn the ring opening reaction of **M28** through a barrier of 141.1 ± 0.9 kJ mol^{-1} (**TS41**) is much less facile than those of **M17** (k_{26} and k_{30}). This is clearly a result of the vinylic nature of **M28**, with the process being endothermic by 70.9 ± 3.5 kJ mol^{-1}. The ring opening of **M17** is shown to be exothermic (−2.90 ± 1.3 kJ mol^{-1}), with the radical formed being allylic in nature.

Table 1: Arrhenius coefficients of high-pressure limiting rate constants for for reactions relevant to hydrogen atom addition at C-3 of 2-methylfuran. $k(\mathrm{s}^{-1}) = AT^n \exp(-E_a/R)$, AT^n (s^{-1}), E_a/R (K).

No.	Reaction	A	n	E_a/R (K)
k_{41}	M28 → M29	2.92×10^{11}	0.66	16915.
k_{42}	M29 → M30	1.50×10^{09}	0.90	−65.
k_{43}	M30 → M31	2.28×10^{09}	1.22	1524.
k_{44}	M31 → P2 + P27	8.98×10^{10}	1.00	12619.
k_{45}	M30 → M32	6.08×10^{02}	2.58	2663.
k_{46}	M32 → M33	6.36×10^{09}	0.64	626.
k_{47}	M33 → P3 + P28	1.38×10^{09}	1.31	17053.
k_{48}	M32 → M34	2.66×10^{08}	0.82	8272.
k_{49}	M34 → P17 + P29	1.55×10^{10}	1.02	17412.
k_{50}	M34 → P17 + P30	1.74×10^{10}	0.98	15751.
k_{51}	M34 → M35	1.94×10^{12}	0.26	13712.
k_{52}	M35 → P6 + P31	9.41×10^{12}	0.42	7590.

A similar scenario arises upon Ḣ atom addition at C-4, Figure 3, where ring opening of the adduct proceeds through a barrier of 145.7 ± 2.2 kJ mol^{-1} with the formation of a secondary vinylic radical (**M37**) being endothermic by 80.1 ± 2.5 kJ mol^{-1}. Computed rate constants for ring opening reactions of C-3 and C-4 Ḣ atom addition adducts are in excellent agreement, k_{41} and k_{54} respectively.

The fate of these acyclic intermediates is of a lesser importance than those formed from addition at C-2, as β-scission of a C–H bond to reform 2MF and hydrogen atom dominates over ring opening based on our computed

Table 2: Arrhenius coefficients of high-pressure limiting rate constants for for reactions relevant to hydrogen atom addition at C-4 of 2-methylfuran. $k(\mathrm{s}^{-1}) = AT^n \exp(-E_a/R)$, AT^n (s^{-1}), E_a/R (K).

No.	Reaction	A	n	E_a/R (K)
k_{54}	M36 → M37	2.98×10^{12}	0.39	17520.
k_{55}	M37 → M38	5.81×10^{08}	0.93	−334.
k_{56}	M38 → P4 + P32	4.63×10^{10}	0.98	11385.
k_{57}	M37 → M39	4.08×10^{12}	−0.01	615.
k_{58}	M39 → M40	1.41×10^{09}	0.92	183.
k_{59}	M40 → P6 + P33	1.11×10^{11}	0.64	3744.

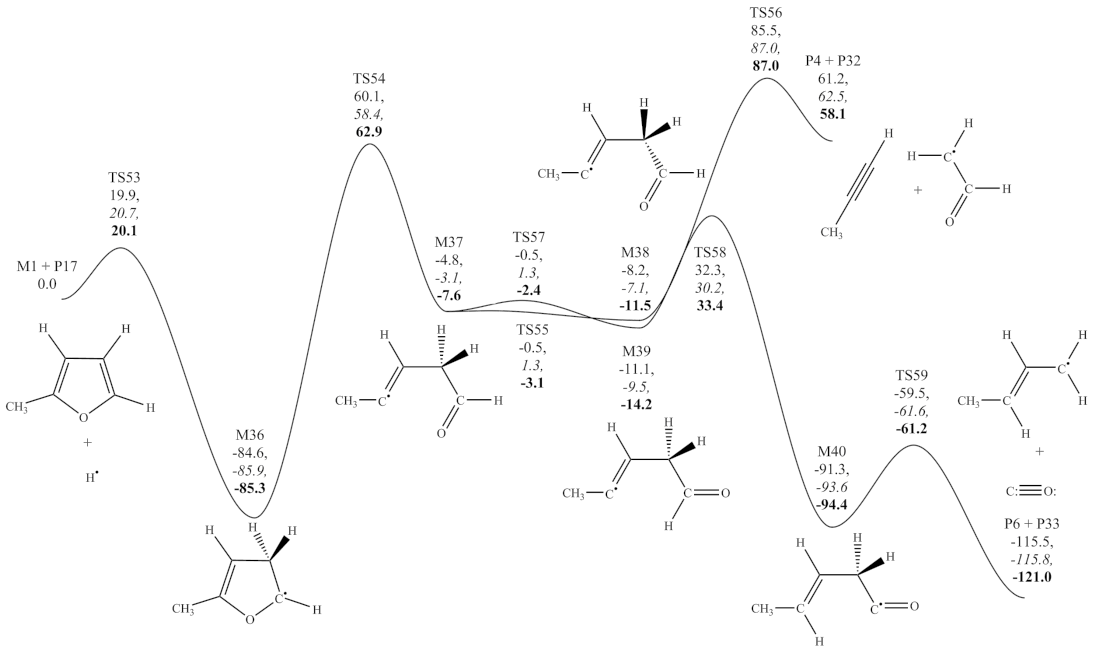

Figure 3: Potential energy surface for hydrogen atom addition at carbon 4 of 2-methylfuran. CBS-QB3, *CBS-APNO* and **G3** energies in kJ mol^{-1} at 0 K relative to reactants.

kinetics and thermochemistry. As a result, RRKM/ME analysis has not been applied to addition at C-3 and C-4, although the fate of the ring opening products has nontheless been investigated to gain further mechanistic information into the decomposition pathways of furanic species.

M29 can undergo isomerisation *via* a 1→5 hydrogen shift to form a more stable primary radical (**M32**) with the ultimate formation of ketene and an allyl radical through a transition state (**TS47**) at 61.7 ± 4.9 kJ mol^{-1} above 2MF and hydrogen atom. The formation of acetylene and the acetonyl radical is also possible *via* **TS44**, and the rate constant for its formation from **M31** is seen to become competitive with that of the hydrogen transfer reaction (k_{47}) at temperatures above 1600 K. Ring closing to form a cyclopenteneone radical (**M34**), which can occur with a computed barrier of 113.8 ± 1.1 kJ mol^{-1}, is unlikely despite the modest activation energy for the process.

M37 can form a more stable aldehydic radical (**M40**) *via* hydrogen transfer through **TS58**. The subsequent decarbonylation reaction forming CO and $\dot{C}H_2$—CH=CH—CH_3 through **TS59** is quite quite rapid. The endothermic formation of CH≡C—CH and $\dot{C}H_2$—CH=O radicals can also occur and despite the large barrier (95.4 ± 2.7 kJ mol^{-1}) when compared with the hydrogen transfer reaction, its formation should become competitive above 1500 K.

3 Influence of $\langle \Delta E_d \rangle$ on RRKM/ME Derived $k(T, p)$

In order to evaluate the influence of $\langle \Delta E_d \rangle$ on the computed temperature- and pressure-dependent rate constants, test calculations with $\langle \Delta E_d \rangle$ = 500 cm^{-1} and 2000 cm^{-1} were carried out on some potential energy surfaces. The pressure chosen was 2.5 atm., equivalent to the average pressure in the shock tube pyrolysis study of Lifshitz *et al.*.

The results show a small variation in the computed rate constants for the unimolecular decomposition reactions of 2-methylfuran (Figures 4–7), with the largest variations observed at the highest temperatures studied (2000 K) where fall-off in the high-pressure limiting rate constants is greatest. Relative to the $\langle \Delta E_d \rangle$ = 1000 cm^{-1} computations, the rate constants computed with $\langle \Delta E_d \rangle$ = 500 cm^{-1} and 2000 cm^{-1} vary by ≈ a factor of two at 2000 K. Under the conditions of Lifshitz *et al.* study (1200–1500 K, once their temperature profile is corrected), the variation in the computed rate constants with the various values of $\langle \Delta E_d \rangle$ chosen is minimal, and the rate constants are close to the high-pressure limiting rate constants in all cases.

Test calculations were also carried out on the reaction 2-methylfuran + hydrogen atom → products (C-2 addition, Figures 8–11). The largest variation observed in the computed rate constants was ≈ a factor of 7 at 600 K for the reaction 2-methylfuran + hydrogen atom → **P9** (formyl radical) + **P24** (1,3-butadiene) with $\langle \Delta E_d \rangle$ = 500 cm^{-1}. However, it should be noted that this is a very minor reaction pathway whose branching ratio is ≈ 5 × 10^{-08} under these conditions (600 K, 2.5 atm, $\langle \Delta E_d \rangle$ = 1000 cm^{-1}). The uncertainty in this reaction pathway due to the choice of $\langle \Delta E_d \rangle$ is of little concern with respect to kinetic modelling studies. For all other reactions pathways, reducing $\langle \Delta E_d \rangle$ to 500 cm^{-1} led to a variation of ≈ a factor of 2–3 from the rate constants computed with $\langle \Delta E_d \rangle$ = 1000 cm^{-1}. Increasing $\langle \Delta E_d \rangle$ to 2000 cm^{-1} resulted in a variation in the computed rate constants of ≈ a factor of 2.

3.1 Unimolecular Decomposition of 2-Methlyfuran

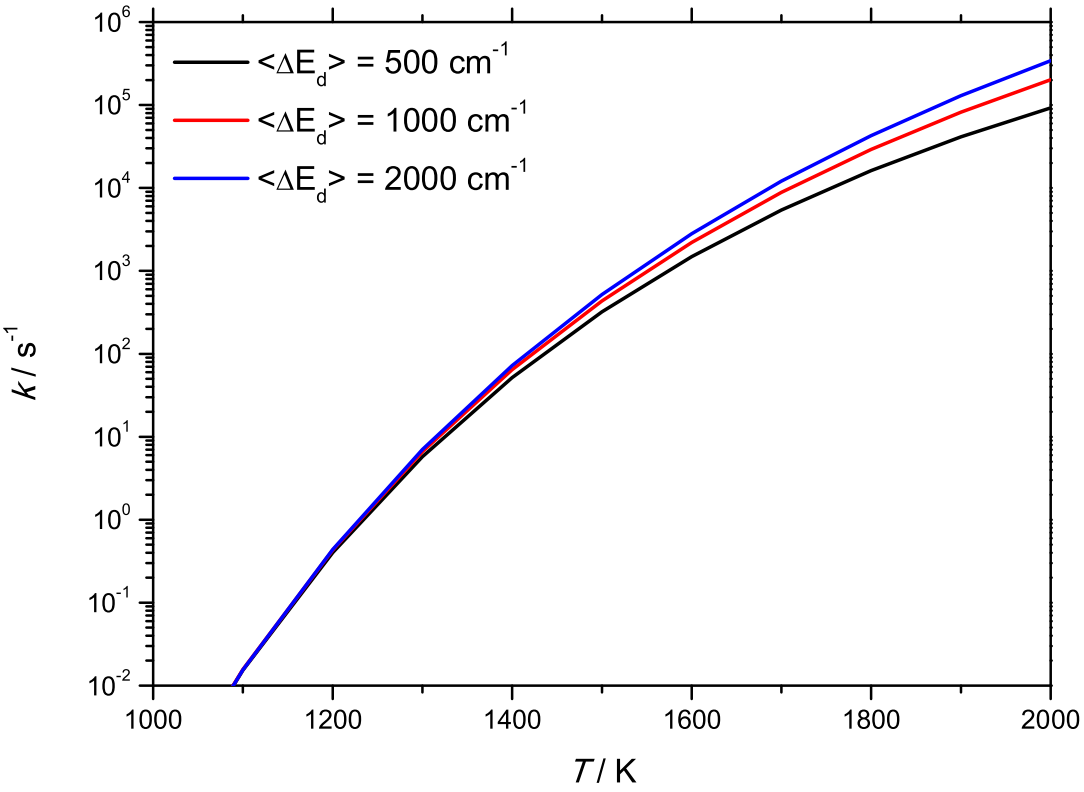

Figure 4: Influence of altering $\langle \Delta E_d \rangle$ ± a factor of 2 on the computed rate constant for the reaction 2-methylfuran → **P3** + **P4** (ketene + propyne) at a pressure of 2.5 atm.

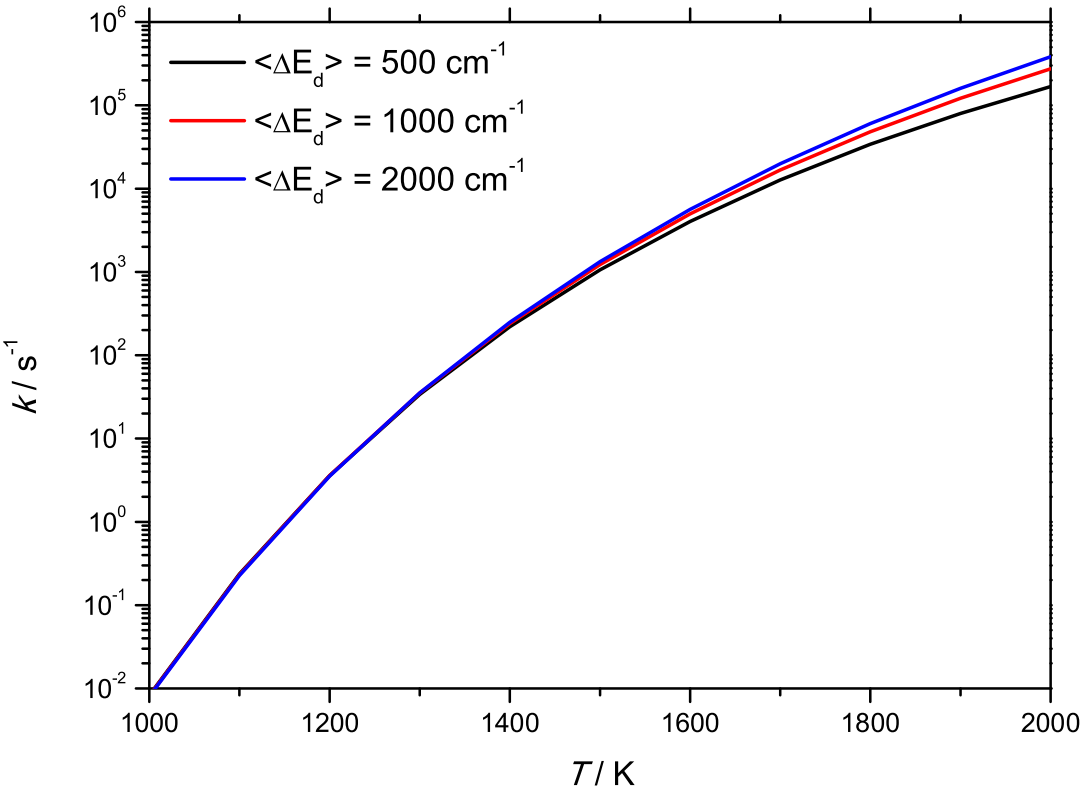

Figure 5: Influence of altering $\langle \Delta E_d \rangle$ ± a factor of 2 on the computed rate constant for the reaction 2-methylfuran → **M6** (2,3-pentadiene-1-al) at a pressure of 2.5 atm.

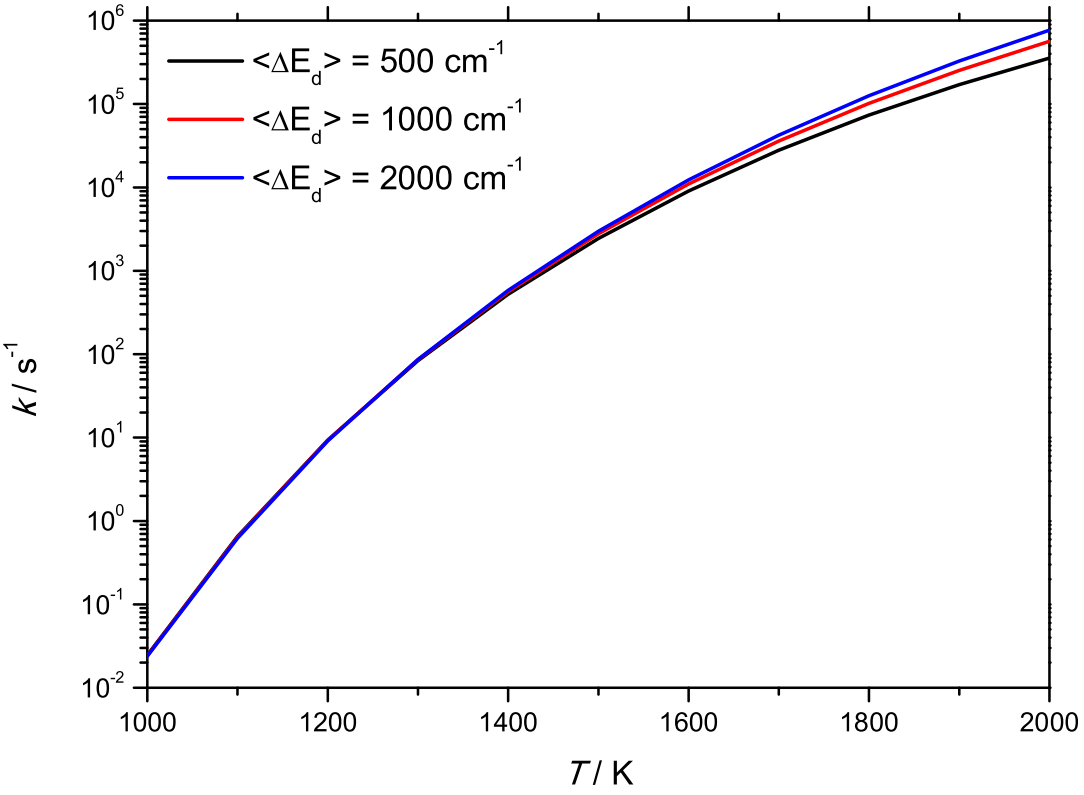

Figure 6: Influence of altering $\langle \Delta E_d \rangle$ ± a factor of 2 on the computed rate constant for the reaction 2-methylfuran → **M9** (3,4-pentadiene-2-one) at a pressure of 2.5 atm.

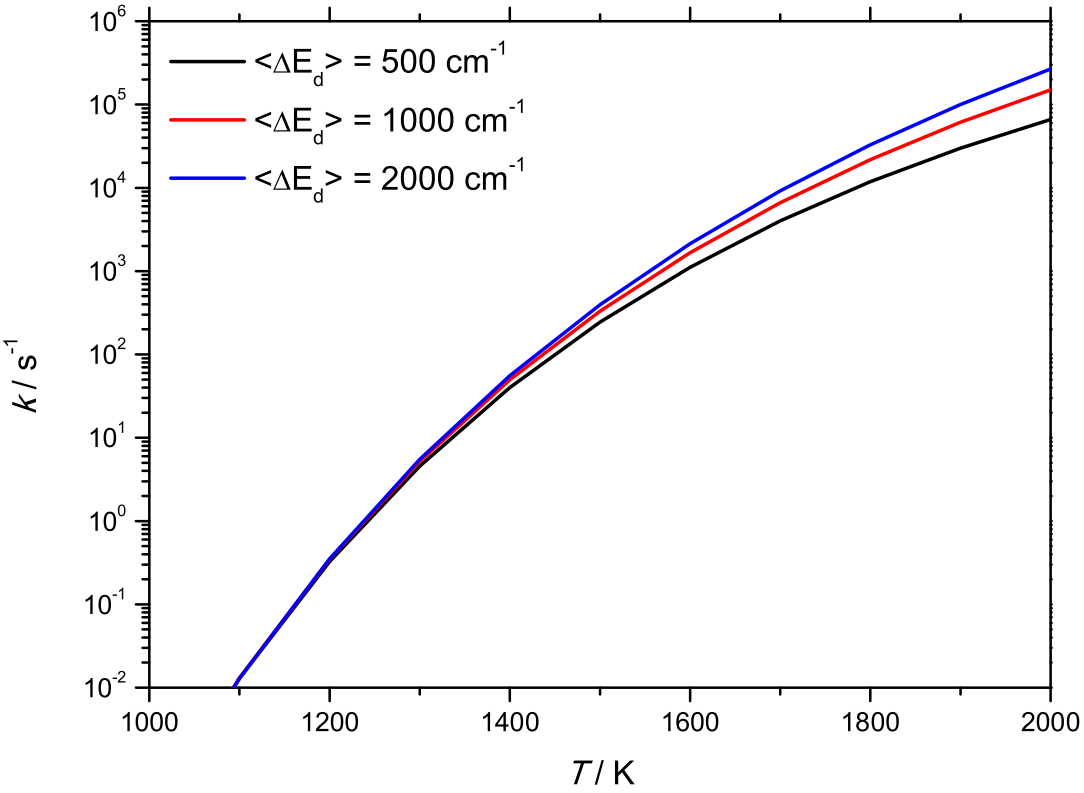

Figure 7: Influence of altering $\langle \Delta E_d \rangle$ ± a factor of 2 on the computed rate constant for the reaction 2-methylfuran → **M10** + **P17** (2-furanylmethyl + hydrogen atom) at a pressure of 2.5 atm.

3.2 Hydrogen Atom Addition at Carbon 2 of 2-Methylfuran

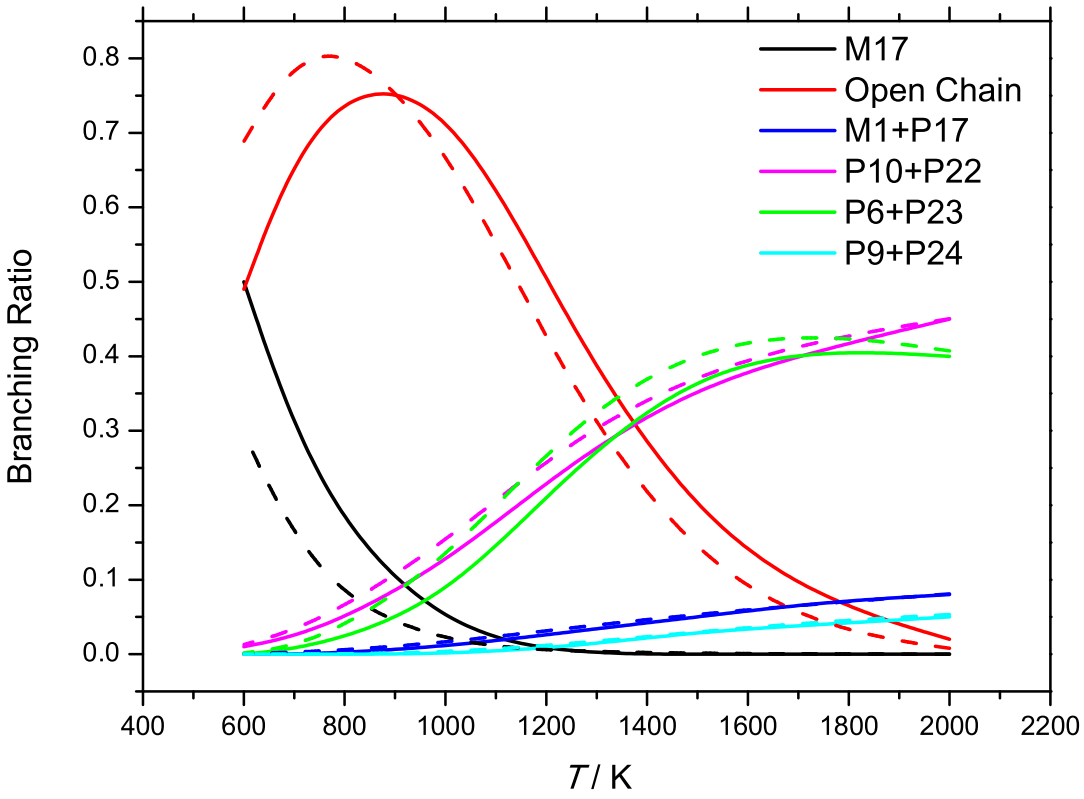

Figure 8: Computed product branching ratios at 2.5 atm. for the reaction 2-methylfuran + hydrogen atom (C-2 addition) → products. $\langle \Delta E_d \rangle$ = 2000 cm^{-1} (—); $\langle \Delta E_d \rangle$ = 500 cm^{-1} (– –).

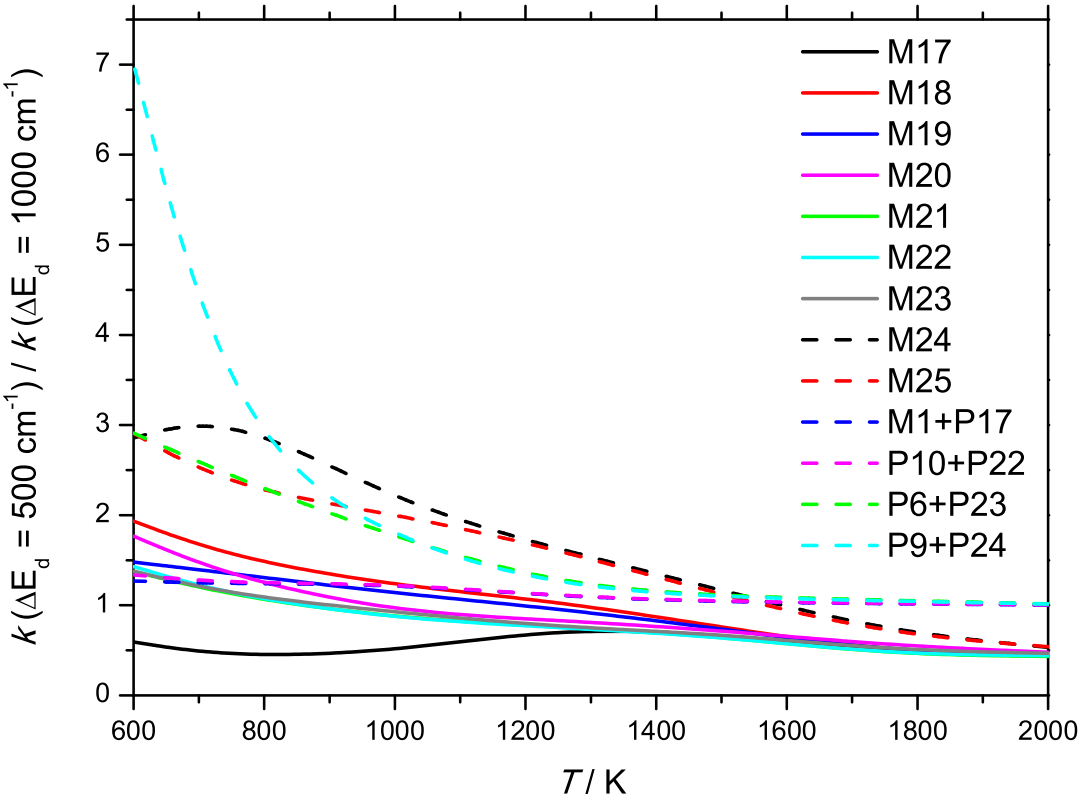

Figure 9: Ratio of computed rate constants for the reaction 2-methylfuran + hydrogen atom → products at 2.5 atm., with $\langle \Delta E_d \rangle$ = 500 cm^{-1} and $\langle \Delta E_d \rangle$ = 1000 cm^{-1}.

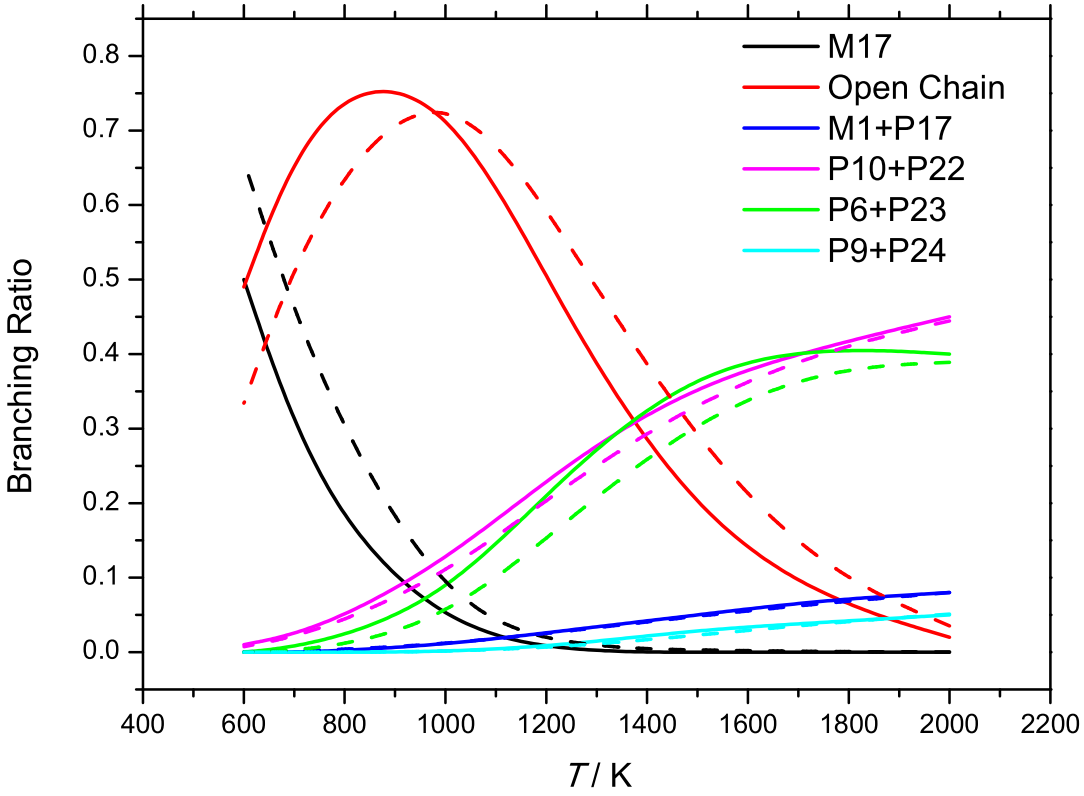

Figure 10: Computed product branching ratios at 2.5 atm. for the reaction 2-methylfuran + hydrogen atom (C-2 addition) → products. $\langle \Delta E_d \rangle$ = 2000 cm^{-1} (—); $\langle \Delta E_d \rangle$ = 2000 cm^{-1} (– –).

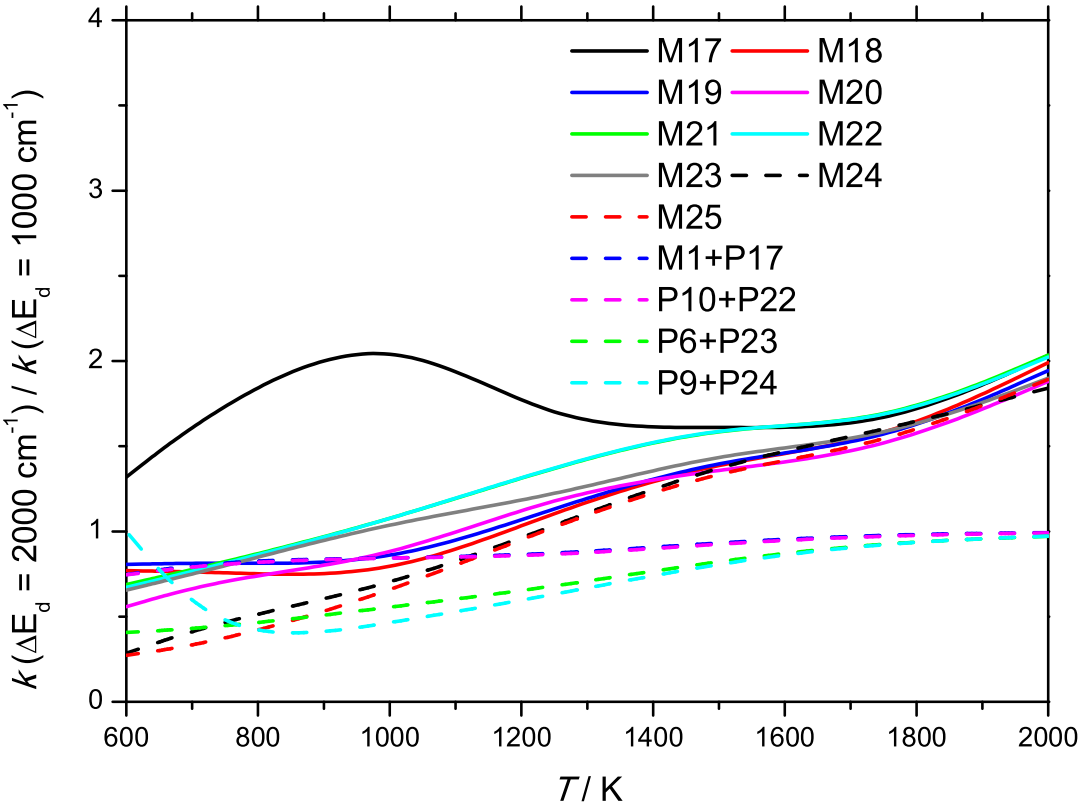

Figure 11: Ratio of computed rate constants for the reaction 2-methylfuran + hydrogen atom → products at 2.5 atm., with $\langle \Delta E_d \rangle$ = 2000 cm^{-1} and $\langle \Delta E_d \rangle$ = 1000 cm^{-1}.

4 Pressure Dependent Rate Constants from RRKM/ME Calculations

4.1 Chemkin-PRO Compatible PLOG Rate Constants

Table 3: Chemkin-PRO PLOG format pressure- (atm) and temperature-dependent rate constants for the unimolecular decomposition of 2-methylfuran and related intermediates. $k(\mathrm{s}^{-1}) = AT^n \exp(-E_a/RT)$.

Reaction	p (atm)	A	n	E_a (cal/mol)
M1 → M3	0.01	5.12E+66	-15.39	97801
	0.1	1.25E+57	-12.47	93815
	1	4.11E+38	-7.10	82916
	2.5	9.13E+31	-5.19	78799
	10	4.49E+23	-2.80	73549
	100	3.41E+15	-0.48	68305
M3 → P3 + P4	0.01	3.51E+48	-10.26	45743
	0.1	4.87E+54	-11.66	53545
	1	4.56E+48	-9.71	52461
	2.5	9.25E+43	-8.31	50120
	10	1.15E+36	-6.01	45637
	100	3.68E+25	-2.98	39180
M1 → M6	0.01	2.17E+72	-17.14	105418
	0.1	2.77E+63	-14.37	102515
	1	3.81E+43	-8.58	91138
	2.5	1.10E+36	-6.41	86543
	10	1.98E+26	-3.60	80450
	100	1.95E+16	-0.74	74027
M1 → M9	0.01	4.07E+70	-16.58	102965
	0.1	2.59E+61	-13.75	99646
	1	9.73E+41	-8.09	88398
	2.5	5.63E+34	-6.01	83964
	10	3.26E+25	-3.35	78165
	100	1.55E+16	-0.68	72168
M1 → M10 + P17	0.01	2.89E+92	-22.81	127594
	0.1	1.06E+87	-20.85	128912
	1	1.42E+65	-14.34	117910
	2.5	2.15E+55	-11.48	112302
	10	1.63E+41	-7.39	103833
	100	1.97E+24	-2.53	93217
M6 → P5 + P6	0.01	7.52E+57	-13.07	70107
	0.1	2.45E+45	-9.31	64145
	1	2.26E+34	-6.06	58261
	2.5	1.52E+30	-4.84	55869
	10	9.55E+24	-3.32	52837
	100	3.45E+18	-1.46	48961
M6 → P6 + P7	0.01	1.82E+82	-19.88	99104
	0.1	1.35E+66	-14.92	92199
	1	5.20E+48	-9.73	83042
	2.5	3.19E+42	-7.90	79592
	10	4.14E+35	-5.86	75903
	100	3.60E+27	-3.48	71654

Table 3: Chemkin-PRO PLOG format pressure- (atm) and temperature-dependent rate constants for the unimolecular decomposition of 2-methylfuran and related intermediates. $k(\mathrm{s}^{-1}) = AT^n \exp(-E_a/RT)$.

Reaction	p (atm)	A	n	E_a (cal/mol)
M9 → P3 + P4	0.01	4.63E+98	-24.44	115044
	0.1	5.48E+87	-20.97	111832
	1	2.57E+73	-16.59	105899
	2.5	1.72E+67	-14.74	102980
	10	7.68E+57	-11.97	98229
	100	2.61E+43	-7.73	90132
M9 → P13 + P14	0.01	9.56E+85	-21.57	106694
	0.1	2.05E+76	-18.47	104322
	1	2.69E+62	-14.22	98759
	2.5	1.40E+56	-12.33	95815
	10	2.65E+46	-9.44	90900
	100	1.02E+31	-4.93	82324

Table 4: Chemkin-PRO PLOG format pressure- (atm) and temperature-dependent rate constants for the unimolecular decomposition of 2-furanylmethyl radical and related intermediates. $k(\mathrm{s}^{-1}) = AT^n \exp(-E_a/RT)$.

Reaction	p (atm)	A	n	E_a (cal/mol)
M10 → M11	0.01	4.49E+61	-14.18	64492
	0.1	5.05E+59	-13.42	65593
	1	4.62E+50	-10.65	61945
	2.5	4.98E+45	-9.17	59475
	10	1.88E+37	-6.70	54959
	100	7.14E+23	-2.79	47253
M11 → P17 + P18	0.01	3.18E+29	-7.07	46866
	0.1	4.47E+47	-11.61	58081
	1	7.77E+62	-15.19	71711
	2.5	1.31E+66	-15.81	76149
	10	3.54E+65	-15.23	79663
	100	5.91E+47	-9.66	73572
M11 → M12	0.01	1.92E+23	-3.09	12414
	0.1	1.36E+24	-3.27	13699
	1	9.86E+22	-2.88	13663
	2.5	1.01E+22	-2.58	13262
	10	1.11E+20	-2.00	12301
	100	3.10E+16	-0.96	10330
M12 → M13	0.01	2.29E+35	-7.31	30103
	0.1	7.37E+40	-8.62	35996
	1	1.60E+41	-8.48	38761
	2.5	2.25E+39	-7.87	38506
	10	2.28E+34	-6.34	36515
	100	1.01E+23	-2.98	30549
M13 → M14	0.01	5.27E+27	-4.36	17157
	0.1	4.79E+24	-3.47	15507
	1	2.97E+20	-2.25	13109
	2.5	3.12E+18	-1.68	11914
	10	3.55E+15	-0.83	10112
	100	3.02E+11	0.33	7517
M14 → P6 + P19	0.01	2.72E+50	-10.60	38351
	0.1	2.76E+56	-12.06	45564
	1	6.26E+55	-11.63	48704
	2.5	1.11E+46	-8.82	42672
	10	2.95E+42	-7.69	42310
	100	1.33E+27	-3.25	33671
M13 → M15	0.01	8.53E+34	-6.33	24268
	0.1	9.35E+30	-5.17	22282
	1	1.15E+25	-3.45	19007
	2.5	1.33E+22	-2.60	17242
	10	6.13E+17	-1.35	14614
	100	3.37E+11	0.44	10639
M15 → M16	0.01	1.30E+34	-6.30	24079
	0.1	1.62E+30	-5.15	22128
	1	2.36E+24	-3.45	18897
	2.5	2.95E+21	-2.61	17154

Table 4: Chemkin-PRO PLOG format pressure- (atm) and temperature-dependent rate constants for the unimolecular decomposition of 2-furanylmethyl radical and related intermediates. $k(\mathrm{s}^{-1}) = AT^n \exp(-E_a/RT)$.

Reaction	p (atm)	A	n	E_a (cal/mol)
	10	1.55E+17	-1.38	14559
	100	1.10E+11	0.38	10649
M16 → P17 + P20	0.01	2.21E+77	-18.51	85730
	0.1	6.80E+81	-19.49	92440
	1	3.18E+73	-16.76	91956
	2.5	7.85E+58	-12.53	83194
	10	4.40E+50	-9.98	80861
	100	3.51E+23	-2.13	65606

Table 5: Chemkin-PRO PLOG format pressure- (atm) and temperature-dependent rate constants for the chemically activated recombination of hydrogen atom with 2-methylfuran at carbon 2. $k(\mathrm{cm^3 mol^{-1} s^{-1}}) = AT^n \exp(-E_a/RT)$.

Reaction	p (atm)	A	n	E_a (cal/mol)
M1 + P17 → P10 + P22	0.01	5.93E+17	-1.13	10160
	0.1	6.31E+15	-0.49	10818
	1	6.25E+15	-0.44	12156
	2.5	6.28E+15	-0.43	12614
	10	7.55E+15	-0.43	13614
	100	2.47E+21	-1.92	19575
M1 + P17 → P6 + P23	0.01	3.28E+24	-3.07	13756
	0.1	1.22E+31	-4.83	20365
	1	3.52E+33	-5.39	25717
	2.5	6.30E+31	-4.83	26504
	10	1.69E+27	-3.43	27006
	100	1.27E+17	-0.43	26869
M1 + P17 → P9 + P24	0.01	4.08E+34	-6.02	26367
	0.1	2.42E+34	-5.81	29573
	1	9.29E+52	-10.88	46873
	2.5	4.08E+52	-10.63	50324
	10	1.52E+52	-10.34	55297
	100	3.16E+21	-1.47	43388
M1 + P17 → M17	0.01	9.42E+64	-16.86	22009
	0.1	4.08E+65	-16.74	23378
	1	1.91E+39	-8.86	8696
	2.5	1.53E+38	-8.43	8247
	10	6.02E+43	-9.88	11916
	100	2.32E+61	-14.59	24263
M1 + P17 → M18	0.01	2.70E+78	-20.34	33228
	0.1	6.04E+77	-19.70	36451
	1	1.25E+55	-12.72	27383
	2.5	3.26E+53	-12.08	28627
	10	6.16E+44	-9.38	25899
	100	3.31E+30	-5.02	21526
M1 + P17 → M19	0.01	1.39E+75	-19.25	30503
	0.1	6.80E+76	-19.31	34924
	1	6.02E+54	-12.51	26305
	2.5	9.25E+49	-10.96	25364
	10	9.05E+41	-8.47	22964
	100	1.32E+29	-4.53	19323
M1 + P17 → M21	0.01	2.78E+68	-17.43	23706
	0.1	2.14E+73	-18.47	28937
	1	6.73E+58	-13.83	24722
	2.5	2.87E+55	-12.69	24563
	10	1.01E+51	-11.17	24850
	100	1.98E+39	-7.45	23483
M1 + P17 → M22	0.01	4.29E+67	-17.15	23482
	0.1	1.30E+72	-18.06	28630
	1	2.15E+58	-13.63	24825
	2.5	2.21E+55	-12.60	24917

Table 5: Chemkin-PRO PLOG format pressure- (atm) and temperature-dependent rate constants for the chemically activated recombination of hydrogen atom with 2-methylfuran at carbon 2. $k(\mathrm{cm^3 mol^{-1} s^{-1}}) = AT^n \exp(-E_a/RT)$.

Reaction	p (atm)	A	n	E_a (cal/mol)
	10	9.14E+50	-11.10	25255
	100	9.96E+38	-7.30	23686
M1 + P17 → M23	0.01	7.53E+72	-18.62	26476
	0.1	1.17E+77	-19.39	32694
	1	7.07E+58	-13.68	26972
	2.5	4.14E+51	-11.46	24431
	10	1.98E+45	-9.45	23414
	100	3.59E+38	-7.20	24843
M1 + P17 → M24	0.01	3.01E+70	-18.18	32181
	0.1	1.20E+91	-23.67	48986
	1	1.58E+77	-19.09	48486
	2.5	4.57E+69	-16.73	46964
	10	4.01E+51	-11.33	39795
	100	4.54E+48	-10.01	48245
M1 + P17 → M25	0.01	9.09E+78	-20.71	37095
	0.1	6.30E+92	-24.28	49388
	1	1.90E+73	-18.04	45934
	2.5	1.94E+69	-16.70	46393
	10	7.29E+58	-13.45	44651
	100	5.86E+13	-0.26	23754

Table 6: Chemkin-PRO PLOG format pressure- (atm) and temperature-dependent rate constants for the chemically activated recombination of hydrogen atom with 2-methylfuran at carbon 5. $k(\mathrm{cm^3 mol^{-1} s^{-1}}) = AT^n \exp(-E_a/RT)$.

Reaction	p (atm)	A	n	E_a (cal/mol)
M1 + P17 → P10 + P34	0.01	1.07E+39	-6.67	30846
	0.1	1.50E+47	-8.88	38568
	1	5.03E+47	-8.89	42758
	2.5	8.28E+44	-8.04	42837
	10	6.18E+36	-5.65	40637
	100	1.44E+32	-4.18	44351
M1 + P17 → P6 + P36	0.01	1.07E+47	-9.58	29917
	0.1	1.48E+51	-10.63	36022
	1	5.31E+47	-9.49	38643
	2.5	1.28E+43	-8.11	37934
	10	4.80E+41	-7.57	41809
	100	7.91E+39	-6.79	51714
M1 + P17 → M41	0.01	4.76E+68	-17.25	26292
	0.1	9.15E+51	-12.17	18071
	1	9.18E+32	-6.58	6260
	2.5	5.44E+32	-6.47	5802
	10	2.88E+39	-8.30	9788
	100	1.09E+60	-13.93	23557
M1 + P17 → M42	0.01	2.33E+68	-16.69	25474
	0.1	9.96E+60	-14.22	24242
	1	2.28E+51	-11.16	21670
	2.5	6.26E+48	-10.32	21476
	10	6.08E+44	-8.99	21593
	100	5.60E+37	-6.72	22140
M1 + P17 → M43	0.01	1.17E+72	-17.75	29767
	0.1	3.88E+62	-14.68	27048
	1	1.83E+53	-11.69	24764
	2.5	5.42E+51	-11.14	25267
	10	9.73E+47	-9.89	25627
	100	1.39E+41	-7.65	26453
M1 + P17 → M44	0.01	5.30E+58	-14.38	24546
	0.1	2.52E+58	-13.88	27696
	1	1.07E+56	-12.76	31267
	2.5	3.18E+57	-13.02	34452
	10	1.27E+55	-12.07	37352
	100	1.53E+40	-7.38	37071
M1 + P17 → M45	0.01	2.97E+55	-13.40	21399
	0.1	9.84E+56	-13.41	25744
	1	1.13E+55	-12.43	29560
	2.5	5.76E+55	-12.48	32226
	10	5.12E+54	-11.91	36035
	100	4.91E+40	-7.48	36344

4.2 Comparison of RRKM/ME Results from the ChemRate and Multiwell Codes for the Thermal Decomposition of 2-furanylmethyl and related intermediates

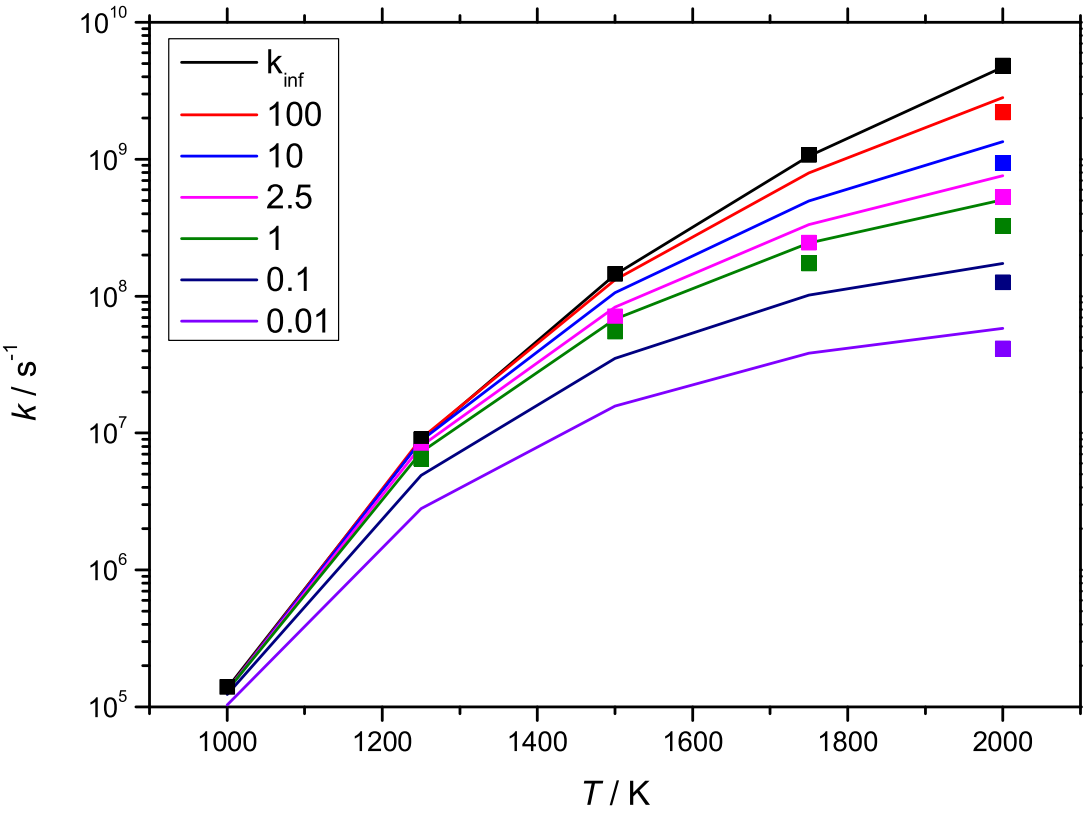

Figure 12: Computed rate constants (p (atm)) for the reaction M10 → M11 from the ChemRate (lines) and Multiwell (symbols) codes.

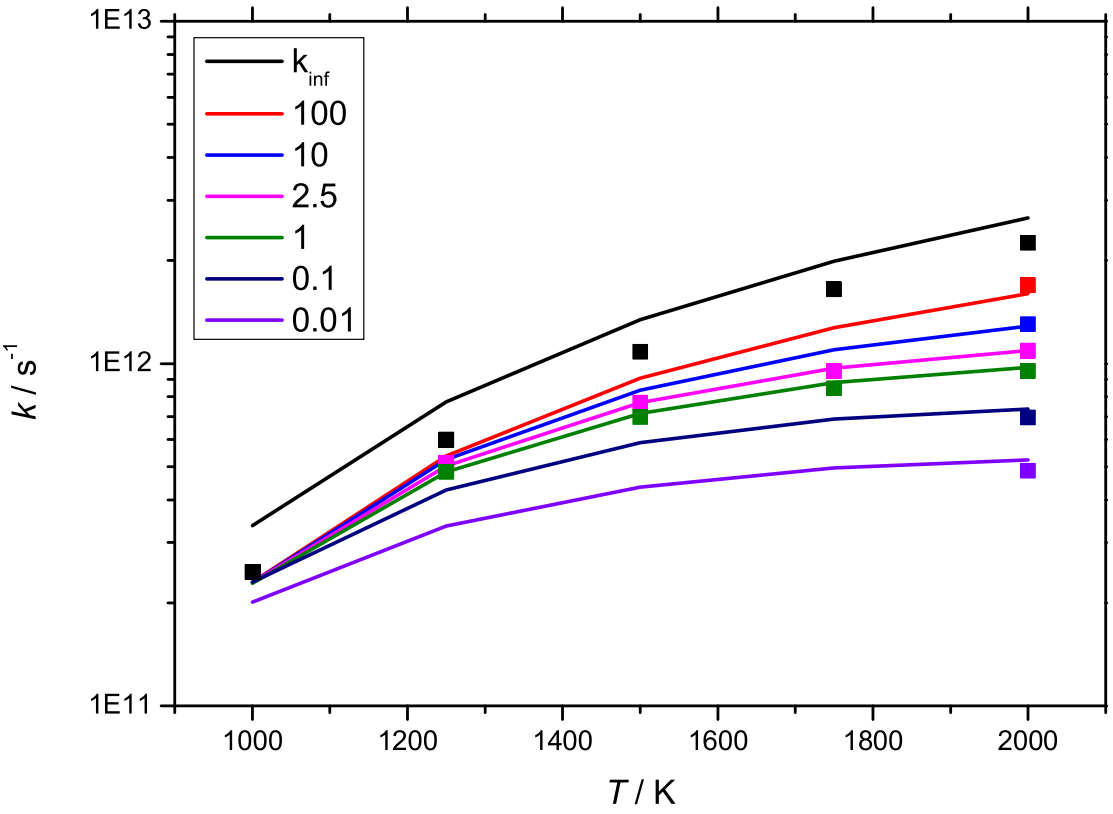

Figure 13: Computed rate constants (p (atm)) for the reaction M11 → M12 from the ChemRate (lines) and Multi-well (symbols) codes.

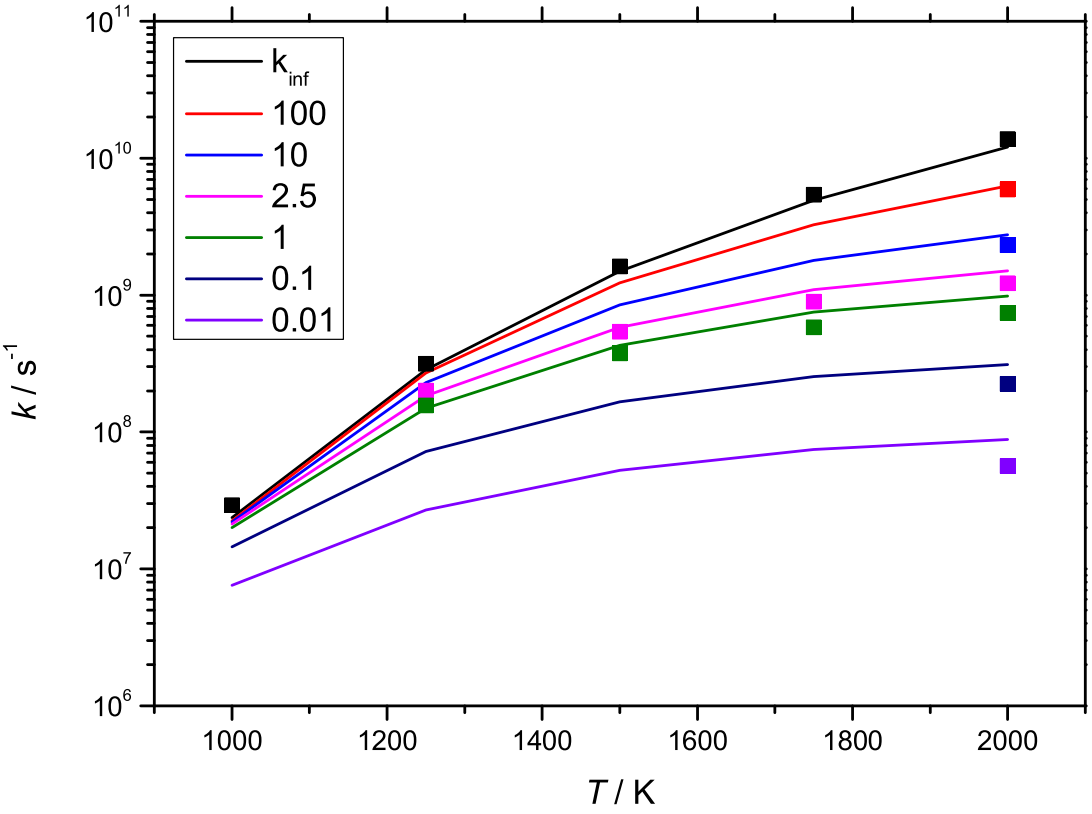

Figure 14: Computed rate constants (p (atm)) for the reaction M12 → M13 from the ChemRate (lines) and Multiwell (symbols) codes.

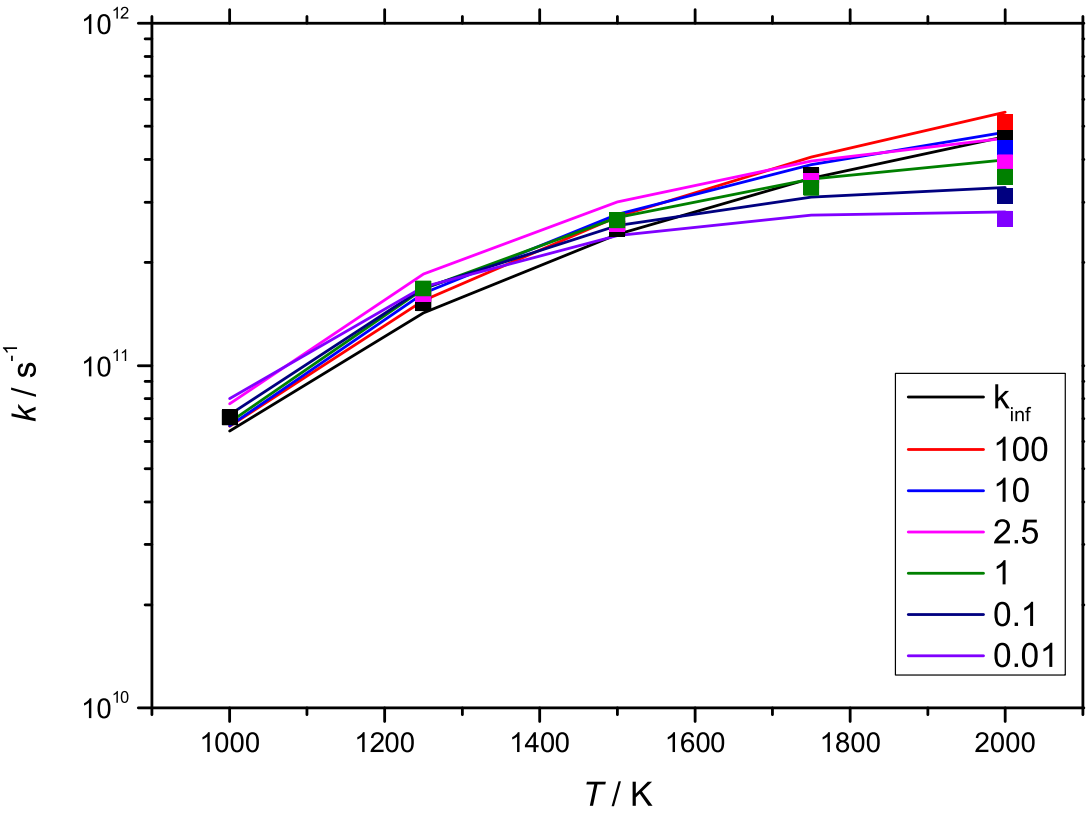

Figure 15: Computed rate constants (p (atm)) for the reaction M13 → M14 from the ChemRate (lines) and Multi-well (symbols) codes.

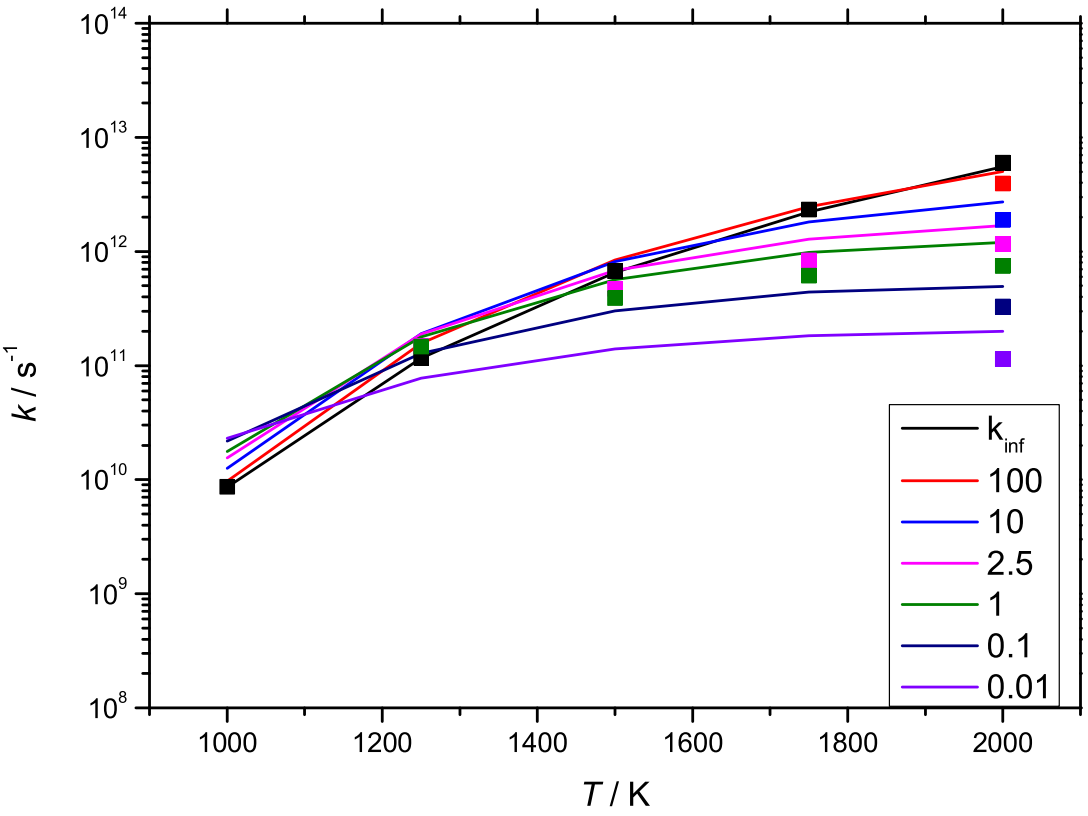

Figure 16: Computed rate constants (p (atm)) for the reaction M14 → P6 + P19 from the ChemRate (lines) and Multiwell (symbols) codes.

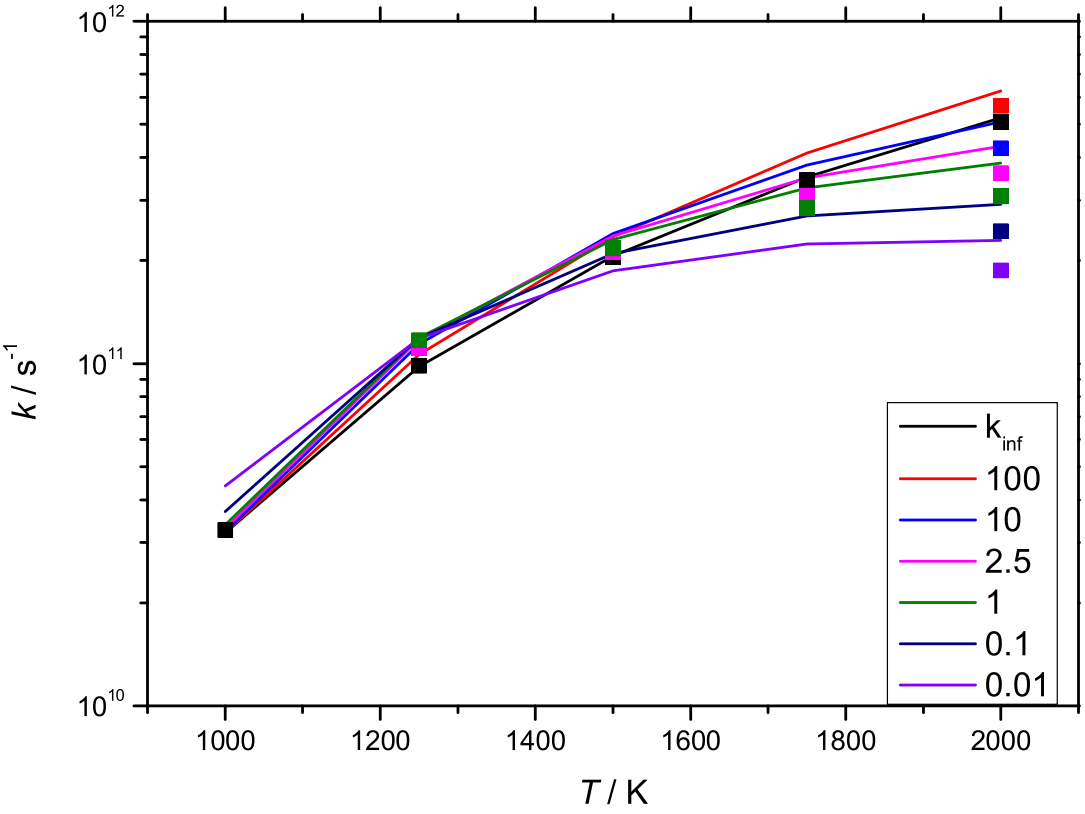

Figure 17: Computed rate constants (p (atm)) for the reaction M13 → M15 from the ChemRate (lines) and Multi-well (symbols) codes.

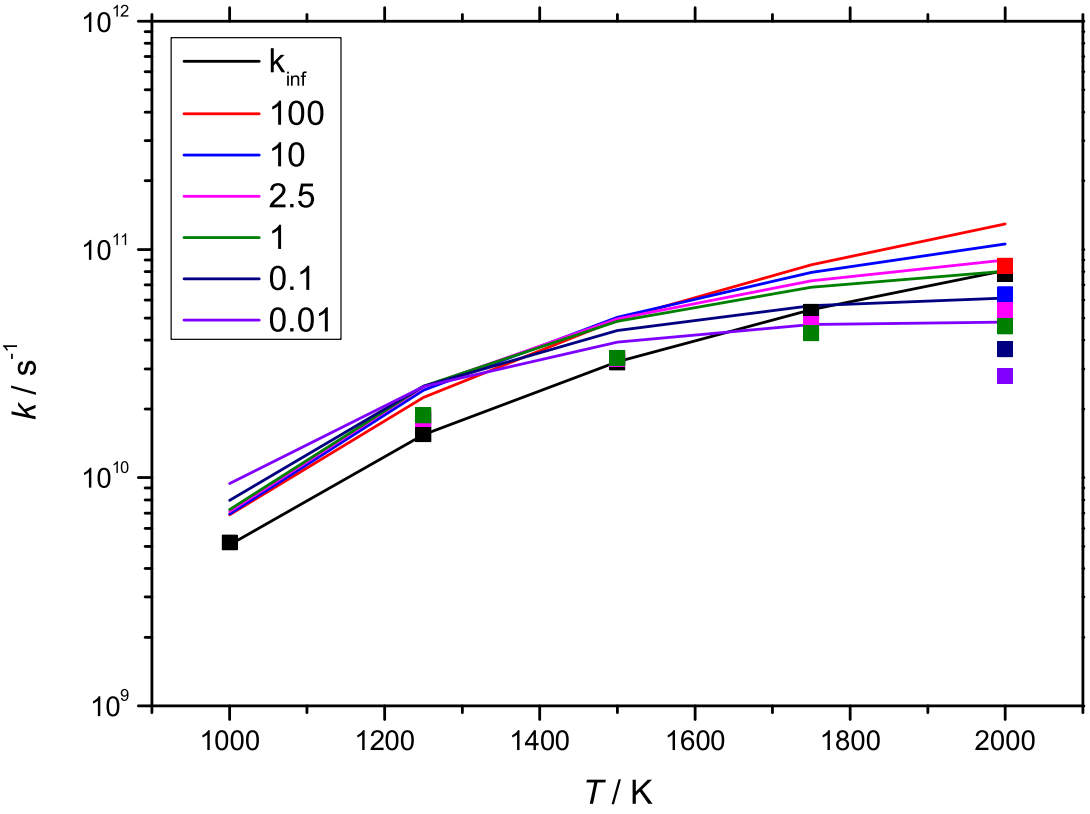

Figure 18: Computed rate constants (p (atm)) for the reaction M15 → M16 from the ChemRate (lines) and Multi-well (symbols) codes.

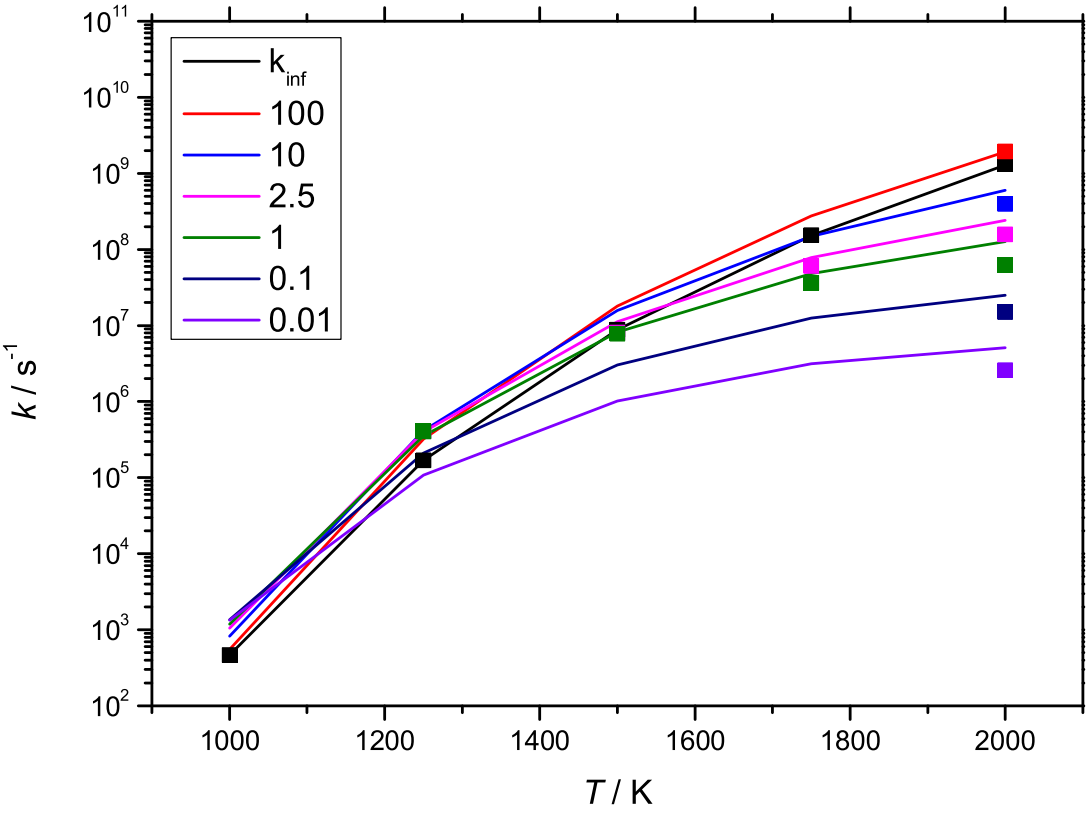

Figure 19: Computed rate constants (p (atm)) for the reaction M16 → P17 + P20 from the ChemRate (lines) and Multiwell (symbols) codes.

5 Comparison of High Pressure Limiting Rate Constants with Literature

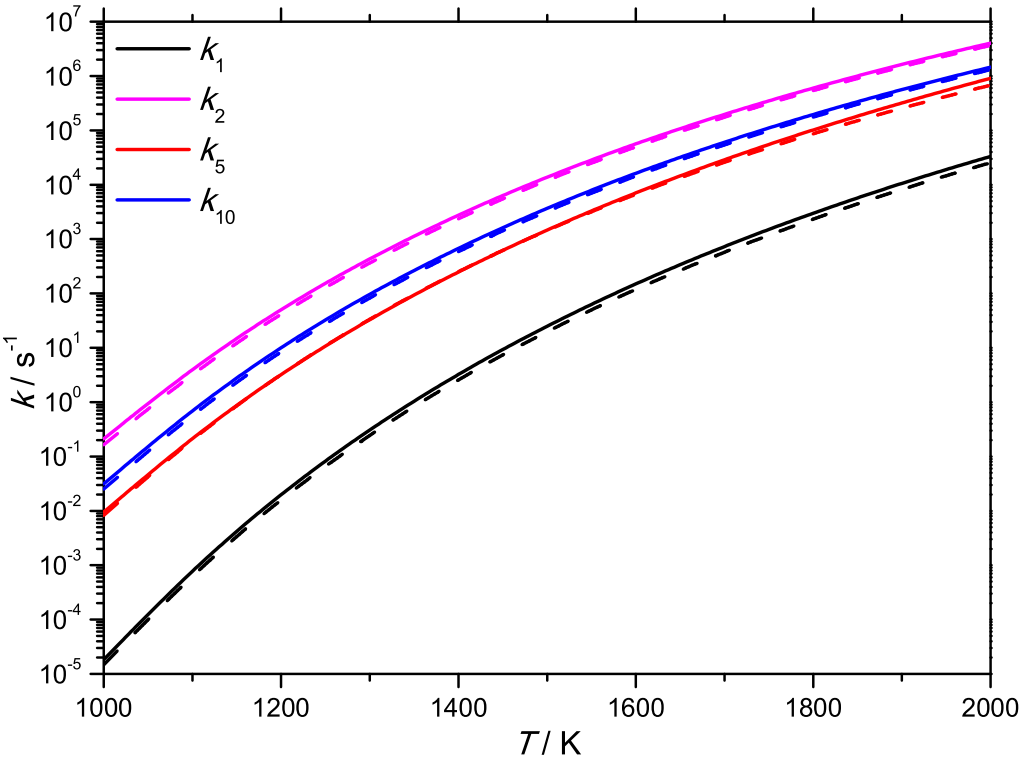

Figure 20: Calculated high-pressure limiting rate constants for hydrogen and methyl group shifts in 2-methylfuran. — Davis and Sarathy [2], – – *this study*. Legend refers to notation in main text. Rate Constants from [2] are multipled by 2 for direct comparison with the results of *this study*, as optical isomer corrections were not accounted for therein.

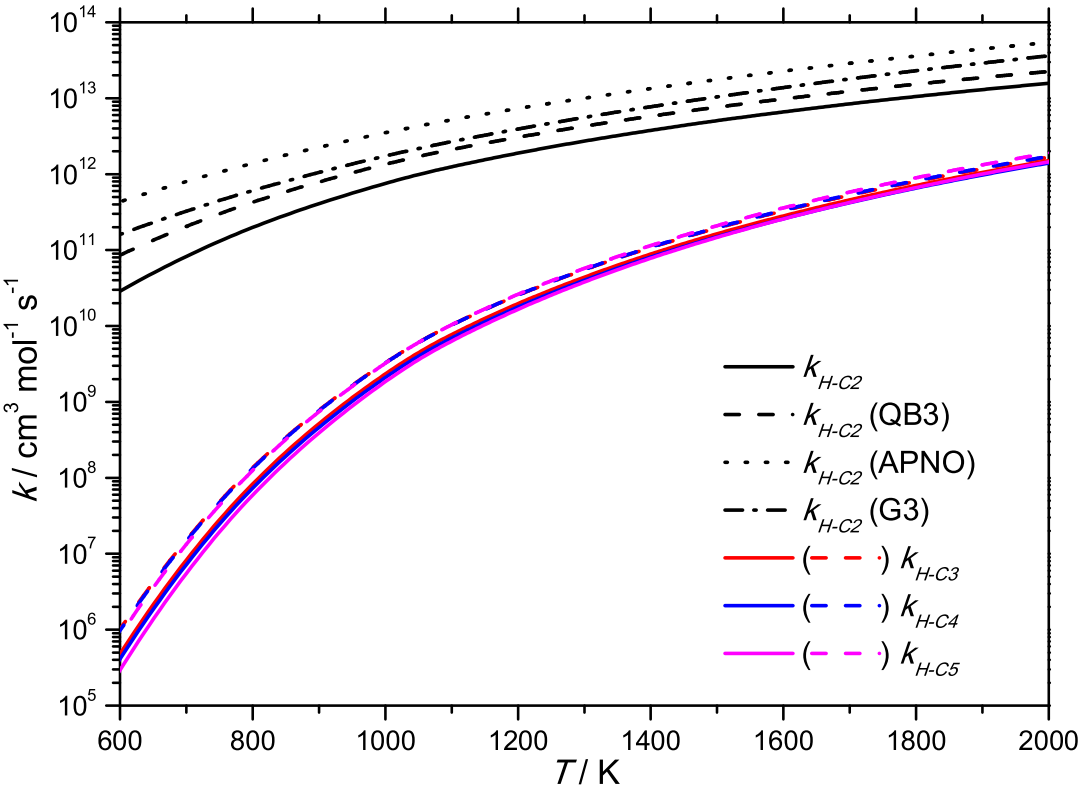

Figure 21: Calculated high pressure limiting rate constants for hydrogen atom abstraction from 2-methylfuran by hydrogen atom. — Davis and Sarathy [2], – – *this study*. Legend refers to notation in main text.

6 Comparison of Mechanism with Literature Oxidation Experiments

6.1 Atmospheric Pressure Ignition Delay Times of 1% 2-Methylfuran/Argon Mixtures

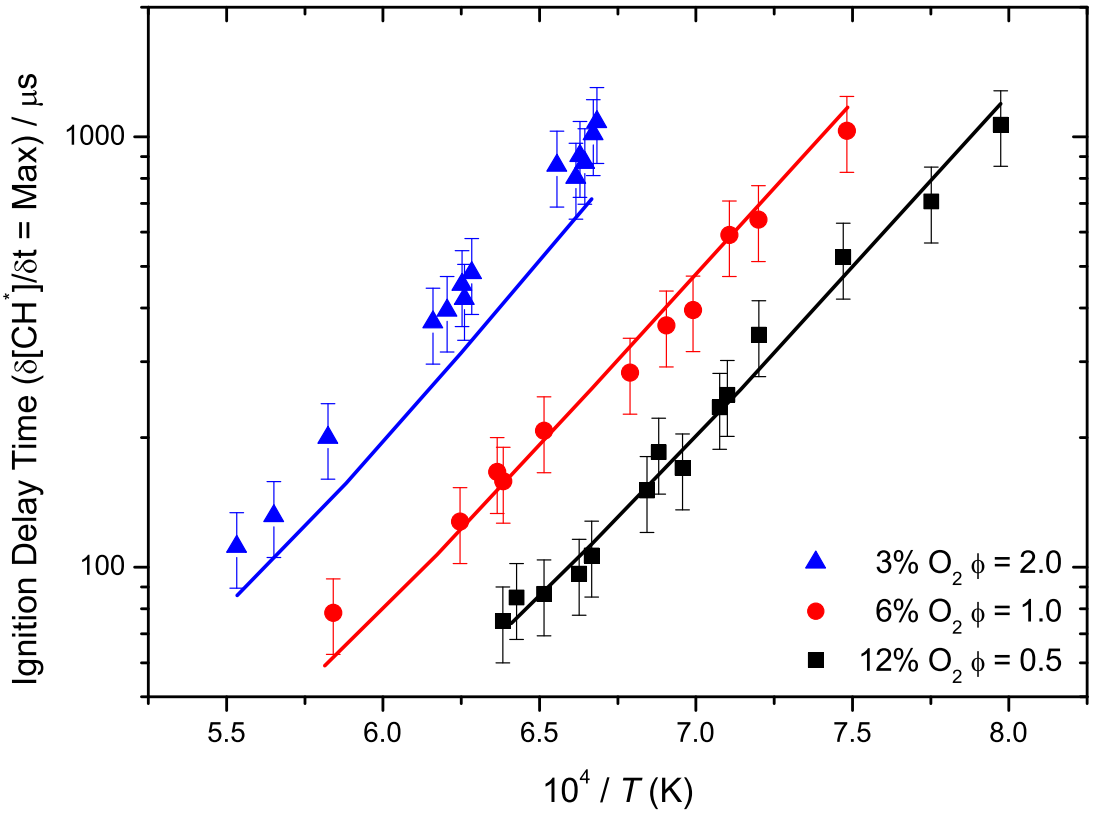

Figure 22: Atmospheric pressures experimental ignition delay times (symbols, [5]) as a function of temperature and O_2 concentration with 20% uncertainty bars and current model predictions (lines).

6.2 Ignition Delay Times of 2-Methylfuran/O_2/Argon Mixtures at Elevated Pressures

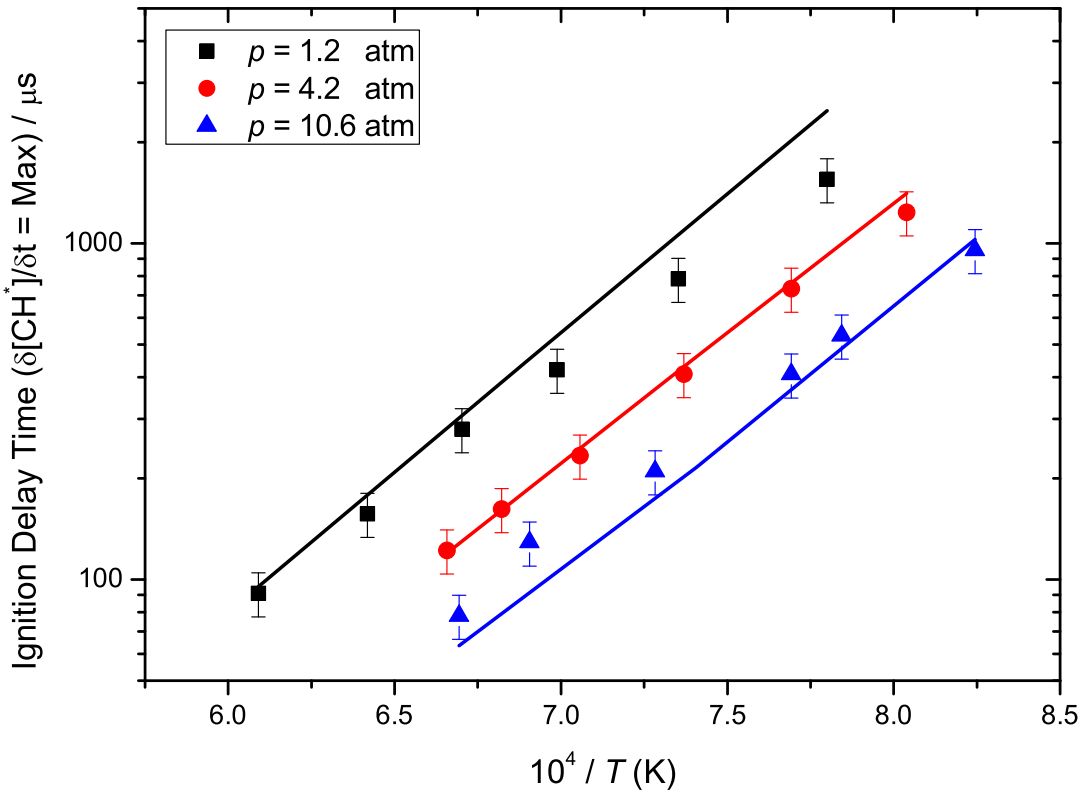

Figure 23: Experimental ignition delay times with 15% uncertainty bars (symbols, [6]) for 0.752% 2MF, 4.511% O_2 and 94.737% Ar (ϕ = 1.0) with modelling calculations (lines).

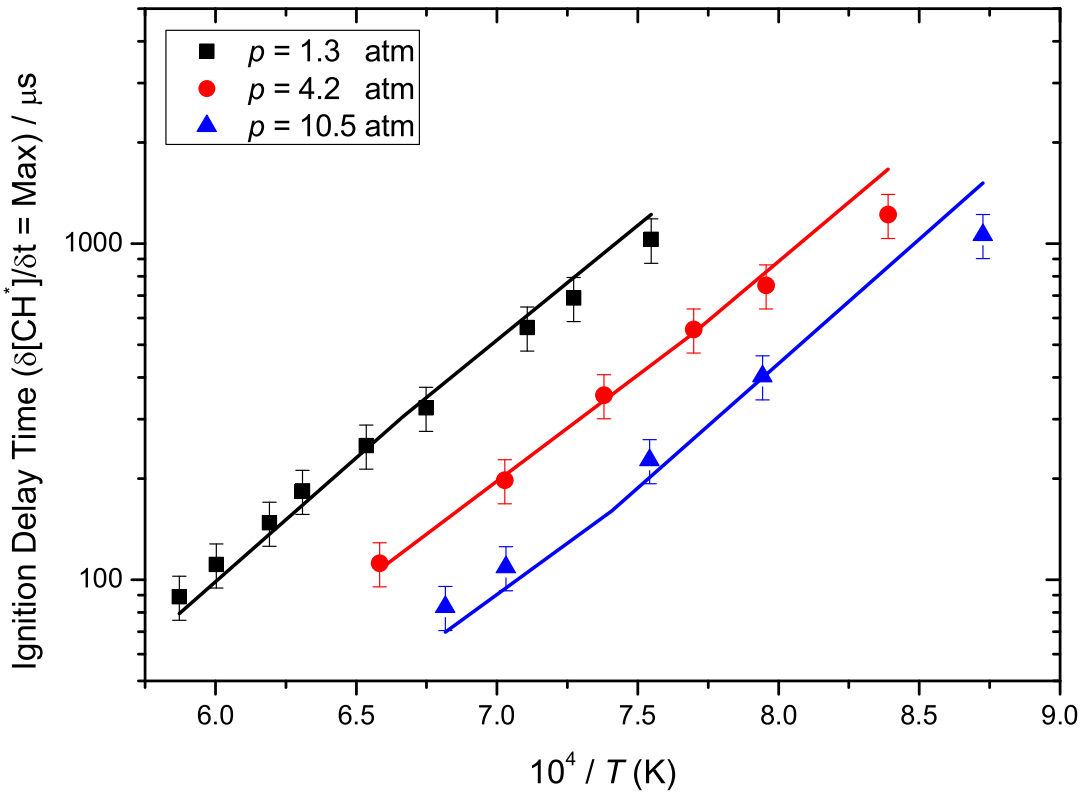

Figure 24: Experimental ignition delay times with 15% uncertainty bars (symbols, [6]) for 1.98% 2MF, 5.941% O_2 and 92.079% Ar (ϕ = 2.0) with modelling calculations (lines).

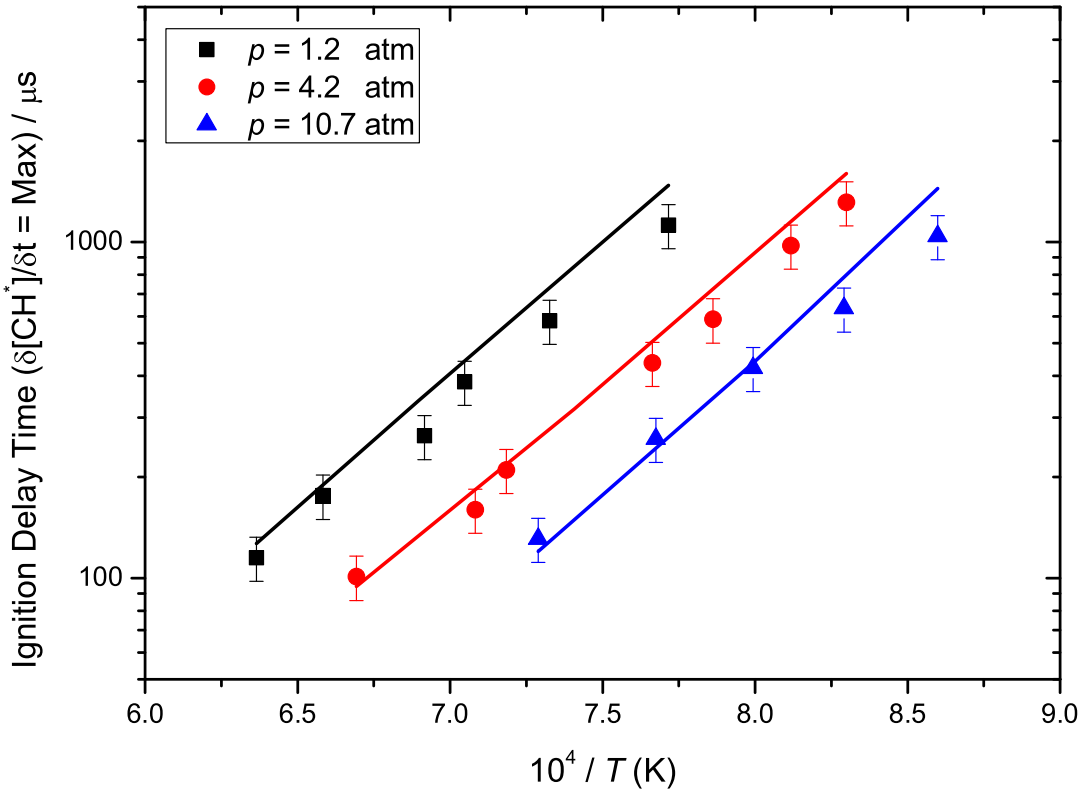

Figure 25: Experimental ignition delay times with 15% uncertainty bars (symbols, [6]) for 1.0% 2MF, 6.0% O_2 and 93.0% Ar (ϕ = 1.0) with modelling calculations (lines).

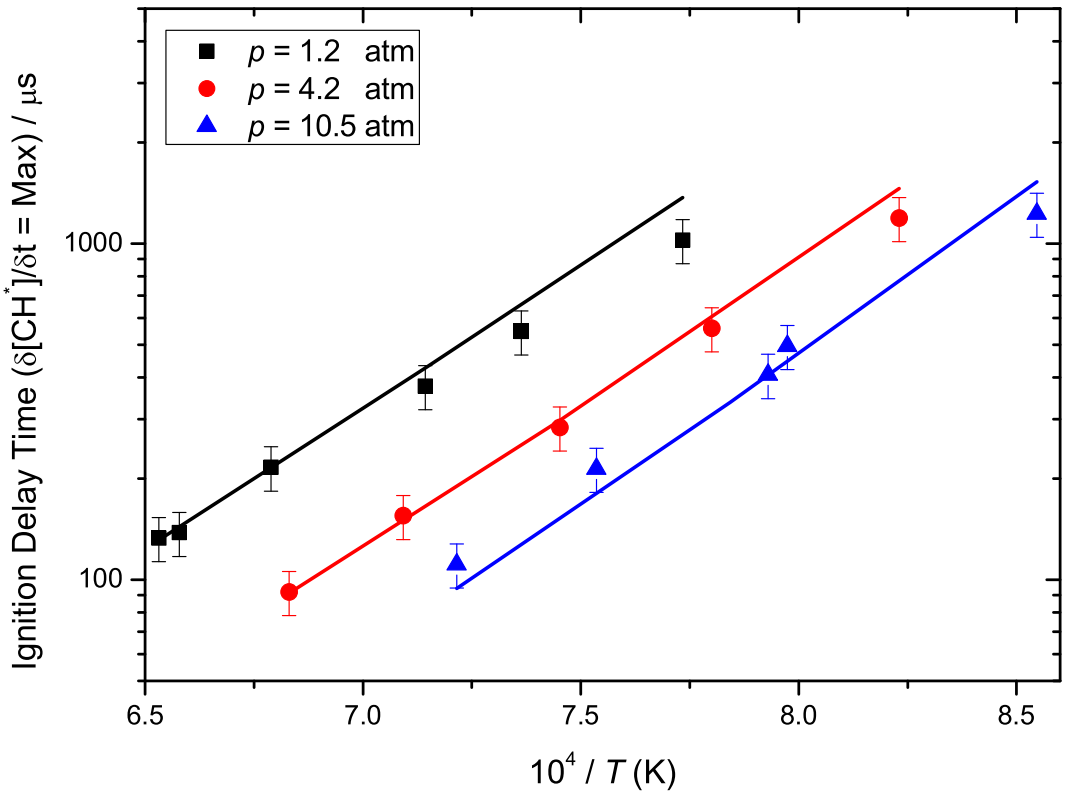

Figure 26: Experimental ignition delay times with 15% uncertainty bars (symbols, [6]) for 0.503% 2MF, 6.030% O_2 and 93.467% Ar (ϕ = 0.5) with modelling calculations (lines).

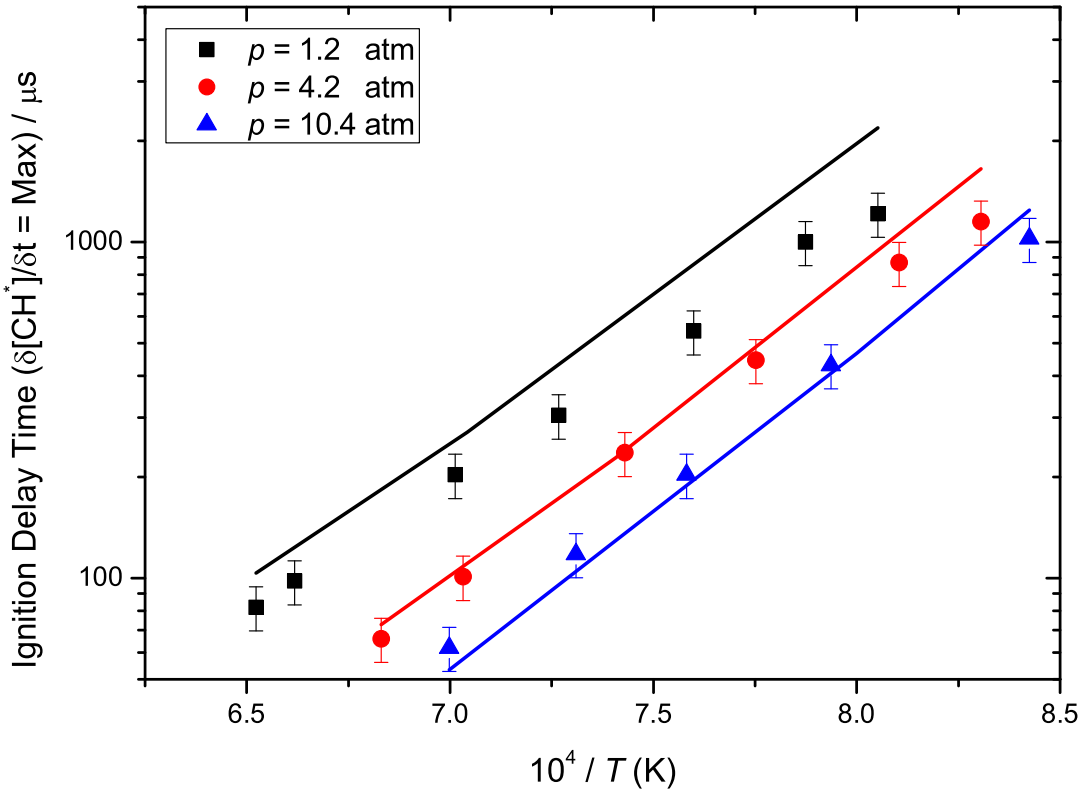

Figure 27: Experimental ignition delay times with 15% uncertainty bars (symbols, [6]) for 0.252% 2MF, 6.045% O_2 and 93.703% (ϕ = 0.25) Ar with modelling calculations (lines).

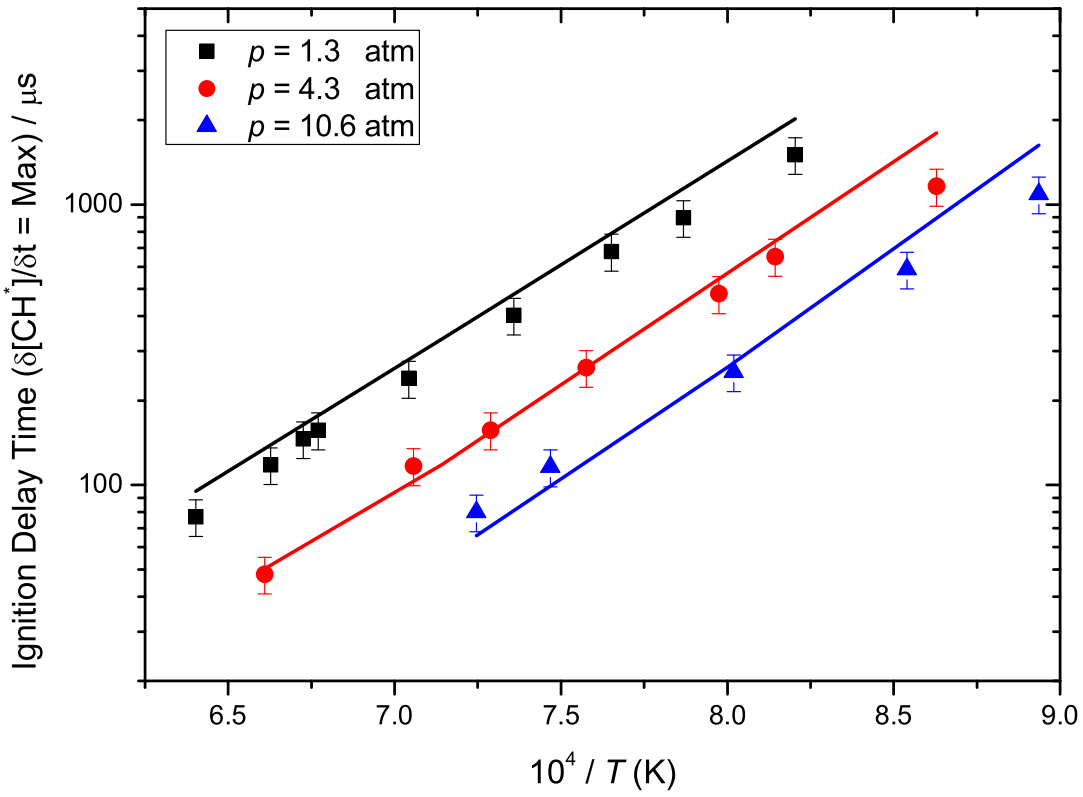

Figure 28: Experimental ignition delay times with 15% uncertainty bars (symbols, [6]) for 1.506% 2MF, 9.036% O_2 and 89.448% Ar (ϕ = 1.0) with modelling calculations (lines).

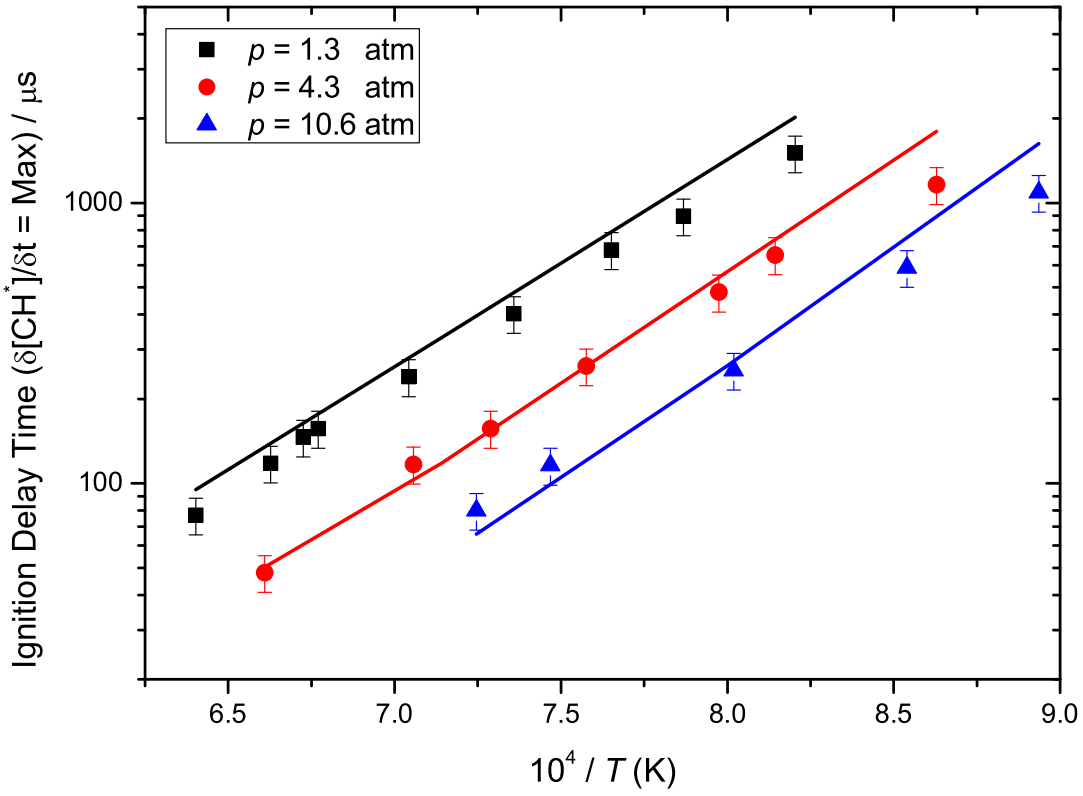

Figure 29: Experimental ignition delay times with 15% uncertainty bars (symbols, [6]) for 3.383% 2MF, 20.298% O_2 and 76.319% Ar (ϕ = 1.0) with modelling calculations (lines).

6.3 Atmospheric Pressure Laminar Burning Velocities of 2-Methylfuran-Synthetic Air Mixtures

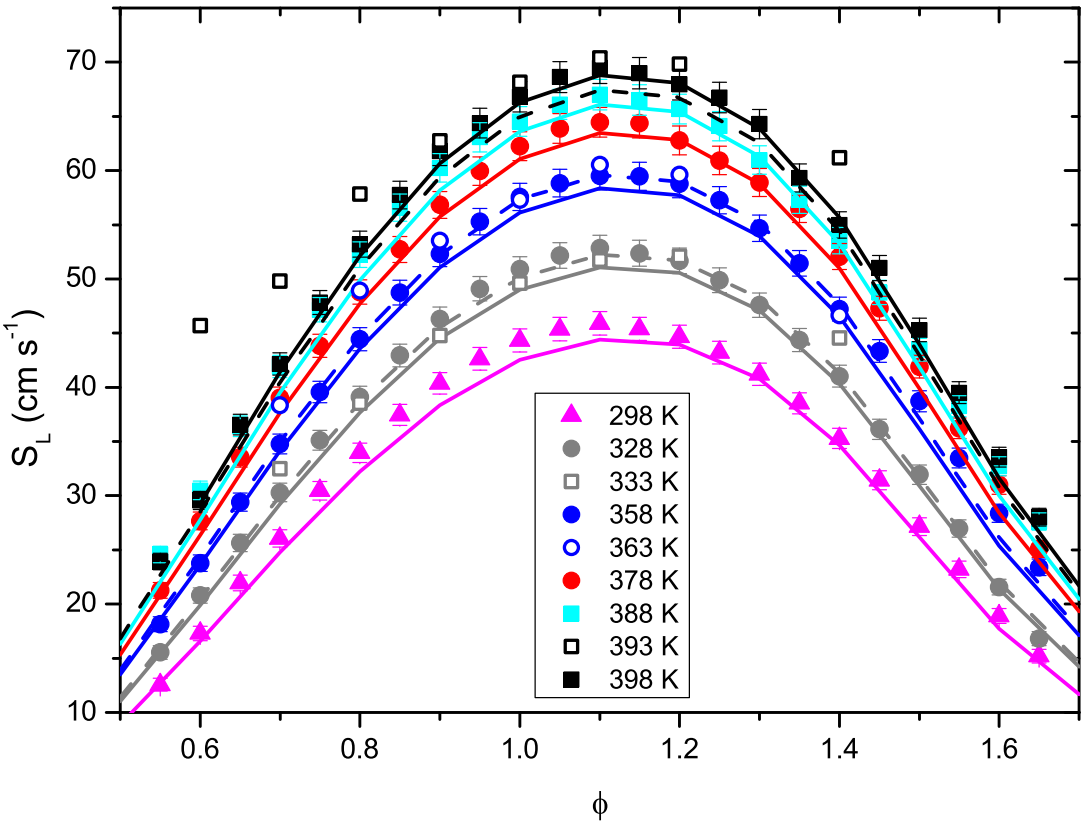

Figure 30: Experimental laminar burning velocities (symbols) as a function of unburnt gas temperature and equivalence ratio with current model predictions (lines). Closed symbols [5] (—) , open symbols [7] (– –).

6.4 Speciation in Low-Pressure 2-Methylfuran/O_2/Ar Flames

6.4.1 ϕ = 1.0

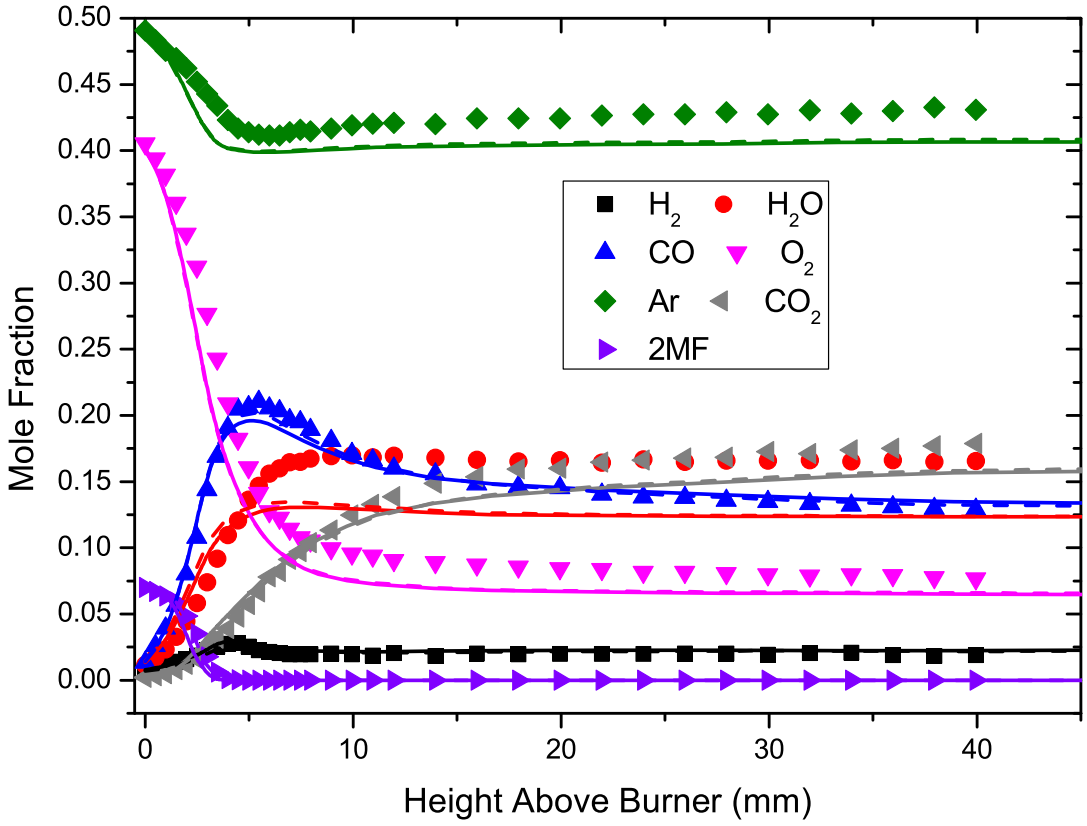

Figure 31: Experimental profiles [8] for main species measured in ϕ = 1.0 2-methylfuran/O_2/Ar flame with model calculations from *this work* (—) and the study of Tran *et al.* [8] (– –).

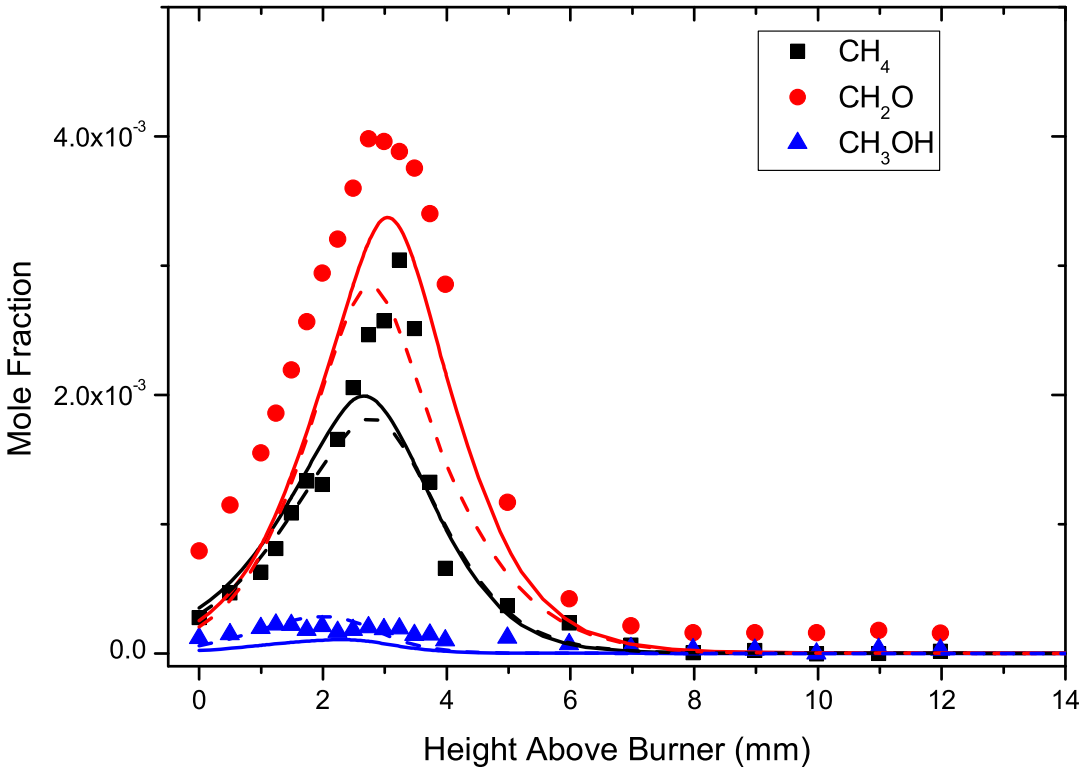

Figure 32: Experimental profiles [8] for methane, formaldehyde and methanol measured in ϕ = 1.0 2-methylfuran/O_2/Ar flame with model calculations from *this work* (—) and the study of Tran *et al.* [8] (– –).

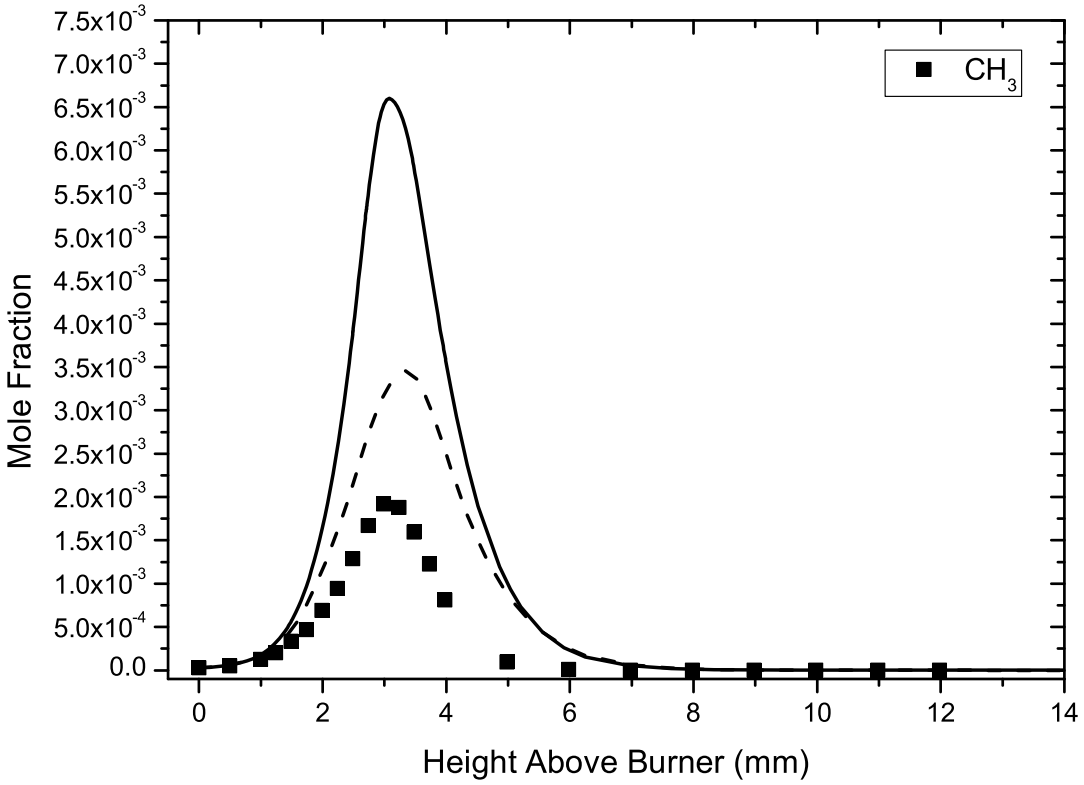

Figure 33: Experimental profile [8] for methyl radical measured in ϕ = 1.0 2-methylfuran/O_2/Ar flame with model calculations from *this work* (—) and the study of Tran *et al.* [8] (– –). Refer to [8] for a discussion on the uncertainties (up to a factor of 4) in the determination of concentrations of small radicals.

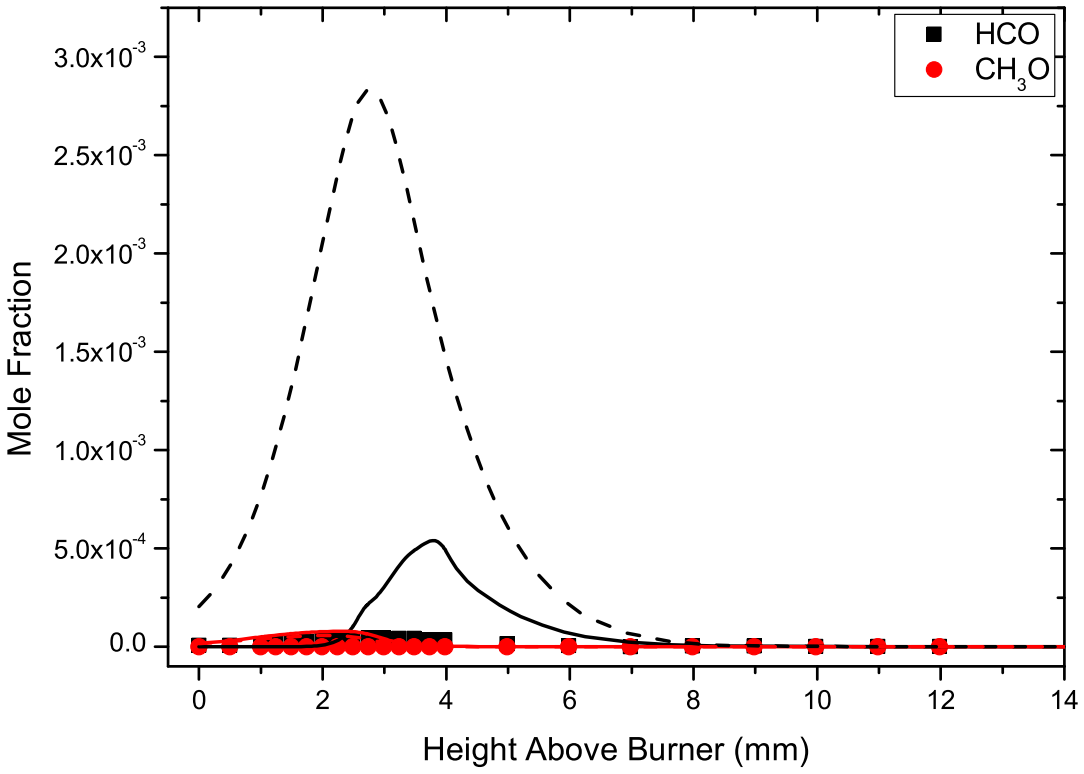

Figure 34: Experimental profiles [8] for formyl and methoxy radicals measured in ϕ = 1.0 2-methylfuran/O_2/Ar flame with model calculations from *this work* (—) and the study of Tran *et al.* [8] (– –).

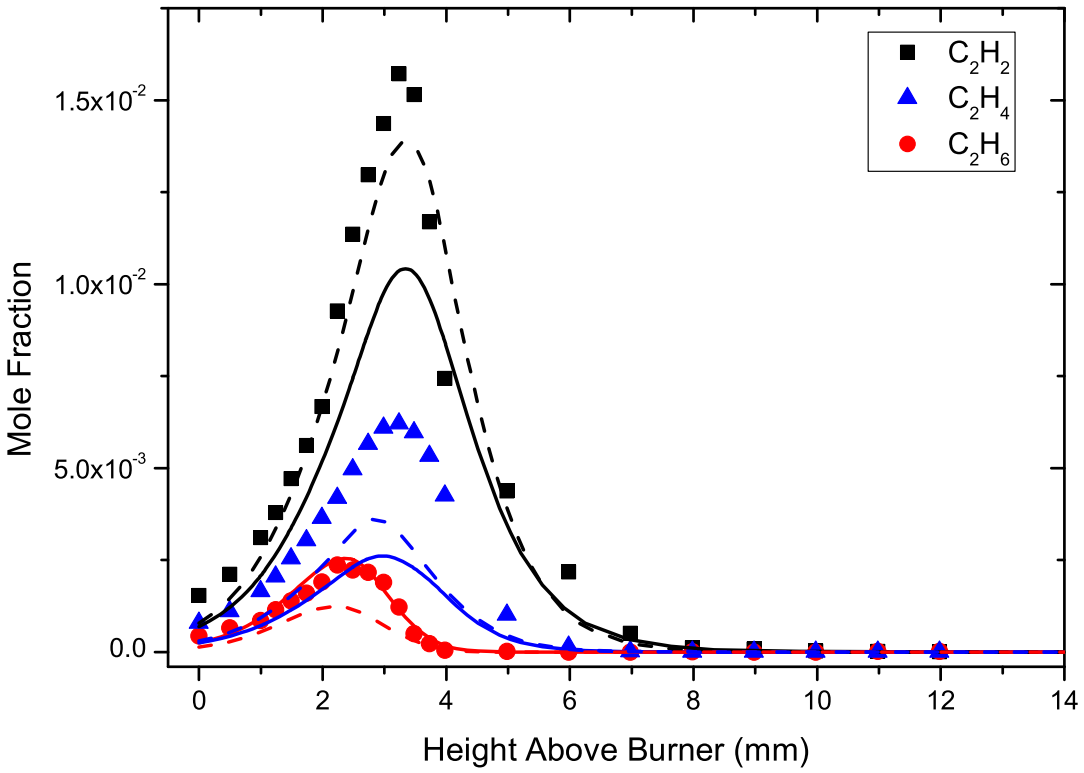

Figure 35: Experimental profiles [8] for acetylene, ethylene and ethane measured in ϕ = 1.0 2-methylfuran/O_2/Ar flame with model calculations from *this work* (—) and the study of Tran *et al.* [8] (– –).

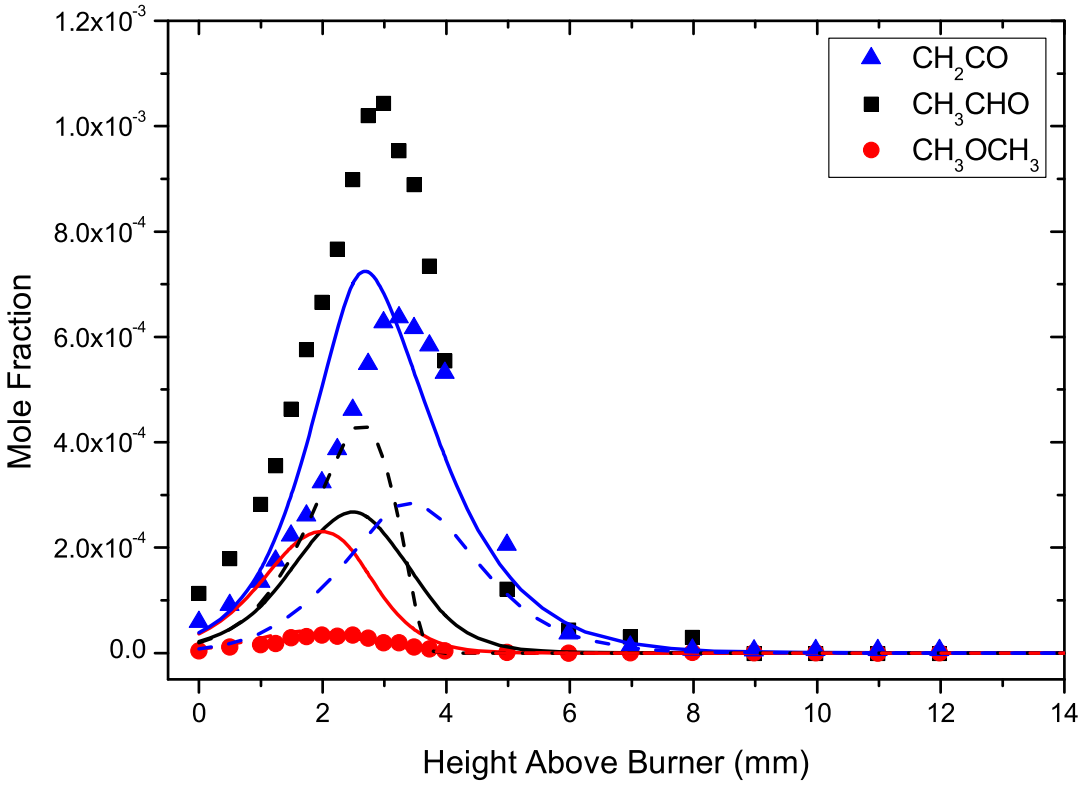

Figure 36: Experimental profiles [8] for ketene, acetaldehyde and dimethyl ether measured in ϕ = 1.0 2-methylfuran/O_2/Ar flame with model calculations from *this work* (—) and the study of Tran *et al.* [8] (– –).

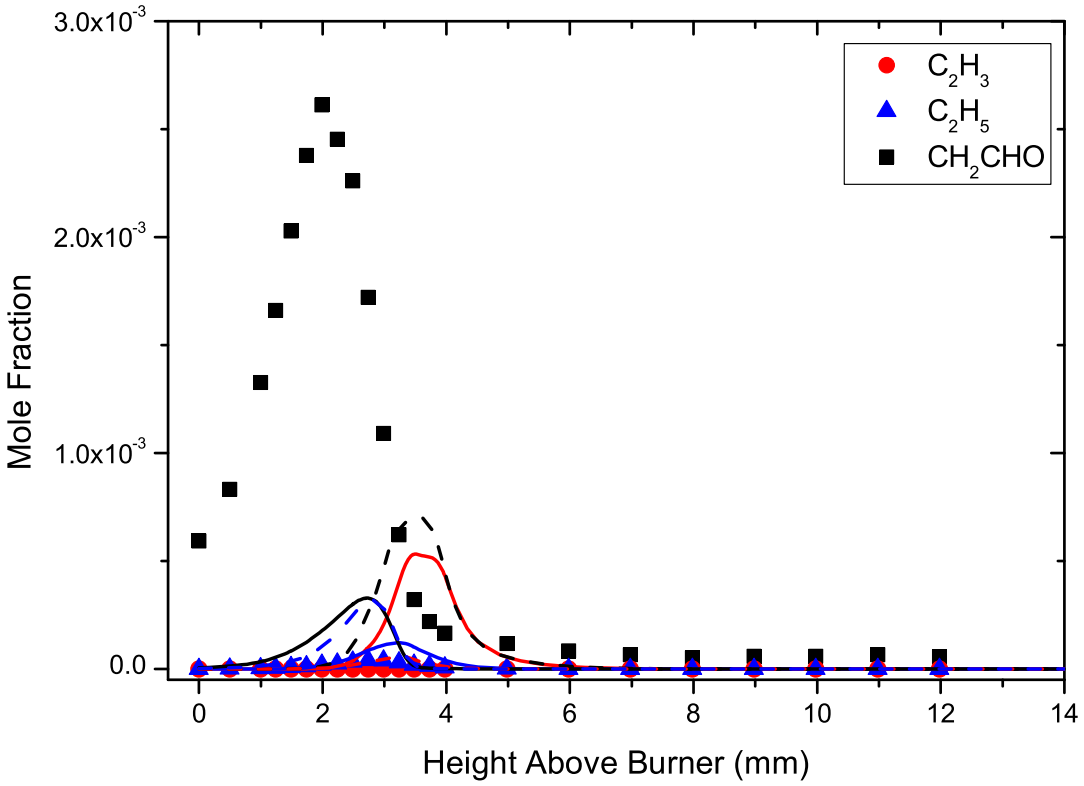

Figure 37: Experimental profiles [8] for vinyl, ethyl and vinoxy radicals measured in ϕ = 1.0 2-methylfuran/O_2/Ar flame with model calculations from *this work* (—) and the study of Tran *et al.* [8] (– –).

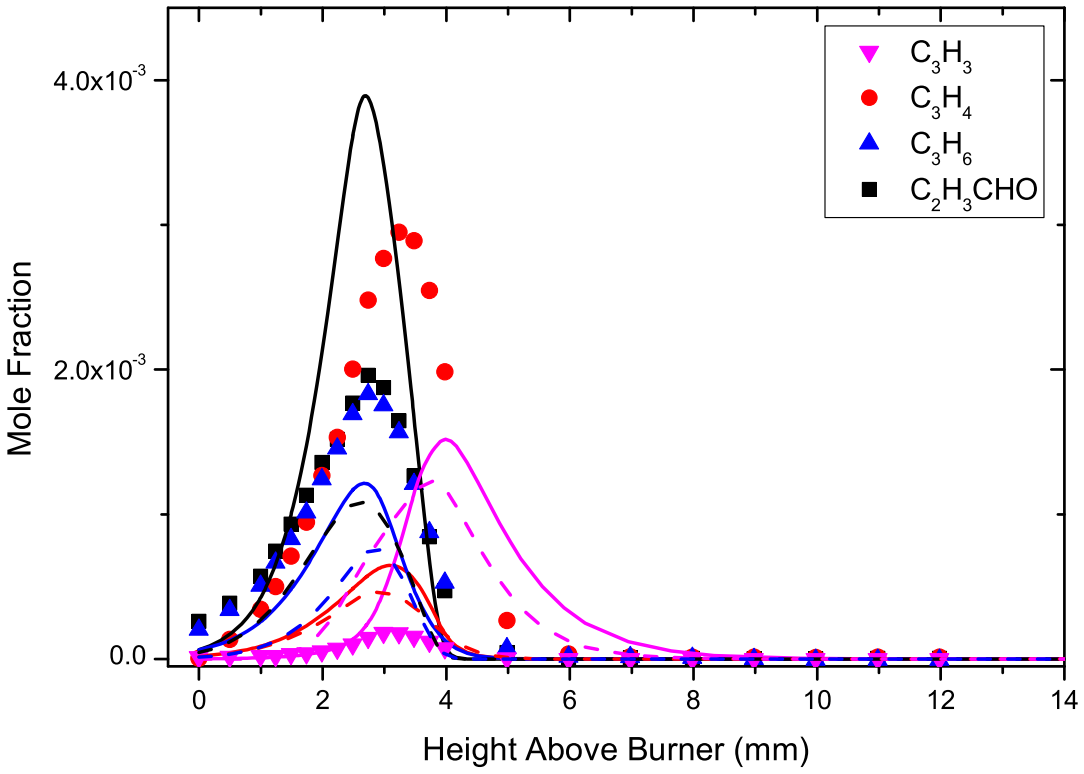

Figure 38: Experimental profiles [8] for propargyl radical, propyne, propene and acrolein measured in ϕ = 1.0 2-methylfuran/O_2/Ar flame with model calculations from *this work* (—) and the study of Tran *et al.* [8] (– –).

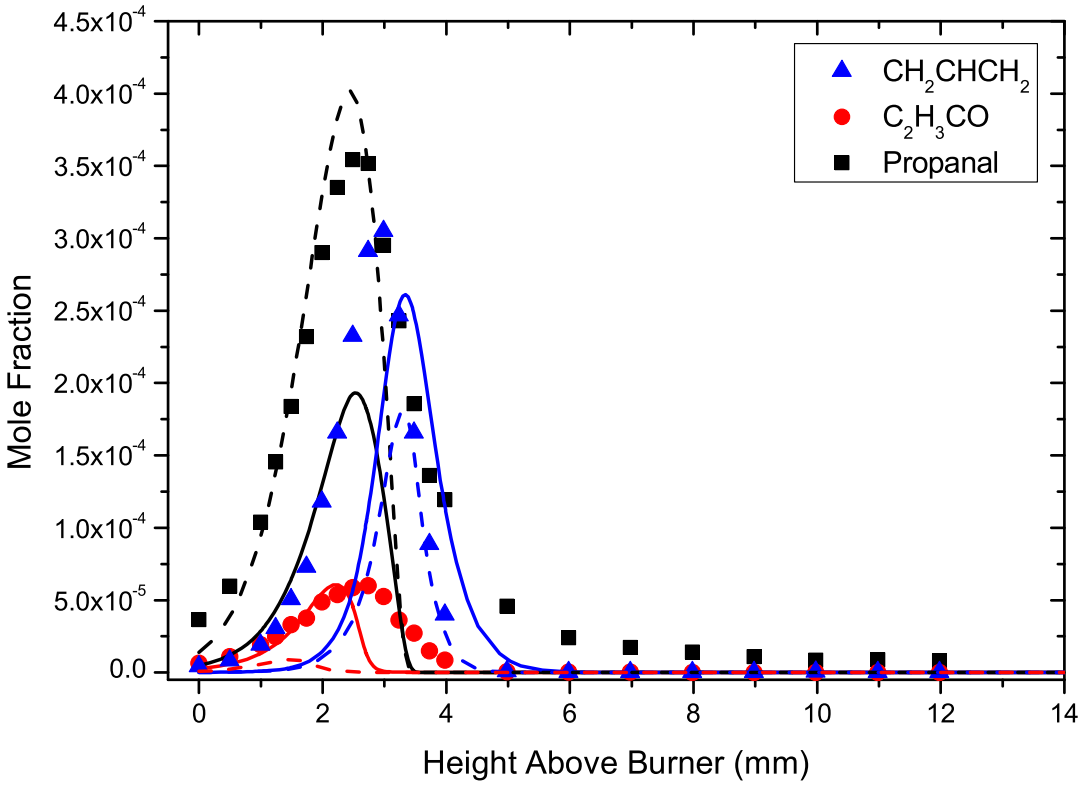

Figure 39: Experimental profiles [8] for allyl and acrolein radicals and propanal measured in ϕ = 1.0 2-methylfuran/O_2/Ar flame with model calculations from *this work* (—) and the study of Tran *et al.* [8] (– –).

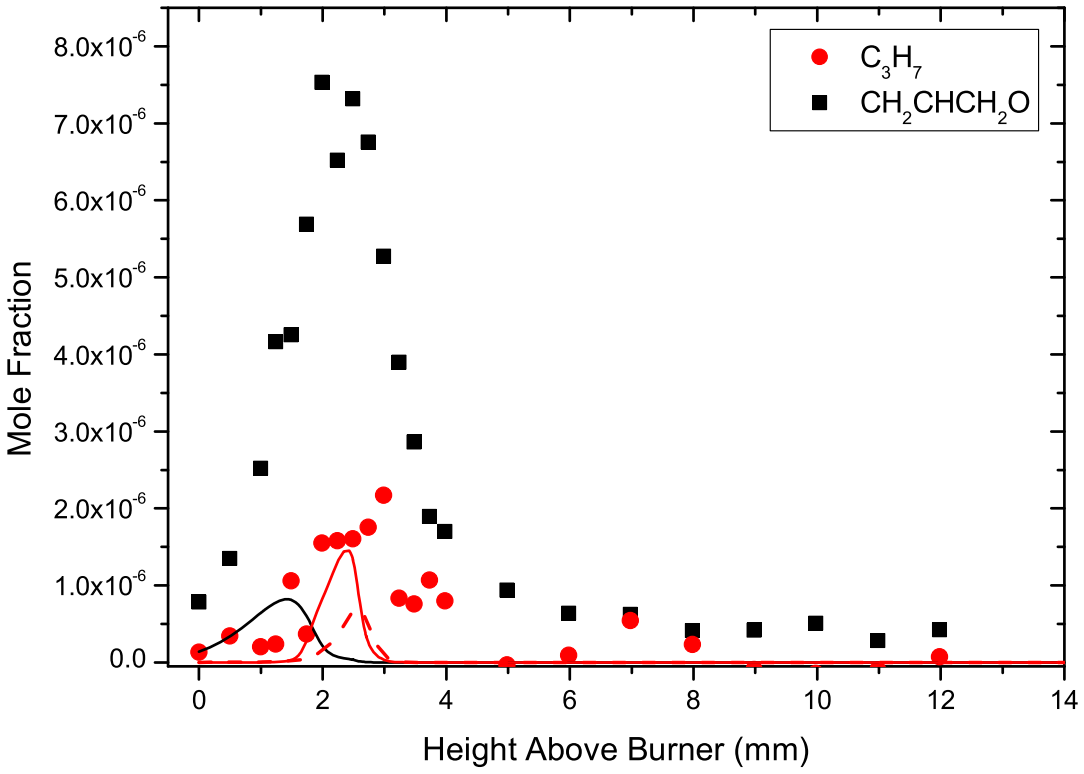

Figure 40: Experimental profiles [8] for *n*-propyl and allyloxy radicals measured in ϕ = 1.0 2-methylfuran/O_2/Ar flame with model calculations from *this work* (—) and the study of Tran *et al.* [8] (– –).

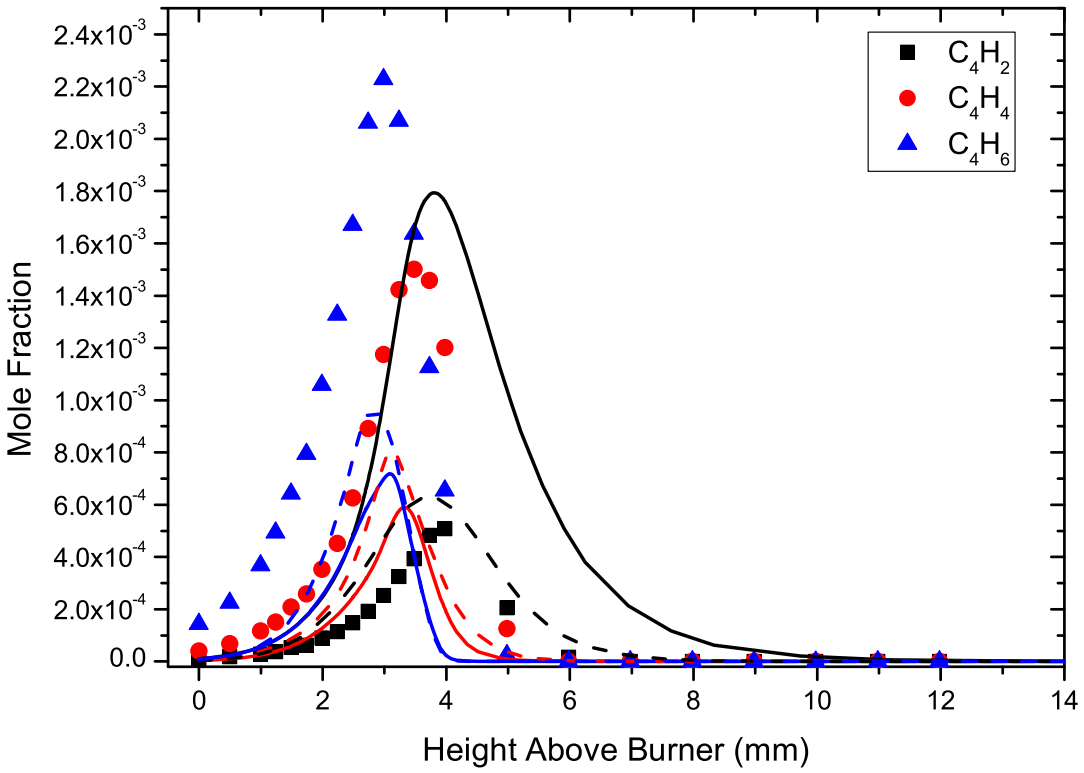

Figure 41: Experimental profiles [8] for diacetylene, vinylacetylene and 1,3-butadiene measured in ϕ = 1.0 2-methylfuran/O_2/Ar flame with model calculations from *this work* (—) and the study of Tran *et al.* [8] (– –).

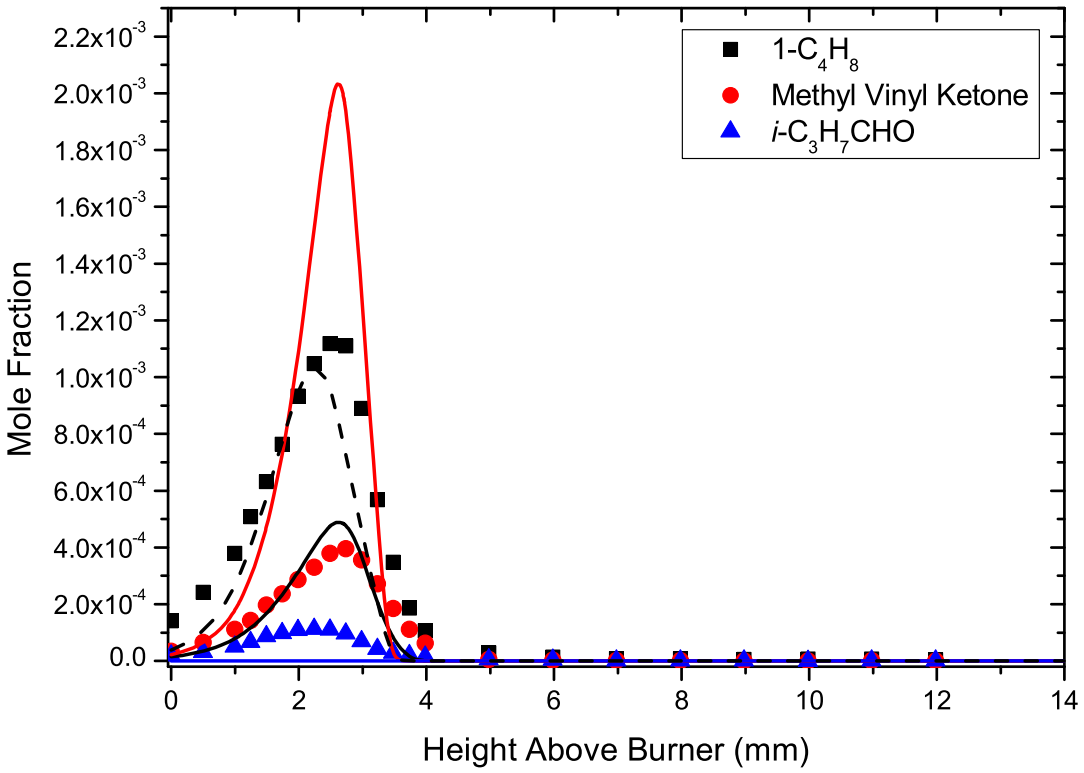

Figure 42: Experimental profiles [8] for 1-butene, methyl vinyl ketone and *butanal* measured in ϕ = 1.0 2-methylfuran/O_2/Ar flame with model calculations from *this work* (—) and the study of Tran *et al.* [8] (– –).

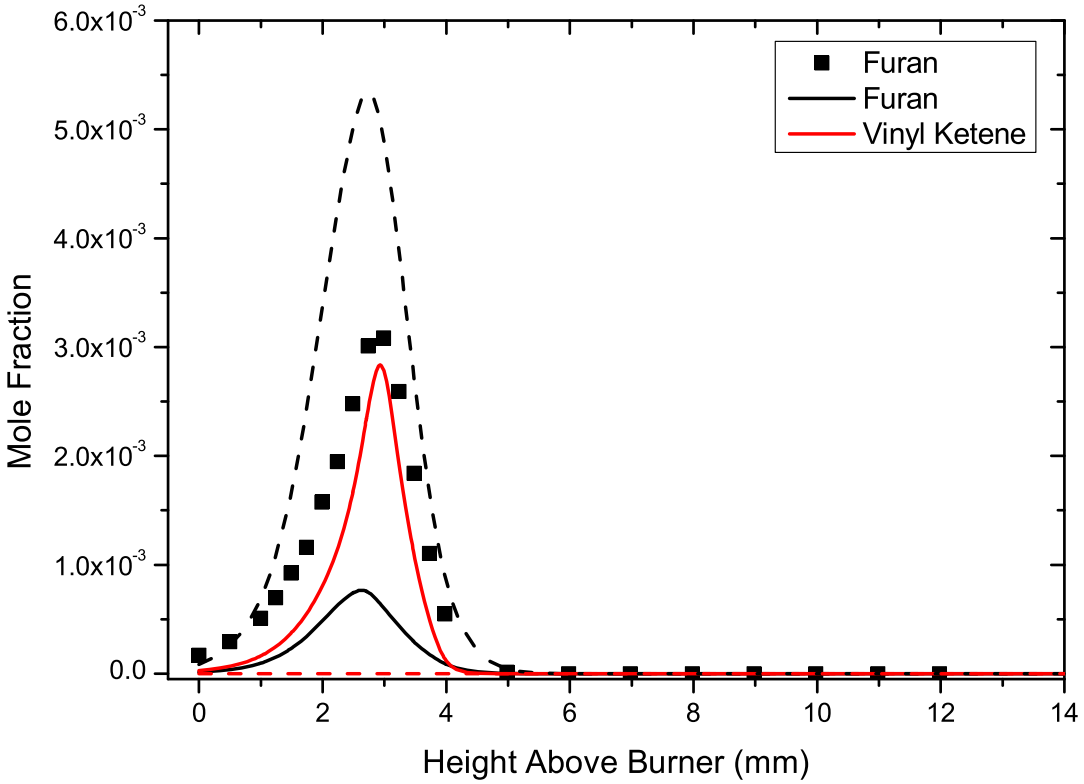

Figure 43: Experimental profiles [8] for furan measured in ϕ = 1.0 2-methylfuran/O_2/Ar flame with model calculations from *this work* (—) and the study of Tran *et al.* [8] (– –). Vinyl ketene yields, which were not quantified experimentally, are included for comparison.

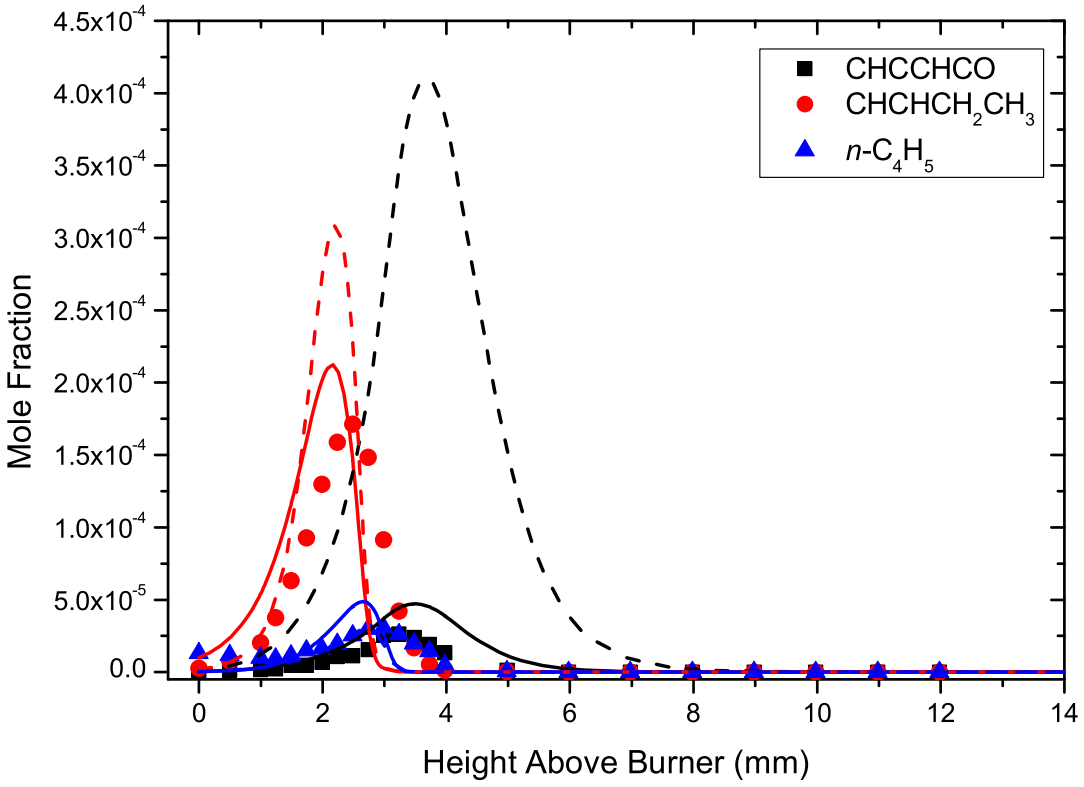

Figure 44: Experimental profiles [8] for acetylenylketene, *n*-butenyl and *n*-butadienyl measured in ϕ = 1.0 2-methylfuran/O_2/Ar flame with model calculations from *this work* (—) and the study of Tran *et al.* [8] (– –).

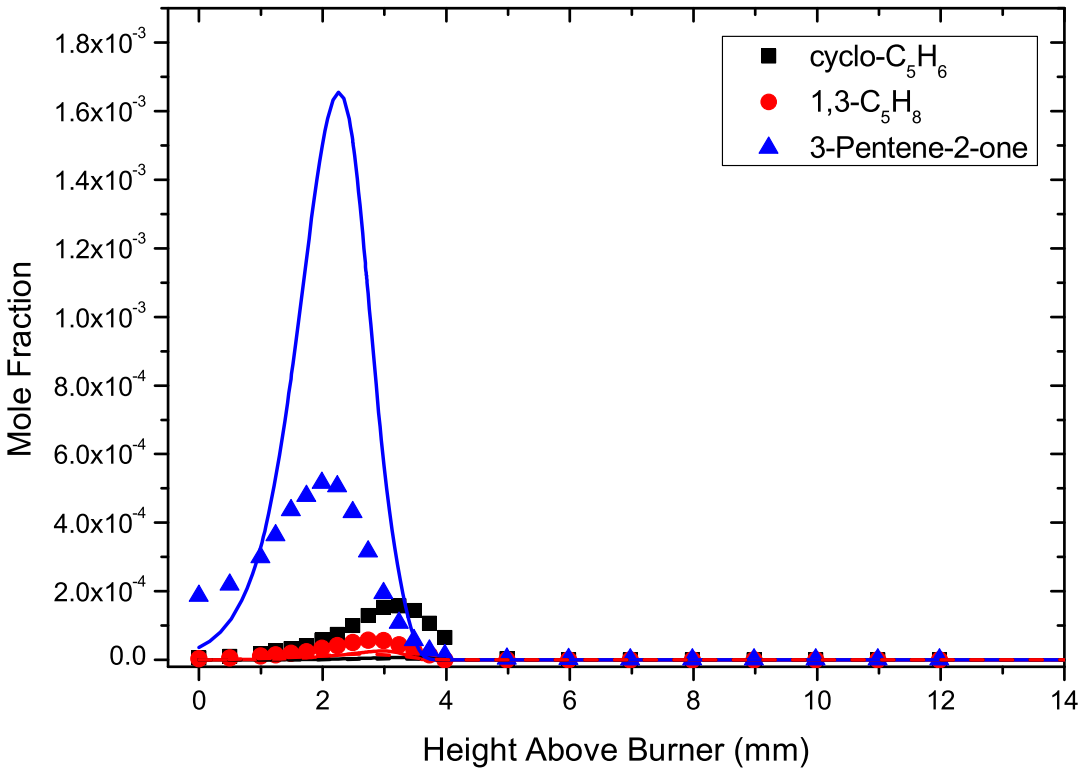

Figure 45: Experimental profiles [8] for 1,3-cyclopentadiene, 1,3-pentadiene and 3-pentene-2-one measured in ϕ = 1.0 2-methylfuran/O_2/Ar flame with model calculations from *this work* (—) and the study of Tran *et al.* [8] (– –).

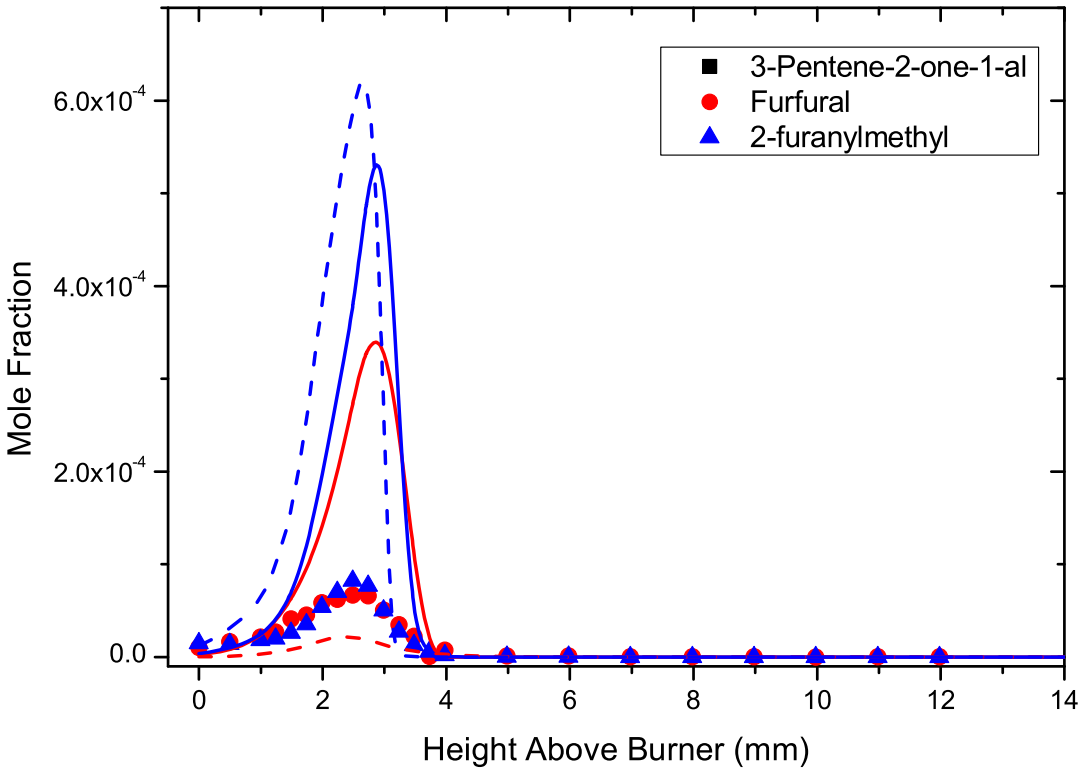

Figure 46: Experimental profiles [8] for 3-pentene-2-one-1-al, furfural and 2-furanylmethyl measured in ϕ = 1.0 2-methylfuran/O_2/Ar flame with model calculations from *this work* (—) and the study of Tran *et al.* [8] (– –).

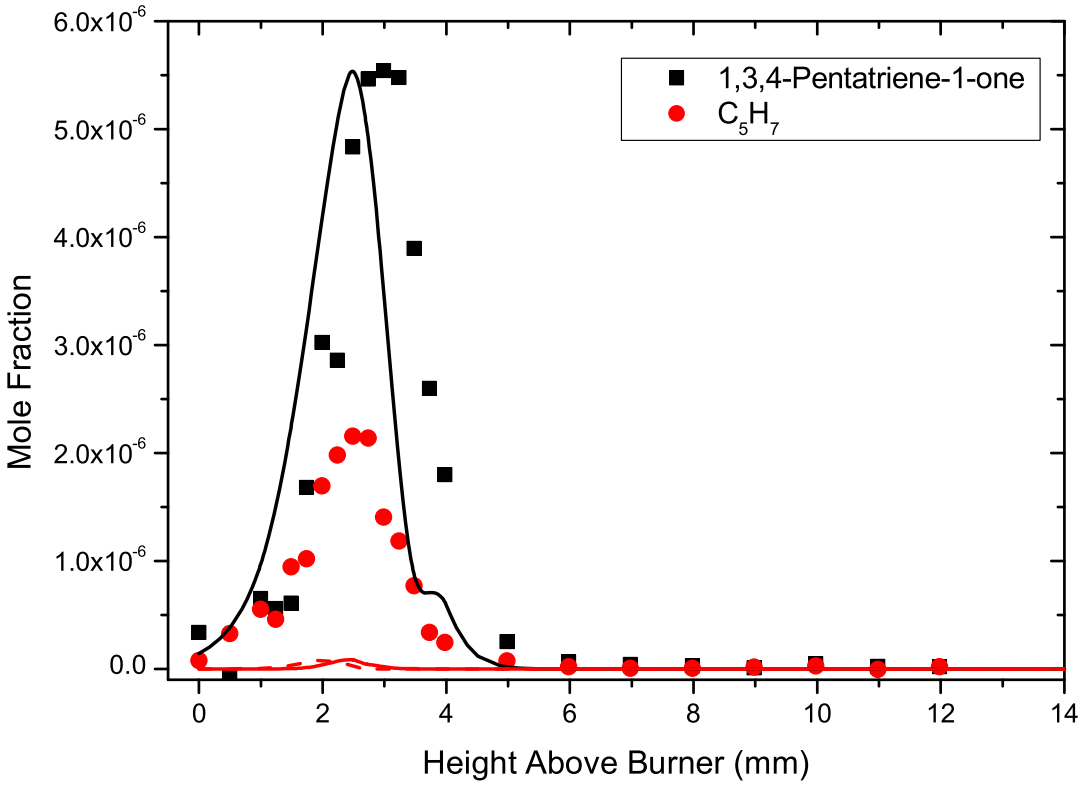

Figure 47: Experimental profiles [8] for 1,3,4-pentatriene-1-one and cyclopenteneyl radical measured in ϕ = 1.0 2-methylfuran/O_2/Ar flame with model calculations from *this work* (—) and the study of Tran *et al.* [8] (– –).

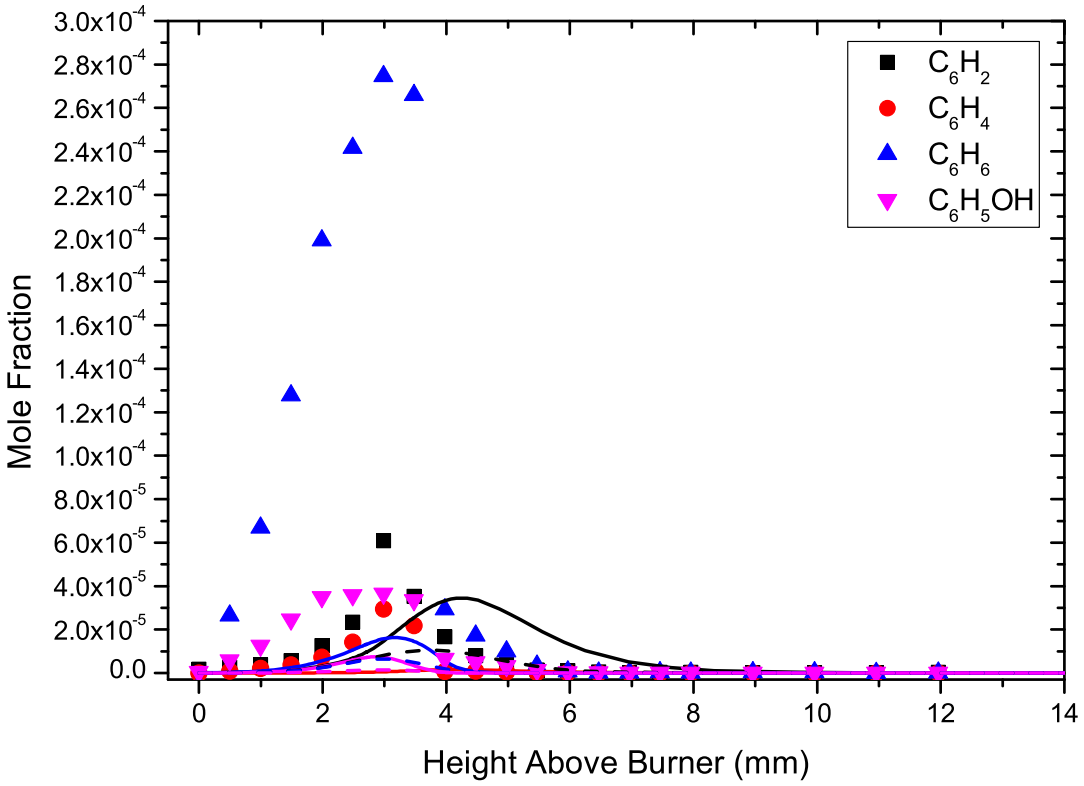

Figure 48: Experimental profiles [8] for triacetylene, benzyne, benzene and phenol measured in ϕ = 1.0 2-methylfuran/O_2/Ar flame with model calculations from *this work* (—) and the study of Tran *et al.* [8] (– –).

6.4.2 ϕ = 1.7

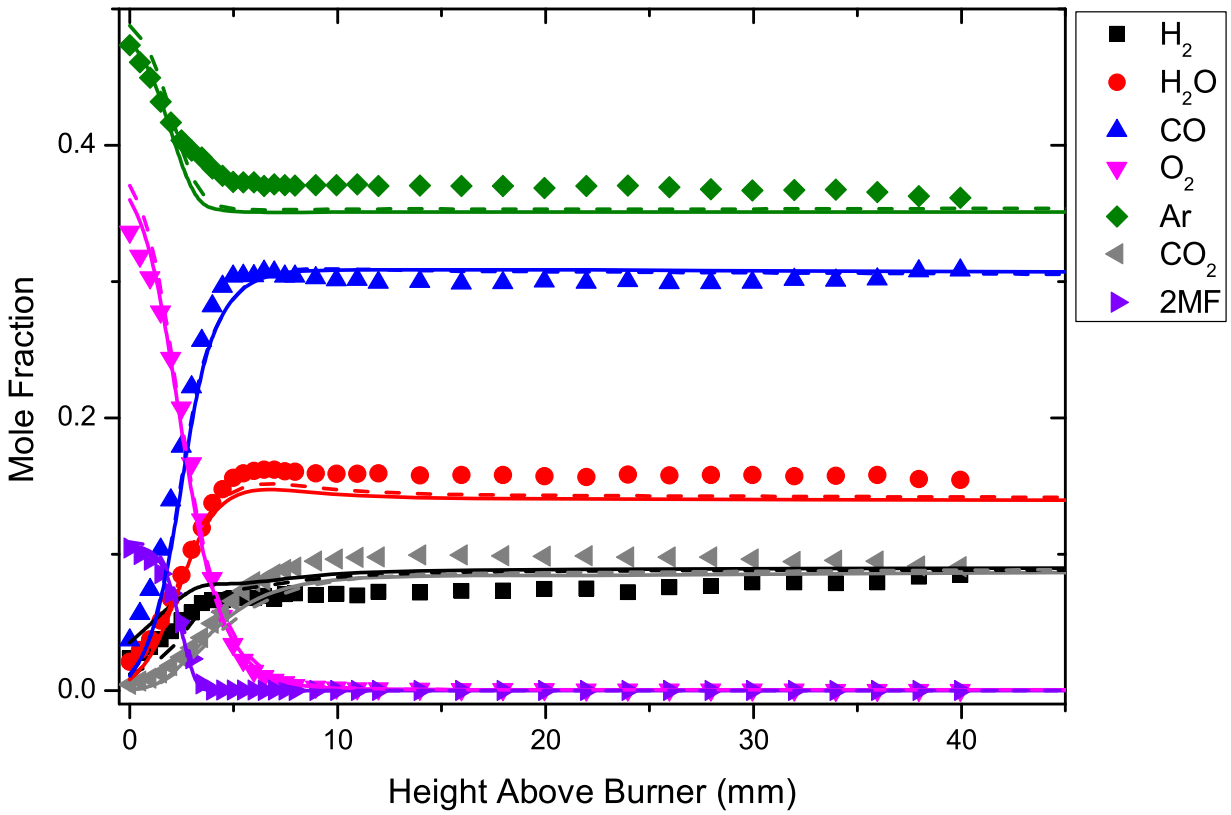

Figure 49: Experimental profiles [8] for main species measured in ϕ = 1.7 2-methylfuran/O_2/Ar flame with model calculations from *this work* (—) and the study of Tran *et al.* [8] (– –).

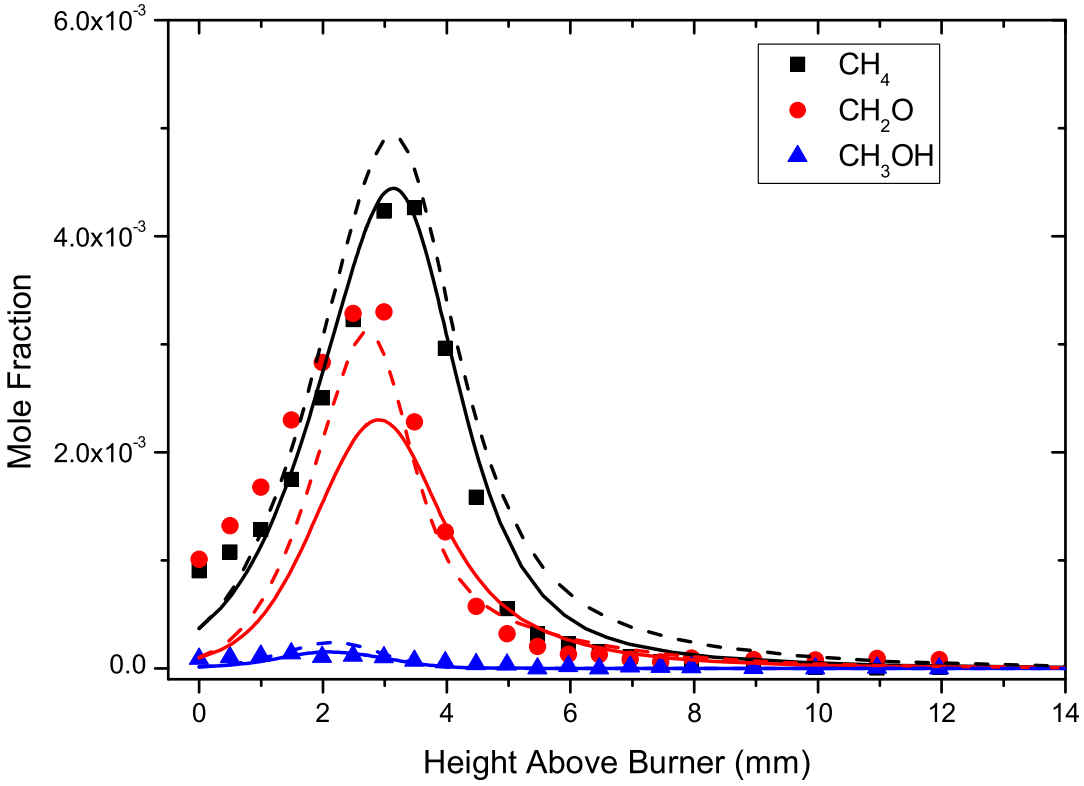

Figure 50: Experimental profiles [8] for methane, formaldehyde and methanol measured in ϕ = 1.7 2-methylfuran/O_2/Ar flame with model calculations from *this work* (—) and the study of Tran *et al.* [8] (– –).

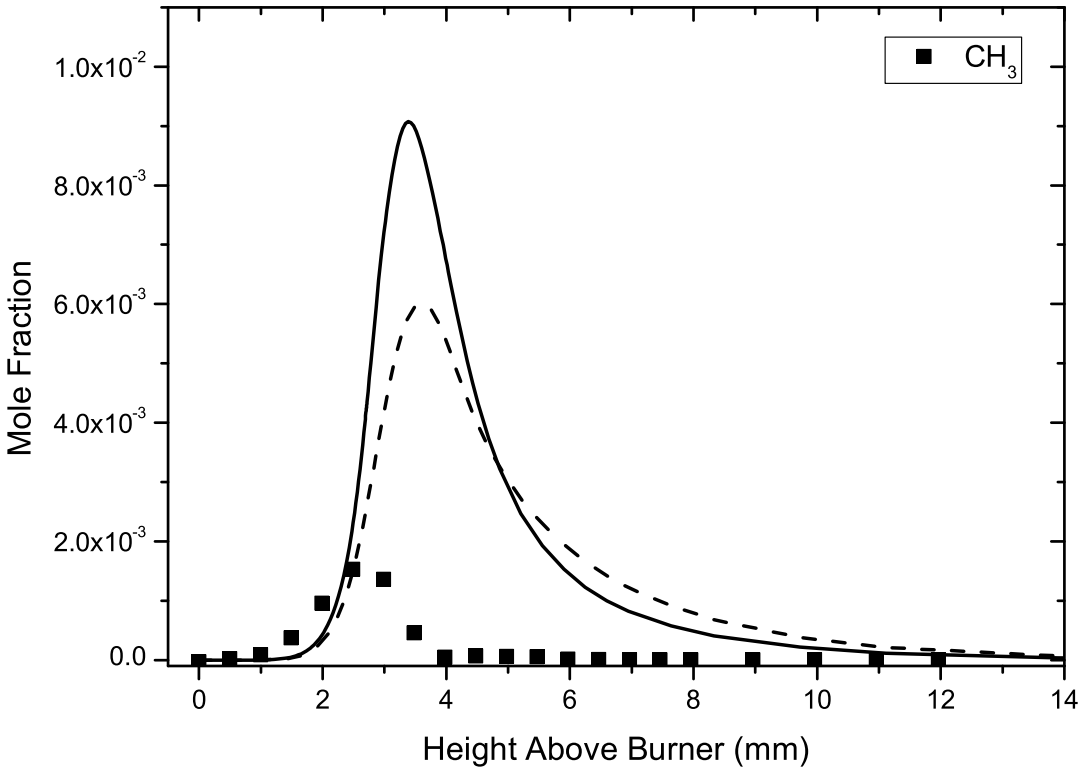

Figure 51: Experimental profile [8] for methyl radical measured in ϕ = 1.7 2-methylfuran/O_2/Ar flame with model calculations from *this work* (—) and the study of Tran *et al.* [8] (– –). Refer to [8] for a discussion on the uncertainties (up to a factor of 4) in the determination of concentrations of small radicals.

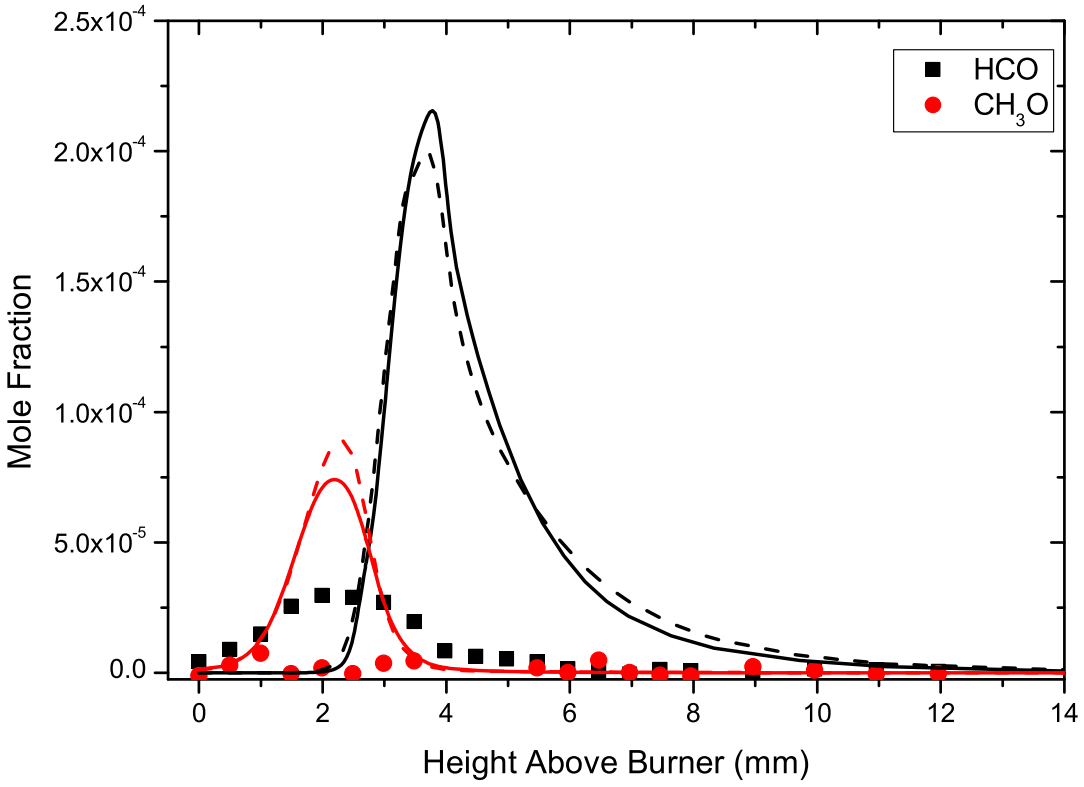

Figure 52: Experimental profiles [8] for formyl and methoxy radicals measured in ϕ = 1.7 2-methylfuran/O_2/Ar flame with model calculations from *this work* (—) and the study of Tran *et al.* [8] (– –).

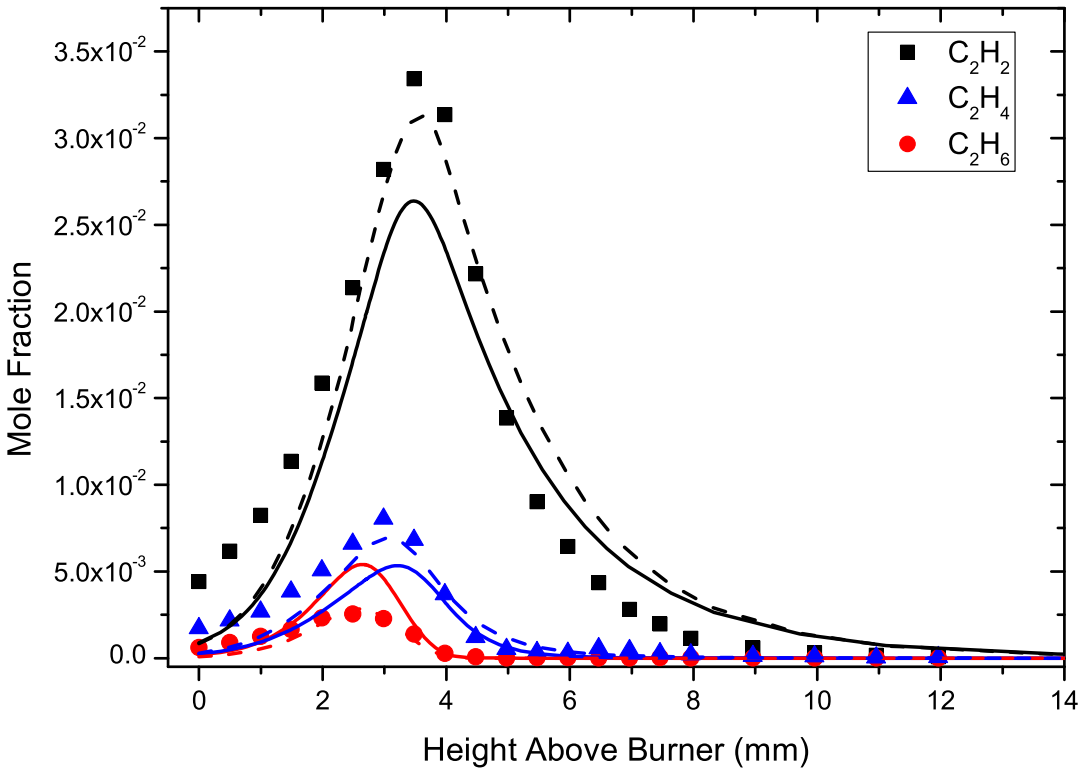

Figure 53: Experimental profiles [8] for acetylene, ethylene and ethane measured in ϕ = 1.7 2-methylfuran/O_2/Ar flame with model calculations from *this work* (—) and the study of Tran *et al.* [8] (– –).

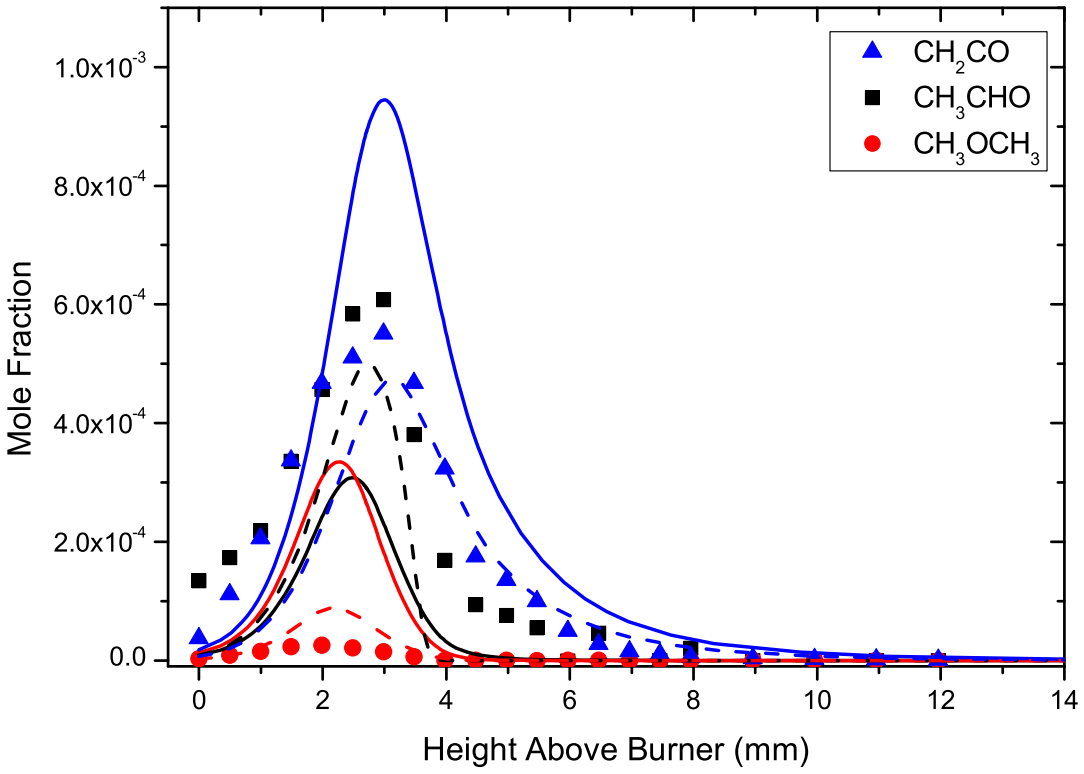

Figure 54: Experimental profiles [8] for ketene, acetaldehyde and dimethyl ether measured in ϕ = 1.7 2-methylfuran/O_2/Ar flame with model calculations from *this work* (—) and the study of Tran *et al.* [8] (– –).

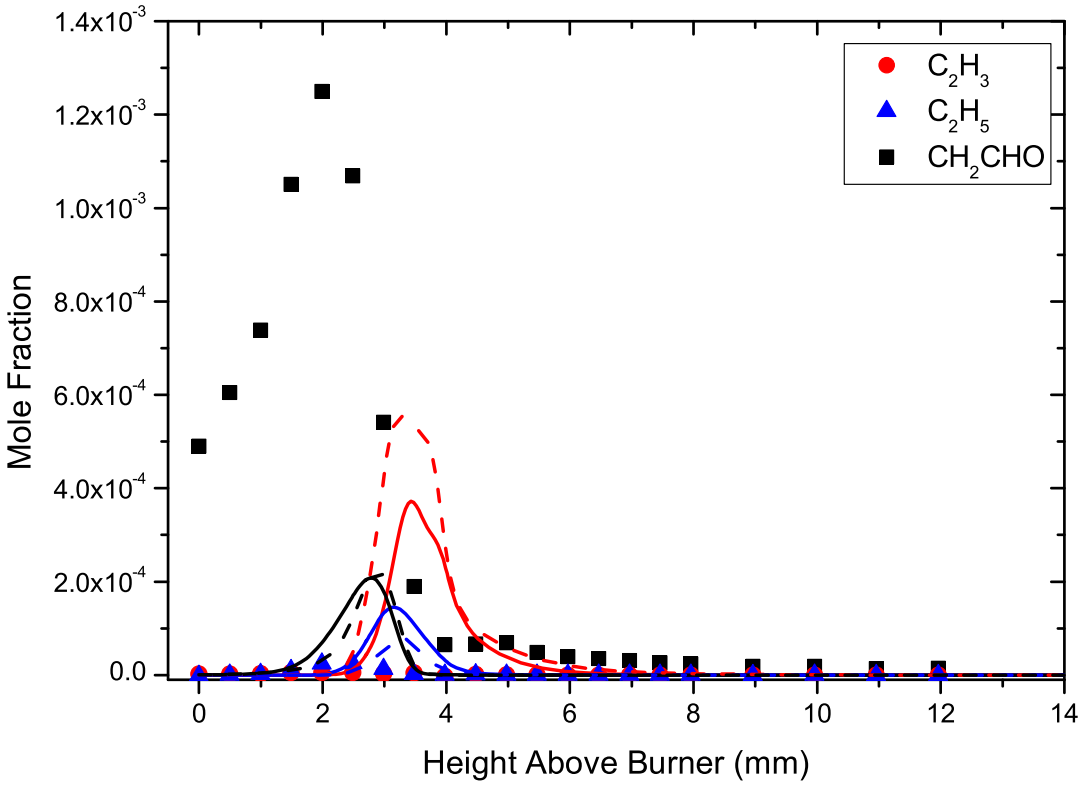

Figure 55: Experimental profiles [8] for vinyl, ethyl and vinoxy radicals measured in ϕ = 1.7 2-methylfuran/O_2/Ar flame with model calculations from *this work* (—) and the study of Tran *et al.* [8] (– –).

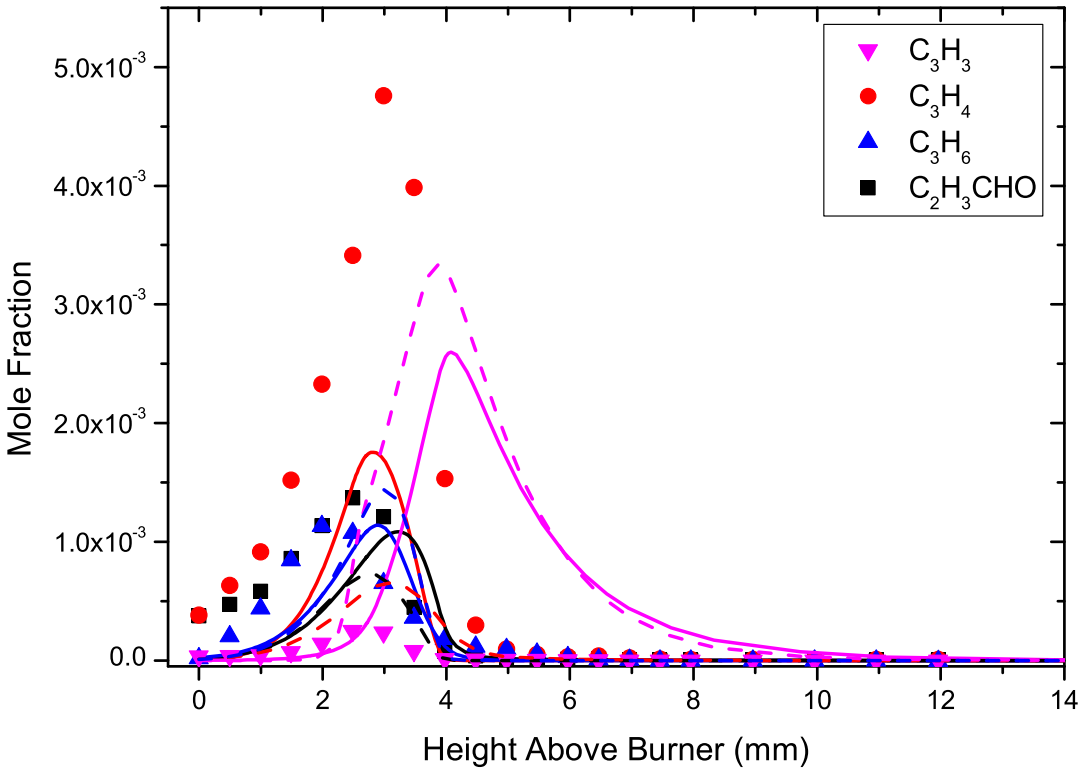

Figure 56: Experimental profiles [8] for propargyl radical, propyne, propene and acrolein measured in ϕ = 1.7 2-methylfuran/O_2/Ar flame with model calculations from *this work* (—) and the study of Tran *et al.* [8] (– –).

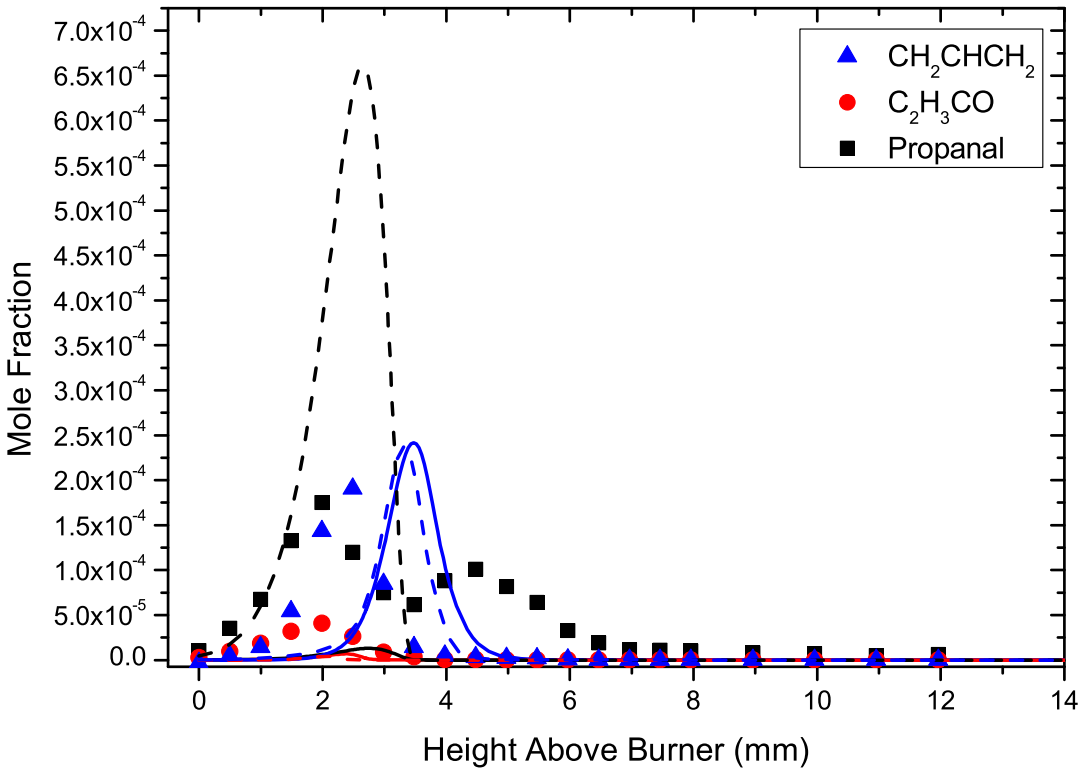

Figure 57: Experimental profiles [8] for allyl and acrolein radicals and propanal measured in ϕ = 1.7 2-methylfuran/O_2/Ar flame with model calculations from *this work* (—) and the study of Tran *et al.* [8] (– –).

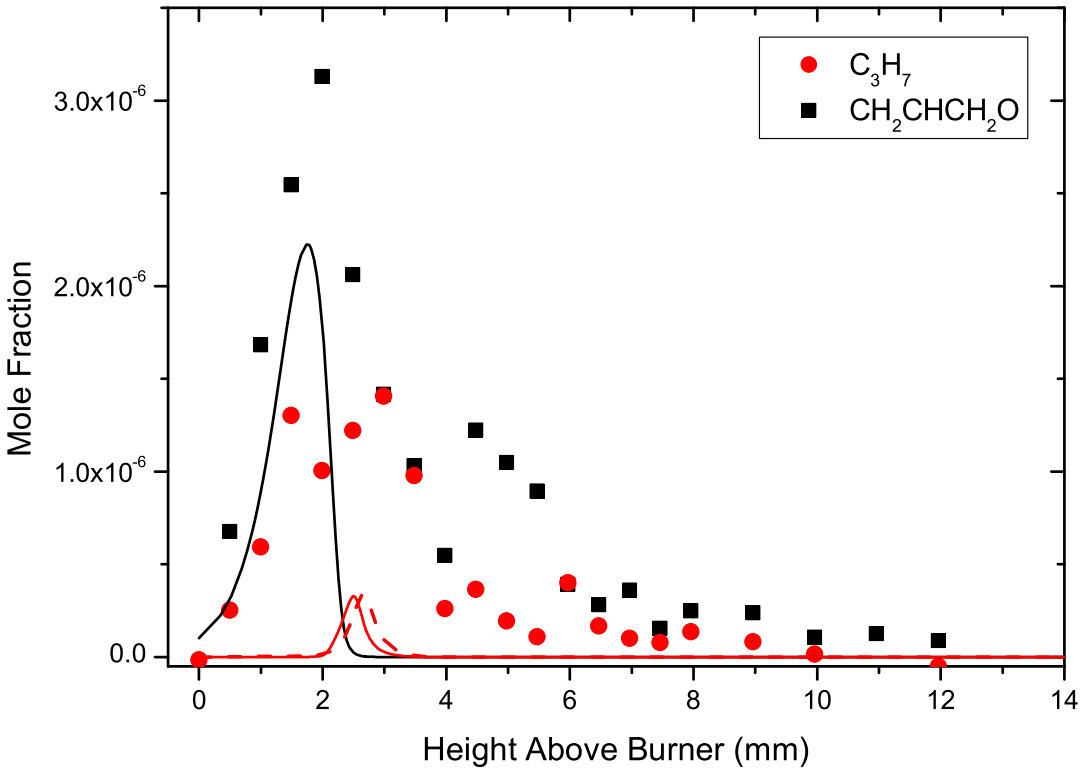

Figure 58: Experimental profiles [8] for *n*-propyl and allyloxy radicals measured in ϕ = 1.7 2-methylfuran/O_2/Ar flame with model calculations from *this work* (—) and the study of Tran *et al.* [8] (– –).

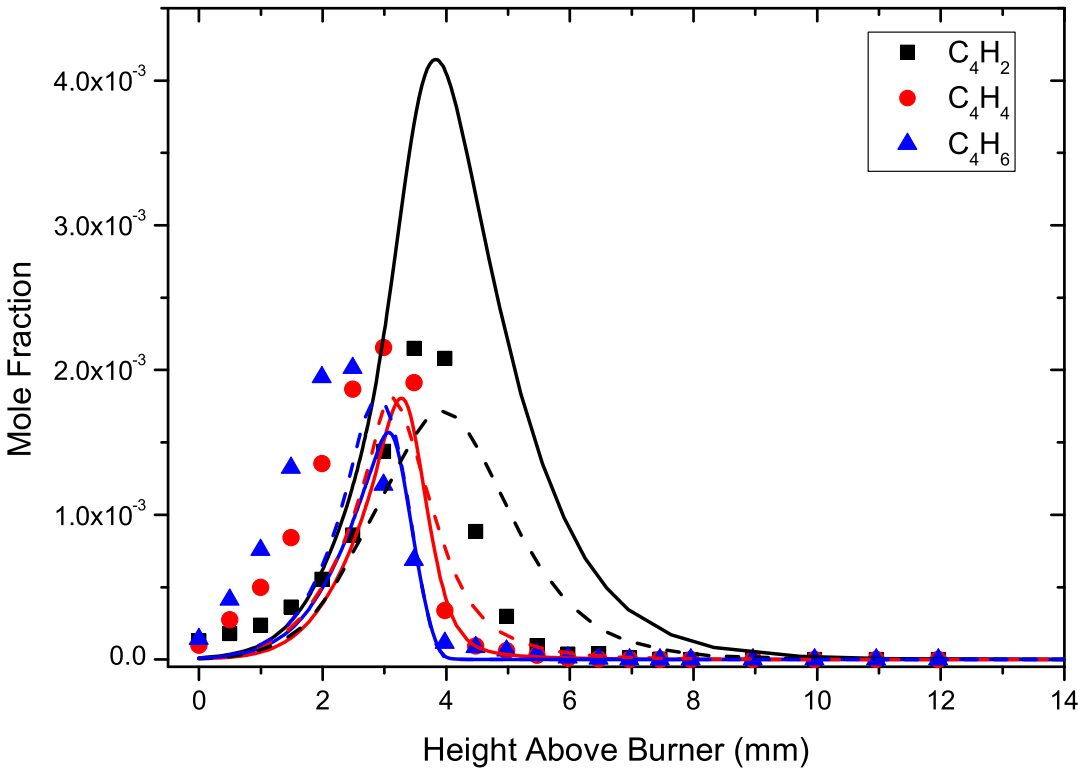

Figure 59: Experimental profiles [8] for diacetylene, vinylacetylene and 1,3-butadiene measured in ϕ = 1.7 2-methylfuran/O_2/Ar flame with model calculations from *this work* (—) and the study of Tran *et al.* [8] (– –).

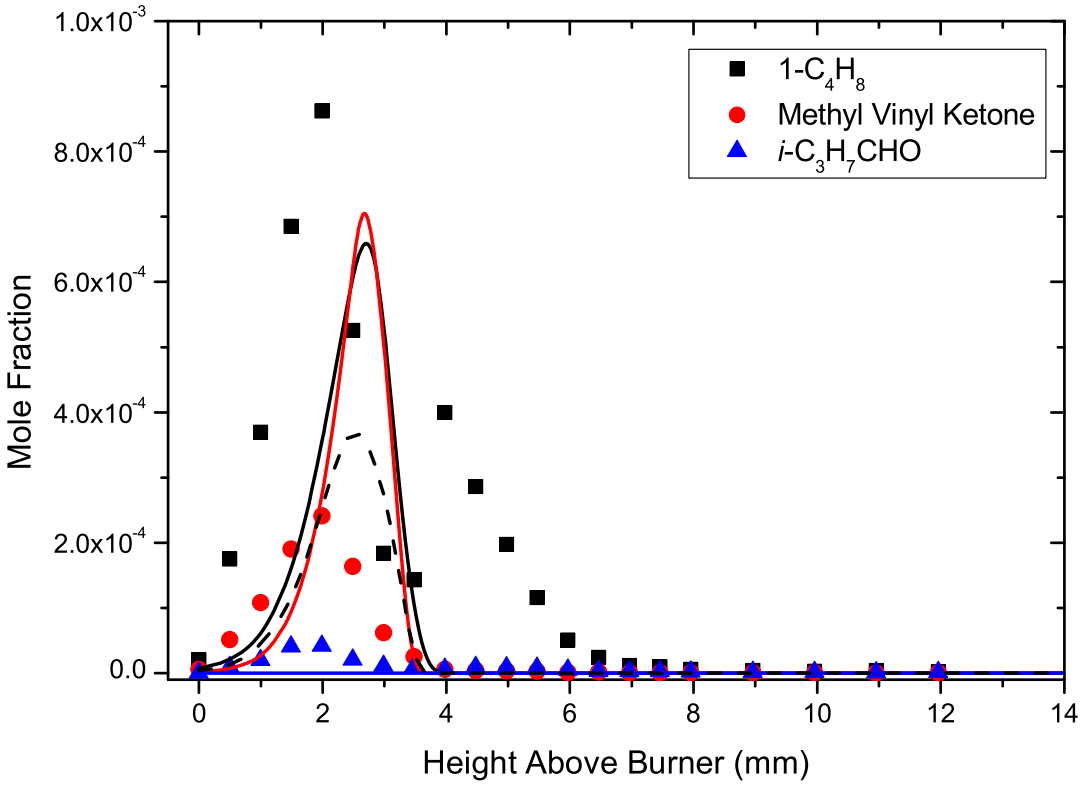

Figure 60: Experimental profiles [8] for 1-butene, methyl vinyl ketone and *i*-butanal measured in ϕ = 1.7 2-methylfuran/O_2/Ar flame with model calculations from *this work* (—) and the study of Tran *et al.* [8] (– –).

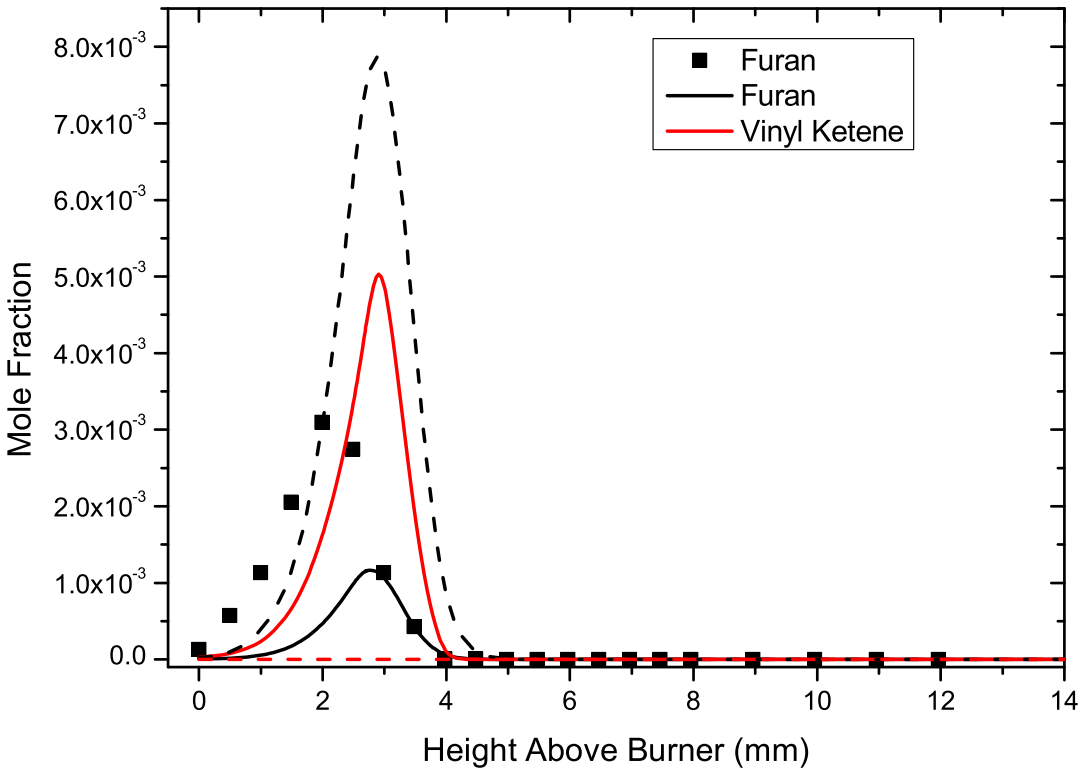

Figure 61: Experimental profile [8] for furan measured in ϕ = 1.7 2-methylfuran/O_2/Ar flame with model calculations from *this work* (—) and the study of Tran *et al.* [8] (– –). Vinyl ketene yields, which were not quantified experimentally, are included for comparison.

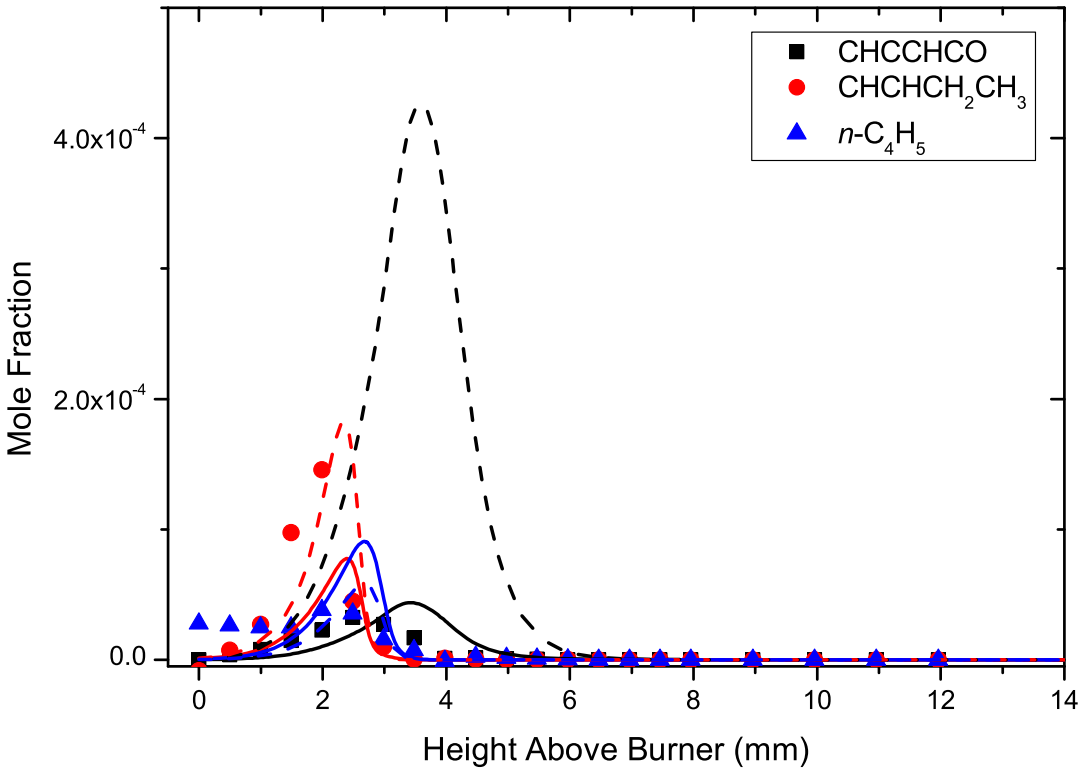

Figure 62: Experimental profiles [8] for acetylenylketene, *n*-butenyl and *n*-butadienyl measured in ϕ = 1.7 2-methylfuran/O_2/Ar flame with model calculations from *this work* (—) and the study of Tran *et al.* [8] (– –).

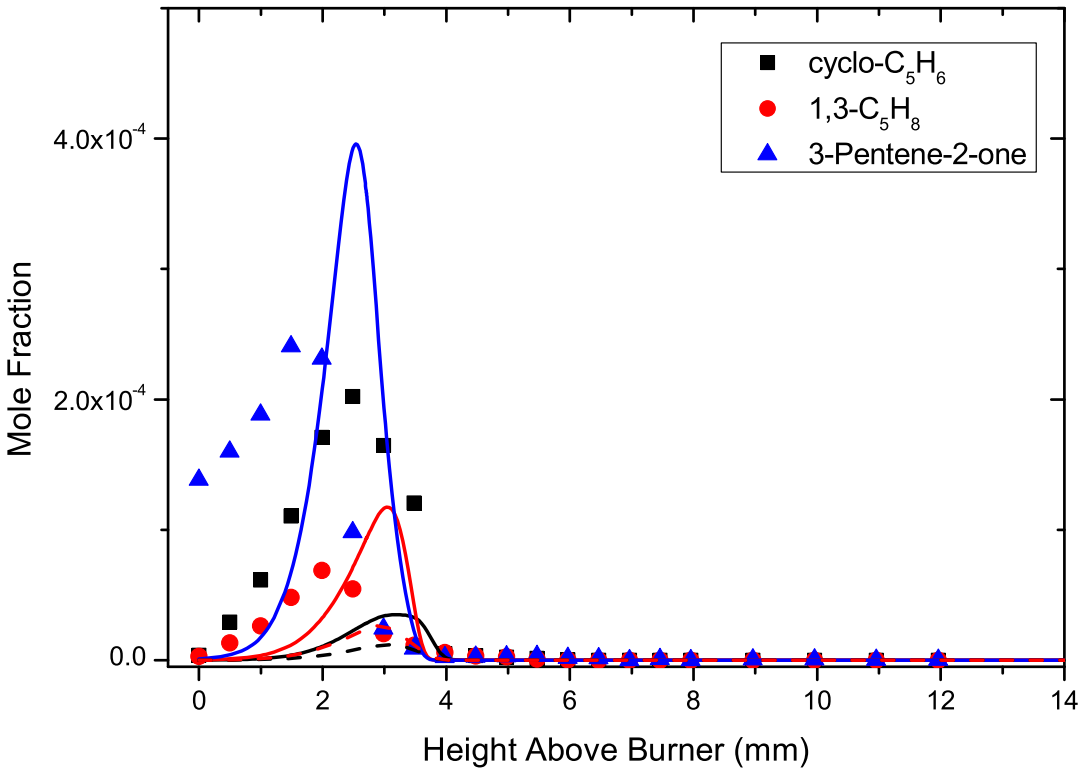

Figure 63: Experimental profiles [8] for 1,3-cyclopentadiene, 1,3-pentadiene and 3-pentene-2-one measured in ϕ = 1.7 2-methylfuran/O_2/Ar flame with model calculations from *this work* (—) and the study of Tran *et al.* [8] (– –).

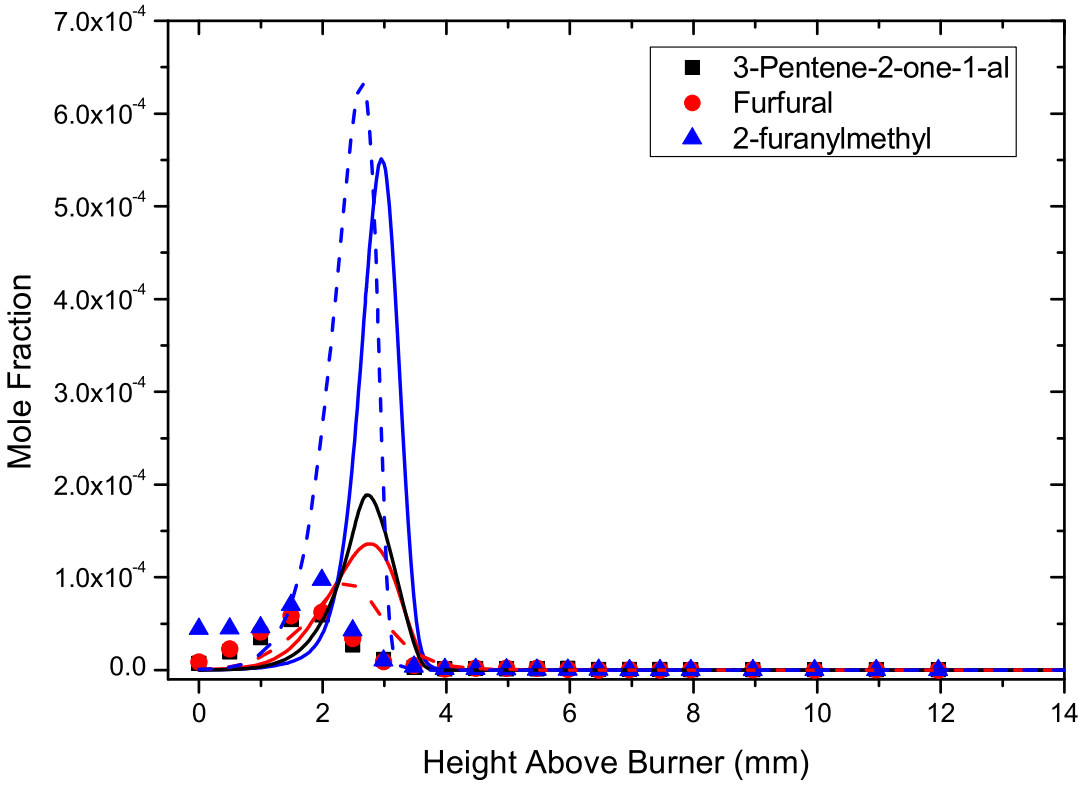

Figure 64: Experimental profiles [8] for 3-pentene-2-one-1-al, furfural and 2-furanylmethyl measured in ϕ = 1.7 2-methylfuran/O_2/Ar flame with model calculations from *this work* (—) and the study of Tran *et al.* [8] (– –).

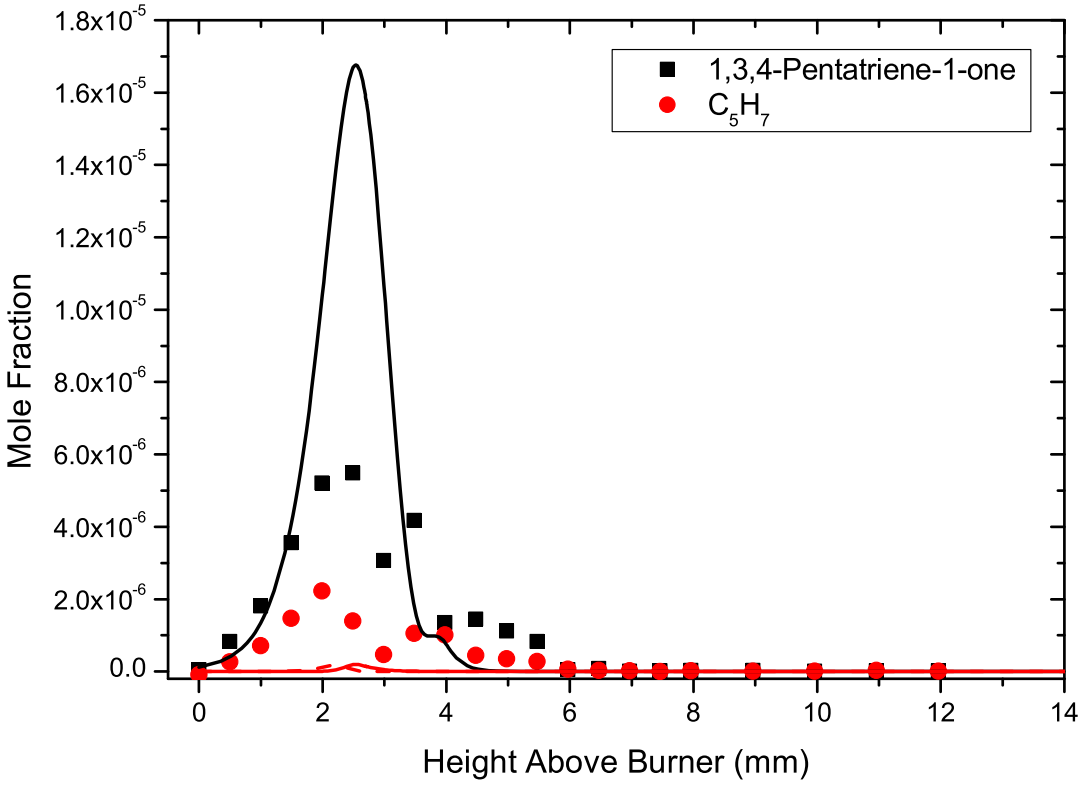

Figure 65: Experimental profiles [8] for 1,3,4-pentatriene-1-one and cyclopenteneyl radical measured in ϕ = 1.7 2-methylfuran/O_2/Ar flame with model calculations from *this work* (—) and the study of Tran *et al.* [8] (– –).

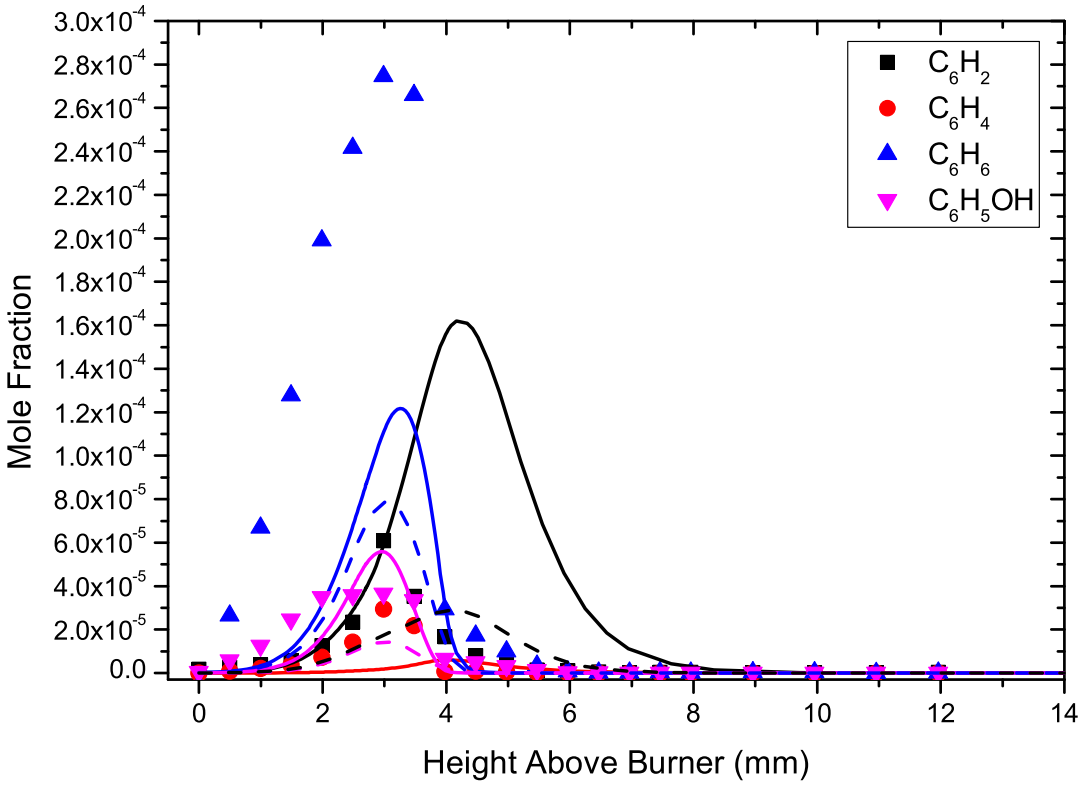

Figure 66: Experimental profiles [8] for triacetylene, benzyne, benzene and phenol measured in ϕ = 1.7 2-methylfuran/O_2/Ar flame with model calculations from *this work* (—) and the study of Tran *et al.* [8] (– –).

7 Electronic Energies of Stationary Points

Table 7: Electronic energies of potential energy surface minima (hartrees) at 0 and 298.15 K, at the CBS-QB3, G3 and CBS-APNO levels of theory.

	0 K			298 K		
SPECIES KEY	CBS-QB3	CBS-APNO	G3	CBS-QB3	CBS-APNO	G3
M1	-268.878010	-269.239467	-269.140183	-268.871675	-269.233241	-269.133826
M2	-268.780525	-269.141719	-269.043882	-268.774038	-269.135313	-269.037350
M3	-268.790419	-269.151663	-269.053756	-268.783748	-269.145113	-269.047076
M4		-269.140879	-269.043143		-269.134552	-269.036692
M5	-268.828555	-269.189009	-269.092552	-268.820712	-269.181216	-269.084637
M6	-268.833058	-269.193615	-269.097062	-268.825259	-269.185891	-269.089199
M7	-268.787268	-269.148816	-269.050872	-268.780430	-269.142226	-269.044166
M8	-268.837026	-269.197901	-269.101105	-268.829150	-269.190105	-269.093191
M9	-268.840399	-269.201196	-269.104571	-268.832544	-269.193440	-269.096683
M10	-268.242558	-268.603230	-268.502648	-268.236633	-268.597206	-268.496472
M11	-268.196518	-268.556205	-268.457185	-268.189076	-268.548544	-268.449384
M12	-268.198158	-268.557780	-268.458999	-268.190710	-268.550103	-268.451174
M13	-268.219529	-268.580434	-268.482047	-268.212108	-268.572919	-268.474365
M14	-268.208236			-268.200944		
M15	-268.218942	-268.580115	-268.481620	-268.211640	-268.572689	-268.474032
M16	-268.252517	-268.613698	-268.513834	-268.246553	-268.607680	-268.507688
INT1	-267.571448	-267.932155	-267.834361	-267.565545	-267.926013	-267.828070
M17	-269.426024	-269.788171	-269.689663	-269.419313	-269.781369	-269.682704
M18	-269.419453	-269.780791	-269.683088	-269.411631	-269.772651	-269.674835
M19	-269.422043	-269.783263	-269.685168	-269.414092	-269.775271	-269.677043
M20	-269.413783	-269.776428		-269.405853	-269.768529	
M21	-269.427416	-269.788712	-269.691038	-269.419638	-269.780759	-269.682943
M22	-269.426484	-269.787669	-269.689808	-269.418482	-269.779554	-269.681562
M23	-269.428124	-269.790975	-269.691527	-269.420239	-269.782884	-269.683333
M24	-269.415684	-269.777058	-269.680532	-269.407798	-269.769087	-269.672401
M25	-269.415089	-269.776869	-269.680052	-269.407249	-269.768921	-269.671971
M26	-269.413862	-269.775588	-269.676084	-269.406485	-269.767901	-269.668250
M27	-269.425835	-269.787791	-269.689875	-269.419137	-269.780990	-269.682923
M28	-269.408650	-269.770785	-269.671905	-269.401728	-269.763978	-269.664959
M29	-269.381422	-269.742612	-269.646344	-269.372996	-269.734233	-269.637806
M30	-269.383034	-269.744449	-269.648290	-269.374692	-269.736172	-269.639862
M31	-269.382326	-269.743711	-269.647581	-269.373964	-269.735414	-269.639119
M32	-269.407525	-269.769347	-269.671789	-269.399593	-269.761489	-269.663765
M33	-269.407433	-269.769275		-269.399482	-269.761382	
M34	-269.428082	-269.790832	-269.692642	-269.421092	-269.783930	-269.685582
M35	-269.407639	-269.770444	-269.672986	-269.399634	-269.762501	-269.664909
M36	-269.410042	-269.772122	-269.673673	-269.403112	-269.765325	-269.666743
M37	-269.379642	-269.740604	-269.644070	-269.371172	-269.732068	-269.635386
M38	-269.380945	-269.742131	-269.645575	-269.372547	-269.733722	-269.637029
M39	-269.382060	-269.743034	-269.646592	-269.373606	-269.734593	-269.638004
M40	-269.412609	-269.775079	-269.677128	-269.404353	-269.766854	-269.668761
M41	-269.428563	-269.790408	-269.691568	-269.421611	-269.783345	-269.684359
M42	-269.431395	-269.792770	-269.695758	-269.423471	-269.784789	-269.687634
M43	-269.428054	-269.789416	-269.692063	-269.420328	-269.781622	-269.684128
M44	-269.410349	-269.771902	-269.672273	-269.402454	-269.763992	-269.664221
M45	-269.412705	-269.774042	-269.674618	-269.404677	-269.765995	-269.666431
M46	-269.371297	-269.733934	-269.635435	-269.363147	-269.725758	-269.627143
M47	-269.409124	-269.772176		-269.400918	-269.763967	
M48	-269.410381	-269.772863		-269.402134	-269.764632	

Table 8: Electronic energies of transition states (hartrees) at 0 and 298.15 K, at the CBS-QB3, G3 and CBS-APNO levels of theory.

	0 K			298 K		
SPECIES KEY	CBS-QB3	CBS-APNO	G3	CBS-QB3	CBS-APNO	G3
TS1	-268.746128	-269.107874	-269.008275	-268.740121	-269.101944	-269.002235
TS2	-268.773442	-269.136209	-269.036282	-268.767167	-269.130023	-269.029972
TS3	-268.736922	-269.097899	-268.999123	-268.729195	-269.090488	-268.991566
TS4	-268.742039	-269.103398	-269.004371	-268.734061	-269.095741	-268.996592
TS5	-268.765437	-269.127648	-269.028449	-268.759340	-269.121616	-269.022294
TS6		-269.141949	-269.044112		-269.135611	-269.037656
TS7	-268.820518	-269.180773	-269.084361	-268.813204	-269.173574	-269.077045
TS8	-268.763132	-269.124961		-268.755571	-269.117871	
TS9	-268.733495		-268.999152	-268.725922		-268.990439
TS10	-268.767849	-269.130172	-269.030746	-268.761602	-269.124020	-269.024476
TS11	-268.785869	-269.148513	-269.050644	-268.779309	-269.142682	-269.043801
TS12	-268.830516	-269.190787	-269.094588	-268.823329	-269.183716	-269.087389
TS13	-268.730957	-269.095001	-268.995346	-268.723270	-269.087148	-268.987478
TS14	-268.178692			-268.172433		
TS15	-268.112920	-268.473401		-268.104830	-268.465089	
TS16	-268.182698	-268.542470	-268.445277	-268.175565	-268.535099	-268.437750
TS17	-268.159951	-268.521173	-268.420075	-268.153223	-268.514191	-268.412942
TS18	-268.206930			-268.199944		
TS19	-268.170360			-268.161919		
TS20	-268.202003	-268.563008	-268.466357	-268.194987	-268.555959	-268.459123
TS21	-268.200554	-268.559642		-268.194340	-268.553295	
TS22	-268.164829	-268.522351	-268.424624	-268.157818	-268.515558	-268.417652
TS23a	-267.546464	-267.907822	-267.807266	-267.540672	-267.902207	-267.801553
TS23b	-267.562621	-267.925368	-267.826986	-267.556788	-267.919413	-267.820903
TS24	-269.373163	-269.734491	-269.637586	-269.366305	-269.727653	-269.630582
TS25	-269.376918	-269.742674	-269.639333	-269.369585	-269.735143	-269.631822
TS26	-269.387892		-269.653768	-269.381358		-269.647004
TS27	-269.410890			-269.403242		
TS28	-269.374059	-269.738351		-269.366838	-269.730931	
TS29	-269.374986			-269.365906		
TS30	-269.391722		-269.656570	-269.384961		-269.649555
TS31	-269.413417	-269.774823	-269.678314	-269.405852	-269.767189	-269.670551
TS32	-269.375835	-269.738354		-269.368472	-269.730935	
TS33	-269.407053			-269.399739		
TS34	-269.363161		-269.626267	-269.355898		-269.618977
TS35	-269.412277	-269.773763	-269.676817	-269.405105	-269.766518	-269.669444
TS36	-269.364913			-269.356503		
TS37	-269.387089			-269.380657		
TS38	-269.354847	-269.716069		-269.347955	-269.708892	
TS39	-269.367642	-269.732494	-269.634278	-269.360573	-269.725327	-269.626942
TS40	-269.371151	-269.732199	-269.634047	-269.364094	-269.725194	-269.626882
TS41	-269.354972	-269.717347	-269.617813	-269.347845	-269.710280	-269.610590
TS42	-269.380722	-269.741929	-269.645722	-269.373264	-269.734504	-269.638155
TS43	-269.377260	-269.739114	-269.643047	-269.369064	-269.730871	-269.634623
TS44	-269.343865	-269.705182	-269.607780	-269.334910	-269.696102	-269.598493
TS45	-269.367034	-269.730287	-269.631275	-269.360109	-269.723315	-269.624150
TS46	-269.404123	-269.765792		-269.396928	-269.758647	
TS47	-269.353030	-269.717239		-269.343925	-269.707691	
TS48	-269.378690	-269.741084	-269.642710	-269.371989	-269.734258	-269.635746
TS49	-269.373026	-269.73388	-269.63722	-269.36597	-269.727	-269.6302

Table 8: Electronic energies of transition states (hartrees) at 0 and 298.15 K, at the CBS-QB3, G3 and CBS-APNO levels of theory.

	0 K			298 K		
SPECIES KEY	CBS-QB3	CBS-APNO	G3	CBS-QB3	CBS-APNO	G3
TS50	-269.37811	-269.73877	-269.64237	-269.37108	-269.73188	-269.63536
TS51	-269.385097	-269.74764	-269.64883	-269.37827	-269.74076	-269.64181
TS52	-269.384934	-269.747059	-269.649809	-269.376235	-269.738711	-269.641320
TS53	-269.370262	-269.73152	-269.63352	-269.36327	-269.72456	-269.6264
TS54	-269.354953	-269.71717	-269.61723	-269.34776	-269.70998	-269.60989
TS55	-269.379522	-269.74044	-269.64393	-269.37186	-269.73275	-269.6361
TS56	-269.345266	-269.70628	-269.60805	-269.33647	-269.69728	-269.59888
TS57	-269.378011	-269.7389	-269.64236	-269.37019	-269.73111	-269.63445
TS58	-269.365541	-269.72791	-269.62847	-269.35782	-269.72024	-269.62065
TS59	-269.400480	-269.762863	-269.664487	-269.392072	-269.754421	-269.655913
TS60	-269.37516	-269.73576	-269.63883	-269.36789	-269.72868	-269.63158
TS61	-269.393982			-269.38721		
TS62	-269.35303	-269.71724		-269.34393	-269.70769	
TS63	-269.421257	-269.78309	-269.68674	-269.41391	-269.77571	-269.67921
TS64	-269.380615			-269.3735		
TS65	-269.407735			-269.40046		
TS66	-269.338546	-269.70256	-269.60613	-269.32958	-269.694	-269.59737
TS67	-269.369328	-269.73206	-269.63502	-269.36156	-269.72418	-269.62701
TS68	-269.366156	-269.72932	-269.63061	-269.3586	-269.72164	-269.62278
TS69	-269.408708			-269.4012		
TS70	-269.399381	-269.76199	-269.66354	-269.39098	-269.75359	-269.65499

Table 9: Electronic energies of fragmentation products (hartrees) at 0 and 298.15 K, at the CBS-QB3, G3 and CBS-APNO levels of theory.

	0 K			298 K		
SPECIES KEY	CBS-QB3	CBS-APNO	G3	CBS-QB3	CBS-APNO	G3
P1	-191.599268	-191.845578	-191.775326	-191.593607	-191.839978	-191.769643
P2	-77.187419	-77.301546	-77.275962	-77.183653	-77.297904	-77.272274
P3	-152.375854	-152.563747	-152.506868	-152.371390	-152.559357	-152.502428
P4	-116.421682	-116.595023	-116.555356	-116.416763	-116.590234	-116.550501
P5	-155.646207	-155.877658	-155.825190	-155.640225	-155.871804	-155.819230
P6	-113.182008	-113.311629	-113.267369	-113.178703	-113.308324	-113.264064
P7	-155.648350	-155.879729	-155.827386	-155.642329	-155.873765	-155.821333
P8	-155.008157	-155.239852	-155.185648	-155.001788	-155.233378	-155.179038
P9	-113.704761	-113.835367	-113.791540	-113.700959	-113.831568	-113.787739
P10	-39.744800	-39.803679	-39.793293	-39.740785	-39.799517	-39.789047
P11	-228.963076	-229.265558	-229.179231	-228.956860	-229.259312	-229.172852
P12	-228.965879	-229.268213	-229.182184	-228.959574	-229.261867	-229.175706
P13	-152.942049	-153.131169	-153.073738	-152.937133	-153.126240	-153.068768
P14	-115.778670	-115.951756	-115.911633	-115.773628	-115.946653	-115.906398
P15	-228.958465	-229.260954		-228.951912	-229.254681	
P16	-228.960097	-229.262597		-228.953791	-229.256365	
P17	-0.499818	-0.499946	-0.501003	-0.497457	-0.497585	-0.498642
P18	-267.618427	-267.978869	-267.880816	-267.611059	-267.971636	-267.873455
P19	-154.991766	-155.223308	-155.168855	-154.986126	-155.217479	-155.163060
P20	-267.663797	-268.024160	-267.925018	-267.658107	-268.018546	-267.919292
P21	-151.708757	-151.897602	-151.840730	-151.704285	-151.892633	-151.835687

Table 9: Electronic energies of fragmentation products (hartrees) at 0 and 298.15 K, at the CBS-QB3, G3 and CBS-APNO levels of theory.

	0 K			298 K		
SPECIES KEY	CBS-QB3	CBS-APNO	G3	CBS-QB3	CBS-APNO	G3
P22	-229.643105	-229.946256	-229.859940	-229.638424	-229.941643	-229.855244
P23	-156.196597	-156.428403	-156.377094	-156.190323	-156.422134	-156.370723
P24	-155.662340	-155.893410	-155.841379	-155.656670	-155.887776	-155.835664
P25	-75.649720	-75.723054	-75.694904	-75.646415	-75.719750	-75.691600
P26	-193.712772	-194.002045	-193.933769	-193.707641	-193.996961	-193.928586
P27	-192.168433	-192.414918	-192.344792	-192.162382	-192.408912	-192.338706
P28	-117.009514	-117.183147	-117.144897	-117.004726	-117.178269	-117.139937
P29	-268.876456	-269.238313	-269.139753	-268.870251	-269.232171	-269.133501
P30	-268.882498	-269.244390	-269.145813	-268.876332	-269.238235	-269.139558
P31	-156.211316	-156.443511		-156.204705	-156.436817	
P32	-152.932833	-153.120583	-153.063707	-152.928348	-153.116108	-153.059187
P33	-156.239817	-156.471904	-156.419916	-156.233541	-156.465498	-156.413404
P34	-229.618062	-229.921239	-229.837341	-229.611692	-229.914963	-229.830972
P35	-116.971430	-117.144744	-117.106687	-116.966319	-117.139622	-117.101499
P36	-156.238812	-156.471114	-156.418959	-156.232480	-156.464603	-156.412360

8 Geometries of Stationary Points

Table 10: Cartesian coordinates for minima (M1–M9) on the C_5H_6O potential energy surface.

At. No.	X	Y	Z	At. No.	X	Y	Z	At. No.	X	Y	Z
	M1 CBS-QB3				M1 CBS-APNO				M1 G3		
6	-1.3972860	-0.7320440	-0.0003310	6	1.3927340	-0.7385560	0.0000170	6	1.3850100	-0.7244670	0.0002030
6	-1.5470180	0.6156580	0.0000750	6	1.5467530	0.6161820	-0.0000140	6	1.5442920	0.6037180	-0.0000830
6	-0.2201260	1.1624850	-0.0002060	6	0.2301130	1.1648740	0.0000110	6	0.2133730	1.1545860	0.0003150
6	0.6385010	0.1064790	-0.0000320	6	-0.6394200	0.1094460	-0.0000160	6	-0.6260720	0.1065660	0.0000970
8	-0.0724600	-1.0625710	0.0004010	1	2.0790690	-1.5719760	0.0000040	1	2.0691420	-1.5445490	0.0002030
1	-2.0866490	-1.5590600	-0.0005010	1	2.4846490	1.1541030	0.0000200	1	2.4719150	1.1378390	-0.0002960
1	-2.4790830	1.1581260	0.0001350	1	-0.0435490	2.2113760	-0.0000100	1	-0.0610060	2.1896860	0.0004070
1	0.0551460	2.2054040	-0.0003490	8	0.0660410	-1.0659870	-0.0000080	8	0.0770890	-1.0428640	0.0003130
6	2.1200270	-0.0142950	0.0000460	6	-2.1193260	-0.0110440	0.0000050	6	-2.1165790	-0.0193690	0.0001650
1	2.4752220	-0.5550800	0.8829750	1	-2.4740500	-0.5483110	0.8845330	1	-2.5025150	-0.1257360	1.0083890
1	2.4752730	-0.5555600	-0.8825670	1	-2.5655000	0.9857600	-0.0000740	1	-2.5851070	0.8513660	-0.4460060
1	2.5751800	0.9770390	-0.0002120	1	-2.4740680	-0.5484650	-0.8844210	1	-2.4092830	-0.8919000	-0.5693880
	M2 CBS-QB3				M2 CBS-APNO				M2 G3		
6	-0.1492760	-1.2416440	0.1830600	6	-0.1574110	-1.2280120	0.1900220	6	-0.1551530	-1.2325270	0.1951300
6	0.6815710	0.0063920	0.4390310	6	0.6836120	0.0079400	0.4547540	6	0.6835270	0.0092230	0.4594380
6	-0.2536920	1.1552460	0.1549810	6	-0.2577760	1.1469470	0.1576080	6	-0.2573180	1.1481060	0.1606530
6	-1.4188330	0.6287560	-0.1820400	6	-1.3989870	0.6079270	-0.1860600	6	-1.3982930	0.6087610	-0.1881440
8	-1.3452150	-0.8022600	-0.1550200	8	-1.3322350	-0.7853810	-0.1583960	8	-1.3317560	-0.7849960	-0.1603980
1	0.9110130	-0.0409230	1.5166180	1	0.9236360	-0.0320510	1.5188300	1	0.9331640	-0.0250440	1.5209740
1	-0.0227870	2.2077000	0.2191990	1	-0.0445030	2.1948110	0.2175250	1	-0.0399470	2.1950730	0.2216700
6	2.0118060	-0.0057190	-0.3358600	6	1.9925310	-0.0095000	-0.3440820	6	1.9883090	-0.0096400	-0.3486250
1	2.5737770	-0.9099290	-0.0978140	1	2.5696150	-0.8930010	-0.0984830	1	2.5664580	-0.8934350	-0.1081970
1	1.8314750	0.0108900	-1.4128800	1	1.7953280	-0.0163360	-1.4112330	1	1.7851730	-0.0146730	-1.4140530
1	2.6187630	0.8644300	-0.0763860	1	2.5883520	0.8683030	-0.1167430	1	2.5876000	0.8660980	-0.1250460
1	-2.3799750	1.0277260	-0.4636120	1	-2.3463620	1.0095070	-0.4761880	1	-2.3448350	1.0084140	-0.4828710
	M3 CBS-QB3				M3 CBS-APNO				M3 G3		
6	0.6439790	0.1579560	0.0024620	6	0.6439790	0.1579560	0.0024620	6	0.6439790	0.1579560	0.0024620
6	-0.2642690	1.1345250	0.0043940	6	-0.2642690	1.1345250	0.0043940	6	-0.2642690	1.1345250	0.0043940
6	-1.3527320	-1.0005910	-0.0097340	6	-1.3527320	-1.0005910	-0.0097340	6	-1.3527320	-1.0005910	-0.0097340
8	-0.0358480	-1.1155640	-0.0012160	8	-0.0358480	-1.1155640	-0.0012160	8	-0.0358480	-1.1155640	-0.0012160
1	-0.0520920	2.1960150	0.0043090	1	-0.0520920	2.1960150	0.0043090	1	-0.0520920	2.1960150	0.0043090
6	2.1212890	0.0588870	-0.0002950	6	2.1212890	0.0588870	-0.0002950	6	2.1212890	0.0588870	-0.0002950
1	2.4726270	-0.4797900	0.8843310	1	2.4726270	-0.4797900	0.8843310	1	2.4726270	-0.4797900	0.8843310

Table 10: Cartesian coordinates for minima (M1–M9) on the C_5H_6O potential energy surface.

At. No.	X	Y	Z	At. No.	X	Y	Z	At. No.	X	Y	Z
1	2.4678030	-0.4870240	-0.8824530	1	2.4678030	-0.4870240	-0.8824530	1	2.4678030	-0.4870240	-0.8824530
1	2.5650550	1.0562690	-0.0054050	1	2.5650550	1.0562690	-0.0054050	1	2.5650550	1.0562690	-0.0054050
6	-1.6168070	0.4953470	-0.0077500	6	-1.6168070	0.4953470	-0.0077500	6	-1.6168070	0.4953470	-0.0077500
1	-2.1697440	0.6988660	0.9232880	1	-2.1697440	0.6988660	0.9232880	1	-2.1697440	0.6988660	0.9232880
1	-2.1856170	0.8634390	-0.8487990	1	-2.1856170	0.8634390	-0.8487990	1	-2.1856170	0.8634390	-0.8487990
	M4 CBS-APNO				M4 G3						
6	0.6573740	0.1104670	0.4573750	6	0.6568900	0.1088130	0.4618080				
6	-0.2090140	1.2888490	0.1939490	6	-0.2068130	1.2916710	0.2001730				
6	-1.4316920	0.6976830	-0.1856940	6	-1.4283190	0.6985240	-0.1877020				
6	-1.2988450	-0.6637620	-0.1646530	6	-1.3000660	-0.6619700	-0.1675370				
8	-0.1373900	-1.0963620	0.1862150	8	-0.1365920	-1.0994860	0.1895520				
1	0.8785540	0.0704110	1.5188170	1	0.8861040	0.0613780	1.5202840				
1	-2.3345090	1.2064250	-0.4609980	1	-2.3298130	1.2084060	-0.4664030				
6	1.9273750	0.0388620	-0.3716220	6	1.9227290	0.0395900	-0.3763490				
1	2.5597510	0.8833120	-0.1289190	1	2.5538970	0.8871790	-0.1434640				
1	2.4620900	-0.8811160	-0.1657860	1	2.4646310	-0.8756760	-0.1713280				
1	1.6922830	0.0772350	-1.4298020	1	1.6798420	0.0709870	-1.4323290				
1	-2.0302340	-1.4179680	-0.3991580	1	-2.0284550	-1.4161480	-0.4055390				
	M5 CBS-QB3				M5 CBS-APNO				M5 G3		
6	1.5424880	0.1460880	0.5420400	6	1.5288190	0.1496570	0.5433010	6	1.5295850	0.1485540	0.5446340
6	0.3640730	0.5686210	0.1949000	6	0.3580180	0.5616530	0.1930950	6	0.3561110	0.5605850	0.1953100
6	-0.8385120	0.9690990	-0.1515840	6	-0.8314760	0.9650180	-0.1561800	6	-0.8342880	0.9661800	-0.1552400
6	-2.0172880	0.0644720	-0.1621670	6	-2.0059590	0.0550690	-0.1608510	6	-2.0068160	0.0579010	-0.1624360
8	-2.0079780	-1.1067240	0.1314010	8	-1.9863410	-1.0909530	0.1332740	8	-1.9851350	-1.0942690	0.1331310
1	1.8108530	0.2111130	1.5958380	1	1.7878120	0.2256820	1.5879310	1	1.7933080	0.2213870	1.5876870
1	-1.0118410	2.0024640	-0.4446110	1	-0.9927700	1.9878020	-0.4534910	1	-0.9949380	1.9892090	-0.4513340
6	2.5680510	-0.4395150	-0.3968000	6	2.5502830	-0.4395180	-0.3954420	6	2.5516140	-0.4373840	-0.3965590
1	3.4926860	0.1450350	-0.3679680	1	3.4644680	0.1459290	-0.3724150	1	3.4648600	0.1489150	-0.3767970
1	2.8162730	-1.4614550	-0.0951590	1	2.7954990	-1.4516570	-0.0894130	1	2.8020870	-1.4488140	-0.0939460
1	2.2015940	-0.4618490	-1.4231670	1	2.1796630	-0.4663530	-1.4119660	1	2.1802840	-0.4651100	-1.4126430
1	-2.9586210	0.5658890	-0.4744730	1	-2.9420500	0.5349420	-0.4703650	1	-2.9417570	0.5335440	-0.4722650
	M6 CBS-QB3				M6 CBS-APNO				M6 G3		
6	-1.7442360	-0.3319760	0.4333050	6	-1.7292250	-0.3340990	0.4339550	6	-1.7315030	-0.3356490	0.4339930
6	-0.5051300	-0.4734280	0.0622870	6	-0.4982040	-0.4651480	0.0648060	6	-0.4992680	-0.4696920	0.0629780

Table 10: Cartesian coordinates for minima (M1–M9) on the C_5H_6O potential energy surface.

At. No.	X	Y	Z	At. No.	X	Y	Z	At. No.	X	Y	Z
6	0.7542570	-0.5860430	-0.2940800	6	0.7473990	-0.5855490	-0.2982960	6	0.7489110	-0.5866010	-0.2990220
6	1.7859190	0.3428240	0.2141530	6	1.7803340	0.3409380	0.2131850	6	1.7783140	0.3408650	0.2143100
8	2.9544920	0.2777440	-0.0871870	8	2.9241950	0.2767620	-0.0862680	8	2.9282830	0.2790080	-0.0855690
1	-2.0686320	-0.8651700	1.3262500	1	-2.0431810	-0.8714520	1.3156420	1	-2.0492420	-0.8695310	1.3156260
1	1.0910280	-1.3655710	-0.9727850	1	1.0654780	-1.3589050	-0.9764200	1	1.0714860	-1.3575800	-0.9769910
6	-2.7765530	0.5049200	-0.2811250	6	-2.7587270	0.5049170	-0.2792620	6	-2.7596110	0.5068870	-0.2785810
1	-3.6171130	-0.1181290	-0.6016320	1	-3.5892800	-0.1160860	-0.6010000	1	-3.5924140	-0.1091250	-0.6024680
1	-3.1764490	1.2718600	0.3890680	1	-3.1532570	1.2635400	0.3899020	1	-3.1539330	1.2665090	0.3888730
1	-2.3546080	0.9960410	-1.1581920	1	-2.3348390	0.9937850	-1.1470780	1	-2.3353800	0.9960490	-1.1457820
1	1.4042910	1.1212330	0.9075460	1	1.4120570	1.1086760	0.9027730	1	1.4121650	1.1067540	0.9032200
	M7 CBS-QB3				M7 CBS-APNO				M7 G3		
6	-1.5501020	0.8521630	0.0041880	6	-1.5501020	0.8521630	0.0041880	6	-1.5501020	0.8521630	0.0041880
6	-0.1994300	1.1927880	0.0053090	6	-0.1994300	1.1927880	0.0053090	6	-0.1994300	1.1927880	0.0053090
6	0.6184300	0.0510780	-0.0028530	6	0.6184300	0.0510780	-0.0028530	6	0.6184300	0.0510780	-0.0028530
8	-0.0439250	-1.0754660	-0.0081910	8	-0.0439250	-1.0754660	-0.0081910	8	-0.0439250	-1.0754660	-0.0081910
1	0.2158820	2.1962770	0.0050550	1	0.2158820	2.1962770	0.0050550	1	0.2158820	2.1962770	0.0050550
6	2.1024020	-0.0494040	-0.0024690	6	2.1024020	-0.0494040	-0.0024690	6	2.1024020	-0.0494040	-0.0024690
1	2.4372130	-0.5801770	0.8930390	1	2.4372130	-0.5801770	0.8930390	1	2.4372130	-0.5801770	0.8930390
1	2.4375530	-0.6224150	-0.8710450	1	2.4375530	-0.6224150	-0.8710450	1	2.4375530	-0.6224150	-0.8710450
1	2.5558060	0.9422340	-0.0245310	1	2.5558060	0.9422340	-0.0245310	1	2.5558060	0.9422340	-0.0245310
6	-1.5206660	-0.6101310	-0.0064930	6	-1.5206660	-0.6101310	-0.0064930	6	-1.5206660	-0.6101310	-0.0064930
1	-1.8952870	-1.0259690	0.9362640	1	-1.8952870	-1.0259690	0.9362640	1	-1.8952870	-1.0259690	0.9362640
1	-2.1035740	-0.9251890	-0.8593450	1	-2.1035740	-0.9251890	-0.8593450	1	-2.1035740	-0.9251890	-0.8593450
	M8 CBS-QB3				M8 CBS-APNO				M8 G3		
6	-2.2823030	-0.4727510	0.0000310	6	-2.2735410	-0.4639860	0.0002960	6	-2.2758370	-0.4642080	0.0003010
1	-2.3957270	-1.1127940	-0.8810010	1	-2.3832040	-1.0967410	-0.8764100	1	-2.3915150	-1.0967120	-0.8754130
1	-2.3959080	-1.1134660	0.8805430	1	-2.3825170	-1.0972860	0.8766870	1	-2.3915410	-1.0975010	0.8754290
1	-3.0557810	0.2933710	0.0002140	1	-3.0402760	0.2976740	0.0008090	1	-3.0411030	0.2989010	0.0006010
6	-0.9150690	0.1861580	0.0004050	6	-0.9100720	0.1874170	-0.0000920	6	-0.9099140	0.1845260	0.0006530
8	-0.7781950	1.3890190	-0.0001170	8	-0.7718660	1.3659350	-0.0001380	8	-0.7720500	1.3692040	-0.0003500
6	0.2477200	-0.7614490	-0.0002420	6	0.2505650	-0.7587480	-0.0003710	6	0.2493370	-0.7587870	-0.0008690
1	0.0366750	-1.8279650	-0.0003160	1	0.0529060	-1.8172370	-0.0008430	1	0.0506710	-1.8170020	-0.0007150
6	1.4912890	-0.3480210	-0.0001140	6	1.4814930	-0.3380100	-0.0000810	6	1.4823240	-0.3370330	-0.0002590
6	2.7160660	0.0803830	0.0000980	6	2.7002120	0.0820840	0.0002550	6	2.7039620	0.0803730	0.0004090

Table 10: Cartesian coordinates for minima (M1–M9) on the C_5H_6O potential energy surface.

At. No.	X	Y	Z	At. No.	X	Y	Z	At. No.	X	Y	Z
1	3.2450660	0.2707790	0.9287330	1	3.2178990	0.2663780	0.9249960	1	3.2251140	0.2637060	0.9229730
1	3.2450160	0.2720010	-0.9283040	1	3.2181690	0.2671940	-0.9241740	1	3.2255410	0.2657570	-0.9214840
	M9 CBS-QB3				M9 CBS-APNO				M9 G3		
6	-0.9753250	1.4063990	0.0000250	6	-0.9883380	1.3966540	-0.0000180	6	-0.9812710	1.3982520	-0.0000220
1	-0.4334720	1.7639680	0.8798620	1	-0.4566130	1.7541040	0.8757140	1	-0.4495030	1.7573600	0.8746800
1	-0.4328720	1.7639010	-0.8794660	1	-0.4563370	1.7541250	-0.8755720	1	-0.4493170	1.7573670	-0.8746060
1	-1.9861330	1.8107460	-0.0003200	1	-1.9971640	1.7845220	-0.0001600	1	-1.9880040	1.7911620	-0.0001170
6	-1.0520410	-0.1072470	0.0000820	6	-1.0476490	-0.1129180	-0.0000130	6	-1.0459190	-0.1122960	-0.0000130
8	-2.1105370	-0.7000130	-0.0001290	8	-2.0794290	-0.7028190	0.0000490	8	-2.0862960	-0.6983710	0.0000610
6	0.2248670	-0.8837880	0.0002770	6	0.2323270	-0.8829280	-0.0000520	6	0.2291340	-0.8864350	-0.0000660
1	0.0979920	-1.9629920	-0.0006260	1	0.1260080	-1.9539640	-0.0000810	1	0.1186560	-1.9568100	-0.0001140
6	1.4230960	-0.3545520	0.0000130	6	1.4145910	-0.3426790	-0.0000190	6	1.4144950	-0.3477260	-0.0000170
6	2.6104840	0.1754220	-0.0000980	6	2.5932440	0.1856980	0.0000340	6	2.5934360	0.1841700	0.0000420
1	3.1263170	0.4032130	0.9277820	1	3.0972180	0.4103530	0.9237850	1	3.0996200	0.4109910	0.9216330
1	3.1259800	0.4038660	-0.9279930	1	3.0972680	0.4104470	-0.9236690	1	3.0996680	0.4111070	-0.9215000

Table 11: Cartesian coordinates for minima (M10–M16) on the C_5H_5O potential energy surface.

At. No.	X	Y	Z	At. No.	X	Y	Z	At. No.	X	Y	Z
	M10 CBS-QB3				M10 CBS-APNO				M10 G3		
6	-1.3324220	-0.7272260	0.0005610	6	-1.3273830	-0.7233340	0.0004400	6	-1.3287010	-0.7246340	0.0004940
6	-1.4676890	0.6362810	-0.0003270	6	-1.4647080	0.6353550	-0.0000310	6	-1.4666490	0.6350560	-0.0000630
6	-0.1635750	1.1697930	-0.0000010	6	-0.1564570	1.1654880	-0.0001510	6	-0.1584730	1.1661000	-0.0001330
6	0.7295670	0.0804240	-0.0002570	6	0.7217530	0.0659990	-0.0000750	6	0.7227530	0.0679490	-0.0000860
8	-0.0215460	-1.0868460	-0.0003390	8	-0.0246150	-1.0759610	-0.0004230	8	-0.0235530	-1.0771200	-0.0004650
1	-2.0432010	-1.5365440	0.0008710	1	-2.0379940	-1.5206550	0.0005480	1	-2.0364390	-1.5242330	0.0006100
1	-2.3991490	1.1803090	-0.0000620	1	-2.3888520	1.1754670	0.0000370	1	-2.3904620	1.1761030	0.0000170
1	0.1232930	2.2092020	0.0005130	1	0.1367500	2.1948130	-0.0002890	1	0.1321550	2.1964380	-0.0002850
6	2.1008390	-0.0065140	-0.0000410	6	2.0958340	-0.0067430	0.0002200	6	2.0980010	-0.0059690	0.0002260
1	2.5930190	-0.9683850	0.0002300	1	2.5944370	-0.9565750	-0.0001670	1	2.5976950	-0.9547830	-0.0001200
1	2.6980770	0.8936340	0.0015420	1	2.6783410	0.8940540	0.0008360	1	2.6838850	0.8924310	0.0008700
	M11 CBS-QB3				M11 CBS-APNO				M11 G3		
6	1.0458270	0.9794320	0.0000230	6	1.0363760	0.9756390	0.0002600	6	1.0421120	0.9746780	0.0000120
6	-0.3502970	1.1878600	-0.0000420	6	-0.3644170	1.1868540	-0.0003380	6	-0.3590260	1.1869810	0.0000610
6	1.6998950	-0.3114300	0.0000280	6	1.7153310	-0.2996480	0.0002400	6	1.7186470	-0.2997160	0.0000900
6	-1.3119050	0.2545460	0.0000100	6	-1.3340720	0.2535700	-0.0002260	6	-1.3317590	0.2526390	-0.0003200
6	-2.3065020	-0.5748460	0.0000150	6	-2.3219820	-0.5951750	0.0002900	6	-2.3310860	-0.5886280	0.0001550
8	1.1236850	-1.3892690	-0.0000280	8	1.1635440	-1.3753970	-0.0003360	8	1.1595060	-1.3799980	-0.0001290
1	2.8085010	-0.2659230	0.0001020	1	2.8058990	-0.2490850	0.0008100	1	2.8072580	-0.2567090	0.0005300
1	1.6855050	1.8560540	0.0000170	1	1.6634380	1.8503450	0.0005170	1	1.6695240	1.8487180	-0.0000470
1	-2.7278310	-0.9561020	-0.9271160	1	-2.7359220	-0.9707580	-0.9213430	1	-2.7511390	-0.9617730	-0.9192580
1	-2.7281040	-0.9557420	0.9271710	1	-2.7364080	-0.9690710	0.9223920	1	-2.7507420	-0.9612290	0.9199670
1	-0.6896490	2.2224950	-0.0001550	1	-0.6927790	2.2142990	-0.0010370	1	-0.6842830	2.2152550	-0.0001470
	M12 CBS-QB3				M12 CBS-APNO				M12 G3		
6	0.7508650	0.8407160	0.0000020	6	-0.7591190	0.8340430	0.0000020	6	0.7604260	0.8355370	0.0000000
6	-0.6449070	1.0584230	-0.0000030	6	0.6365160	1.0699380	-0.0000010	6	-0.6353040	1.0749530	-0.0000010
6	1.3829680	-0.4580290	-0.0000050	6	-1.3752070	-0.4689330	0.0000020	6	1.3704700	-0.4687950	-0.0000020
6	-1.6002290	0.1182860	-0.0000010	6	1.6007170	0.1269170	-0.0000010	6	-1.6020690	0.1304510	0.0000000
6	-2.5497260	-0.7655430	0.0000030	6	2.5481490	-0.7686170	0.0000000	6	-2.5473990	-0.7723120	0.0000010
8	2.5957660	-0.6134040	0.0000040	8	-2.5791350	-0.6106810	-0.0000020	8	2.5806450	-0.6147030	0.0000020
1	0.6996370	-1.3304920	-0.0000200	1	-0.7209560	-1.3398310	0.0000070	1	0.7171600	-1.3378110	-0.0000080
1	1.4160230	1.6970750	0.0000130	1	-1.4276680	1.6760630	0.0000000	1	1.4306000	1.6755570	0.0000040
1	-2.9646500	-1.1573080	-0.9266060	1	2.9554100	-1.1538250	0.9213970	1	-2.9549730	-1.1608810	-0.9191830

Table 11: Cartesian coordinates for minima (M10–M16) on the C_5H_5O potential energy surface.

At. No.	X	Y	Z	At. No.	X	Y	Z	At. No.	X	Y	Z
1	-2.9646550	-1.1572930	0.9266170	1	2.9554060	-1.1538310	-0.9213970	1	-2.9549730	-1.1608800	0.9191850
1	-0.9863070	2.0921320	-0.0000070	1	0.9645480	2.0967820	-0.0000010	1	-0.9597170	2.1026410	-0.0000020
	M13 CBS-QB3				M13 CBS-APNO				M13 G3		
6	0.8084350	0.9761030	-0.0002270	6	0.8261090	0.9746950	-0.0002540	6	-0.8228150	0.9790970	0.0003050
6	-0.6180350	0.8355780	-0.0000100	6	-0.6119170	0.8343820	0.0000520	6	0.6145460	0.8351330	-0.0000440
6	1.6990600	-0.0120340	0.0007130	6	1.6977400	-0.0182690	0.0001690	6	-1.6984950	-0.0152440	-0.0003110
6	-1.3265630	-0.3788430	0.0001040	6	-1.3145360	-0.3813990	-0.0001890	6	1.3154610	-0.3830680	0.0002360
6	-2.6875460	-0.4937010	-0.0000710	6	-2.6888880	-0.4818240	0.0001000	6	2.6912420	-0.4851190	-0.0001280
8	2.4893550	-0.8640170	-0.0003670	8	2.4595140	-0.8657760	0.0000790	8	-2.4682570	-0.8680170	-0.0000450
1	-0.7437290	-1.2996580	0.0003770	1	-0.7452840	-1.2988140	-0.0006200	1	0.7443960	-1.2987090	0.0007640
1	1.2542730	1.9654780	-0.0000800	1	1.2764010	1.9502780	-0.0001730	1	-1.2684420	1.9569800	0.0002950
1	-3.3274660	0.3821230	-0.0003820	1	-3.3137920	0.3944240	0.0005240	1	3.3179110	0.3891730	-0.0006460
1	-3.1710920	-1.4617510	0.0000690	1	-3.1759890	-1.4392990	-0.0001040	1	3.1793990	-1.4415590	0.0001140
1	-1.1789340	1.7633300	-0.0001030	1	-1.1684970	1.7541130	0.0004700	1	1.1731500	1.7534660	-0.0005200
	M14 CBS-QB3										
6	-0.7524310	0.8180140	-0.0000060								
6	0.5965560	0.7823360	-0.0000240								
6	-1.5707220	-0.3969840	-0.0000030								
6	1.4159970	-0.4136160	-0.0000160								
6	2.7537090	-0.3738060	0.0000770								
8	-2.7552170	-0.4895590	-0.0000430								
1	0.8944500	-1.3652250	-0.0000210								
1	-1.2846510	1.7680530	-0.0000390								
1	3.2938760	0.5677790	0.0001400								
1	3.3481710	-1.2792960	0.0001920								
1	1.1312430	1.7294960	-0.0000920								
	M15 CBS-QB3				M15 CBS-APNO				M15 G3		
6	0.5821270	1.1031570	-0.0000600	6	-0.6140650	1.0959450	0.0003460	6	-0.6094410	1.1022370	0.0002090
6	-0.8497870	1.1072100	0.0001670	6	0.8310510	1.1124850	-0.0001060	6	0.8356580	1.1127720	-0.0001370
6	1.4148130	0.0660920	-0.0001530	6	-1.4237550	0.0530870	0.0000520	6	-1.4229350	0.0578930	0.0000290
6	-1.7274950	0.0056730	0.0002530	6	1.7276740	0.0303580	-0.0002650	6	1.7290380	0.0261670	-0.0002500
6	-1.4139900	-1.3244250	0.0000660	6	1.4346210	-1.3172480	0.0001560	6	1.4315930	-1.3219360	0.0001350
8	2.1901550	-0.7990160	-0.0002650	8	-2.1592370	-0.8166780	-0.0001750	8	-2.1667480	-0.8172000	-0.0000380
1	-2.7829990	0.2656040	0.0004930	1	2.7699800	0.3032440	-0.0007600	1	2.7721100	0.2946160	-0.0006760

Table 11: Cartesian coordinates for minima (M10–M16) on the C_5H_5O potential energy surface.

At. No.	X	Y	Z	At. No.	X	Y	Z	At. No.	X	Y	Z
1	1.1076320	2.0539120	-0.0002440	1	-1.1457540	2.0308100	0.0007280	1	-1.1355280	2.0402500	0.0007610
1	-0.3957960	-1.6943850	-0.0002120	1	0.4330930	-1.7055680	0.0007360	1	0.4296310	-1.7076320	0.0006540
1	-2.1934730	-2.0754300	0.0001730	1	2.2278550	-2.0420610	-0.0000410	1	2.2208240	-2.0504140	-0.0000330
1	-1.2906100	2.0961900	0.0002720	1	1.2555650	2.0992340	-0.0003510	1	1.2634730	2.0979820	-0.0003160
	M16 CBS-QB3				M16 CBS-APNO				M16 G3		
6	0.0508700	1.1958500	-0.0000240	6	0.0489500	1.1958930	-0.0000540	6	0.0481890	1.1963190	-0.0000530
6	1.3786630	0.7524340	-0.0002170	6	1.3773760	0.7515260	-0.0001520	6	1.3783260	0.7531590	-0.0001630
6	-0.8460370	0.0426790	0.0001160	6	-0.8402900	0.0378080	0.0001050	6	-0.8385310	0.0378510	0.0000770
6	1.4414030	-0.6304100	-0.0000500	6	1.4340840	-0.6357750	-0.0001450	6	1.4358800	-0.6352450	-0.0001430
6	0.0596540	-1.2072060	-0.0000050	6	0.0426520	-1.2086610	0.0000490	6	0.0442550	-1.2099470	0.0000470
8	-2.0638150	0.0408940	0.0001950	8	-2.0392940	0.0502240	0.0001930	8	-2.0437070	0.0496640	0.0002180
1	2.3516130	-1.2148340	-0.0001710	1	2.3326680	-1.2217860	-0.0002460	1	2.3337140	-1.2220240	-0.0002250
1	-0.2936610	2.2205110	-0.0000270	1	-0.2957250	2.2114640	-0.0000630	1	-0.2973240	2.2112480	-0.0000510
1	-0.1498910	-1.8277050	-0.8784900	1	-0.1681520	-1.8158930	-0.8756980	1	-0.1662080	-1.8187580	-0.8745220
1	-0.1497250	-1.8275990	0.8785970	1	-0.1679420	-1.8157990	0.8759140	1	-0.1660100	-1.8186610	0.8747330
1	2.2448560	1.4023870	-0.0003820	1	2.2368650	1.3954780	-0.0002620	1	2.2367720	1.3980570	-0.0002680

Table 12: Cartesian coordinates for minima (M17–M27) on the C_5H_7O potential energy surface.

At. No.	X	Y	Z	At. No.	X	Y	Z	At. No.	X	Y	Z
	M17 CBS-QB3				M17 CBS-APNO				M17 G3		
6	0.694148	0.063394	0.463505	6	0.690391	0.049158	0.463494	6	0.691269	0.049414	0.466486
6	-0.247967	1.196513	0.172534	6	-0.250048	1.190761	0.171930	6	-0.250555	1.191043	0.176299
6	-1.352862	-0.725611	-0.166626	6	-1.341770	-0.730710	-0.165511	6	-1.341800	-0.730899	-0.168059
8	-0.110917	-1.132565	0.214200	8	-0.099322	-1.113380	0.212620	8	-0.098253	-1.114474	0.216589
1	0.013679	2.240029	0.258207	1	0.009082	2.227102	0.259276	1	0.009801	2.227130	0.262696
6	1.955091	0.002605	-0.397924	6	1.944226	0.009632	-0.396748	6	1.941763	0.010488	-0.400686
1	2.523542	-0.904113	-0.178365	1	2.519467	-0.884164	-0.180159	1	2.519632	-0.881964	-0.188011
1	1.690370	0.007862	-1.457269	1	1.681198	0.007103	-1.449239	1	1.673079	0.007441	-1.451046
1	2.589436	0.869178	-0.191637	1	2.565750	0.877797	-0.194977	1	2.564656	0.878081	-0.204111
6	-1.464414	0.653252	-0.203676	6	-1.468963	0.645503	-0.203775	6	-1.468911	0.645870	-0.205870
1	-2.356697	1.192835	-0.485870	1	-2.358415	1.175280	-0.480869	1	-2.356732	1.177065	-0.485829
1	-2.059750	-1.508351	-0.390535	1	-2.039259	-1.510374	-0.385594	1	-2.035068	-1.513442	-0.390189
1	0.982784	0.022163	1.524994	1	0.973743	0.028224	1.514262	1	0.980070	0.025979	1.514758
	M18 CBS-QB3				M18 CBS-APNO				M18 G3		
6	1.726596	-0.103753	0.000004	6	1.745185	-0.129551	-0.000046	6	1.746193	-0.128608	-0.000031
6	0.882559	1.075962	0.000014	6	0.912605	1.057046	-0.000078	6	0.915576	1.057033	-0.000049
6	-0.514366	1.260337	-0.000008	6	-0.487674	1.259043	0.000050	6	-0.485219	1.260663	0.000033
6	-1.593123	0.401671	-0.000008	6	-1.590851	0.426368	0.000066	6	-1.591012	0.428784	0.000043
8	1.392001	-1.280607	-0.000015	8	1.386686	-1.281279	0.000127	8	1.382886	-1.286068	0.000083
1	1.459353	1.997601	0.000029	1	1.490836	1.966710	-0.000162	1	1.494104	1.965867	-0.000105
1	-0.795583	2.311650	-0.000024	1	-0.743279	2.307012	0.000135	1	-0.738813	2.308512	0.000087
6	-1.655861	-1.084952	0.000016	6	-1.712562	-1.067134	-0.000101	6	-1.714417	-1.065314	-0.000065
1	-2.223257	-1.428926	0.874816	1	-2.279645	-1.383946	0.873283	1	-2.280843	-1.384673	0.872330
1	-2.223097	-1.428957	-0.874878	1	-2.280339	-1.383682	-0.873127	1	-2.281252	-1.384503	-0.872255
1	-0.673964	-1.548787	0.000097	1	-0.762304	-1.570100	-0.000526	1	-0.764172	-1.568364	-0.000320
1	-2.561640	0.898470	-0.000032	1	-2.534557	0.949598	0.000221	1	-2.534044	0.951673	0.000139
1	2.807344	0.148214	0.000011	1	2.815580	0.090003	-0.000182	1	2.815202	0.084684	-0.000122
	M19 CBS-QB3				M19 CBS-APNO				M19 G3		
6	-1.362396	-0.397532	0.000000	6	-1.358266	-0.406627	0.000000	6	1.355693	-0.406355	0.000000
6	-0.686288	0.884432	0.000000	6	-0.700845	0.878312	0.000000	6	0.701486	0.878323	0.000000
6	0.686260	1.171020	0.000000	6	0.676136	1.176077	0.000000	6	-0.676560	1.177171	0.000000
6	1.791626	0.342982	0.000000	6	1.790364	0.351842	0.000000	6	-1.791673	0.352170	0.000000
8	-2.582817	-0.489620	0.000000	8	-2.569306	-0.491702	0.000000	8	2.573434	-0.492179	0.000000

Table 12: Cartesian coordinates for minima (M17–M27) on the C_5H_7O potential energy surface.

At. No.	X	Y	Z	At. No.	X	Y	Z	At. No.	X	Y	Z
1	-1.373234	1.725857	0.000000	1	-1.384630	1.709802	0.000000	1	1.385009	1.709222	0.000000
1	0.918794	2.233304	0.000000	1	0.896492	2.231057	0.000000	1	-0.896330	2.231787	0.000000
6	1.833733	-1.153485	0.000000	6	1.839773	-1.152210	0.000000	6	-1.840792	-1.152410	0.000000
1	2.863516	-1.513267	0.000001	1	2.868579	-1.491547	0.000001	1	-2.868867	-1.493478	-0.000001
1	1.333157	-1.574054	0.879402	1	1.356341	-1.572125	0.877985	1	-1.357869	-1.573616	-0.877193
1	1.333157	-1.574055	-0.879401	1	1.356342	-1.572125	-0.877985	1	-1.357870	-1.573616	0.877193
1	2.753713	0.846176	0.000000	1	2.740701	0.857579	0.000000	1	-2.742377	0.856029	0.000000
1	-0.744176	-1.311502	0.000000	1	-0.762348	-1.313385	0.000000	1	0.761903	-1.312285	0.000000
	M20 CBS-QB3				M20 CBS-APNO						
6	-1.607064	-0.402419	0.058716	6	-1.620222	-0.401056	0.064440				
6	-0.835404	0.833152	-0.133135	6	-0.829677	0.832191	-0.134320				
6	0.483614	0.901161	0.099296	6	0.477739	0.896573	0.096338				
6	1.371438	-0.208974	0.568996	6	1.379328	-0.204436	0.576015				
8	-2.771572	-0.573980	-0.097690	8	-2.756726	-0.573330	-0.098897				
1	-1.391173	1.704279	-0.478869	1	-1.378017	1.692472	-0.482440				
1	0.976203	1.856661	-0.076517	1	0.962717	1.844383	-0.084457				
6	2.517468	-0.495020	-0.417042	6	2.505280	-0.496523	-0.421884				
1	3.128884	0.395649	-0.589011	1	3.103896	0.389882	-0.612654				
1	3.170812	-1.278836	-0.027009	1	3.164240	-1.266503	-0.034557				
1	2.128173	-0.827631	-1.382275	1	2.103845	-0.840939	-1.369651				
1	1.801318	0.083943	1.535573	1	1.814845	0.109777	1.522568				
1	0.778033	-1.109624	0.738644	1	0.807595	-1.102924	0.768829				
	M21 CBS-QB3				M21 CBS-APNO				M21 G3		
6	-1.953476	-0.023528	0.000008	6	-1.973461	-0.014542	0.000003	6	-1.974875	-0.011758	0.000003
6	-0.974808	1.046139	-0.000182	6	-0.974731	1.034202	-0.000182	6	-0.977059	1.035043	-0.000188
6	0.423110	0.909204	-0.000161	6	0.428271	0.887592	-0.000157	6	0.426729	0.887746	-0.000162
6	1.130817	-0.269360	0.000044	6	1.147810	-0.287532	0.000047	6	1.147879	-0.288423	0.000052
8	-1.711650	-1.223995	0.000218	8	-1.749153	-1.201215	0.000214	8	-1.747169	-1.204969	0.000222
1	-1.384144	2.052012	-0.000358	1	-1.365329	2.037871	-0.000358	1	-1.366560	2.038741	-0.000371
1	0.995686	1.835678	-0.000326	1	0.987841	1.810286	-0.000320	1	0.986112	1.809897	-0.000330
1	-3.006934	0.325108	-0.000051	1	-3.008614	0.334852	-0.000059	1	-3.009235	0.332159	-0.000060
6	2.619286	-0.342267	0.000056	6	2.646473	-0.333120	0.000058	6	2.647537	-0.331726	0.000058
1	2.981289	-0.894776	0.875862	1	3.015191	-0.865174	0.874136	1	3.019875	-0.861826	0.873295
1	2.981288	-0.895130	-0.875526	1	3.015193	-0.865540	-0.873795	1	3.019874	-0.862144	-0.872986

Table 12: Cartesian coordinates for minima (M17–M27) on the C_5H_7O potential energy surface.

At. No.	X	Y	Z	At. No.	X	Y	Z	At. No.	X	Y	Z
1	3.083658	0.646574	-0.000142	1	3.081479	0.660750	-0.000149	1	3.081375	0.662476	-0.000123
1	0.572788	-1.198634	0.000208	1	0.621295	-1.222922	0.000212	1	0.624642	-1.224842	0.000223
	M22 CBS-QB3				M22 CBS-APNO				M22 G3		
6	-1.701467	-0.405909	-0.000059	6	-1.701115	-0.413821	-0.000050	6	-1.700169	-0.414677	-0.000051
6	-0.831706	0.750007	-0.000020	6	-0.841276	0.744298	-0.000025	6	-0.842097	0.742824	-0.000024
6	0.572561	0.739602	0.000012	6	0.568596	0.739123	0.000015	6	0.568880	0.738858	0.000015
6	1.404223	-0.355677	0.000053	6	1.402759	-0.360400	0.000042	6	1.404928	-0.361073	0.000043
8	-2.921276	-0.324965	-0.000076	8	-2.908945	-0.317101	-0.000083	8	-2.914709	-0.315499	-0.000083
1	-1.348789	1.704149	-0.000021	1	-1.354729	1.689775	-0.000039	1	-1.355092	1.687948	-0.000037
1	1.055169	1.715488	0.000009	1	1.039376	1.709369	0.000025	1	1.039062	1.708772	0.000024
1	-1.213989	-1.401465	-0.000083	1	-1.242780	-1.401984	-0.000040	1	-1.246365	-1.402591	-0.000045
6	2.893846	-0.272702	0.000078	6	2.899810	-0.267663	0.000084	6	2.902713	-0.266838	0.000084
1	3.315945	-0.778992	0.876823	1	3.318419	-0.760210	0.874674	1	3.323915	-0.757660	0.873859
1	3.315975	-0.779021	-0.876637	1	3.318468	-0.760220	-0.874478	1	3.323962	-0.757673	-0.873662
1	3.244566	0.761507	0.000066	1	3.235280	0.763609	0.000087	1	3.237662	0.764394	0.000085
1	0.976596	-1.353871	0.000070	1	0.984882	-1.352758	0.000034	1	0.988995	-1.353762	0.000038
	M23 CBS-QB3				M23 CBS-APNO				M23 G3		
6	-1.936611	0.544046	0.000082	6	-1.940558	0.544370	-0.000079	6	-1.939663	0.548146	-0.000090
6	-0.486302	0.583157	0.000083	6	-0.494620	0.573280	0.000002	6	-0.495554	0.575588	-0.000007
6	0.276098	-0.590553	0.000041	6	0.275252	-0.603115	-0.000015	6	0.273734	-0.602362	-0.000021
6	1.647267	-0.683398	0.000052	6	1.651876	-0.684002	0.000047	6	1.652018	-0.685172	0.000047
8	-2.603201	-0.481603	-0.000341	8	-2.598198	-0.471513	-0.000160	8	-2.599411	-0.474669	-0.000142
1	-0.016464	1.561068	0.000127	1	-0.028266	1.541889	0.000078	1	-0.026894	1.542754	0.000071
1	-0.296893	-1.513472	0.000005	1	-0.277487	-1.526174	-0.000079	1	-0.279270	-1.524717	-0.000087
6	2.628566	0.441901	0.000126	6	2.632181	0.452607	0.000158	6	2.634090	0.450923	0.000160
1	3.283970	0.379142	0.876994	1	3.275834	0.396274	0.874770	1	3.278437	0.396713	0.873929
1	3.284523	0.378780	-0.876296	1	3.276523	0.395833	-0.873913	1	3.279139	0.396262	-0.873057
1	2.157174	1.424713	-0.000217	1	2.155412	1.424246	-0.000278	1	2.158648	1.423060	-0.000284
1	2.075784	-1.682210	0.000037	1	2.081924	-1.672140	0.000059	1	2.082339	-1.672558	0.000060
1	-2.436597	1.533880	-0.000228	1	-2.443146	1.513343	-0.000038	1	-2.444857	1.513109	-0.000026
	M24 CBS-QB3				M24 CBS-APNO				M24 G3		
6	1.915903	0.478725	0.000217	6	1.915226	0.471064	0.000076	6	1.914635	0.474571	0.000039
6	0.414878	0.674455	0.000358	6	0.419555	0.671708	0.000156	6	0.418330	0.674913	0.000162
6	-0.378043	-0.591705	0.000269	6	-0.375409	-0.601273	0.000129	6	-0.373105	-0.601190	0.000134

Table 12: Cartesian coordinates for minima (M17–M27) on the C_5H_7O potential energy surface.

At. No.	X	Y	Z	At. No.	X	Y	Z	At. No.	X	Y	Z
6	-1.767186	-0.646929	-0.000078	6	-1.768776	-0.649802	-0.000091	6	-1.767449	-0.651492	-0.000088
8	2.476453	-0.586450	-0.000296	8	2.466710	-0.573805	0.000046	8	2.466893	-0.576586	0.000050
1	0.176924	1.311729	-0.866748	1	0.186292	1.292948	-0.865903	1	0.181132	1.295649	-0.864853
1	0.194366	-1.511263	0.000490	1	0.181058	-1.519310	0.000310	1	0.185027	-1.517829	0.000319
6	-2.630816	0.428706	-0.000388	6	-2.625810	0.440815	-0.000312	6	-2.626632	0.438957	-0.000309
1	-2.276086	1.452817	-0.000376	1	-2.264426	1.453660	-0.000328	1	-2.267551	1.452077	-0.000322
1	-3.703344	0.283025	-0.000671	1	-3.691403	0.302435	-0.000474	1	-3.691958	0.301993	-0.000475
1	-2.209324	-1.640373	-0.000116	1	-2.215676	-1.630646	-0.000082	1	-2.213774	-1.632246	-0.000081
1	2.500314	1.424662	-0.000176	1	2.495372	1.403436	0.000042	1	2.496036	1.402968	0.000068
1	0.177109	1.311488	0.867699	1	0.186386	1.292845	0.866319	1	0.181274	1.295517	0.865317
	M25 CBS-QB3				M25 CBS-APNO				M25 G3		
6	1.554961	-0.106496	-0.305356	6	1.520630	-0.093199	-0.354365	6	1.504298	-0.091369	-0.363666
6	0.584749	-0.871568	0.589720	6	0.570490	-0.835555	0.561717	6	0.570474	-0.859317	0.547743
6	-0.717329	-1.103779	-0.126930	6	-0.766515	-1.092466	-0.090720	6	-0.778335	-1.097497	-0.089087
6	-1.711245	-0.138668	-0.270081	6	-1.761380	-0.126942	-0.244165	6	-1.758017	-0.114106	-0.236513
8	1.884119	1.036644	-0.123586	8	2.058298	0.921323	-0.073895	8	2.048164	0.920341	-0.060898
1	0.448564	-0.290521	1.505364	1	0.473771	-0.265805	1.478409	1	0.488931	-0.312417	1.479767
1	-0.875329	-2.076258	-0.579746	1	-0.956911	-2.081237	-0.469473	1	-0.987732	-2.084579	-0.460803
6	-1.663693	1.160460	0.190719	6	-1.683440	1.198648	0.160841	6	-1.651127	1.212313	0.163288
1	-0.792392	1.560497	0.694379	1	-0.804491	1.605202	0.626722	1	-0.761034	1.604081	0.619206
1	-2.497248	1.833172	0.034515	1	-2.510118	1.866320	0.001878	1	-2.465015	1.896305	0.011078
1	-2.610086	-0.450413	-0.797206	1	-2.673628	-0.447370	-0.720911	1	-2.680537	-0.418812	-0.702744
1	1.927349	-0.676311	-1.184126	1	1.689492	-0.563569	-1.332031	1	1.657830	-0.530919	-1.354694
1	1.041532	-1.833007	0.847073	1	1.036799	-1.787043	0.806720	1	1.038495	-1.816528	0.764795
	M26 CBS-QB3				M26 CBS-APNO				M26 G3		
6	-1.616681	0.007683	0.121307	6	-1.623473	0.031808	0.159440	6	-1.623094	0.027820	0.157885
6	-0.792690	1.097151	0.208097	6	-0.772057	1.089344	0.228276	6	-0.775851	1.091589	0.227530
6	0.579264	1.226623	-0.122275	6	0.602680	1.198163	-0.166291	6	0.599452	1.203088	-0.162608
6	1.588218	0.226847	-0.211644	6	1.622279	0.210994	-0.206369	6	1.618100	0.213091	-0.208322
8	-1.319315	-1.227307	-0.323796	8	-1.381375	-1.189936	-0.345734	8	-1.371425	-1.195172	-0.346572
1	-1.308023	2.012742	0.482567	1	-1.235724	2.004531	0.555825	1	-1.243508	2.006101	0.550534
1	0.911393	2.239485	-0.330844	1	0.919884	2.193994	-0.427862	1	0.916756	2.199038	-0.422747
6	1.610125	-1.014487	0.355830	6	1.623833	-1.035510	0.375820	6	1.621467	-1.033141	0.377437
1	2.460879	-1.668935	0.213313	1	2.488881	-1.668045	0.292288	1	2.482218	-1.670053	0.288479

Table 12: Cartesian coordinates for minima (M17–M27) on the C_5H_7O potential energy surface.

At. No.	X	Y	Z	At. No.	X	Y	Z	At. No.	X	Y	Z
1	0.841818	-1.358627	1.038438	1	0.804285	-1.400472	0.966363	1	0.809284	-1.392269	0.980699
1	-0.376466	-1.280765	-0.548418	1	-0.543078	-1.217235	-0.774090	1	-0.521073	-1.218573	-0.765202
1	2.479410	0.525832	-0.760641	1	2.531750	0.515842	-0.699146	1	2.523759	0.513896	-0.709685
1	-2.663906	0.085824	0.388063	1	-2.634574	0.122076	0.507233	1	-2.636478	0.108553	0.498966
	M27 CBS-QB3				M27 CBS-APNO				M27 G3		
6	0.782089	0.002682	0.443721	6	0.784309	-0.008014	0.434208	6	0.784970	-0.008684	0.435124
6	-0.120199	-1.186992	0.236486	6	-0.130027	-1.190319	0.213637	6	-0.130378	-1.191075	0.215695
6	-1.388179	-0.777402	-0.150607	6	-1.403052	-0.765980	-0.146259	6	-1.403851	-0.766519	-0.146683
6	-1.475193	0.607567	-0.203118	6	-1.469100	0.623876	-0.188319	6	-1.469027	0.624396	-0.190107
8	1.950993	-0.030747	-0.385432	8	1.938320	-0.045563	-0.367616	8	1.938565	-0.046172	-0.369547
1	0.218592	-2.207260	0.357752	1	0.195051	-2.208165	0.322010	1	0.194726	-2.208585	0.324885
1	-2.207144	-1.449235	-0.379672	1	-2.227799	-1.421063	-0.360803	1	-2.228114	-1.421524	-0.362298
6	-0.153953	1.223036	0.169901	6	-0.127512	1.218966	0.162064	6	-0.127949	1.219835	0.164293
1	-0.241922	1.876703	1.045688	1	-0.192099	1.872351	1.028016	1	-0.192814	1.870998	1.031705
1	0.271642	1.839578	-0.630421	1	0.284902	1.814134	-0.648870	1	0.286390	1.818501	-0.642707
1	1.656003	-0.238514	-1.279399	1	1.684591	-0.174457	-1.264999	1	1.680187	-0.171220	-1.273251
1	-2.358169	1.173736	-0.468515	1	-2.339906	1.201029	-0.436054	1	-2.337911	1.203171	-0.439846
1	1.185667	0.037623	1.459724	1	1.160998	0.009505	1.449633	1	1.166427	0.010313	1.447956

Table 13: Cartesian coordinates for minima (M28–M35) on the C_5H_7O potential energy surface.

At. No.	X	Y	Z	At. No.	X	Y	Z	At. No.	X	Y	Z
	M28 CBS-QB3				M28 CBS-APNO				M28 G3		
6	-0.676700	0.052177	-0.231132	6	-0.672554	0.045880	-0.281354	6	-0.673156	0.047103	-0.282951
6	0.243995	1.226897	-0.040132	6	0.242515	1.227290	-0.051000	6	0.244811	1.228336	-0.054865
6	1.368914	-0.783457	0.053404	6	1.349728	-0.776044	0.062854	6	1.350172	-0.778038	0.064893
8	0.043188	-1.130443	-0.064627	8	0.045118	-1.118901	-0.080989	8	0.044024	-1.120334	-0.086055
1	0.194864	1.945397	-0.871091	1	0.213140	1.933094	-0.878352	1	0.221042	1.929644	-0.886418
6	-2.120132	-0.023611	0.099908	6	-2.104398	-0.024237	0.125608	6	-2.104799	-0.023320	0.129540
1	-2.561227	-0.940599	-0.298738	1	-2.575729	-0.908049	-0.290029	1	-2.577420	-0.907976	-0.282048
1	-2.301318	-0.016851	1.188691	1	-2.205273	-0.068678	1.211588	1	-2.206218	-0.064273	1.214567
1	-2.657473	0.827868	-0.325474	1	-2.640147	0.850973	-0.227019	1	-2.643618	0.849066	-0.224233
6	1.581247	0.531113	0.065402	6	1.570175	0.521102	0.084722	6	1.570454	0.520651	0.089777
1	2.540336	1.017560	0.153099	1	2.525552	0.992234	0.194812	1	2.523894	0.995093	0.203289
1	2.051083	-1.617531	0.115548	1	2.032481	-1.597388	0.141589	1	2.028730	-1.602133	0.145311
1	0.004287	1.808989	0.870281	1	-0.023760	1.785078	0.850344	1	-0.023495	1.794868	0.839612
	M29 CBS-QB3				M29 CBS-APNO				M29 G3		
6	0.793325	0.181622	-0.031208	6	0.802679	0.187293	-0.052225	6	0.801326	0.184902	-0.050540
6	-0.208657	-0.966492	-0.076408	6	-0.211858	-0.941552	-0.116216	6	-0.211410	-0.946786	-0.110115
6	-1.667507	-0.599221	0.019711	6	-1.673054	-0.589248	-0.013616	6	-1.672959	-0.591067	-0.017931
6	-2.182913	0.602353	0.066487	6	-2.209979	0.606656	0.174977	6	-2.206811	0.609788	0.176357
8	0.466914	1.342885	-0.072598	8	0.515237	1.331090	-0.161806	8	0.509411	1.333132	-0.161741
1	-0.024850	-1.516517	-1.011291	1	-0.032280	-1.461364	-1.058277	1	-0.027947	-1.478207	-1.044629
1	-2.341135	-1.464768	0.047598	1	-2.340327	-1.439475	-0.098480	1	-2.339409	-1.439717	-0.112890
1	0.053599	-1.683394	0.713389	1	0.040408	-1.668135	0.654676	1	0.036694	-1.666369	0.668658
6	2.252895	-0.231025	0.077685	6	2.238099	-0.251620	0.153314	6	2.240133	-0.247671	0.150198
1	2.490904	-1.055125	-0.600311	1	2.486178	-1.099565	-0.477644	1	2.502784	-1.066291	-0.512588
1	2.890996	0.625883	-0.133750	1	2.903437	0.574500	-0.056109	1	2.898924	0.591519	-0.024001
1	2.454653	-0.580340	1.096061	1	2.370672	-0.562399	1.186698	1	2.375181	-0.599184	1.169562
1	-3.182342	1.007758	0.131481	1	-3.225302	0.938554	0.266177	1	-3.223188	0.938197	0.261998
	M30 CBS-QB3				M30 CBS-APNO				M30 G3		
6	-1.292050	1.207644	0.381865	6	-1.395692	1.156076	0.322749	6	-1.391202	1.161340	0.314752
6	-0.875782	-0.194859	-0.017768	6	-0.856020	-0.214350	-0.021467	6	-0.854749	-0.214156	-0.016809
6	0.345428	-0.784004	0.690204	6	0.350145	-0.700746	0.767974	6	0.351015	-0.697456	0.775204
6	1.670914	-0.205655	0.234506	6	1.663277	-0.110932	0.301102	6	1.661855	-0.100469	0.308001
6	1.868858	0.645439	-0.737132	6	1.854201	0.578662	-0.812474	6	1.851243	0.559691	-0.828606

Table 13: Cartesian coordinates for minima (M28–M35) on the C_5H_7O potential energy surface.

At. No.	X	Y	Z	At. No.	X	Y	Z	At. No.	X	Y	Z
1	2.698546	1.144884	-1.212852	1	2.704248	1.033097	-1.279586	1	2.701935	1.013273	-1.294368
1	2.541323	-0.578131	0.788453	1	2.515192	-0.309021	0.939873	1	2.507562	-0.265489	0.962663
1	0.251784	-0.630803	1.772999	1	0.213931	-0.457971	1.819813	1	0.212009	-0.456988	1.826836
1	0.340966	-1.862683	0.509106	1	0.388373	-1.781264	0.679891	1	0.392016	-1.777913	0.688460
8	-1.492080	-0.840688	-0.831949	8	-1.363865	-0.898507	-0.846568	8	-1.366638	-0.905831	-0.840979
1	-2.046609	1.576560	-0.311472	1	-2.085216	1.479529	-0.444855	1	-2.093810	1.471901	-0.446033
1	-0.435750	1.884867	0.407936	1	-0.596222	1.878742	0.439074	1	-0.591516	1.887519	0.402400
1	-1.717825	1.179421	1.391376	1	-1.924859	1.092682	1.271032	1	-1.904068	1.120636	1.272631
	M31 CBS-QB3				M31 CBS-APNO				M31 G3		
6	-0.810081	0.155222	0.195651	6	-0.805094	0.157059	0.193809	6	-0.805504	0.157735	0.193669
6	0.403130	-0.342620	0.976807	6	0.399344	-0.363722	0.960900	6	0.396488	-0.374815	0.957032
6	1.675907	-0.353614	0.124456	6	1.659238	-0.395053	0.105355	6	1.644551	-0.430009	0.083297
6	1.909090	0.388260	-0.926020	6	1.928053	0.428732	-0.897626	6	1.950424	0.448787	-0.866840
8	-1.133642	1.320148	0.216826	8	-1.116592	1.301507	0.242665	8	-1.103875	1.311322	0.241274
1	0.551506	0.316959	1.836672	1	0.556138	0.279517	1.820201	1	0.568893	0.273501	1.809125
1	2.448878	-1.041823	0.468957	1	2.396243	-1.134673	0.377602	1	2.332962	-1.234318	0.286910
1	0.226564	-1.356573	1.350010	1	0.199196	-1.368002	1.322331	1	0.185273	-1.371669	1.330707
6	-1.564875	-0.879963	-0.615305	6	-1.573564	-0.848542	-0.632853	6	-1.586191	-0.837651	-0.634989
1	-2.092852	-1.559303	0.062913	1	-2.110801	-1.519478	0.033154	1	-2.110685	-1.525875	0.022635
1	-2.288633	-0.387241	-1.263058	1	-2.281111	-0.336159	-1.270011	1	-2.305807	-0.317569	-1.251742
1	-0.875887	-1.487004	-1.208798	1	-0.898329	-1.451604	-1.231026	1	-0.920237	-1.425839	-1.257700
1	1.420534	1.150086	-1.514834	1	1.423538	1.247491	-1.371077	1	1.481989	1.326912	-1.263145
	M32 CBS-QB3				M32 CBS-APNO				M32 G3		
6	1.352368	1.100790	-0.604133	6	1.448612	1.044383	-0.597807	6	1.423157	1.062071	-0.595734
6	0.933066	-0.143772	-0.023383	6	0.926086	-0.152113	-0.013265	6	0.927255	-0.147792	-0.019506
6	-0.269986	-0.855978	-0.634848	6	-0.272713	-0.832072	-0.647372	6	-0.272119	-0.839492	-0.640871
6	-1.605347	-0.244959	-0.278814	6	-1.609704	-0.227172	-0.285529	6	-1.610531	-0.236104	-0.278468
6	-1.832587	0.659850	0.668959	6	-1.843502	0.686879	0.634321	6	-1.844398	0.682634	0.638167
1	-2.834378	1.026054	0.861324	1	-2.843653	1.036713	0.819999	1	-2.843559	1.032507	0.826203
1	-2.445608	-0.617742	-0.860721	1	-2.442620	-0.621048	-0.847135	1	-2.442590	-0.634499	-0.836729
1	-0.168667	-0.871424	-1.727295	1	-0.167956	-0.816002	-1.729896	1	-0.171423	-0.835383	-1.723776
1	-0.240060	-1.897482	-0.299086	1	-0.259947	-1.873848	-0.342672	1	-0.252109	-1.878437	-0.327508
8	1.527886	-0.618676	0.947788	8	1.447459	-0.620122	0.990868	8	1.474985	-0.622325	0.975312
1	2.207365	1.607755	-0.174467	1	2.296636	1.516307	-0.137491	1	2.271885	1.541549	-0.146525

Table 13: Cartesian coordinates for minima (M28–M35) on the C_5H_7O potential energy surface.

At. No.	X	Y	Z	At. No.	X	Y	Z	At. No.	X	Y	Z
1	-1.041019	1.058053	1.294758	1	-1.063706	1.113324	1.241152	1	-1.066134	1.115365	1.241297
1	0.834195	1.548605	-1.443499	1	1.008900	1.486104	-1.472988	1	0.963875	1.509602	-1.456989
	M33 CBS-QB3				M33 CBS-APNO				M33 G3		
6	-1.695044	1.095574	-0.222748	6	-1.790063	1.022731	-0.218694	6	-1.781662	1.028163	-0.223280
6	-1.042954	-0.154402	0.058659	6	-1.035861	-0.160669	0.068177	6	-1.035451	-0.156621	0.069148
6	0.282368	-0.135251	0.832278	6	0.280852	-0.050247	0.823719	6	0.280945	-0.055353	0.826853
6	1.402217	0.488347	0.039774	6	1.389986	0.500640	-0.037997	6	1.392868	0.501349	-0.028889
6	2.459921	-0.173346	-0.418931	6	2.479253	-0.161872	-0.367801	6	2.475610	-0.165191	-0.375346
1	3.234166	0.324323	-0.991620	1	3.238491	0.282799	-0.986979	1	3.237594	0.281349	-0.988814
1	1.312762	1.552704	-0.169579	1	1.259820	1.509185	-0.400630	1	1.269146	1.516902	-0.371367
1	0.135444	0.423815	1.765158	1	0.142106	0.596814	1.687497	1	0.142729	0.580607	1.698914
1	0.518648	-1.169591	1.085054	1	0.537775	-1.039630	1.178958	1	0.535933	-1.048453	1.173118
8	-1.538845	-1.218181	-0.314829	8	-1.450203	-1.250904	-0.298057	8	-1.458585	-1.250727	-0.297839
1	-2.622434	1.077709	-0.781296	1	-2.706288	0.929594	-0.771217	1	-2.696596	0.941796	-0.777497
1	2.590169	-1.235223	-0.235781	1	2.653035	-1.170751	-0.033146	1	2.643316	-1.180870	-0.061037
1	-1.297048	2.046190	0.112501	1	-1.468325	1.995722	0.105553	1	-1.457305	2.000400	0.098480
	M34 CBS-QB3				M34 CBS-APNO				M34 G3		
6	-0.066209	-1.217053	0.134804	6	-0.061520	-1.208993	0.160699	6	-0.063144	-1.211255	0.151034
6	0.893485	-0.029088	0.009955	6	0.887838	-0.027660	0.011171	6	0.886833	-0.028223	0.009827
6	0.078374	1.272755	0.038611	6	0.086057	1.269970	0.033708	6	0.089086	1.272068	0.034238
6	-1.342590	0.828273	0.039800	6	-1.342920	0.820737	0.087454	6	-1.341208	0.825222	0.079961
6	-1.478641	-0.658274	-0.127674	6	-1.460704	-0.662462	-0.161082	6	-1.466999	-0.661074	-0.150126
1	-1.809732	-0.912015	-1.147420	1	-1.715268	-0.857229	-1.204115	1	-1.746320	-0.869855	-1.183109
1	-2.187654	1.503827	0.048989	1	-2.177872	1.494207	0.025967	1	-2.173830	1.500322	0.011752
1	0.368448	1.862389	0.920871	1	0.390169	1.871049	0.887908	1	0.389856	1.867676	0.893627
1	0.361896	1.891797	-0.826452	1	0.327997	1.850377	-0.856097	1	0.336600	1.859457	-0.848899
8	2.090444	-0.102562	-0.091731	8	2.062651	-0.102111	-0.102754	8	2.067564	-0.105160	-0.098256
1	0.242707	-2.021691	-0.534191	1	0.259820	-2.035388	-0.460122	1	0.250412	-2.026255	-0.488731
1	-2.233925	-1.085749	0.540994	1	-2.238333	-1.122623	0.439513	1	-2.232666	-1.111235	0.473141
1	0.028192	-1.597743	1.158081	1	-0.000221	-1.533056	1.197275	1	0.008026	-1.559261	1.178668
	M35 CBS-QB3				M35 CBS-APNO				M35 G3		
6	-0.806868	0.947842	0.132370	6	-0.805240	0.947872	0.131785	6	-0.804968	0.955416	0.126254
6	-1.481918	-0.322617	-0.372100	6	-1.477421	-0.327053	-0.355346	6	-1.461634	-0.329111	-0.357092
6	2.220197	-0.949061	-0.161707	6	2.208194	-0.943518	-0.161971	6	2.189066	-0.953117	-0.163535

Table 13: Cartesian coordinates for minima (M28–M35) on the C_5H_7O potential energy surface.

At. No.	X	Y	Z	At. No.	X	Y	Z	At. No.	X	Y	Z
6	1.525355	0.009183	0.442963	6	1.520059	0.004957	0.440187	6	1.513739	0.003418	0.442446
6	0.677892	1.035806	-0.257039	6	0.673074	1.034706	-0.258273	6	0.677072	1.044111	-0.253155
1	0.774365	0.924839	-1.340711	1	0.771130	0.928252	-1.333620	1	0.781597	0.945938	-1.328495
1	1.545659	0.073151	1.530264	1	1.543641	0.066051	1.518552	1	1.537167	0.062093	1.520132
1	2.809765	-1.664247	0.400496	1	2.793372	-1.652779	0.396539	1	2.764914	-1.673285	0.389582
1	2.223915	-1.053734	-1.242351	1	2.213127	-1.047489	-1.234307	1	2.193997	-1.054587	-1.235413
8	-2.359293	-0.928922	0.132412	8	-2.344201	-0.924797	0.124441	8	-2.334691	-0.929328	0.126435
1	-1.367031	1.769439	-0.330052	1	-1.362990	1.759820	-0.328190	1	-1.360973	1.764637	-0.340078
1	1.034519	2.040426	-0.001245	1	1.031410	2.028207	0.000145	1	1.035442	2.035000	0.013802
1	-0.954799	1.014584	1.217377	1	-0.948069	1.014541	1.207063	1	-0.954272	1.030527	1.199484

Table 14: Cartesian coordinates for minima (M36–M40) on the C_5H_7O potential energy surface.

At. No.	X	Y	Z	At. No.	X	Y	Z	At. No.	X	Y	Z
	M36 CBS-QB3				M36 CBS-APNO				M36 G3		
6	-0.674190	0.117638	0.003781	6	-0.661212	0.113469	0.002717	6	-0.661849	0.114872	0.003086
6	0.177664	1.145552	0.000080	6	0.169525	1.137434	-0.000360	6	0.172092	1.137719	0.001910
6	1.332021	-0.854292	-0.082199	6	1.322926	-0.857526	-0.100037	6	1.323733	-0.859719	-0.100359
8	-0.025138	-1.108014	0.008102	8	-0.025574	-1.094102	0.009540	8	-0.026640	-1.095452	0.007370
1	-0.099533	2.188542	-0.001379	1	-0.117661	2.169351	-0.001578	1	-0.109619	2.171314	0.000875
6	-2.158603	0.039766	0.002063	6	-2.146992	0.038057	0.003194	6	-2.149068	0.039495	0.003385
1	-2.515830	-0.489842	-0.886231	1	-2.493032	-0.496575	-0.875888	1	-2.498611	-0.491999	-0.875714
1	-2.516441	-0.511172	0.877044	1	-2.491987	-0.504189	0.878083	1	-2.497612	-0.503230	0.876082
1	-2.594071	1.039271	0.014196	1	-2.579338	1.030509	0.008169	1	-2.582102	1.031433	0.010465
6	1.593536	0.618848	0.009554	6	1.588618	0.621824	0.012408	6	1.590257	0.620766	0.010732
1	2.197935	0.997821	-0.828802	1	2.188125	0.992912	-0.816685	1	2.187143	0.991904	-0.820244
1	2.143126	0.904692	0.924052	1	2.120295	0.882329	0.929222	1	2.127080	0.882928	0.923485
1	1.963354	-1.670275	0.236615	1	1.940998	-1.641071	0.294820	1	1.935846	-1.637533	0.313569
	M37 CBS-QB3				M37 CBS-APNO				M37 G3		
6	-1.851375	-0.284318	-0.000049	6	-1.877695	-0.248837	0.000032	6	-1.875921	-0.252480	0.000024
6	-1.113567	1.033585	0.000178	6	-1.085801	1.034409	0.000218	6	-1.091470	1.036277	0.000220
6	0.391969	0.990251	-0.000182	6	0.417738	0.954465	-0.000191	6	0.412517	0.957931	-0.000193
6	1.154809	-0.074979	0.000222	6	1.167578	-0.133334	0.000292	6	1.163132	-0.133921	0.000299
8	-1.355972	-1.379591	-0.000168	8	-1.446825	-1.347338	-0.000379	8	-1.433120	-1.352699	-0.000385
1	-1.487795	1.601942	-0.865497	1	-1.430963	1.606365	-0.862450	1	-1.437357	1.609079	-0.861365
1	0.870035	1.979411	-0.000820	1	0.915957	1.918794	-0.000860	1	0.907128	1.923023	-0.000870
6	2.584507	-0.409989	0.000030	6	2.624049	-0.409937	0.000081	6	2.621921	-0.405414	0.000087
1	2.852178	-1.002427	-0.880663	1	2.906976	-0.984828	-0.876265	1	2.909386	-0.979486	-0.875096
1	3.209792	0.497135	-0.000714	1	3.195366	0.517748	-0.000664	1	3.193389	0.521640	-0.000663
1	2.852680	-1.001330	0.881306	1	2.907449	-0.983709	0.877009	1	2.909857	-0.978358	0.875855
1	-2.959762	-0.166682	0.000131	1	-2.964848	-0.082133	0.000279	1	-2.961583	-0.097234	0.000287
1	-1.487408	1.601376	0.866404	1	-1.430548	1.605862	0.863393	1	-1.436940	1.608567	0.862319
	M38 CBS-QB3				M38 CBS-APNO				M38 G3		
6	-2.436648	-0.805208	0.037308	6	-2.412585	-0.827684	0.026778	6	-2.395357	-0.839975	0.031190
6	-1.695077	0.399879	-0.352641	6	-1.717653	0.427166	-0.349523	6	-1.718911	0.424692	-0.350147
6	-0.550375	1.014421	-0.183331	6	-0.555637	1.026772	-0.151415	6	-0.559516	1.037665	-0.152663
6	0.603978	0.497337	0.670152	6	0.593678	0.465208	0.663502	6	0.597552	0.488076	0.660446
6	1.790050	0.111679	-0.192606	6	1.772927	0.105959	-0.211182	6	1.762818	0.101162	-0.221603

Table 14: Cartesian coordinates for minima (M36–M40) on the C_5H_7O potential energy surface.

At. No.	X	Y	Z	At. No.	X	Y	Z	At. No.	X	Y	Z
8	2.328454	-0.964394	-0.167779	8	2.346661	-0.925979	-0.162544	8	2.335577	-0.936838	-0.151953
1	-1.848635	-1.442195	0.715306	1	-1.779153	-1.466324	0.638599	1	-1.756695	-1.467521	0.648338
1	-2.696183	-1.407507	-0.838876	1	-2.695802	-1.385966	-0.859849	1	-2.668361	-1.409196	-0.851516
1	-3.370622	-0.547795	0.546743	1	-3.317370	-0.610516	0.585892	1	-3.305732	-0.637201	0.586308
1	-0.374899	1.965772	-0.686607	1	-0.393417	1.992359	-0.607585	1	-0.405136	2.003373	-0.609599
1	0.319393	-0.368805	1.268694	1	0.309957	-0.413824	1.226299	1	0.315440	-0.377094	1.245159
1	0.930404	1.297534	1.348652	1	0.933369	1.223237	1.368958	1	0.948595	1.256751	1.348284
1	2.141336	0.909492	-0.884970	1	2.084749	0.884338	-0.920924	1	2.067749	0.855866	-0.954696
	M39 CBS-QB3				M39 CBS-APNO				M39 G3		
6	2.739535	-0.586586	0.041984	6	2.751824	-0.562355	0.037817	6	2.755384	-0.561842	0.038390
6	1.333094	-0.166808	0.027147	6	1.312790	-0.207215	0.020854	6	1.314171	-0.210130	0.028106
6	0.600278	0.919543	0.016667	6	0.592829	0.901117	0.019916	6	0.594659	0.903142	0.014046
6	-0.910936	0.968471	0.016185	6	-0.916302	0.966576	0.023152	6	-0.915032	0.965576	0.026094
6	-1.557800	-0.359972	-0.319892	6	-1.582543	-0.338437	-0.339724	6	-1.578096	-0.341653	-0.337254
8	-2.504771	-0.820682	0.262365	8	-2.461652	-0.828663	0.279758	8	-2.475350	-0.823497	0.273729
1	2.986419	-1.191984	-0.835662	1	3.020200	-1.141350	-0.840167	1	3.019893	-1.154790	-0.831247
1	2.966317	-1.185969	0.929137	1	2.992775	-1.154935	0.914577	1	3.007775	-1.140248	0.921184
1	3.409080	0.287565	0.046705	1	3.365641	0.336976	0.054403	1	3.370480	0.336153	0.035173
1	1.104744	1.894294	0.017286	1	1.108996	1.854255	0.039834	1	1.108440	1.856743	0.014382
1	-1.247356	1.690602	-0.742650	1	-1.241026	1.703648	-0.711566	1	-1.246636	1.706735	-0.700954
1	-1.307185	1.314058	0.975915	1	-1.294067	1.286363	0.988643	1	-1.290408	1.280300	0.994113
1	-1.098875	-0.890994	-1.182200	1	-1.210894	-0.813773	-1.255873	1	-1.193257	-0.827473	-1.238775
	M40 CBS-QB3				M40 CBS-APNO				M40 G3		
6	2.735241	-0.482842	-0.026171	6	2.731941	-0.480271	-0.024383	6	2.732399	-0.482288	-0.027264
6	1.489523	0.319282	-0.257759	6	1.482683	0.320686	-0.254311	6	1.485506	0.325379	-0.249836
6	0.342894	0.162382	0.401021	6	0.343503	0.149026	0.388879	6	0.341317	0.144535	0.387059
6	-0.896102	0.968887	0.141707	6	-0.893856	0.964973	0.140293	6	-0.893909	0.965673	0.146390
6	-2.120489	0.127997	-0.249899	6	-2.109804	0.121816	-0.233642	6	-2.105114	0.124716	-0.252776
8	-2.293257	-1.027198	-0.084159	8	-2.295344	-1.010962	-0.088567	8	-2.300459	-1.010480	-0.082291
1	3.571245	0.162435	0.265435	1	3.552072	0.164608	0.281018	1	3.554003	0.153091	0.292625
1	3.043115	-1.001387	-0.940892	1	3.039871	-0.981053	-0.938661	1	3.045345	-0.970515	-0.946250
1	2.592052	-1.230550	0.756965	1	2.585116	-1.232229	0.742723	1	2.581280	-1.246220	0.726787
1	0.257600	-0.609880	1.161850	1	0.257482	-0.623377	1.136027	1	0.249664	-0.638889	1.120778
1	-0.744127	1.724574	-0.632363	1	-0.743746	1.704196	-0.637085	1	-0.736188	1.721274	-0.613453

Table 14: Cartesian coordinates for minima (M36–M40) on the C_5H_7O potential energy surface.

At. No.	X	Y	Z	At. No.	X	Y	Z	At. No.	X	Y	Z
1	-1.229945	1.510877	1.037486	1	-1.201276	1.507137	1.033043	1	-1.206973	1.489866	1.047841
1	1.549709	1.087288	-1.028605	1	1.546433	1.091034	-1.009539	1	1.555347	1.107143	-0.991431

Table 15: Cartesian coordinates for minima (M41–M48) on the C_5H_7O potential energy surface.

At. No.	X	Y	Z	At. No.	X	Y	Z	At. No.	X	Y	Z
	M41 CBS-QB3				M41 CBS-APNO				M41 G3		
6	0.682677	0.094983	-0.000004	6	0.676720	0.096931	0.000006	6	0.677601	0.098476	0.000006
6	-0.157072	1.196196	-0.000002	6	-0.152641	1.199821	0.000004	6	-0.154179	1.201415	0.000004
6	-1.443116	-0.737802	-0.000002	6	-1.426902	-0.747369	0.000008	6	-1.427776	-0.748090	0.000005
8	-0.032333	-1.074574	0.000001	8	-0.042489	-1.059379	-0.000010	8	-0.042866	-1.060203	-0.000006
1	0.181820	2.222117	0.000002	1	0.183458	2.217766	0.000013	1	0.179336	2.220354	0.000010
6	2.158931	-0.037727	0.000002	6	2.155438	-0.045409	-0.000001	6	2.157492	-0.045680	-0.000001
1	2.506001	-0.590661	0.880906	1	2.487717	-0.595344	0.876792	1	2.492337	-0.594827	0.875725
1	2.506007	-0.590668	-0.880896	1	2.487712	-0.595306	-0.876819	1	2.492332	-0.594792	-0.875752
1	2.631507	0.945507	-0.000001	1	2.630842	0.928454	0.000019	1	2.634505	0.927132	0.000017
6	-1.473235	0.759822	0.000003	6	-1.470826	0.755616	-0.000012	6	-1.472005	0.755427	-0.000010
1	-2.371871	1.356745	0.000001	1	-2.366522	1.343388	-0.000017	1	-2.368649	1.341804	-0.000011
1	-1.901949	-1.199642	-0.886217	1	-1.887021	-1.190743	-0.879893	1	-1.886862	-1.193679	-0.878411
1	-1.901958	-1.199637	0.886219	1	-1.887007	-1.190718	0.879941	1	-1.886858	-1.193661	0.878441
	M42 CBS-QB3				M42 CBS-APNO				M42 G3		
6	-0.835461	0.154691	-0.000010	6	-0.845085	0.158474	-0.000010	6	-0.844527	0.154909	-0.000010
6	0.184554	-0.899372	0.000015	6	0.180830	-0.891299	0.000026	6	0.179502	-0.892572	0.000028
6	1.575997	-0.718007	0.000020	6	1.575605	-0.714140	0.000028	6	1.575472	-0.715355	0.000030
6	2.256108	0.475178	0.000000	6	2.278439	0.475921	-0.000005	6	2.280121	0.474928	-0.000006
8	-0.566073	1.349376	-0.000034	8	-0.579148	1.331216	-0.000047	8	-0.576704	1.334212	-0.000049
1	-0.182495	-1.921333	0.000033	1	-0.182188	-1.905160	0.000056	1	-0.183299	-1.906231	0.000060
1	2.168372	-1.630571	0.000041	1	2.153631	-1.624512	0.000060	1	2.152877	-1.625491	0.000063
6	-2.282194	-0.316758	0.000004	6	-2.284276	-0.312432	0.000004	6	-2.286311	-0.310780	0.000004
1	-2.942601	0.549012	-0.000131	1	-2.943312	0.544573	-0.000092	1	-2.942431	0.548355	-0.000085
1	-2.487837	-0.933238	-0.880936	1	-2.482875	-0.922869	-0.876539	1	-2.491778	-0.919814	-0.875545
1	-2.487882	-0.932982	0.881115	1	-2.482904	-0.922689	0.876667	1	-2.491804	-0.919647	0.875665
1	3.339657	0.482559	0.000006	1	3.353474	0.456128	0.000001	1	3.354601	0.456396	0.000000
1	1.727345	1.417157	-0.000022	1	1.784272	1.425659	-0.000038	1	1.789925	1.425953	-0.000040
	M43 CBS-QB3				M43 CBS-APNO				M43 G3		
6	-1.000869	-0.101949	0.000020	6	-0.999225	-0.103169	-0.000583	6	0.995645	-0.102475	-0.000049
6	0.182929	-0.967796	-0.000018	6	0.181956	-0.967049	-0.000186	6	-0.180229	-0.968720	0.000111
6	1.556548	-0.673600	-0.000034	6	1.558812	-0.669461	0.000036	6	-1.558423	-0.671712	0.000128
6	2.205609	0.536259	-0.000081	6	2.211079	0.548616	-0.000016	6	-2.211144	0.547361	-0.000039
8	-2.105816	-0.633739	-0.000097	8	-2.083125	-0.641932	0.000363	8	2.087428	-0.640719	-0.000136

Table 15: Cartesian coordinates for minima (M41–M48) on the C_5H_7O potential energy surface.

At. No.	X	Y	Z	At. No.	X	Y	Z	At. No.	X	Y	Z
1	-0.095409	-2.016724	-0.000052	1	-0.086387	-2.008778	-0.000023	1	0.088571	-2.009765	0.000191
1	2.198396	-1.552086	-0.000020	1	2.195354	-1.539524	0.000292	1	-2.194969	-1.541059	0.000250
6	-0.886349	1.411324	0.000183	6	-0.911257	1.405682	0.000099	6	0.907941	1.406937	0.000000
1	-1.891679	1.830039	0.000377	1	-1.916188	1.804394	0.000709	1	1.912522	1.806309	-0.000406
1	-0.347113	1.764859	0.883750	1	-0.384332	1.762772	0.879002	1	0.382557	1.768175	-0.877788
1	-0.347407	1.765041	-0.883494	1	-0.385110	1.763526	-0.878955	1	0.383284	1.768195	0.878207
1	3.288158	0.565765	-0.000089	1	3.285546	0.571278	0.000198	1	-3.284987	0.572599	-0.000030
1	1.694375	1.487586	-0.000117	1	1.707930	1.494068	-0.000224	1	-1.709141	1.492953	-0.000244
	M44 CBS-QB3				M44 CBS-APNO				M44 G3		
6	1.037867	-0.038514	-0.017438	6	1.031429	-0.024184	-0.015920	6	1.029232	-0.020861	-0.015696
6	-0.114786	-0.944901	-0.288167	6	-0.100002	-0.952544	-0.208144	6	-0.094867	-0.956742	-0.190999
6	-1.424944	-0.707031	-0.151801	6	-1.422247	-0.728968	-0.120096	6	-1.422720	-0.737376	-0.111312
6	-2.118094	0.540017	0.312960	6	-2.151734	0.537597	0.238945	6	-2.156264	0.535115	0.221425
8	2.102002	-0.525392	0.394149	8	2.130696	-0.519392	0.295982	8	2.144087	-0.513858	0.272259
1	0.205395	-1.946846	-0.558106	1	0.227332	-1.958579	-0.407746	1	0.237188	-1.964360	-0.370978
1	-2.092581	-1.537238	-0.374040	1	-2.057060	-1.579464	-0.310251	1	-2.053601	-1.592708	-0.287285
6	0.966358	1.368964	-0.298311	6	0.961795	1.382464	-0.225024	6	0.950930	1.386896	-0.207666
1	1.830222	1.974467	-0.053170	1	1.846536	1.961213	-0.036486	1	1.835136	1.968671	-0.030718
1	0.129828	1.822973	-0.812808	1	0.093138	1.869672	-0.620670	1	0.075046	1.877064	-0.581387
1	-1.439785	1.272840	0.749575	1	-1.551720	1.210356	0.837525	1	-1.578206	1.194315	0.856007
1	-2.871073	0.286940	1.065815	1	-3.045116	0.295442	0.804922	1	-3.079653	0.302256	0.740265
1	-2.656416	1.018779	-0.513925	1	-2.474130	1.070303	-0.653725	1	-2.426472	1.083437	-0.678493
	M45 CBS-QB3				M45 CBS-APNO				M45 G3		
6	-0.958206	-0.122294	0.000001	6	-0.972100	-0.106348	-0.000017	6	-0.973307	-0.102042	0.000089
6	0.078605	0.943533	0.000107	6	0.075689	0.932149	0.000090	6	0.073314	0.933827	0.000119
6	1.410558	0.781162	0.000058	6	1.410595	0.772834	0.000067	6	1.411909	0.774186	0.000054
6	2.197586	-0.490923	-0.000093	6	2.224832	-0.488546	-0.000073	6	2.226456	-0.488071	-0.000075
8	-0.704861	-1.337534	0.000055	8	-0.712674	-1.319383	0.000027	8	-0.710419	-1.321584	-0.000039
1	-0.304498	1.960063	0.000210	1	-0.294931	1.943927	0.000188	1	-0.296603	1.945559	0.000206
1	2.006970	1.692565	0.000141	1	1.990358	1.683303	0.000168	1	1.992366	1.683312	0.000125
6	-2.331347	0.311918	-0.000107	6	-2.342681	0.297081	-0.000084	6	-2.344599	0.294293	-0.000087
1	-3.105647	-0.444518	-0.000178	1	-3.100501	-0.463260	-0.000110	1	-3.100786	-0.466826	-0.000217
1	-2.612110	1.358375	-0.000114	1	-2.634838	1.330948	-0.000105	1	-2.643289	1.325687	-0.000116
1	1.558737	-1.368756	-0.000476	1	1.617291	-1.377665	-0.000493	1	1.618909	-1.377245	-0.000428

Table 15: Cartesian coordinates for minima (M41–M48) on the C_5H_7O potential energy surface.

At. No.	X	Y	Z	At. No.	X	Y	Z	At. No.	X	Y	Z
1	2.855885	-0.519163	0.876331	1	2.872745	-0.502861	0.873650	1	2.874855	-0.505711	0.872748
1	2.856380	-0.518669	-0.876154	1	2.873254	-0.502340	-0.873422	1	2.875261	-0.505264	-0.872602
	M46 CBS-QB3				M46 CBS-APNO				M46 G3		
6	-1.131262	0.171783	-0.098688	6	-1.117784	0.187228	-0.071427	6	-1.120799	0.182333	-0.067976
6	-0.040747	-0.753090	-0.570319	6	-0.060492	-0.710739	-0.572832	6	-0.059320	-0.707249	-0.576486
6	1.358160	-0.348768	-0.550414	6	1.375998	-0.355670	-0.549953	6	1.375937	-0.340495	-0.561916
6	1.923362	0.599783	0.453961	6	1.952631	0.610083	0.442437	6	1.956164	0.606755	0.447026
8	-1.615811	1.258691	-0.208057	8	-1.684862	1.207086	-0.192966	8	-1.702534	1.202134	-0.184633
1	-0.323718	-1.436103	-1.366410	1	-0.360507	-1.336711	-1.397830	1	-0.356805	-1.331633	-1.404289
1	1.943505	-0.571655	-1.435217	1	1.938506	-0.573452	-1.440540	1	1.926223	-0.522466	-1.467552
6	-0.919046	-0.995631	0.747916	6	-0.888687	-1.004659	0.735852	6	-0.874434	-1.010586	0.733040
1	-1.591189	-1.842921	0.667184	1	-1.587755	-1.821542	0.681211	1	-1.568722	-1.832604	0.685510
1	-0.477618	-0.851627	1.730417	1	-0.402448	-0.882716	1.689127	1	-0.383129	-0.890489	1.684248
1	1.646224	1.643722	0.237110	1	1.620774	1.630378	0.247152	1	1.601340	1.625863	0.293860
1	3.014551	0.553711	0.466180	1	3.035719	0.601777	0.397909	1	3.037676	0.622635	0.378270
1	1.571936	0.390882	1.470449	1	1.664620	0.368121	1.462237	1	1.698400	0.327072	1.464882
	M47 CBS-QB3				M47 CBS-APNO				M47 G3		
6	1.883223	0.233325	-0.191661	6	1.863218	0.203823	-0.211570	6	1.858485	0.202742	-0.224133
6	-0.531003	0.949159	-0.031647	6	-0.532452	0.944063	-0.031181	6	-0.535708	0.944850	-0.027651
6	-1.744541	0.463733	-0.296005	6	-1.734625	0.464231	-0.291156	6	-1.739203	0.465234	-0.287174
6	-2.287274	-0.901890	0.009219	6	-2.286684	-0.901398	0.008502	6	-2.288995	-0.903169	0.005914
8	2.665374	-0.641852	-0.305596	8	2.665489	-0.625366	-0.295296	8	2.677687	-0.622254	-0.287055
1	-0.305712	1.968329	-0.333501	1	-0.316362	1.957227	-0.329403	1	-0.320859	1.959428	-0.320105
1	-2.442997	1.133939	-0.792623	1	-2.426199	1.130736	-0.783026	1	-2.433680	1.131982	-0.773009
6	0.600628	0.231259	0.649087	6	0.606035	0.234680	0.650724	6	0.606812	0.234015	0.646713
1	0.880078	0.762290	1.569745	1	0.894579	0.780348	1.547604	1	0.899435	0.774969	1.545155
1	0.368085	-0.802885	0.917755	1	0.375513	-0.782503	0.939988	1	0.374802	-0.782141	0.938014
1	-2.641727	-1.386636	-0.906669	1	-2.627502	-1.374607	-0.908465	1	-2.634730	-1.372573	-0.910825
1	-3.151106	-0.831509	0.679551	1	-3.148758	-0.820574	0.665675	1	-3.147240	-0.830881	0.668582
1	-1.555806	-1.562230	0.476552	1	-1.568133	-1.560081	0.478088	1	-1.567566	-1.564788	0.466606
	M48 CBS-QB3				M48 CBS-APNO				M48 G3		
6	1.888253	-0.542927	-0.169915	6	1.896682	-0.524650	-0.165058	6	1.885531	-0.533491	-0.185100
6	-0.281207	0.591479	0.524530	6	-0.278095	0.581097	0.495227	6	-0.275293	0.582663	0.492878
6	-1.532673	0.676227	0.069160	6	-1.528074	0.674388	0.075785	6	-1.527304	0.676745	0.071708

Table 15: Cartesian coordinates for minima (M41–M48) on the C_5H_7O potential energy surface.

At. No.	X	Y	Z	At. No.	X	Y	Z	At. No.	X	Y	Z
6	-2.410138	-0.425030	-0.450186	6	-2.433786	-0.412833	-0.431643	6	-2.436203	-0.411929	-0.428153
8	2.427863	0.427285	-0.568162	8	2.444794	0.425208	-0.533186	8	2.451870	0.425900	-0.523235
1	0.212209	1.502940	0.848988	1	0.218838	1.481251	0.815397	1	0.225337	1.482282	0.806563
1	-1.990634	1.663311	0.071934	1	-1.973426	1.657134	0.095478	1	-1.971057	1.659505	0.083734
6	0.566756	-0.645418	0.607508	6	0.565964	-0.661949	0.569657	6	0.566093	-0.661212	0.574774
1	0.888849	-0.843930	1.639174	1	0.844897	-0.882250	1.598941	1	0.860554	-0.864732	1.603134
1	0.057278	-1.550151	0.274824	1	0.069835	-1.544275	0.191472	1	0.058860	-1.547236	0.221064
1	-2.730627	-0.208555	-1.475024	1	-2.770015	-0.179188	-1.438386	1	-2.774911	-0.186110	-1.435543
1	-3.322366	-0.506610	0.151043	1	-3.320838	-0.483148	0.192711	1	-3.322815	-0.480230	0.196560
1	-1.923565	-1.401267	-0.452226	1	-1.963789	-1.387504	-0.453939	1	-1.967879	-1.387327	-0.446266

Table 16: Cartesian coordinates of all transition state structures.

At. No.	X	Y	Z	At. No.	X	Y	Z	At. No.	X	Y	Z
	TS1 CBS-QB3				TS1 CBS-APNO				TS1 G3		
6	1.429601	-0.054846	0.338495	6	1.403890	-0.134241	0.329556	6	1.406305	-0.134398	0.329264
6	0.813886	1.110723	0.062061	6	0.876361	1.069055	0.101008	6	0.878424	1.069266	0.099985
6	-0.429571	0.710126	-0.577947	6	-0.381303	0.763224	-0.559233	6	-0.379441	0.762793	-0.557690
6	-0.473886	-0.707602	-0.722768	6	-0.508112	-0.619272	-0.740908	6	-0.511338	-0.620666	-0.741610
8	0.695095	-1.130812	-0.057898	8	0.627975	-1.125951	-0.094557	8	0.625986	-1.127747	-0.092677
1	2.382744	-0.273077	0.798026	1	2.331756	-0.413958	0.787681	1	2.333796	-0.417737	0.784642
1	1.169086	2.105513	0.277494	1	1.284474	2.024142	0.354634	1	1.284958	2.026096	0.350854
1	-1.081858	1.371024	-1.131743	1	-1.024884	1.473662	-1.038252	1	-1.020731	1.476547	-1.035301
6	-1.706733	-0.048632	0.577458	6	-1.694785	-0.053506	0.572424	6	-1.694038	-0.050969	0.570636
1	-2.644092	-0.203810	0.057615	1	-2.640622	-0.071307	0.060708	1	-2.640530	-0.055669	0.059634
1	-1.461656	-0.881093	1.228124	1	-1.530269	-0.954361	1.138236	1	-1.544341	-0.955890	1.133956
1	-1.724772	0.869321	1.169864	1	-1.620568	0.797860	1.236364	1	-1.620510	0.792474	1.244124
	TS2 CBS-QB3				TS2 CBS-APNO				TS2 G3		
6	-1.550163	0.538402	-0.033105	6	-1.538129	0.530778	-0.041553	6	-1.535988	0.531454	-0.041602
6	-0.233650	1.150716	-0.007636	6	-0.227378	1.143250	-0.006470	6	-0.228026	1.144454	-0.005424
6	0.630355	0.112927	-0.004364	6	0.614398	0.102109	-0.004989	6	0.615308	0.102839	-0.004345
8	-0.051041	-1.079237	0.001881	8	-0.045898	-1.057120	-0.003105	8	-0.046874	-1.057470	-0.001444
1	0.010548	2.200381	0.007977	1	0.019462	2.183035	0.017393	1	0.015517	2.185357	0.019257
6	2.113699	0.024717	0.006216	6	2.100188	0.021407	0.008825	6	2.102544	0.019908	0.007927
1	2.462069	-0.498289	0.901282	1	2.434613	-0.512150	0.892260	1	2.440342	-0.514002	0.889418
1	2.465288	-0.541445	-0.860796	1	2.444628	-0.526892	-0.861575	1	2.448468	-0.526912	-0.862349
1	2.560918	1.018696	-0.016896	1	2.538242	1.010989	0.002900	1	2.543020	1.008158	0.002554
6	-1.424272	-0.896531	-0.100200	6	-1.415284	-0.871969	-0.101947	6	-1.420392	-0.871248	-0.104120
1	-1.812685	-0.168679	0.990692	1	-1.788563	-0.280507	0.988312	1	-1.793527	-0.292198	0.982892
1	-2.493623	1.041842	-0.202774	1	-2.483970	1.029033	-0.137649	1	-2.479503	1.034912	-0.134832
	TS3 CBS-QB3				TS3 CBS-APNO				TS3 G3		
6	0.003612	-1.208487	0.190299	6	-0.029777	-1.212805	0.189446	6	-0.017078	-1.215087	0.191421
6	0.776789	-0.077130	0.480871	6	0.775428	-0.091511	0.486958	6	0.785342	-0.097147	0.490966
6	-0.527003	1.305328	0.172858	6	-0.504422	1.299413	0.169113	6	-0.522640	1.310010	0.169660
6	-1.659493	0.958111	-0.197381	6	-1.600687	0.886117	-0.197050	6	-1.609956	0.871450	-0.196873
8	-1.109278	-1.369108	-0.157790	8	-1.142246	-1.240131	-0.158460	8	-1.138187	-1.238439	-0.159602
1	0.971533	-0.004510	1.554147	1	0.964149	-0.015746	1.550338	1	0.977380	-0.013654	1.552050
1	0.056902	2.180616	0.405102	1	0.038428	2.190326	0.390528	1	0.018001	2.201512	0.391856

Table 16: Cartesian coordinates of all transition state structures.

At. No.	X	Y	Z	At. No.	X	Y	Z	At. No.	X	Y	Z
6	2.002699	0.199231	-0.379803	6	1.997322	0.161106	-0.378849	6	1.998686	0.169955	-0.381645
1	2.836091	-0.459456	-0.127379	1	2.800768	-0.523599	-0.133916	1	2.811610	-0.507260	-0.146785
1	1.769681	0.079830	-1.439529	1	1.754057	0.053079	-1.429524	1	1.750598	0.065225	-1.430933
1	2.330063	1.228427	-0.215308	1	2.356159	1.170220	-0.209918	1	2.350500	1.180870	-0.212167
1	-2.669668	0.865645	-0.515776	1	-2.602776	0.792857	-0.517541	1	-2.608715	0.745725	-0.518378
	TS4 CBS-QB3				TS4 CBS-APNO				TS4 G3		
6	-1.010330	0.497589	0.000007	6	-0.916639	0.499158	0.000057	6	-0.918022	0.509926	0.000026
6	-0.070701	1.309402	0.000042	6	0.008347	1.306534	-0.000007	6	0.010325	1.315457	0.000048
6	1.492491	-0.779080	-0.000037	6	1.413041	-0.862553	-0.000087	6	1.410494	-0.868443	-0.000044
8	0.510125	-1.429671	-0.000062	8	0.347999	-1.338688	-0.000017	8	0.333765	-1.337088	-0.000051
1	0.141906	2.363938	0.000077	1	0.227710	2.349588	-0.000026	1	0.243623	2.355605	0.000085
6	-2.279362	-0.219153	0.000020	6	-2.225717	-0.163480	0.000144	6	-2.223617	-0.162841	0.000012
1	-2.364185	-0.863291	-0.879824	1	-2.328138	-0.791708	-0.876695	1	-2.324571	-0.792505	-0.875694
1	-2.364144	-0.863326	0.879843	1	-2.328018	-0.791713	0.876994	1	-2.324573	-0.792536	0.875695
1	-3.135109	0.468245	0.000054	1	-3.025517	0.571961	0.000201	1	-3.031336	0.563393	0.000024
6	1.734721	0.593222	0.000016	6	1.752361	0.502075	-0.000115	6	1.764234	0.489657	0.000003
1	2.219808	0.959994	-0.904742	1	2.240750	0.840485	-0.902227	1	2.253117	0.830134	-0.899955
1	2.219805	0.959924	0.904804	1	2.240865	0.840494	0.901932	1	2.253134	0.830069	0.899975
	TS5 CBS-QB3				TS5 CBS-APNO				TS5 G3		
6	0.224799	1.282731	-0.050411	6	0.209595	1.266222	-0.065200	6	0.208200	1.266103	-0.066025
6	1.537924	0.641910	-0.061293	6	1.541853	0.622354	-0.046633	6	1.541138	0.622510	-0.046024
6	1.386266	-0.703989	-0.045247	6	1.380484	-0.697299	-0.028918	6	1.383280	-0.697769	-0.027929
8	0.087471	-1.071419	0.062145	8	0.078949	-1.039446	0.045367	8	0.077786	-1.040711	0.046468
1	2.483704	1.161148	-0.113125	1	2.479307	1.137656	-0.088811	1	2.477701	1.140007	-0.085958
6	-0.623311	0.149077	0.096896	6	-0.610144	0.134911	0.051556	6	-0.608154	0.134714	0.047205
1	-0.398641	0.822643	1.115243	1	-0.359137	0.875601	1.071638	1	-0.359899	0.901600	1.060397
6	-2.102427	-0.000948	-0.098158	6	-2.095747	-0.003957	-0.071279	6	-2.095564	-0.005244	-0.069356
1	-2.521546	-0.756142	0.569598	1	-2.483503	-0.715734	0.648200	1	-2.484008	-0.707837	0.657952
1	-2.589018	0.957630	0.078378	1	-2.562753	0.960445	0.072195	1	-2.562724	0.960191	0.064259
1	-2.304169	-0.303203	-1.128571	1	-2.333390	-0.360983	-1.067474	1	-2.337736	-0.372770	-1.060132
1	2.090405	-1.523414	-0.069404	1	2.071633	-1.514809	-0.035838	1	2.070971	-1.517392	-0.035493
					TS6 CBS-APNO				TS6 G3		
				6	0.768439	0.240417	0.490019	6	0.767112	0.242469	0.493139
				6	-0.111898	1.285751	0.176239	6	-0.111597	1.288855	0.179247

Table 16: Cartesian coordinates of all transition state structures.

At. No.	X	Y	Z	At. No.	X	Y	Z	At. No.	X	Y	Z
				6	-1.331297	0.814664	-0.195576	6	-1.329643	0.813777	-0.196900
				6	-1.357121	-0.614727	-0.151002	6	-1.356473	-0.612960	-0.152758
				8	-0.336828	-1.210419	0.187435	8	-0.333949	-1.214976	0.190516
				1	0.903767	0.051380	1.543734	1	0.908282	0.050483	1.544230
				1	-2.189448	1.392379	-0.481790	1	-2.188395	1.389629	-0.486062
				6	1.946973	-0.080372	-0.384389	6	1.942638	-0.079613	-0.387133
				1	2.728369	0.643044	-0.176010	1	2.723655	0.647849	-0.194616
				1	2.319291	-1.072899	-0.169428	1	2.322735	-1.067735	-0.168175
				1	1.679051	-0.006539	-1.430727	1	1.665884	-0.018196	-1.431510
				1	-2.236976	-1.198413	-0.397000	1	-2.232786	-1.197382	-0.401572
	TS7 CBS-QB3				TS7 CBS-APNO				TS7 G3		
6	-1.616736	-0.151596	-0.561445	6	-1.606142	-0.106481	-0.571864	6	-1.608163	-0.112786	-0.572492
6	-0.441277	0.350180	-0.300200	6	-0.437320	0.360969	-0.272004	6	-0.437748	0.359340	-0.278163
6	0.742137	0.825366	-0.030768	6	0.737610	0.815739	0.026409	6	0.738175	0.816351	0.020536
6	1.873189	-0.039774	0.478111	6	1.865312	-0.077286	0.468210	6	1.864248	-0.072270	0.471262
8	2.658304	-0.605170	-0.233786	8	2.638618	-0.575383	-0.270420	8	2.643476	-0.577890	-0.266060
1	-1.794890	-0.529994	-1.566992	1	-1.779019	-0.396944	-1.596452	1	-1.785572	-0.415290	-1.592213
1	0.972196	1.882122	-0.163168	1	0.950887	1.871995	-0.028555	1	0.952689	1.871617	-0.044103
6	-2.759200	-0.246348	0.418260	6	-2.744590	-0.273510	0.401464	6	-2.745837	-0.269563	0.404320
1	-3.631610	0.300935	0.047061	1	-3.604390	0.306863	0.079569	1	-3.606877	0.307346	0.080826
1	-3.065408	-1.288670	0.553069	1	-3.050615	-1.314533	0.449422	1	-3.054340	-1.308813	0.464814
1	-2.484718	0.161491	1.391821	1	-2.462715	0.049990	1.395680	1	-2.463174	0.062965	1.395176
1	1.949312	-0.111490	1.584753	1	1.947686	-0.230892	1.550404	1	1.945421	-0.221136	1.551207
	TS8 CBS-QB3				TS8 CBS-APNO						
6	1.215642	0.010170	0.522557	6	1.112947	0.039487	0.508824				
6	0.511072	1.143286	0.054854	6	0.527538	1.247043	0.038497				
6	-0.747739	1.134079	-0.220360	6	-0.769434	1.123234	-0.215288				
6	-1.348676	-0.386557	0.075545	6	-1.278655	-0.250436	0.035144				
8	-2.423761	-0.798173	-0.042884	8	-2.186550	-0.926235	-0.017967				
1	1.513288	0.071659	1.573996	1	1.334198	0.031950	1.569073				
1	-1.500362	1.825575	-0.562570	1	-1.506214	1.825647	-0.556561				
6	2.289211	-0.632657	-0.348433	6	2.146403	-0.681612	-0.328572				
1	3.204202	-0.035262	-0.339028	1	3.088180	-0.146461	-0.262251				
1	2.533968	-1.628912	0.027083	1	2.299615	-1.691058	0.035542				

Table 16: Cartesian coordinates of all transition state structures.

At. No.	X	Y	Z	At. No.	X	Y	Z	At. No.	X	Y	Z
1	1.952052	-0.722827	-1.382940	1	1.847068	-0.717262	-1.369030				
1	0.169877	-0.734775	0.521554	1	-0.003235	-0.759240	0.495330				
									TS9 G3		
								6	1.612817	0.273984	0.421807
								6	0.547488	0.888027	-0.034041
								6	-0.611372	1.348699	-0.355389
								6	-1.855746	-0.246320	0.478756
								8	-2.370818	-0.981065	-0.200258
								1	2.102260	0.678863	1.293718
								1	-0.776087	2.145372	-1.061854
								6	2.260413	-0.917534	-0.240348
								1	3.265956	-0.679825	-0.578248
								1	2.344753	-1.752537	0.451125
								1	1.687091	-1.246164	-1.099150
								1	-1.379034	0.621672	0.971757
	TS10 CBS-QB3				TS10 CBS-APNO				TS10 G3		
6	-1.584641	0.766631	-0.103169	6	-1.585216	0.740628	-0.100551	6	-1.587954	0.737818	-0.100494
6	-0.191681	1.181764	-0.001408	6	-0.177568	1.174452	-0.004005	6	-0.180687	1.173690	-0.003989
6	0.627957	0.095855	-0.009750	6	0.620162	0.104475	-0.008923	6	0.621451	0.106684	-0.008353
8	-0.096757	-1.059820	-0.009355	8	-0.112521	-1.035963	-0.010504	8	-0.111809	-1.038024	-0.008308
1	0.149876	2.206750	0.025168	1	0.154573	2.192549	0.008990	1	0.148085	2.193146	0.010172
6	2.105754	-0.063196	0.010000	6	2.096820	-0.074262	0.012775	6	2.099307	-0.072374	0.012137
1	2.423430	-0.612557	0.900938	1	2.395793	-0.629809	0.895864	1	2.402367	-0.628784	0.892821
1	2.445486	-0.627912	-0.862873	1	2.421277	-0.631995	-0.859776	1	2.426984	-0.627075	-0.860703
1	2.590810	0.913004	0.008031	1	2.588836	0.889491	0.018674	1	2.591767	0.890925	0.019860
6	-1.429988	-0.636307	-0.024082	6	-1.403574	-0.637519	-0.036825	6	-1.402355	-0.637724	-0.038406
1	-1.863160	-0.036125	0.987235	1	-1.844366	0.050167	0.980992	1	-1.856904	0.058994	0.973001
1	-2.136782	-1.433083	-0.213205	1	-2.119693	-1.429340	-0.135536	1	-2.116394	-1.431570	-0.134052
	TS11 CBS-QB3								TS11 G3		
6	-1.528570	0.865155	0.000086					6	1.506331	0.860193	0.000004
6	-0.187839	1.185019	-0.000030					6	0.189693	1.162642	0.000005
6	0.620938	0.011721	-0.000090					6	-0.627405	-0.030328	-0.000001
8	-0.013372	-1.100113	-0.000020					8	-0.045296	-1.120422	-0.000012
1	0.247116	2.177808	-0.000044					1	-0.250169	2.142441	0.000009

Table 16: Cartesian coordinates of all transition state structures.

At. No.	X	Y	Z	At. No.	X	Y	Z	At. No.	X	Y	Z
6	2.113095	-0.035589	0.000000					6	-2.127411	-0.007068	0.000002
1	2.465110	-0.579283	0.880732					1	-2.490658	-0.534591	-0.874826
1	2.465246	-0.582298	-0.878784					1	-2.490648	-0.534504	0.874887
1	2.541908	0.966450	-0.001588					1	-2.516093	1.002377	-0.000043
6	-1.619226	-0.548554	-0.000011					6	1.729681	-0.506329	0.000001
1	-2.001074	-1.024264	0.903403					1	2.042307	-0.993499	-0.906545
1	-2.001715	-1.024025	-0.903289					1	2.042291	-0.993503	0.906549
	TS12 CBS-QB3				TS12 CBS-APNO				TS12 G3		
6	-1.727762	1.089712	-0.192852	6	-1.715724	1.087987	-0.176909	6	-1.710658	1.094231	-0.172896
1	-1.874376	1.621045	0.752786	1	-1.857499	1.599275	0.771077	1	-1.864375	1.599714	0.776075
1	-1.124477	1.743451	-0.830499	1	-1.118728	1.739823	-0.807897	1	-1.109305	1.752446	-0.792534
1	-2.689104	0.890240	-0.665797	1	-2.672701	0.895600	-0.642981	1	-2.663297	0.909160	-0.650179
6	-0.985571	-0.206849	0.043317	6	-0.978767	-0.210836	0.040174	6	-0.978800	-0.208957	0.041280
8	-1.401175	-1.278933	-0.317682	8	-1.397804	-1.254276	-0.328012	8	-1.406794	-1.252871	-0.334180
6	0.330753	-0.085917	0.800302	6	0.331901	-0.111636	0.791495	6	0.331467	-0.121182	0.791890
1	0.260973	-0.119960	1.886239	1	0.278561	-0.165036	1.867474	1	0.277380	-0.187419	1.866939
6	1.484948	0.025719	0.210186	6	1.474819	0.017958	0.202342	6	1.476784	0.012493	0.203498
6	2.628768	0.133810	-0.404760	6	2.613279	0.144743	-0.399218	6	2.615436	0.147042	-0.399278
1	3.056729	1.103501	-0.639189	1	3.024477	1.116581	-0.609223	1	3.028949	1.119743	-0.598970
1	3.192852	-0.745661	-0.699240	1	3.175279	-0.721328	-0.701657	1	3.179619	-0.712434	-0.714854
	TS13 CBS-QB3				TS13 CBS-APNO				TS13 G3		
6	-1.384114	-0.775515	0.030655	6	-1.403979	-0.718343	0.011160	6	-1.381226	-0.759365	0.013083
6	-2.068624	0.403747	-0.217842	6	-2.099738	0.461801	-0.134043	6	-2.096495	0.414716	-0.109654
1	-2.720221	0.784665	0.567813	1	-2.687054	0.800316	0.706079	1	-2.677344	0.737602	0.741200
6	-0.302622	-1.350423	0.234936	6	-0.415752	-1.422301	0.145573	6	-0.333771	-1.387556	0.119881
1	0.243628	-2.257964	0.384817	1	0.058775	-2.365690	0.241341	1	0.194821	-2.304420	0.198549
6	1.169702	0.194778	0.013681	6	1.248667	0.202902	-0.002307	6	1.196639	0.203024	0.001770
6	0.507419	1.393526	0.213296	6	0.541761	1.396076	0.136342	6	0.510985	1.411554	0.108556
1	-0.904367	1.100375	-0.135224	1	-0.773244	1.134816	-0.053267	1	-0.862991	1.118336	-0.058726
1	0.311936	1.637407	1.253705	1	0.590501	1.753181	1.154776	1	0.537543	1.813612	1.109655
1	0.870493	2.212447	-0.399951	1	0.857438	2.114830	-0.605076	1	0.782737	2.105884	-0.670459
8	2.142471	-0.402458	-0.262436	8	2.157329	-0.453479	-0.160315	8	2.150395	-0.423459	-0.132148
1	-2.471805	0.546057	-1.220030	1	-2.530799	0.669562	-1.101684	1	-2.554712	0.622420	-1.064854
	TS14 CBS-QB3										

Table 16: Cartesian coordinates of all transition state structures.

At. No.	X	Y	Z	At. No.	X	Y	Z	At. No.	X	Y	Z
6	-0.968845	0.265473	-0.089454								
6	0.014368	1.212190	-0.092206								
6	1.334832	0.791470	0.088533								
6	1.442017	-0.615412	0.066503								
8	0.401306	-1.303749	-0.082349								
1	-0.234530	2.233565	-0.362846								
1	2.184318	1.456356	0.146631								
6	-2.184970	-0.204804	0.085556								
1	-2.509789	-1.123799	-0.388869								
1	-2.883413	0.293743	0.752899								
1	2.408554	-1.123379	0.157378								
	TS15 CBS-QB3				TS15 CBS-APNO						
6	-0.839295	1.005081	-0.096718	6	-0.809649	1.016674	-0.110765				
6	0.618519	1.116878	-0.077298	6	0.631532	1.129029	-0.067146				
6	-1.492574	-0.159238	-0.019548	6	-1.489681	-0.147696	0.056184				
6	1.492049	0.138309	-0.002367	6	1.491273	0.119210	-0.018858				
6	2.358974	-0.828150	0.078859	6	2.330753	-0.874515	0.044317				
8	-1.934791	-1.226010	-0.113469	8	-2.024080	-1.129730	-0.174971				
1	-2.373398	0.640179	1.641012	1	-1.719111	0.154053	2.007357				
1	-1.444764	1.898957	-0.131115	1	-1.420063	1.899418	-0.091531				
1	2.727318	-1.184533	1.038075	1	2.666614	-1.264583	0.991570				
1	2.750341	-1.319792	-0.808690	1	2.716440	-1.338779	-0.848885				
1	0.992797	2.135983	-0.129101	1	1.023391	2.131512	-0.081138				
	TS16 CBS-QB3				TS16 CBS-APNO				TS16 G3		
6	0.820775	1.026572	0.037963	6	0.834311	1.024752	0.032689	6	0.837487	1.025955	0.035895
6	-0.558870	1.135471	-0.151981	6	-0.546952	1.154209	-0.150606	6	-0.543852	1.157464	-0.151912
6	1.505555	-0.248210	0.410200	6	1.500702	-0.262722	0.402362	6	1.497253	-0.264050	0.405432
6	-1.454712	0.135061	-0.033960	6	-1.450138	0.150497	-0.012980	6	-1.449674	0.151947	-0.018520
6	-2.321368	-0.826853	0.055540	6	-2.308902	-0.830335	0.049862	6	-2.311938	-0.829962	0.051164
8	1.915288	-1.052811	-0.388063	8	1.873945	-1.061918	-0.384017	8	1.875174	-1.064853	-0.386116
1	1.639234	-0.420722	1.502364	1	1.649699	-0.430451	1.476272	1	1.637703	-0.439592	1.476230
1	1.447123	1.905408	-0.074960	1	1.468974	1.887270	-0.074335	1	1.473576	1.887239	-0.069721
1	-2.578998	-1.446151	-0.802696	1	-2.539903	-1.429228	-0.817447	1	-2.548729	-1.433743	-0.810368
1	-2.825687	-1.063335	0.991453	1	-2.814773	-1.078521	0.969775	1	-2.816657	-1.075533	0.971857

Table 16: Cartesian coordinates of all transition state structures.

At. No.	X	Y	Z	At. No.	X	Y	Z	At. No.	X	Y	Z
1	-0.952259	2.115046	-0.418229	1	-0.929681	2.127866	-0.410088	1	-0.922941	2.132335	-0.411429
	TS17 CBS-QB3				TS17 CBS-APNO				TS17 G3		
6	-0.783101	1.060567	0.067026	6	-0.776909	1.037001	0.000000	6	0.779308	1.034894	0.000106
6	0.580295	1.119013	-0.047036	6	0.588065	1.044780	-0.000001	6	-0.589386	1.046475	-0.000009
6	-1.246172	-0.299661	-0.099359	6	-1.289347	-0.342308	-0.000001	6	1.289595	-0.344290	0.000182
6	1.220324	-0.136748	-0.165408	6	1.194917	-0.255099	-0.000002	6	-1.199381	-0.251153	-0.000052
6	2.363723	-0.742450	0.101143	6	2.486368	-0.651055	0.000002	6	-2.492093	-0.652351	-0.000006
8	-2.264526	-0.887463	0.091836	8	-2.369434	-0.782825	0.000001	8	2.378038	-0.781869	-0.000203
1	-0.077769	-0.837790	-0.401194	1	-0.061360	-0.958377	0.000000	1	0.053252	-0.958927	0.000479
1	-1.457962	1.895865	0.195681	1	-1.419340	1.897046	0.000009	1	1.422671	1.893693	0.000226
1	3.147054	-0.258728	0.684688	1	3.295395	0.064939	0.000002	1	-3.304913	0.058071	-0.000753
1	2.564766	-1.756936	-0.228262	1	2.752972	-1.692888	0.000001	1	-2.756109	-1.694312	0.000606
1	1.129701	2.052973	-0.123802	1	1.169241	1.951969	-0.000001	1	-1.167466	1.954980	-0.000254
	TS18 CBS-QB3								TS18 G3		
6	-0.674268	0.435145	-0.085112					6	-0.683837	0.434998	-0.084008
6	0.504473	-0.241308	-0.102548					6	0.506536	-0.244230	-0.085231
6	-1.945236	-0.203152	-0.227393					6	-1.954466	-0.243181	-0.236984
6	1.794745	0.387086	0.017245					6	1.785705	0.394528	0.018000
6	2.954381	-0.286711	0.090840					6	2.963809	-0.282826	0.083116
8	-3.035362	-0.134504	0.223057					8	-3.022369	-0.111936	0.224223
1	1.808139	1.474373	0.046941					1	1.799275	1.471652	0.044782
1	-0.695069	1.525219	-0.057462					1	-0.711836	1.512979	-0.095034
1	2.980788	-1.371364	0.076500					1	2.996242	-1.357884	0.064007
1	3.904297	0.226955	0.170514					1	3.902749	0.233321	0.156478
1	0.480179	-1.325510	-0.179139					1	0.486040	-1.320315	-0.133372
	TS19 CBS-QB3										
6	-0.384860	0.691451	0.000023								
6	0.675530	-0.089781	0.000006								
6	-2.469957	-0.619058	-0.000032								
6	2.064918	0.375933	0.000015								
6	3.118974	-0.445234	-0.000005								
8	-3.413227	0.009497	-0.000010								
1	2.218718	1.451628	0.000038								
1	-0.598790	1.751076	0.000046								

Table 16: Cartesian coordinates of all transition state structures.

At. No.	X	Y	Z	At. No.	X	Y	Z	At. No.	X	Y	Z
1	2.997802	-1.523718	-0.000028								
1	4.133268	-0.064722	0.000002								
1	0.527190	-1.170111	-0.000018								
	TS20 CBS-QB3				TS20 CBS-APNO				TS20 G3		
6	0.761935	1.026456	-0.159361	6	0.786833	1.023852	-0.153915	6	0.781512	1.030878	-0.155310
6	-0.639761	1.109800	0.015388	6	-0.628703	1.112856	0.007226	6	-0.632852	1.114813	0.013268
6	1.509784	-0.076945	-0.029504	6	1.505000	-0.089101	-0.030699	6	1.502614	-0.085116	-0.034325
6	-1.461859	-0.028212	0.470237	6	-1.454627	-0.027494	0.470572	6	-1.452832	-0.030997	0.473640
6	-2.081525	-0.890939	-0.333537	6	-2.080070	-0.873410	-0.331780	6	-2.075988	-0.878279	-0.334114
8	2.185406	-1.019397	0.069379	8	2.145978	-1.028037	0.066836	8	2.151190	-1.029730	0.068059
1	-1.560704	-0.165378	1.550566	1	-1.537676	-0.165653	1.540488	1	-1.532808	-0.175434	1.542167
1	1.335212	1.908071	-0.432279	1	1.368979	1.890729	-0.410971	1	1.358615	1.899823	-0.416862
1	-2.021313	-0.803996	-1.413564	1	-2.029051	-0.779830	-1.403375	1	-2.028105	-0.780063	-1.404635
1	-2.671623	-1.709514	0.064818	1	-2.665207	-1.686517	0.061422	1	-2.655903	-1.697355	0.052608
1	-1.096264	2.085024	-0.103904	1	-1.075473	2.085344	-0.090681	1	-1.086044	2.083078	-0.096712
	TS21 CBS-QB3				TS21 CBS-APNO						
6	-0.212922	-1.171084	0.114064	6	0.285901	1.142892	0.102396				
6	1.165193	-0.962101	0.014956	6	-1.080042	1.033769	0.037936				
6	-1.069909	-0.098162	-0.101473	6	1.043906	-0.091024	-0.149474				
6	1.580872	0.367602	-0.131323	6	-1.614458	-0.269352	-0.134944				
6	0.663361	1.363884	0.172111	6	-0.770621	-1.362336	0.170573				
8	-2.162076	0.335776	-0.106592	8	2.182470	-0.320680	-0.074574				
1	2.521140	0.593587	-0.625775	1	-2.539921	-0.407159	-0.667166				
1	-0.670566	-2.144697	0.251382	1	0.813691	2.068612	0.248111				
1	0.083783	1.299801	1.087532	1	-0.295732	-1.411667	1.135144				
1	0.752351	2.363619	-0.238769	1	-0.916987	-2.314158	-0.311360				
1	1.850327	-1.799351	-0.031649	1	-1.708921	1.906121	0.032941				
	TS22 CBS-QB3				TS22 CBS-APNO				TS22 G3		
6	-0.112041	-1.236518	0.087725	6	-0.093839	-1.218780	0.083269	6	-0.094435	-1.219312	0.083863
6	-1.364350	-0.768663	0.038748	6	-1.380409	-0.746071	0.026386	6	-1.383617	-0.745163	0.028891
6	0.819151	-0.055951	-0.052378	6	0.833535	-0.052936	-0.041844	6	0.831932	-0.053885	-0.043736
6	-1.346168	0.720020	-0.130731	6	-1.369940	0.697683	-0.119793	6	-1.371768	0.697583	-0.119973
6	-0.079683	1.157901	-0.167520	6	-0.065451	1.151889	-0.121326	6	-0.065008	1.150382	-0.128472
8	2.025137	-0.076032	-0.082605	8	2.015725	-0.072941	-0.090182	8	2.020240	-0.074460	-0.088706

Table 16: Cartesian coordinates of all transition state structures.

At. No.	X	Y	Z	At. No.	X	Y	Z	At. No.	X	Y	Z
1	-2.242405	1.320988	-0.207424	1	-2.250023	1.305059	-0.202082	1	-2.251050	1.306113	-0.200709
1	0.229951	-2.253809	0.203586	1	0.236377	-2.232925	0.185545	1	0.235725	-2.233071	0.187742
1	0.288784	2.161104	-0.316906	1	0.287350	2.143942	-0.317680	1	0.288958	2.142328	-0.321947
1	0.297303	1.826164	2.219187	1	0.329724	1.716484	2.018076	1	0.337763	1.740659	2.037829
1	-2.276181	-1.346923	0.107333	1	-2.272600	-1.339753	0.077450	1	-2.275937	-1.337984	0.083293
	TS23a CBS-QB3				TS23a CBS-APNO				TS23a G3		
6	0.109750	1.188630	-0.032731	6	0.098830	1.177958	-0.047201	6	0.102000	1.175739	-0.047813
6	1.456409	0.806805	-0.111312	6	1.425670	0.815279	-0.108481	6	1.428242	0.814214	-0.106479
6	-0.820504	-0.039991	-0.009311	6	-0.818745	-0.045990	-0.008857	6	-0.817638	-0.045489	-0.010664
6	1.379787	-0.714904	0.007431	6	1.364624	-0.709745	0.004006	6	1.364422	-0.710283	0.003639
6	0.128096	-1.192826	-0.003311	6	0.132053	-1.192288	0.001815	6	0.130598	-1.193334	0.002329
8	-2.025271	-0.043901	0.007078	8	-1.998013	-0.040391	0.009473	8	-2.002779	-0.037003	0.010991
1	2.281510	-1.312615	0.053996	1	2.262841	-1.296730	0.036654	1	2.261578	-1.298432	0.037298
1	-0.270913	2.192986	-0.195450	1	-0.285726	2.179869	-0.128502	1	-0.283216	2.177008	-0.131377
1	-0.204097	-2.221598	0.027058	1	-0.186708	-2.215600	0.032769	1	-0.189107	-2.216213	0.030156
1	0.874433	1.406141	0.953183	1	0.979112	1.384303	0.935604	1	0.987228	1.388583	0.929919
	TS23b CBS-QB3				TS23b CBS-APNO				TS23b G3		
6	0.229503	1.381528	0.212423	6	0.406138	1.406143	0.269881	6	0.418465	1.409991	0.259309
6	1.288316	0.709316	-0.379869	6	1.276552	0.631537	-0.445855	6	1.293269	0.620071	-0.434960
6	-0.835093	-0.221125	0.038887	6	-0.882982	-0.220614	0.024483	6	-0.886825	-0.216993	0.025885
6	1.432833	-0.612865	-0.007699	6	1.339111	-0.702423	-0.044656	6	1.339961	-0.710968	-0.039493
6	0.170550	-1.210631	0.113213	6	0.085856	-1.230800	0.166133	6	0.075801	-1.231326	0.157679
8	-1.988775	-0.059257	-0.148577	8	-1.964272	0.074366	-0.178218	8	-1.976986	0.082735	-0.172072
1	2.371508	-1.147705	0.069976	1	2.242139	-1.284280	-0.002226	1	2.235258	-1.303393	0.009234
1	-0.263383	2.223936	-0.266176	1	0.000329	2.322202	-0.128330	1	0.020020	2.320631	-0.157226
1	-0.071725	-2.260263	0.219626	1	-0.206604	-2.238499	0.388877	1	-0.220900	-2.238988	0.375798
1	0.157146	1.380751	1.303462	1	0.330267	1.302589	1.347496	1	0.337484	1.335221	1.338246
	TS24 CBS-QB3				TS24 CBS-APNO				TS24 G3		
6	1.560099	0.615001	-0.068495	6	1.556558	0.609942	-0.076281	6	1.557922	0.610937	-0.078462
6	0.244748	1.160611	-0.034851	6	0.245794	1.161286	-0.022532	6	0.248856	1.162348	-0.019784
6	-0.627574	0.096936	0.057045	6	-0.622869	0.091619	0.102604	6	-0.623889	0.092289	0.110429
8	0.090747	-1.070399	0.010240	8	0.089573	-1.059687	0.016042	8	0.089413	-1.062042	0.019849
6	1.409155	-0.736584	-0.035749	6	1.396847	-0.735937	-0.043732	6	1.398697	-0.737358	-0.045442
1	2.493181	1.154249	-0.103039	1	2.486511	1.137307	-0.126023	1	2.487226	1.139659	-0.131518

Table 16: Cartesian coordinates of all transition state structures.

At. No.	X	Y	Z	At. No.	X	Y	Z	At. No.	X	Y	Z
1	-0.033918	2.202430	-0.038178	1	-0.031635	2.195110	-0.020150	1	-0.026713	2.196919	-0.017239
6	-2.100786	-0.023743	-0.144085	6	-2.089195	-0.020055	-0.164886	6	-2.088930	-0.019192	-0.171924
1	-2.516366	-0.817867	0.477970	1	-2.526436	-0.821304	0.417544	1	-2.530949	-0.827501	0.396216
1	-2.591193	0.914164	0.119190	1	-2.585981	0.908058	0.090290	1	-2.590749	0.903775	0.090645
1	-2.329875	-0.252803	-1.190366	1	-2.262170	-0.229175	-1.217612	1	-2.256435	-0.214994	-1.227528
1	-0.764431	0.249922	2.038767	1	-0.809244	0.195236	2.009568	1	-0.842966	0.196134	2.017384
1	2.102776	-1.560229	-0.029442	1	2.089562	-1.548865	-0.052990	1	2.089337	-1.551806	-0.055651
	TS25 CBS-QB3				TS25 CBS-APNO				TS25 G3		
6	0.349216	1.175192	0.316862	6	0.339650	1.172493	0.320714	6	0.342482	1.171970	0.321992
6	1.400848	0.612548	-0.454401	6	1.400693	0.619224	-0.437144	6	1.402850	0.621515	-0.439705
6	1.276936	-0.741991	-0.347876	6	1.274943	-0.734623	-0.340741	6	1.280085	-0.733665	-0.344921
8	0.219259	-1.067889	0.446084	8	0.218811	-1.066630	0.431171	8	0.223986	-1.068601	0.430168
1	0.132545	2.220145	0.470502	1	0.113353	2.206903	0.477219	1	0.116174	2.206293	0.479944
1	2.157011	1.139974	-1.014275	1	2.159887	1.144623	-0.979180	1	2.158437	1.150607	-0.983544
6	-0.405652	0.109576	0.784857	6	-0.431570	0.087959	0.759496	6	-0.425443	0.086865	0.762844
1	-1.076098	0.043827	1.625074	1	-1.048223	0.027637	1.631043	1	-1.042072	0.022058	1.633596
6	-2.230310	-0.018315	-0.590883	6	-2.199982	-0.011771	-0.580707	6	-2.216484	-0.011260	-0.578300
1	-2.669836	-0.941066	-0.230231	1	-2.649958	-0.927124	-0.232851	1	-2.670367	-0.921118	-0.224005
1	-2.774677	0.895640	-0.383439	1	-2.758775	0.889906	-0.388246	1	-2.767889	0.894296	-0.388068
1	-1.703680	-0.067592	-1.535703	1	-1.711727	-0.065932	-1.538946	1	-1.732084	-0.073279	-1.536954
1	1.834440	-1.569885	-0.751959	1	1.842558	-1.542668	-0.748115	1	1.844983	-1.542599	-0.753770
	TS26 CBS-QB3				TS26 G3						
6	-1.306511	-0.705208	0.135840	6	-1.291456	-0.703114	0.128444				
6	-1.305314	0.677794	0.380340	6	-1.287546	0.669431	0.391810				
6	-0.178395	1.271876	-0.183958	6	-0.178552	1.271572	-0.182628				
6	0.874747	0.365088	-0.507263	6	0.884754	0.386620	-0.500308				
8	-0.291940	-1.242020	-0.426007	8	-0.305435	-1.229019	-0.441411				
1	-2.171150	1.207964	0.753084	1	-2.145851	1.193013	0.765917				
1	-0.198207	2.279189	-0.589064	1	-0.197672	2.269854	-0.585630				
6	1.809937	-0.216005	0.520334	6	1.791028	-0.237480	0.522730				
1	2.200198	-1.182049	0.193997	1	2.167182	-1.189938	0.174113				
1	2.658763	0.467447	0.646119	1	2.637549	0.430494	0.673038				
1	1.318874	-0.332396	1.486721	1	1.285542	-0.371877	1.468012				
1	1.332248	0.474227	-1.492875	1	1.341175	0.498636	-1.472775				

Table 16: Cartesian coordinates of all transition state structures.

At. No.	X	Y	Z	At. No.	X	Y	Z	At. No.	X	Y	Z
1	-2.171980	-1.339495	0.338313	1	-2.153813	-1.320200	0.348326				
	TS27 CBS-QB3										
6	-1.429927	-0.109874	0.386499								
6	-0.625843	1.120929	0.119731								
6	0.738657	1.204035	-0.101520								
6	1.683487	0.184046	-0.119625								
8	-1.979509	-0.759587	-0.468800								
1	-1.213022	2.035720	0.096116								
1	1.120188	2.204553	-0.289928								
6	1.420127	-1.274642	0.100980								
1	2.342125	-1.853529	0.030198								
1	0.988811	-1.468879	1.090931								
1	0.712921	-1.675823	-0.632913								
1	2.708750	0.476731	-0.319730								
1	-1.542714	-0.389042	1.459332								
	TS28 CBS-QB3				TS28 CBS-APNO						
6	-1.222954	-0.218449	0.204094	6	-1.314210	-0.341614	0.030707				
6	-0.751725	1.057354	-0.321867	6	-0.830465	1.035831	-0.186037				
6	0.550719	1.247869	0.001858	6	0.470546	1.123697	0.071519				
6	1.237514	0.072884	0.553718	6	1.152755	-0.126687	0.532647				
8	-2.177769	-0.906033	0.011215	8	-2.371994	-0.828473	-0.046168				
1	-1.415993	1.766995	-0.798947	1	-1.471204	1.832954	-0.515374				
1	1.040441	2.215146	-0.083948	1	1.021992	2.043465	-0.050768				
6	1.848427	-0.959421	-0.377159	6	2.263981	-0.667917	-0.342129				
1	2.794827	-0.599871	-0.800641	1	3.114190	0.013422	-0.370435				
1	2.065188	-1.886899	0.160610	1	2.618487	-1.621151	0.034987				
1	1.181265	-1.192803	-1.210194	1	1.923769	-0.812953	-1.362938				
1	1.856727	0.268695	1.432265	1	1.389822	-0.119836	1.589528				
1	-0.072187	-0.524421	0.847263	1	-0.076744	-0.847972	0.404098				
	TS29 CBS-QB3										
6	-2.018042	-0.711661	0.130445								
6	-0.504868	1.178151	-0.151892								
6	0.770363	1.021332	0.098123								
6	1.460828	-0.235204	0.569801								

Table 16: Cartesian coordinates of all transition state structures.

At. No.	X	Y	Z	At. No.	X	Y	Z	At. No.	X	Y	Z
8	-3.085693	-0.424933	-0.126511								
1	-1.145314	1.980228	-0.489748								
1	1.428877	1.885953	-0.060285								
6	2.520460	-0.729586	-0.426106								
1	3.280273	0.035418	-0.612533								
1	3.028469	-1.617676	-0.041212								
1	2.063915	-0.988054	-1.384849								
1	1.943461	-0.024562	1.532006								
1	0.713418	-1.010035	0.746480								
	TS30 CBS-QB3				TS30 G3						
6	-1.540780	-0.539698	-0.100830	6	-1.546785	-0.522057	-0.069520				
6	-1.384277	0.847040	-0.021764	6	-1.368667	0.851126	-0.007142				
6	-0.028732	1.182549	0.055338	6	-0.007977	1.174081	0.014195				
6	0.810595	0.085147	0.398168	6	0.815658	0.098782	0.395795				
8	-0.499807	-1.290908	-0.007471	8	-0.536838	-1.285350	-0.065227				
1	-2.194285	1.542425	-0.194202	1	-2.170293	1.551750	-0.139918				
1	0.374605	2.101120	-0.359811	1	0.400595	2.049833	-0.460216				
1	-2.495086	-1.025321	-0.308681	1	-2.525378	-0.974655	-0.157641				
6	2.155175	-0.136571	-0.225491	6	2.171314	-0.155230	-0.187141				
1	2.936040	0.337887	0.382509	1	2.938678	0.215978	0.488416				
1	2.378985	-1.204975	-0.257734	1	2.320209	-1.222527	-0.296789				
1	2.207413	0.264049	-1.238898	1	2.291925	0.316987	-1.153460				
1	0.718902	-0.318721	1.404064	1	0.657711	-0.334774	1.364297				
	TS31 CBS-QB3				TS31 CBS-APNO				TS31 G3		
6	-1.789434	-0.106507	0.385294	6	-1.789811	-0.121111	0.380522	6	-1.789197	-0.120293	0.383494
6	-0.861835	0.994974	-0.010633	6	-0.869931	0.991890	-0.007508	6	-0.870709	0.992520	-0.005861
6	0.514233	0.851886	-0.108996	6	0.512956	0.856215	-0.104444	6	0.513168	0.856162	-0.105336
6	1.228006	-0.317769	0.090682	6	1.225616	-0.319551	0.090129	6	1.227069	-0.320490	0.089902
8	-2.326808	-0.859165	-0.389190	8	-2.319272	-0.847499	-0.388132	8	-2.324580	-0.847185	-0.389864
1	-1.323145	1.959633	-0.200215	1	-1.332436	1.947748	-0.185846	1	-1.332375	1.947916	-0.187262
1	1.081743	1.742849	-0.371660	1	1.070270	1.744109	-0.357246	1	1.070150	1.743191	-0.359899
1	-1.984381	-0.196878	1.479199	1	-1.974237	-0.230938	1.457379	1	-1.969059	-0.236486	1.457266
6	2.712774	-0.424167	-0.019667	6	2.717597	-0.421712	-0.021644	6	2.719843	-0.421773	-0.022131
1	3.158349	-0.780040	0.917710	1	3.001296	-1.126896	-0.799567	1	3.160239	-0.774106	0.907505

Table 16: Cartesian coordinates of all transition state structures.

At. No.	X	Y	Z	At. No.	X	Y	Z	At. No.	X	Y	Z
1	3.003016	-1.149015	-0.790453	1	3.165650	0.537728	-0.257307	1	3.006215	-1.128662	-0.796877
1	3.170781	0.536068	-0.268462	1	3.155169	-0.779006	0.907882	1	3.167390	0.536687	-0.261732
1	0.685639	-1.229796	0.327316	1	0.689905	-1.227142	0.317436	1	0.693037	-1.227820	0.319502
	TS32 CBS-QB3										
6	1.354530	-0.306027	-0.123194								
6	0.871326	1.061377	-0.066046								
6	-0.481112	1.084587	0.071243								
6	-1.093662	-0.203245	0.388083								
8	2.414358	-0.842382	-0.014152								
1	1.527262	1.910100	-0.212404								
1	-1.078231	1.974256	-0.114694								
1	0.119327	-0.880455	-0.072224								
6	-2.417510	-0.584398	-0.229180								
1	-2.647428	-1.636783	-0.047567								
1	-3.238135	0.004758	0.202869								
1	-2.424159	-0.417507	-1.309075								
1	-0.974931	-0.529072	1.420874								
	TS33 CBS-QB3										
6	-1.760847	-0.153546	0.350781								
6	-0.644087	0.693204	0.660108								
6	0.426824	1.000924	-0.299911								
6	1.572933	0.334937	-0.444210								
8	-1.911146	-0.730548	-0.724751								
1	-0.636165	1.167963	1.640345								
1	0.238569	1.858745	-0.946480								
6	1.999213	-0.876288	0.329414								
1	2.129346	-1.733075	-0.340407								
1	2.964895	-0.708195	0.818375								
1	1.270552	-1.155093	1.093029								
1	2.268204	0.686894	-1.202466								
1	-2.510445	-0.268244	1.158525								
	TS34 CBS-QB3								TS34 G3		
6	1.663473	-0.354916	0.222031					6	1.662469	-0.364979	0.208758
6	0.339737	-0.104890	0.827974					6	0.348910	-0.116115	0.829707

Table 16: Cartesian coordinates of all transition state structures.

At. No.	X	Y	Z	At. No.	X	Y	Z	At. No.	X	Y	Z
6	-0.520710	0.998048	0.287384					6	-0.511449	0.988116	0.295185
6	-1.647123	0.555590	-0.271156					6	-1.630038	0.565740	-0.264609
8	2.036263	0.118935	-0.831631					8	2.023564	0.127065	-0.824837
1	0.331430	-0.244944	1.912694					1	0.348873	-0.254314	1.903774
1	-0.227771	2.039385	0.352111					1	-0.220155	2.019952	0.373378
6	-1.775209	-0.929609	-0.273272					6	-1.784500	-0.921159	-0.275439
1	-2.549887	-1.387615	0.341467					1	-2.553847	-1.351256	0.350217
1	-1.606350	-1.451698	-1.215120					1	-1.684879	-1.421040	-1.228528
1	-0.502958	-1.040260	0.408624					1	-0.528987	-1.072198	0.387558
1	-2.410925	1.198621	-0.698314					1	-2.374032	1.216960	-0.689835
1	2.315352	-1.050298	0.793813					1	2.312157	-1.064243	0.740527
	TS35 CBS-QB3				TS35 CBS-APNO				TS35 G3		
6	-1.718519	-0.067883	-0.012819	6	-1.734754	-0.048217	-0.031313	6	-1.732961	-0.053512	-0.028654
6	-0.674954	0.910584	0.543122	6	-0.673887	0.858003	0.579517	6	-0.679685	0.863953	0.576314
6	0.544796	1.078284	-0.313228	6	0.530899	1.062919	-0.303166	6	0.526878	1.066694	-0.305637
6	1.636654	0.218718	-0.331604	6	1.650729	0.235485	-0.348860	6	1.646375	0.236682	-0.348753
8	-1.470669	-1.176429	-0.403254	8	-1.529566	-1.155444	-0.386429	8	-1.512103	-1.162202	-0.389497
1	-0.401589	0.518442	1.532825	1	-0.384293	0.405719	1.524421	1	-0.389022	0.422908	1.526055
1	0.557236	1.938749	-0.973215	1	0.511059	1.921935	-0.951465	1	0.506290	1.923493	-0.956125
6	1.779568	-0.950134	0.386200	6	1.842331	-0.938968	0.364773	6	1.837661	-0.936308	0.369829
1	0.987726	-1.337546	1.014089	1	1.083664	-1.350196	1.003559	1	1.079287	-1.346362	1.008884
1	2.684439	-1.539593	0.311992	1	2.756692	-1.494293	0.263847	1	2.750545	-1.493729	0.272362
1	2.458966	0.506107	-0.983189	1	2.443944	0.546075	-1.009869	1	2.440575	0.544557	-1.009197
1	-2.764365	0.312399	-0.013675	1	-2.742063	0.380821	-0.114009	1	-2.744678	0.358781	-0.103661
1	-1.162331	1.875452	0.707182	1	-1.124381	1.818156	0.809244	1	-1.135781	1.822909	0.799065
	TS36 CBS-QB3										
6	-1.866936	0.110186	-0.283793								
6	-0.108861	1.329075	0.673249								
6	0.825789	1.066785	-0.276498								
6	1.651235	-0.129325	-0.367114								
8	-1.905692	-1.042099	-0.031326								
1	-0.203609	0.719879	1.563700								
1	0.968277	1.799316	-1.067286								
6	1.468424	-1.276578	0.303623								

Table 16: Cartesian coordinates of all transition state structures.

At. No.	X	Y	Z	At. No.	X	Y	Z	At. No.	X	Y	Z
1	0.642055	-1.423370	0.989005								
1	2.139728	-2.115241	0.163669								
1	2.477193	-0.072073	-1.071933								
1	-1.964428	0.550278	-1.308153								
1	-0.631588	2.277147	0.684802								
	TS37 CBS-QB3										
6	-1.550008	-0.002934	0.036896								
6	-0.741341	1.132676	0.208104								
6	0.631668	1.260258	-0.069612								
6	1.544873	0.214872	-0.193587								
8	-1.208500	-1.195080	-0.282647								
1	-1.298733	2.046200	0.386334								
1	0.995897	2.266824	-0.258181								
6	1.302072	-1.100905	0.280542								
1	2.042549	-1.859454	0.044467								
1	0.932323	-1.174675	1.306633								
1	0.041744	-1.315522	-0.167674								
1	2.461124	0.421493	-0.743010								
1	-2.630485	0.151967	0.118549								
	TS38 CBS-QB3				TS38 CBS-APNO						
6	-1.097354	0.169985	0.429522	6	-1.105615	0.148216	0.464020				
6	-0.152848	1.202977	0.413708	6	-0.174930	1.228529	0.373364				
6	1.057516	0.932042	-0.341674	6	1.061407	0.953743	-0.302279				
6	1.424443	-0.373560	-0.318820	6	1.462646	-0.349583	-0.296457				
8	-1.663375	-0.397867	-0.676839	8	-1.672491	-0.409277	-0.649225				
1	-0.161332	1.929853	1.219730	1	-0.278316	2.090391	1.011608				
1	1.647709	1.704921	-0.823479	1	1.676888	1.738223	-0.707899				
6	0.638854	-1.275214	0.534746	6	0.647405	-1.324001	0.481000				
1	0.812974	-1.214386	1.606687	1	0.996190	-1.550520	1.478090				
1	0.380110	-2.267353	0.174413	1	0.177102	-2.146560	-0.031621				
1	-1.074694	-0.238775	-1.426554	1	-1.125494	-0.246290	-1.398109				
1	2.263250	-0.742093	-0.906002	1	2.385058	-0.656283	-0.762481				
1	-1.784685	0.073388	1.265028	1	-1.796977	0.103835	1.286322				
	TS39 CBS-QB3				TS39 CBS-APNO				TS39 G3		

Table 16: Cartesian coordinates of all transition state structures.

At. No.	X	Y	Z	At. No.	X	Y	Z	At. No.	X	Y	Z
6	0.070398	0.999075	0.565090	6	0.575854	0.032148	0.750897	6	0.571200	0.032142	0.753582
6	0.524055	-0.266857	0.831382	6	-0.148242	-1.138092	0.462884	6	-0.151462	-1.138795	0.462622
6	-0.413825	-1.231669	0.241849	6	-1.310023	-0.799907	-0.300557	6	-1.312623	-0.801415	-0.302263
6	-1.392736	-0.571250	-0.402495	6	-1.399759	0.561930	-0.429474	6	-1.403050	0.562446	-0.430972
8	2.077345	0.021456	-0.647400	8	2.079469	0.007045	-0.623196	8	2.092296	0.006765	-0.620180
1	1.322128	-0.525391	1.508612	1	0.149222	-2.132288	0.737835	1	0.144551	-2.132870	0.739314
1	-0.299431	-2.305116	0.309406	1	-2.003972	-1.512509	-0.706151	1	-2.004701	-1.514773	-0.709335
6	-1.178306	0.914845	-0.265373	6	-0.258574	1.217493	0.310927	6	-0.261051	1.219091	0.309453
1	-2.024498	1.407325	0.233283	1	-0.626042	1.765096	1.178365	1	-0.626147	1.772481	1.173568
1	-1.072774	1.414924	-1.237318	1	0.307234	1.911859	-0.298829	1	0.306024	1.911073	-0.301701
1	1.479942	-0.135894	-1.394606	1	1.638823	-0.533875	-1.264749	1	1.647134	-0.537924	-1.265811
1	-2.216336	-1.011916	-0.947886	1	-2.163283	1.098886	-0.959200	1	-2.164501	1.100414	-0.962309
1	0.534686	1.919557	0.884988	1	1.306728	0.105044	1.530228	1	1.301196	0.106663	1.533183
	TS40 CBS-QB3				TS40 CBS-APNO				TS40 G3		
6	1.554696	0.560770	-0.101653	6	1.554956	0.549106	-0.097716	6	1.556602	0.548530	-0.096705
6	0.223444	1.130250	-0.103338	6	0.227491	1.136179	-0.085386	6	0.230845	1.137578	-0.083949
6	-0.645423	0.058357	-0.066358	6	-0.642493	0.057958	-0.078488	6	-0.643720	0.058770	-0.079582
8	0.062245	-1.099956	0.063714	8	0.062006	-1.092409	0.063607	8	0.060769	-1.095194	0.063091
6	1.393540	-0.772843	0.027052	6	1.375270	-0.775503	0.023877	6	1.376108	-0.778259	0.024437
1	2.489473	1.095431	-0.147150	1	2.490464	1.066018	-0.143272	1	2.491697	1.066582	-0.143776
1	-0.043578	2.133766	-0.393863	1	-0.030226	2.119588	-0.421557	1	-0.022964	2.118162	-0.432613
6	-2.124257	-0.044164	-0.029922	6	-2.123556	-0.040703	-0.024309	6	-2.126239	-0.039235	-0.023074
1	-2.472155	-0.361962	0.959735	1	-2.453836	-0.353994	0.963509	1	-2.460211	-0.343009	0.965839
1	-2.572193	0.925170	-0.251163	1	-2.568792	0.922243	-0.243695	1	-2.571971	0.921390	-0.250651
1	-2.489161	-0.772916	-0.759260	1	-2.488497	-0.765816	-0.744753	1	-2.494374	-0.769016	-0.736611
1	0.100334	1.786970	1.624616	1	0.144252	1.781331	1.560064	1	0.151487	1.800331	1.552821
1	2.077323	-1.601037	0.102691	1	2.060581	-1.592309	0.092983	1	2.058603	-1.597188	0.093502
	TS41 CBS-QB3				TS41 CBS-APNO				TS41 G3		
6	-0.710083	-0.048086	-0.252725	6	-0.717942	-0.002774	-0.364821	6	-0.719334	-0.000291	-0.366274
6	0.205712	1.144439	-0.284597	6	0.247012	1.155385	-0.371139	6	0.248929	1.156099	-0.373192
6	1.544267	0.575003	0.212119	6	1.478169	0.541367	0.294701	6	1.478059	0.542423	0.295136
6	1.619898	-0.726204	0.278964	6	1.465813	-0.772978	0.366783	6	1.466645	-0.776071	0.368919
8	-0.125018	-1.158688	-0.406024	8	-0.125461	-1.117822	-0.577063	8	-0.127300	-1.120784	-0.580914
1	0.357471	1.540098	-1.298238	1	0.502103	1.481782	-1.376633	1	0.503762	1.482188	-1.378657

Table 16: Cartesian coordinates of all transition state structures.

At. No.	X	Y	Z	At. No.	X	Y	Z	At. No.	X	Y	Z
1	2.356300	1.259687	0.440106	1	2.290029	1.156865	0.641483	1	2.286298	1.160646	0.644840
1	-0.170054	1.973352	0.325883	1	-0.134375	2.014582	0.171100	1	-0.131572	2.017102	0.166395
6	-2.086680	0.029651	0.343959	6	-1.962631	0.033722	0.475953	6	-1.962124	0.034593	0.478961
1	-2.693434	0.791302	-0.154139	1	-2.577830	0.892007	0.224554	1	-2.574198	0.897377	0.237497
1	-2.585189	-0.936364	0.265369	1	-2.540111	-0.870662	0.330030	1	-2.545882	-0.864407	0.326215
1	-2.028259	0.307917	1.407250	1	-1.703198	0.108638	1.533482	1	-1.704206	0.097325	1.536815
1	2.324622	-1.515313	0.475646	1	2.104545	-1.568966	0.683627	1	2.111157	-1.564478	0.692913
	TS42 CBS-QB3				TS42 CBS-APNO				TS42 G3		
6	-2.013775	-0.366938	0.577702	6	-2.071419	-0.322483	0.514919	6	-2.080505	-0.314540	0.505247
6	-0.807537	0.152027	-0.178833	6	-0.805745	0.157550	-0.156757	6	-0.803601	0.155182	-0.154562
6	0.280302	-0.871461	-0.515499	6	0.264469	-0.895770	-0.416159	6	0.263028	-0.904386	-0.404032
6	1.656883	-0.510608	0.008315	6	1.672821	-0.513384	-0.026810	6	1.673950	-0.516918	-0.027521
6	2.027924	0.617979	0.552186	6	2.065847	0.621303	0.530176	6	2.065784	0.624947	0.525574
1	2.934243	1.045025	0.953095	1	3.017472	0.994804	0.851035	1	3.020896	0.995707	0.837569
1	2.399893	-1.309318	-0.103793	1	2.417925	-1.274635	-0.225148	1	2.417176	-1.278205	-0.227851
1	0.004200	-1.865292	-0.148936	1	0.000884	-1.825147	0.081448	1	-0.001430	-1.825561	0.108112
1	0.327800	-0.946032	-1.610018	1	0.236132	-1.106304	-1.484949	1	0.228891	-1.134331	-1.468427
8	-0.701774	1.308993	-0.507072	8	-0.663093	1.284924	-0.493108	8	-0.651179	1.286858	-0.491601
1	-2.726105	0.440537	0.740881	1	-2.786274	0.486366	0.574778	1	-2.790135	0.499360	0.554254
1	-1.695907	-0.782727	1.539844	1	-1.838607	-0.682935	1.513712	1	-1.866611	-0.672805	1.508593
1	-2.492721	-1.180133	0.022280	1	-2.498624	-1.154841	-0.038224	1	-2.511295	-1.144745	-0.047679
	TS43 CBS-QB3				TS43 CBS-APNO				TS43 G3		
6	-1.442252	1.212899	-0.141451	6	-1.444569	1.200241	-0.147038	6	-1.431288	1.207248	-0.149593
6	-0.969020	-0.218405	0.029415	6	-0.960971	-0.223366	0.026027	6	-0.958971	-0.220377	0.026580
6	0.371660	-0.441087	0.737631	6	0.367998	-0.440107	0.738632	6	0.365761	-0.447471	0.743634
6	1.516431	0.391904	0.168269	6	1.505277	0.402077	0.187009	6	1.508110	0.395342	0.202116
6	2.519668	-0.076534	-0.507065	6	2.505301	-0.073656	-0.518629	6	2.495008	-0.074895	-0.533056
1	3.348920	-0.463308	-1.051205	1	3.320689	-0.460507	-1.071801	1	3.299112	-0.453928	-1.109348
1	1.446248	1.469165	0.366153	1	1.464677	1.464066	0.401377	1	1.482072	1.450019	0.447979
1	0.235055	-0.171049	1.793541	1	0.218153	-0.186555	1.787643	1	0.213554	-0.205479	1.794876
1	0.596785	-1.505093	0.680035	1	0.600943	-1.493498	0.674464	1	0.595473	-1.501182	0.672002
8	-1.619584	-1.156474	-0.366997	8	-1.597016	-1.145793	-0.364541	8	-1.604849	-1.141317	-0.367835
1	-2.471764	1.213173	-0.496612	1	-2.480897	1.190511	-0.455035	1	-2.465607	1.206343	-0.464059
1	-0.809843	1.725280	-0.873363	1	-0.850658	1.695195	-0.909888	1	-0.831750	1.702174	-0.907630

Table 16: Cartesian coordinates of all transition state structures.

At. No.	X	Y	Z	At. No.	X	Y	Z	At. No.	X	Y	Z
1	-1.367653	1.770965	0.796631	1	-1.334997	1.765996	0.773568	1	-1.325783	1.773506	0.770773
	TS44 CBS-QB3				TS44 CBS-APNO				TS44 G3		
6	-0.889094	0.160016	0.214602	6	-0.908881	0.147902	0.207838	6	-0.915722	0.140185	0.210750
6	0.038263	-0.630202	1.020699	6	0.029562	-0.585411	1.063961	6	0.008601	-0.592059	1.075379
6	1.885440	-0.598981	-0.189644	6	1.911179	-0.550980	-0.114319	6	1.926964	-0.544786	-0.105750
6	2.201396	0.529887	-0.543327	6	2.212390	0.554320	-0.606715	6	2.221988	0.562210	-0.611507
8	-0.910707	1.380684	0.292609	8	-1.020192	1.339765	0.301003	8	-1.032432	1.338518	0.310135
1	0.485037	-0.138151	1.874683	1	0.408972	-0.061409	1.921237	1	0.391385	-0.070776	1.931831
1	2.060176	-1.651782	-0.138684	1	2.228742	-1.559049	0.004841	1	2.254319	-1.548561	0.022546
1	-0.081092	-1.707524	1.077667	1	-0.056736	-1.655763	1.138278	1	-0.062505	-1.663258	1.140453
6	-1.795342	-0.591023	-0.748545	6	-1.703796	-0.646399	-0.804643	6	-1.690616	-0.645426	-0.824813
1	-2.478785	-1.249126	-0.202744	1	-2.365271	-1.343750	-0.297635	1	-2.325892	-1.385559	-0.346926
1	-2.373065	0.123855	-1.332724	1	-2.291198	0.027140	-1.413351	1	-2.303668	0.028599	-1.406864
1	-1.203743	-1.220661	-1.420568	1	-1.037630	-1.224570	-1.437931	1	-1.009937	-1.174684	-1.484688
1	2.233165	1.579733	-0.721208	1	2.031937	1.582683	-0.800193	1	2.008471	1.585345	-0.801791
	TS45 CBS-QB3				TS45 CBS-APNO				TS45 G3		
6	-0.587973	1.358624	0.333214	6	-0.603265	1.357283	0.330694	6	-0.600040	1.359804	0.326771
6	-0.941204	-0.062010	0.051807	6	-0.933508	-0.069774	0.038133	6	-0.933646	-0.067814	0.038035
6	0.154641	-1.071651	0.397148	6	0.154301	-1.072853	0.387656	6	0.152800	-1.074244	0.385005
6	1.525902	-0.604239	-0.062007	6	1.525824	-0.602828	-0.055736	6	1.527273	-0.607628	-0.057358
6	1.803152	0.652662	-0.345243	6	1.787608	0.667644	-0.337333	6	1.794721	0.666900	-0.333306
1	2.713050	1.136639	-0.674932	1	2.707839	1.119233	-0.656012	1	2.716261	1.116636	-0.648631
1	2.292781	-1.374422	-0.153271	1	2.296576	-1.354775	-0.131592	1	2.293170	-1.363216	-0.136407
1	0.171858	-1.229948	1.484361	1	0.154546	-1.230323	1.466379	1	0.151862	-1.236268	1.462950
1	-0.113225	-2.027109	-0.058598	1	-0.102914	-2.017845	-0.074487	1	-0.107210	-2.018085	-0.077895
8	-1.971068	-0.400115	-0.492676	8	-1.949462	-0.404272	-0.482190	8	-1.958805	-0.401997	-0.477385
1	-1.227176	2.085017	-0.163207	1	-1.233767	2.070322	-0.176650	1	-1.223999	2.073983	-0.186205
1	0.613065	1.390999	-0.128739	1	0.642994	1.400653	-0.131829	1	0.652023	1.402195	-0.126299
1	-0.408923	1.579435	1.386277	1	-0.455337	1.570078	1.381234	1	-0.458316	1.578625	1.376690
	TS46 CBS-QB3				TS46 CBS-APNO						
6	-1.355492	1.251425	0.263984	6	-1.517316	1.169571	0.222946				
6	-0.967332	-0.112745	0.038810	6	-0.956075	-0.130496	0.036650				
6	0.248473	-0.674047	0.782419	6	0.259812	-0.565485	0.840499				
6	1.554064	-0.472666	0.030618	6	1.568431	-0.416929	0.081703				

Table 16: Cartesian coordinates of all transition state structures.

At. No.	X	Y	Z	At. No.	X	Y	Z	At. No.	X	Y	Z
6	2.009721	0.679994	-0.450150	6	2.006302	0.689700	-0.483020				
1	2.957741	0.731553	-0.972804	1	2.951118	0.713710	-0.996522				
1	2.151396	-1.368714	-0.113394	1	2.177741	-1.303518	0.021803				
1	0.322007	-0.223447	1.778367	1	0.313048	-0.008376	1.771229				
1	0.066457	-1.741151	0.916081	1	0.112651	-1.607632	1.095908				
8	-1.606356	-0.821863	-0.742179	8	-1.460273	-0.900150	-0.773618				
1	-2.197239	1.644293	-0.292857	1	-2.367127	1.453409	-0.369624				
1	1.462649	1.612459	-0.351327	1	1.446502	1.610201	-0.464706				
1	-0.848764	1.888150	0.979277	1	-1.118682	1.865240	0.938190				
	TS47 CBS-QB3				TS47 CBS-APNO						
6	1.713315	-0.962611	-0.483350	6	1.839991	-0.874090	-0.552189				
6	1.186107	0.209681	-0.063920	6	1.212304	0.238895	-0.009779				
6	-0.446242	-0.345923	1.040287	6	-0.472863	-0.478222	1.005349				
6	-1.406619	-0.572665	0.009041	6	-1.459828	-0.596873	-0.030745				
6	-2.203031	0.391354	-0.523752	6	-2.219290	0.437873	-0.494131				
1	-2.908199	0.168061	-1.314616	1	-2.925839	0.296626	-1.291795				
1	-1.479639	-1.580331	-0.392699	1	-1.575789	-1.563436	-0.495794				
1	-0.083616	-1.195368	1.603996	1	-0.150068	-1.383110	1.489157				
1	-0.497717	0.584619	1.593322	1	-0.513678	0.387649	1.643312				
8	1.266014	1.394172	-0.002772	8	1.220269	1.399919	0.048198				
1	2.778128	-0.983373	-0.687974	1	2.876909	-1.011713	-0.300903				
1	-2.154587	1.416859	-0.173910	1	-2.133890	1.425551	-0.075490				
1	1.156339	-1.882853	-0.475777	1	1.258319	-1.716421	-0.865108				
	TS48 CBS-QB3				TS48 CBS-APNO				TS48 G3		
6	-0.262296	1.280085	0.431803	6	-0.244565	1.275203	0.451621	6	-0.247497	1.278497	0.446595
6	-0.908535	-0.000987	0.075971	6	-0.904559	-0.006366	0.067779	6	-0.904455	-0.004874	0.067907
6	0.064447	-1.218545	0.090177	6	0.038222	-1.216293	0.100936	6	0.037876	-1.215919	0.098323
6	1.437784	-0.632514	0.170213	6	1.436254	-0.661535	0.145190	6	1.437174	-0.663642	0.148865
6	1.608822	0.551270	-0.510762	6	1.588098	0.570901	-0.505426	6	1.597223	0.567960	-0.503615
1	1.120971	0.718345	-1.465505	1	1.131267	0.723667	-1.469230	1	1.151551	0.721329	-1.472008
1	2.103731	-0.899528	0.983605	1	2.102051	-0.935739	0.944673	1	2.091737	-0.931811	0.959016
1	-0.169772	-1.891325	0.919991	1	-0.191700	-1.831830	0.965365	1	-0.194459	-1.839091	0.956523
1	-0.133468	-1.776817	-0.832211	1	-0.168036	-1.816313	-0.780693	1	-0.165337	-1.811033	-0.787257
8	-2.061112	-0.094926	-0.286035	8	-2.031245	-0.077726	-0.302181	8	-2.038081	-0.079060	-0.299339

Table 16: Cartesian coordinates of all transition state structures.

At. No.	X	Y	Z	At. No.	X	Y	Z	At. No.	X	Y	Z
1	-0.735369	2.180957	0.050757	1	-0.680765	2.173865	0.048346	1	-0.683379	2.175012	0.039558
1	2.472233	1.182671	-0.326488	1	2.448016	1.189660	-0.311501	1	2.454902	1.186693	-0.302329
1	0.189246	1.369245	1.413709	1	0.128426	1.347030	1.459884	1	0.127705	1.359246	1.452757
	TS49 CBS-QB3				TS49 CBS-APNO				TS49 G3		
6	-0.056376	-1.220200	-0.121183	6	-0.050534	-1.214830	-0.147250	6	-0.052224	-1.216281	-0.144210
6	0.900532	-0.023685	-0.000009	6	0.892072	-0.022631	-0.004587	6	0.890496	-0.023052	-0.004090
6	0.058856	1.263864	0.015334	6	0.069639	1.263912	0.002378	6	0.070428	1.265645	0.005716
6	-1.352213	0.763951	-0.092055	6	-1.348366	0.772696	-0.082731	6	-1.348128	0.775459	-0.083937
6	-1.422608	-0.581221	-0.106929	6	-1.423207	-0.588777	-0.051893	6	-1.424799	-0.588212	-0.055052
1	-2.211608	1.422113	-0.123918	1	-2.199038	1.427786	-0.107947	1	-2.196884	1.432388	-0.112804
1	0.256675	1.826586	0.936124	1	0.280803	1.830422	0.906092	1	0.280848	1.829937	0.910824
1	0.359675	1.916539	-0.812815	1	0.360218	1.887611	-0.839380	1	0.363644	1.892997	-0.832264
8	2.099282	-0.082330	0.068704	8	2.068463	-0.085833	0.084232	8	2.072753	-0.087506	0.080885
1	0.148629	-1.758318	-1.054436	1	0.113896	-1.679295	-1.117358	1	0.115502	-1.689555	-1.109269
1	-2.335381	-1.143240	-0.256496	1	-2.324921	-1.142520	-0.233385	1	-2.324892	-1.141539	-0.244561
1	0.120046	-1.928024	0.693803	1	0.165667	-1.960078	0.608361	1	0.160654	-1.957400	0.616469
1	-1.901446	-0.893270	1.897156	1	-1.781959	-0.939477	1.814264	1	-1.795531	-0.948131	1.813962
	TS50 CBS-QB3				TS50 CBS-APNO				TS50 G3		
6	0.076819	-1.225746	0.100608	6	0.069703	-1.220315	0.097906	6	0.071647	-1.221030	0.097959
6	-0.883240	-0.033542	-0.032007	6	-0.880027	-0.034115	-0.025378	6	-0.878555	-0.034085	-0.025930
6	-0.037521	1.196797	-0.066119	6	-0.050610	1.200295	-0.031722	6	-0.052914	1.200832	-0.032787
6	1.265849	0.853448	-0.137810	6	1.266349	0.855039	-0.144118	6	1.267651	0.856738	-0.143124
6	1.493970	-0.630587	-0.009749	6	1.489264	-0.632367	-0.010885	6	1.491954	-0.631427	-0.010714
1	2.115600	-0.852461	0.865307	1	2.095577	-0.856579	0.862656	1	2.098389	-0.858007	0.861646
1	2.086006	1.553294	-0.249677	1	2.074923	1.552550	-0.263395	1	2.075732	1.554162	-0.262138
1	-0.455676	2.182325	-0.219621	1	-0.470394	2.168075	-0.227752	1	-0.473893	2.166752	-0.234184
8	-2.085317	-0.092306	-0.117633	8	-2.061191	-0.093790	-0.123026	8	-2.065939	-0.096341	-0.121930
1	-0.103834	-1.710891	1.063185	1	-0.108667	-1.707364	1.050379	1	-0.104935	-1.710159	1.049541
1	2.044329	-1.013134	-0.876401	1	2.026988	-1.019128	-0.871602	1	2.029289	-1.018657	-0.871188
1	-0.148600	-1.959917	-0.675242	1	-0.155598	-1.939350	-0.680468	1	-0.151322	-1.941603	-0.679519
1	-0.350541	1.577015	1.903978	1	-0.341369	1.540897	1.799572	1	-0.344448	1.552069	1.798855
	TS51 CBS-QB3				TS51 CBS-APNO				TS51 G3		
6	-0.242085	-1.234301	0.007257	6	-0.264624	-1.197643	-0.104071	6	-0.272274	-1.197367	-0.093201
6	-1.041860	0.061763	0.142698	6	-1.046910	0.102122	-0.006121	6	-1.047238	0.108524	0.006695

Table 16: Cartesian coordinates of all transition state structures.

At. No.	X	Y	Z	At. No.	X	Y	Z	At. No.	X	Y	Z
6	0.657859	1.458671	0.251530	6	0.668691	1.457735	0.171832	6	0.685881	1.459018	0.178085
6	1.399825	0.501001	-0.395272	6	1.515327	0.446815	-0.299591	6	1.514330	0.440163	-0.309362
6	1.269600	-0.893030	0.152069	6	1.211606	-0.919536	0.257150	6	1.210258	-0.925796	0.248811
1	1.551499	-0.927219	1.209406	1	1.325464	-0.922592	1.338255	1	1.339600	-0.933041	1.327747
1	1.678662	0.631179	-1.436406	1	1.926646	0.517432	-1.293507	1	1.906570	0.507939	-1.310439
1	0.441960	2.415578	-0.212694	1	0.546545	2.379382	-0.371637	1	0.562730	2.382157	-0.361559
1	0.560075	1.445039	1.332632	1	0.463718	1.525828	1.228590	1	0.497629	1.528964	1.237172
8	-2.162632	0.287119	-0.154922	8	-2.192001	0.290788	-0.031984	8	-2.198511	0.298078	-0.042593
1	-0.618025	-1.942907	0.752258	1	-0.738931	-1.948449	0.518824	1	-0.740744	-1.940999	0.542458
1	1.883404	-1.623809	-0.376319	1	1.858656	-1.691145	-0.141742	1	1.848352	-1.699687	-0.159839
1	-0.456556	-1.659436	-0.979191	1	-0.350628	-1.523713	-1.138105	1	-0.371799	-1.537216	-1.120965
	TS52 CBS-QB3				TS52 CBS-APNO				TS52 G3		
6	-0.517719	1.276722	0.179974	6	-0.639995	1.120919	0.159367	6	-0.634496	1.144236	0.155305
6	-1.732228	-0.492297	-0.471293	6	-1.616897	-0.508964	-0.401495	6	-1.600247	-0.501960	-0.411710
6	2.103291	-1.165208	-0.111188	6	2.178923	-1.058700	-0.118776	6	2.142483	-1.077953	-0.122100
6	1.601486	-0.057436	0.424178	6	1.589977	-0.013640	0.426068	6	1.575517	-0.022629	0.429528
6	0.865931	1.014218	-0.334208	6	0.788631	1.017391	-0.322076	6	0.797695	1.030372	-0.313950
1	0.826200	0.763989	-1.399750	1	0.799548	0.799951	-1.385023	1	0.814754	0.824045	-1.378752
1	1.713902	0.114239	1.493970	1	1.673751	0.138530	1.492479	1	1.658065	0.120719	1.496437
1	2.626271	-1.900341	0.490072	1	2.741577	-1.758184	0.474414	1	2.686722	-1.796323	0.464664
1	2.008139	-1.378160	-1.171555	1	2.120369	-1.255221	-1.176406	1	2.084897	-1.265761	-1.180655
8	-2.588442	-0.775022	0.227938	8	-2.544820	-0.776692	0.179729	8	-2.522175	-0.789689	0.184350
1	-1.123040	2.015171	-0.336398	1	-1.247239	1.865842	-0.333694	1	-1.235799	1.887787	-0.345731
1	1.442953	1.953367	-0.268216	1	1.262982	1.991834	-0.195853	1	1.283648	1.996954	-0.174725
1	-0.711458	1.175915	1.243595	1	-0.796259	1.088749	1.227722	1	-0.800598	1.117699	1.221528
	TS53 CBS-QB3				TS53 CBS-APNO				TS53 G3		
6	-0.203543	1.133572	-0.116108	6	-0.197681	1.129564	-0.111123	6	-0.201165	1.129904	-0.110746
6	-1.528355	0.549514	-0.086187	6	-1.528896	0.552398	-0.070531	6	-1.531318	0.552012	-0.068441
6	-1.321869	-0.809755	-0.067594	6	-1.312589	-0.813451	-0.074836	6	-1.312855	-0.816517	-0.074943
8	0.006741	-1.086919	0.021545	8	0.010414	-1.076527	0.026855	8	0.012295	-1.078914	0.027087
6	0.680404	0.111966	-0.021116	6	0.669788	0.106748	-0.019628	6	0.670948	0.108166	-0.019330
1	0.037517	2.183597	-0.155418	1	0.050964	2.169471	-0.152917	1	0.043382	2.171046	-0.154607
1	-2.453636	1.037353	-0.347630	1	-2.436738	1.027932	-0.379533	1	-2.436090	1.025938	-0.390155
6	2.162867	0.037560	0.046762	6	2.154281	0.038041	0.042296	6	2.156852	0.040351	0.042089

Table 16: Cartesian coordinates of all transition state structures.

At. No.	X	Y	Z	At. No.	X	Y	Z	At. No.	X	Y	Z
1	2.566168	-0.565239	-0.772513	1	2.543126	-0.556855	-0.778456	1	2.549122	-0.553320	-0.777442
1	2.589686	1.039028	-0.018165	1	2.577072	1.033269	-0.016396	1	2.579715	1.035327	-0.017123
1	2.492454	-0.417475	0.985805	1	2.475864	-0.423401	0.971055	1	2.482834	-0.419479	0.969690
1	-2.037593	0.937945	1.650549	1	-2.029170	0.933083	1.594930	1	-2.040348	0.944054	1.588010
1	-1.985554	-1.656994	-0.049534	1	-1.973849	-1.651081	-0.050593	1	-1.971743	-1.655753	-0.046847
	TS54 CBS-QB3				TS54 CBS-APNO				TS54 G3		
6	1.462020	-0.722940	-0.134631	6	-1.438242	-0.727285	0.196254	6	-1.444191	-0.724211	0.198330
6	1.497559	0.755267	0.093504	6	-1.505522	0.741800	-0.105676	6	-1.505193	0.745664	-0.104914
6	0.020685	1.170371	-0.043481	6	-0.039524	1.157364	0.026251	6	-0.038421	1.155979	0.023307
6	-0.868225	0.216427	-0.041559	6	0.829905	0.173163	0.038748	6	0.831819	0.167288	0.036461
8	0.389586	-1.302040	0.176041	8	-0.381554	-1.287861	-0.247595	8	-0.387104	-1.292227	-0.249360
1	1.832468	1.025701	1.105167	1	-1.853519	0.946521	-1.116008	1	-1.857840	0.951704	-1.113013
1	-0.218281	2.230067	-0.091772	1	0.237125	2.197736	0.065259	1	0.237992	2.196122	0.064169
6	-2.288898	-0.123598	-0.030225	6	2.282101	-0.092343	0.048470	6	2.287270	-0.090954	0.049901
1	-2.522210	-0.741425	0.843202	1	2.564509	-0.643732	-0.842581	1	2.578785	-0.640274	-0.839163
1	-2.923192	0.773143	0.010671	1	2.845960	0.837594	0.072984	1	2.848766	0.839823	0.077078
1	-2.565426	-0.698849	-0.919149	1	2.558431	-0.688730	0.911774	1	2.567002	-0.686092	0.912748
1	2.176916	-1.211787	-0.808806	1	-1.916378	-1.132296	1.081023	1	-1.914052	-1.123069	1.088940
1	2.164188	1.266313	-0.609295	1	-2.156000	1.269597	0.584025	1	-2.151525	1.277007	0.585608
	TS55 CBS-QB3				TS55 CBS-APNO				TS55 G3		
6	2.625010	-0.430855	0.052758	6	2.635265	-0.419118	0.039863	6	2.633952	-0.415325	0.041050
6	1.240745	0.022958	0.221760	6	1.206496	-0.062669	0.203854	6	1.203280	-0.062036	0.208286
6	0.393333	0.890233	-0.272262	6	0.408015	0.902963	-0.219014	6	0.403112	0.903673	-0.223679
6	-1.049702	1.031730	0.147434	6	-1.058276	1.030944	0.110033	6	-1.062077	1.033130	0.110442
6	-1.893964	-0.231061	0.067899	6	-1.886184	-0.234250	0.076360	6	-1.884605	-0.236327	0.080139
8	-1.493107	-1.340527	-0.155647	8	-1.498680	-1.323911	-0.155311	8	-1.489242	-1.328004	-0.159375
1	2.658080	-1.487659	-0.230192	1	2.735539	-1.393029	-0.428746	1	2.738658	-1.391972	-0.420362
1	3.200715	-0.320114	0.977204	1	3.138740	-0.459115	1.001006	1	3.143461	-0.447656	0.999113
1	3.137231	0.144166	-0.734733	1	3.146309	0.314258	-0.582731	1	3.143562	0.312774	-0.588032
1	0.728855	1.558608	-1.074343	1	0.828931	1.689338	-0.834792	1	0.819195	1.684827	-0.847803
1	-1.560260	1.799606	-0.445574	1	-1.538949	1.727065	-0.575122	1	-1.544377	1.729142	-0.573356
1	-1.136093	1.377959	1.188008	1	-1.203531	1.465310	1.100031	1	-1.204019	1.470185	1.099523
1	-2.976203	-0.046380	0.259270	1	-2.949496	-0.059756	0.296269	1	-2.944521	-0.071958	0.308489
	TS56 CBS-QB3				TS56 CBS-APNO				TS56 G3		

Table 16: Cartesian coordinates of all transition state structures.

At. No.	X	Y	Z	At. No.	X	Y	Z	At. No.	X	Y	Z
6	-2.083606	-0.822732	0.112577	6	-2.076067	-0.923549	0.130360	6	-2.080026	-0.930252	0.130728
6	-1.472510	0.472061	-0.130522	6	-1.595353	0.434094	-0.170818	6	-1.613240	0.434303	-0.170479
6	-0.689296	1.413026	-0.244090	6	-0.770908	1.364278	-0.248647	6	-0.785411	1.366783	-0.247182
6	1.310010	0.893036	0.469032	6	1.220857	0.915546	0.515479	6	1.233162	0.916468	0.516032
6	1.617048	-0.290298	-0.298657	6	1.655210	-0.193900	-0.313281	6	1.665617	-0.186930	-0.315655
8	1.263070	-1.421991	0.008047	8	1.490423	-1.348473	-0.018473	8	1.501940	-1.349274	-0.019329
1	-1.299189	-1.550462	0.350888	1	-1.247811	-1.553687	0.438285	1	-1.245214	-1.557413	0.425488
1	-2.621284	-1.177021	-0.771673	1	-2.538712	-1.364301	-0.745921	1	-2.551480	-1.373249	-0.739592
1	-2.788484	-0.778640	0.947413	1	-2.813285	-0.895648	0.925454	1	-2.807532	-0.915734	0.934936
1	-0.486753	2.426153	-0.515171	1	-0.656367	2.380060	-0.541986	1	-0.671932	2.383533	-0.538048
1	1.012144	0.761957	1.501746	1	0.950134	0.692533	1.531127	1	0.955213	0.692934	1.528715
1	1.807210	1.822219	0.211213	1	1.645952	1.885320	0.323869	1	1.643914	1.891685	0.325481
1	2.181925	-0.118833	-1.238837	1	2.134269	0.064701	-1.261604	1	2.140903	0.070198	-1.263006
	TS57 CBS-QB3				TS57 CBS-APNO				TS57 G3		
6	-2.597238	-0.479726	0.059536	6	-2.624312	-0.463728	0.063341	6	-2.622686	-0.459111	0.064088
6	-1.183788	-0.087782	0.028335	6	-1.179561	-0.133690	0.080625	6	-1.175447	-0.134180	0.083339
6	-0.436899	0.982671	-0.063174	6	-0.445825	0.945959	-0.119191	6	-0.441091	0.948689	-0.122720
6	1.080707	1.043923	-0.099283	6	1.061339	1.042914	-0.049927	6	1.066239	1.044544	-0.047296
6	1.765089	-0.250916	0.304680	6	1.783650	-0.243794	0.296918	6	1.782602	-0.246090	0.297049
8	1.600450	-1.302696	-0.255005	8	1.635764	-1.264540	-0.278100	8	1.622346	-1.270796	-0.279774
1	-2.844008	-1.012541	0.983203	1	-2.946800	-0.845357	1.027125	1	-2.951401	-0.834495	1.028059
1	-2.840836	-1.143996	-0.775620	1	-2.835742	-1.223553	-0.682360	1	-2.837689	-1.222607	-0.676537
1	-3.255759	0.400615	-0.007756	1	-3.218232	0.419030	-0.170131	1	-3.216033	0.421750	-0.175633
1	-0.926282	1.962267	-0.137785	1	-0.949183	1.877572	-0.353982	1	-0.940545	1.879699	-0.363836
1	1.432457	1.857268	0.543815	1	1.342095	1.810357	0.666931	1	1.347519	1.808607	0.672599
1	1.407499	1.285139	-1.120263	1	1.446082	1.367980	-1.016126	1	1.455174	1.375190	-1.009608
1	2.456108	-0.176200	1.173884	1	2.503920	-0.175676	1.122753	1	2.506511	-0.184888	1.116386
	TS58 CBS-QB3				TS58 CBS-APNO				TS58 G3		
6	-2.560386	-0.615720	0.000000	6	-2.550347	-0.612864	0.000003	6	-2.553077	-0.614412	-0.000001
6	-1.153478	-0.155274	0.000000	6	-1.133912	-0.155075	0.000003	6	-1.137324	-0.154304	0.000001
6	-0.571813	1.033874	0.000000	6	-0.563260	1.042051	0.000000	6	-0.563510	1.045007	0.000003
6	0.943160	1.065322	0.000000	6	0.947791	1.060834	0.000004	6	0.948058	1.061095	0.000000
6	1.327316	-0.412182	0.000000	6	1.324082	-0.410937	-0.000001	6	1.323517	-0.412696	0.000006
8	2.395084	-0.927568	-0.000001	8	2.364276	-0.932329	-0.000010	8	2.371258	-0.932691	-0.000008

Table 16: Cartesian coordinates of all transition state structures.

At. No.	X	Y	Z	At. No.	X	Y	Z	At. No.	X	Y	Z
1	-2.774374	-1.231560	0.879573	1	-2.759408	-1.219646	0.875889	1	-2.763522	-1.221552	0.874990
1	-2.774375	-1.231560	-0.879573	1	-2.759405	-1.219653	-0.875879	1	-2.763523	-1.221541	-0.874999
1	-3.263427	0.228937	0.000001	1	-3.234524	0.233005	-0.000002	1	-3.240087	0.228554	0.000005
1	-1.125930	1.972989	0.000001	1	-1.117973	1.967774	-0.000004	1	-1.114763	1.971953	0.000007
1	1.375241	1.557997	0.879721	1	1.372482	1.544316	0.876066	1	1.373476	1.545482	0.874946
1	1.375241	1.557998	-0.879721	1	1.372487	1.544323	-0.876052	1	1.373470	1.545473	-0.874954
1	0.118152	-0.930366	0.000000	1	0.066015	-0.935548	0.000006	1	0.058908	-0.934994	0.000017
	TS59 CBS-QB3				TS59 CBS-APNO				TS59 G3		
6	-2.583099	-0.527405	-0.115478	6	-2.598611	-0.493525	-0.118062	6	-2.598269	-0.494292	-0.119472
6	-1.285358	0.011111	0.396715	6	-1.278945	0.001275	0.395906	6	-1.277466	-0.002830	0.396867
6	-0.420789	0.764216	-0.318472	6	-0.406711	0.745534	-0.314374	6	-0.406950	0.752559	-0.310798
6	0.849052	1.234617	0.170056	6	0.897352	1.170451	0.183328	6	0.897544	1.174608	0.185169
6	2.218255	-0.148039	-0.148567	6	2.164281	-0.131282	-0.181040	6	2.165228	-0.130860	-0.186628
8	1.938479	-1.257060	-0.019251	8	1.938618	-1.229700	-0.013807	8	1.936638	-1.235736	-0.013413
1	-3.426515	-0.175161	0.489878	1	-3.416688	-0.131758	0.500139	1	-3.417023	-0.141655	0.502491
1	-2.601109	-1.622557	-0.064125	1	-2.636236	-1.580015	-0.096116	1	-2.636615	-1.580567	-0.111116
1	-2.761366	-0.233440	-1.152357	1	-2.774747	-0.169239	-1.137926	1	-2.778016	-0.159352	-1.135044
1	-0.662475	0.985585	-1.356419	1	-0.644495	0.997734	-1.335996	1	-0.649225	1.014761	-1.328188
1	0.990944	1.259363	1.248229	1	1.003944	1.190034	1.258635	1	1.006510	1.191671	1.260011
1	1.317439	2.064351	-0.345185	1	1.319882	2.043742	-0.282954	1	1.321577	2.048277	-0.278391
1	-1.033112	-0.228660	1.428464	1	-1.024795	-0.267615	1.410119	1	-1.020834	-0.282350	1.406719
	TS60 CBS-QB3				TS60 CBS-APNO				TS60 G3		
6	-0.139543	1.193132	0.025427	6	-0.136739	1.190993	0.024434	6	-0.137945	1.192584	0.024205
6	-1.475950	0.703194	-0.067057	6	-1.473576	0.705063	-0.064224	6	-1.473661	0.707364	-0.063529
6	-1.378818	-0.660402	-0.125953	6	-1.371391	-0.668222	-0.088280	6	-1.373029	-0.668689	-0.087174
8	-0.064113	-1.032701	-0.127841	8	-0.066059	-1.022107	-0.125643	8	-0.065812	-1.023817	-0.126366
6	0.682614	0.104368	-0.013036	6	0.673831	0.103771	-0.012569	6	0.675732	0.104816	-0.013892
1	0.174043	2.221256	0.113223	1	0.180790	2.210008	0.106097	1	0.177825	2.212445	0.106648
1	-2.389149	1.276432	-0.063688	1	-2.381862	1.270762	-0.061980	1	-2.381223	1.274583	-0.060941
1	-1.879562	-1.085956	1.891196	1	-1.829313	-1.110774	1.739608	1	-1.857489	-1.124870	1.737272
1	-2.089375	-1.442606	-0.327018	1	-2.072260	-1.421592	-0.373639	1	-2.070425	-1.419740	-0.386750
6	2.156954	-0.068244	0.049261	6	2.149813	-0.069236	0.044052	6	2.152615	-0.070009	0.045736
1	2.448616	-0.660839	0.921858	1	2.433720	-0.665156	0.906243	1	2.438141	-0.660178	0.910995
1	2.532135	-0.583928	-0.840085	1	2.510212	-0.576864	-0.845753	1	2.517075	-0.582755	-0.838987

Table 16: Cartesian coordinates of all transition state structures.

At. No.	X	Y	Z	At. No.	X	Y	Z	At. No.	X	Y	Z
1	2.644651	0.904963	0.115390	1	2.635564	0.896259	0.114090	1	2.640318	0.894655	0.110609
	TS61 CBS-QB3										
6	-0.690254	-0.007416	0.030733								
6	0.138869	1.123293	0.118224								
6	1.476463	0.771140	-0.073064								
6	1.712583	-0.618316	0.083740								
8	-0.120800	-1.159536	-0.092285								
1	-0.247869	2.133227	0.123432								
1	2.197763	1.433002	-0.541049								
6	-2.189329	0.035968	-0.026021								
1	-2.535014	-0.448165	-0.943795								
1	-2.619015	-0.519335	0.813022								
1	-2.561524	1.061219	0.002109								
1	2.403442	-1.133701	-0.581621								
1	1.638622	-1.077967	1.064514								
	TS62 CBS-QB3				TS62 CBS-APNO						
6	0.525464	0.405736	-0.268022	6	-0.634691	0.579685	0.246220				
6	-0.226716	-0.694700	-0.443425	6	0.391045	-0.018779	0.971518				
6	-1.641418	-0.713719	-0.092046	6	1.640870	-0.404661	0.399855				
6	-2.382277	0.286698	0.406085	6	2.101667	-0.053094	-0.837383				
8	0.814239	1.536721	-0.196586	8	-1.140723	1.528777	-0.170072				
1	0.251880	-1.594174	-0.795539	1	0.091661	-0.410882	1.926248				
1	-2.117629	-1.674108	-0.271022	1	2.265455	-1.018365	1.025854				
6	2.516814	-0.666980	0.408309	6	-2.047884	-1.248136	-0.377281				
1	2.750624	0.121099	1.111112	1	-2.067108	-0.976940	-1.418306				
1	2.285708	-1.645466	0.806612	1	-1.562960	-2.173240	-0.119058				
1	2.968393	-0.613430	-0.575246	1	-2.898264	-0.955042	0.214444				
1	-3.436753	0.145622	0.604973	1	3.068779	-0.377814	-1.173512				
1	-1.967329	1.264479	0.626385	1	1.522180	0.551977	-1.512675				
	TS63 CBS-QB3				TS63 CBS-APNO				TS63 G3		
6	-1.718519	-0.067883	-0.012818	6	-1.734754	-0.048217	-0.031313	6	-1.732961	-0.053512	-0.028654
6	-0.674954	0.910584	0.543122	6	-0.673887	0.858003	0.579517	6	-0.679685	0.863953	0.576314
6	0.544795	1.078284	-0.313228	6	0.530899	1.062920	-0.303166	6	0.526878	1.066694	-0.305637
6	1.636654	0.218718	-0.331605	6	1.650729	0.235485	-0.348860	6	1.646375	0.236682	-0.348753

Table 16: Cartesian coordinates of all transition state structures.

At. No.	X	Y	Z	At. No.	X	Y	Z	At. No.	X	Y	Z
8	-1.470669	-1.176428	-0.403254	8	-1.529566	-1.155444	-0.386429	8	-1.512103	-1.162202	-0.389497
1	-0.401589	0.518442	1.532825	1	-0.384293	0.405719	1.524421	1	-0.389022	0.422908	1.526055
1	0.557235	1.938748	-0.973215	1	0.511060	1.921935	-0.951465	1	0.506290	1.923493	-0.956125
6	1.779569	-0.950134	0.386200	6	1.842330	-0.938968	0.364773	6	1.837661	-0.936308	0.369829
1	0.987726	-1.337545	1.014090	1	1.083663	-1.350196	1.003559	1	1.079287	-1.346362	1.008884
1	2.684440	-1.539593	0.311992	1	2.756692	-1.494293	0.263847	1	2.750545	-1.493729	0.272362
1	2.458966	0.506107	-0.983189	1	2.443944	0.546075	-1.009869	1	2.440575	0.544557	-1.009197
1	-2.764365	0.312398	-0.013673	1	-2.742063	0.380820	-0.114009	1	-2.744678	0.358781	-0.103661
1	-1.162331	1.875452	0.707182	1	-1.124381	1.818156	0.809244	1	-1.135781	1.822909	0.799066
	TS64 CBS-QB3										
6	-0.982876	-0.042605	0.037334								
6	0.061462	-1.090928	0.160119								
6	1.370295	-0.831038	0.018220								
6	1.925202	0.536855	-0.146826								
8	-2.146450	-0.332201	-0.183138								
1	-0.306312	-2.107628	0.243689								
1	2.070832	-1.665426	-0.015275								
6	-0.514213	1.378832	0.122389								
1	-1.050589	2.066390	-0.528560								
1	-0.418009	1.749448	1.143700								
1	0.781854	1.261681	-0.205695								
1	2.512117	0.697276	-1.052537								
1	2.422483	0.949169	0.732365								
	TS65 CBS-QB3				TS65 CBS-APNO						
6	0.976422	-0.149377	0.038170	6	1.963898	0.518070	0.671407				
6	-0.232096	-0.479784	0.875943	6	1.486499	-0.286412	-0.504347				
6	-1.494790	-0.230305	0.533003	6	0.235149	-0.573487	-0.811808				
6	-1.961457	0.444864	-0.723137	6	-0.972337	-0.149285	-0.025203				
8	1.411416	-0.953367	-0.795450	6	-1.630222	1.072147	-0.355615				
1	-0.019860	-0.994524	1.810167	1	-2.506085	1.354285	0.199609				
1	-2.279090	-0.551004	1.215524	1	1.147673	0.871518	1.289208				
6	1.632107	1.107598	0.251111	1	2.620352	-0.084081	1.293677				
1	2.509188	1.339816	-0.341808	1	2.538447	1.377385	0.334993				
1	1.278410	1.820801	0.985775	1	2.261046	-0.669633	-1.150406				

Table 16: Cartesian coordinates of all transition state structures.

At. No.	X	Y	Z	At. No.	X	Y	Z	At. No.	X	Y	Z
1	-1.134458	0.738848	-1.371605	1	0.028993	-1.174799	-1.682963				
1	-2.551975	1.337617	-0.489673	8	-1.414396	-0.858759	0.876563				
1	-2.614660	-0.222606	-1.295319	1	-1.273180	1.709199	-1.143231				
	TS66 CBS-QB3				TS66 CBS-APNO				TS66 G3		
6	-1.336434	0.283531	-0.061830	6	-1.268963	0.224916	-0.065162	6	-1.282131	0.232052	-0.061802
6	0.393236	-1.015376	-0.477449	6	0.344723	-0.910930	-0.591270	6	0.348697	-0.922840	-0.573463
6	1.610499	-0.676631	-0.141174	6	1.572680	-0.630341	-0.194988	6	1.583755	-0.644081	-0.184208
6	2.092523	0.610715	0.467525	6	2.040345	0.583764	0.556336	6	2.061121	0.584730	0.538354
8	-0.947743	1.305688	-0.518672	8	-1.000544	1.239592	-0.602392	8	-0.990660	1.257526	-0.582888
1	-0.085128	-1.861805	-0.946643	1	-0.059841	-1.741414	-1.134042	1	-0.060650	-1.764846	-1.093533
1	2.380248	-1.438196	-0.316695	1	2.329760	-1.367602	-0.432571	1	2.336076	-1.390521	-0.403569
6	-2.158652	-0.566485	0.536650	6	-2.035000	-0.560347	0.664243	6	-2.068778	-0.560457	0.637077
1	-3.095191	-0.161414	0.902379	1	-2.956209	-0.149468	1.033138	1	-2.997331	-0.154277	0.992152
1	-1.918532	-1.601058	0.703137	1	-1.755669	-1.563305	0.899405	1	-1.802007	-1.568425	0.866778
1	1.287611	1.337638	0.554468	1	1.238024	1.286692	0.727818	1	1.264949	1.298754	0.690228
1	2.888084	1.041056	-0.148244	1	2.824039	1.086373	-0.003302	1	2.850571	1.068563	-0.029103
1	2.517819	0.423756	1.458644	1	2.461534	0.289615	1.513734	1	2.477689	0.314118	1.504403
	TS67 CBS-QB3				TS67 CBS-APNO				TS67 G3		
6	-1.078127	0.229594	-0.186645	6	-1.069414	0.210941	-0.125253	6	-1.068383	0.210364	-0.126288
6	-0.046000	-0.754762	-0.567723	6	-0.024159	-0.678826	-0.632165	6	-0.023848	-0.680751	-0.632521
6	1.347354	-0.569766	-0.368295	6	1.375030	-0.482825	-0.446657	6	1.375232	-0.488167	-0.442175
6	1.953020	0.549509	0.412816	6	1.964608	0.580412	0.433583	6	1.966400	0.579049	0.433215
8	-1.266627	1.415223	-0.267931	8	-1.452102	1.316872	-0.245881	8	-1.445737	1.325029	-0.245909
1	-0.353886	-1.549043	-1.237571	1	-0.342726	-1.393990	-1.369656	1	-0.340657	-1.396036	-1.370969
1	2.010149	-1.337432	-0.755012	1	2.031060	-1.252487	-0.816217	1	2.031200	-1.259998	-0.805867
6	-1.320958	-0.871907	0.718915	6	-1.199830	-0.939591	0.751571	6	-1.208629	-0.939813	0.748858
1	-1.913909	-1.727824	0.430999	1	-1.878015	-1.735357	0.508046	1	-1.891069	-1.731877	0.504227
1	-1.121820	-0.732987	1.777217	1	-0.853322	-0.857001	1.766366	1	-0.868340	-0.862296	1.766049
1	1.279354	1.404516	0.494200	1	1.327167	1.455551	0.490706	1	1.326165	1.451414	0.493706
1	2.882509	0.891562	-0.053314	1	2.931488	0.894124	0.053250	1	2.928912	0.897828	0.046533
1	2.218886	0.233426	1.432521	1	2.123761	0.213526	1.448075	1	2.135040	0.216637	1.447061
	TS68 CBS-QB3				TS68 CBS-APNO				TS68 G3		
6	-1.207609	0.154176	-0.175231	6	-1.247090	0.122422	-0.168677	6	-1.250910	0.114349	-0.172689
6	0.036892	-0.951958	-0.473976	6	0.098733	-0.947870	-0.449913	6	0.102862	-0.948684	-0.448654

Table 16: Cartesian coordinates of all transition state structures.

At. No.	X	Y	Z	At. No.	X	Y	Z	At. No.	X	Y	Z
6	1.319323	-0.396152	-0.500719	6	1.368061	-0.340422	-0.525780	6	1.369066	-0.333377	-0.531539
6	1.819058	0.657157	0.433675	6	1.875922	0.716917	0.411797	6	1.876968	0.719966	0.411565
8	-1.456213	1.317678	-0.280076	8	-1.674407	1.206509	-0.271500	8	-1.687397	1.203455	-0.268224
1	-0.204920	-1.731805	-1.186525	1	-0.125224	-1.732948	-1.148604	1	-0.119009	-1.735430	-1.146455
1	1.913244	-0.586758	-1.389501	1	1.914375	-0.485533	-1.442491	1	1.911676	-0.471937	-1.450662
6	-0.929440	-0.903607	0.764033	6	-0.843930	-0.895581	0.774331	6	-0.834908	-0.896075	0.775981
1	-1.596911	-1.760140	0.735834	1	-1.481047	-1.765464	0.814632	1	-1.464295	-1.771124	0.831896
1	-0.557776	-0.669249	1.763615	1	-0.467806	-0.595805	1.742284	1	-0.455103	-0.586978	1.739421
1	1.556596	1.664301	0.073288	1	1.544442	1.708589	0.104020	1	1.499770	1.706559	0.145418
1	2.908106	0.620842	0.517578	1	2.960662	0.724106	0.420075	1	2.959824	0.766453	0.378957
1	1.402019	0.563685	1.439629	1	1.539681	0.562186	1.431536	1	1.587845	0.527749	1.439238
	TS69 CBS-QB3										
6	1.784265	-0.086456	-0.425171								
6	-0.511857	0.885515	0.084484								
6	-1.779127	0.556103	-0.168910								
6	-2.423918	-0.795648	-0.077815								
8	2.913821	-0.279242	-0.145049								
1	-0.221706	1.925663	-0.038432								
1	-2.443453	1.359351	-0.480482								
6	0.589781	-0.028311	0.539522								
1	0.986691	0.272507	1.518320								
1	0.252589	-1.065563	0.627477								
1	-2.845669	-1.084868	-1.046457								
1	-3.257303	-0.777191	0.632941								
1	-1.736587	-1.583177	0.234364								
	TS70 CBS-QB3				TS70 CBS-APNO				TS70 G3		
6	1.997500	-0.118289	0.097655	6	1.948634	-0.121953	0.055853	6	1.950568	-0.119289	0.049411
6	-0.478966	1.089098	-0.399602	6	-0.446999	1.097932	-0.374995	6	-0.447231	1.102600	-0.373726
6	-1.486000	0.188520	-0.498647	6	-1.484258	0.237473	-0.479190	6	-1.485035	0.237270	-0.479069
6	-1.774441	-0.950157	0.428645	6	-1.789999	-0.934985	0.407263	6	-1.787071	-0.937162	0.407206
8	1.728311	-1.124438	-0.392561	8	1.685823	-1.131801	-0.387703	8	1.680800	-1.140567	-0.383479
1	-0.397469	1.832339	-1.188446	1	-0.361534	1.865784	-1.126330	1	-0.363682	1.871178	-1.123928
1	-2.165602	0.291283	-1.340884	1	-2.176929	0.399421	-1.289609	1	-2.179109	0.397525	-1.287746
6	0.549234	1.121647	0.607865	6	0.626567	1.051059	0.613341	6	0.627295	1.057106	0.611847

Table 16: Cartesian coordinates of all transition state structures.

At. No.	X	Y	Z	At. No.	X	Y	Z	At. No.	X	Y	Z
1	1.123915	2.034827	0.702794	1	1.170181	1.970637	0.744300	1	1.172034	1.975764	0.742503
1	0.355757	0.640196	1.562425	1	0.399822	0.582270	1.558530	1	0.402406	0.588889	1.557489
1	-1.658056	-1.907257	-0.092767	1	-1.758442	-1.856569	-0.167984	1	-1.754372	-1.859688	-0.165795
1	-2.810934	-0.911085	0.782439	1	-2.791523	-0.846986	0.821347	1	-2.787203	-0.854051	0.824700
1	-1.118059	-0.969706	1.299432	1	-1.091832	-1.037310	1.227744	1	-1.087636	-1.038235	1.226589

References

[1] J.M. Simmie, W.K. Metcalfe, J. Phys. Chem. A, 2011, 115, 8877–8888.

[2] A.C. Davis, S. M. Sarathy, J. Phys. Chem. A, 2013, 117, 7670–7685.

[3] K. Sendt, G.B. Backsay, J.C. Mackie, J. Phys. Chem. A, 2000, 104, 1861–1875.

[4] Z. Tian, T. Yuan, R. Fournet, P.-A. Glaude, B. Sirjean, R. Battin-Leclerc, K. Zhang, F. Qi, Combust. Flame, 2011 , 158, 756–773.

[5] K.P. Somers, J.M. Simmie, F. Gillespie, U. Burke, J. Connolly,W.K. Metcalfe, F. Battin-Leclerc, P. Dirrenberger, O. Herbinet, P.-A. Glaude, H.J. Curran, Proc. Combust. Inst., 2013, 34, 225–232.

[6] L. Wei, C. Tang, X. Man, Z. Huang, Energy Fuels, 2013, Just Accepted Manuscript. DOI: 10.1021/ef401809y

[7] X. Ma, C. Jian, H. Xu, H. Ding, S. Shuai, H. Ding, Energy Fuels, 2013, 27, 6212–6221.

[8] L.-S. Tran, C. Togbé, D. Liu, D. Felsmann, P. Oßwald, P.-A. Glaude, R. Fournet, B. Sirjean, F. Battin-Leclerc, K. Kohse-Höinghaus, Combust. Flame, 2013, http://dx.doi.org/10.1016/j.combustflame.2013.05.027